

# GFZ

Helmholtz-Zentrum  
**POTS DAM**

HELMHOLTZ-ZENTRUM POTSDAM

**DEUTSCHES  
GEOFORSCHUNGSZENTRUM**

Rolf L. Romer, Hans-Jürgen Förster, Uwe Kroner,  
Axel Müller, Ronny Rößler, Jochen Rötzler,  
Reimar Seltmann, Thomas Wenzel (eds.)

## **Granites of the Erzgebirge**

**Relation of magmatism  
to the metamorphic and  
tectonic evolution  
of the Variscan Orogen**

**Guidebook to Eurogranites 2012 fieldtrip  
October 7 to October 13, 2012**

Scientific Technical Report STR12/15

Recommended citation:

Romer, R.L., Förster, H.-J., Kroner, U., Müller, A., Röbber, R., Rötzler, J., Seltmann, R., and Wenzel, T. (eds., 2012) Granites of the Erzgebirge - relation of magmatism to the metamorphic and tectonic evolution of the Variscan Orogen. *Scientific Technical Report 12/15*, GFZ German Research Centre for Geosciences.

For individual chapters:

*Author(s)* (2012) *Title*. In: Romer, R.L., Förster, H.-J., Kroner, U., Müller, A., Röbber, R., Rötzler, J., Seltmann, R., and Wenzel, T. (eds.) Granites of the Erzgebirge - relation of magmatism to the metamorphic and tectonic evolution of the Variscan Orogen. *Scientific Technical Report 12/15*, GFZ German Research Centre for Geosciences.

## Imprint

HELMHOLTZ CENTRE POTSDAM  
**GFZ GERMAN RESEARCH CENTRE  
FOR GEOSCIENCES**

Telegrafenberg  
D-14473 Potsdam

Printed in Potsdam, Germany  
September 2012

ISSN 1610-0956

DOI: 10.2312/GFZ.b103-12158  
URN: urn:nbn:de:kobv:b103-12158

This work is published in the GFZ series  
Scientific Technical Report (STR)  
and electronically available at GFZ website  
[www.gfz-potsdam.de](http://www.gfz-potsdam.de) > News > GFZ Publications

# Granites of the Erzgebirge



## Preface

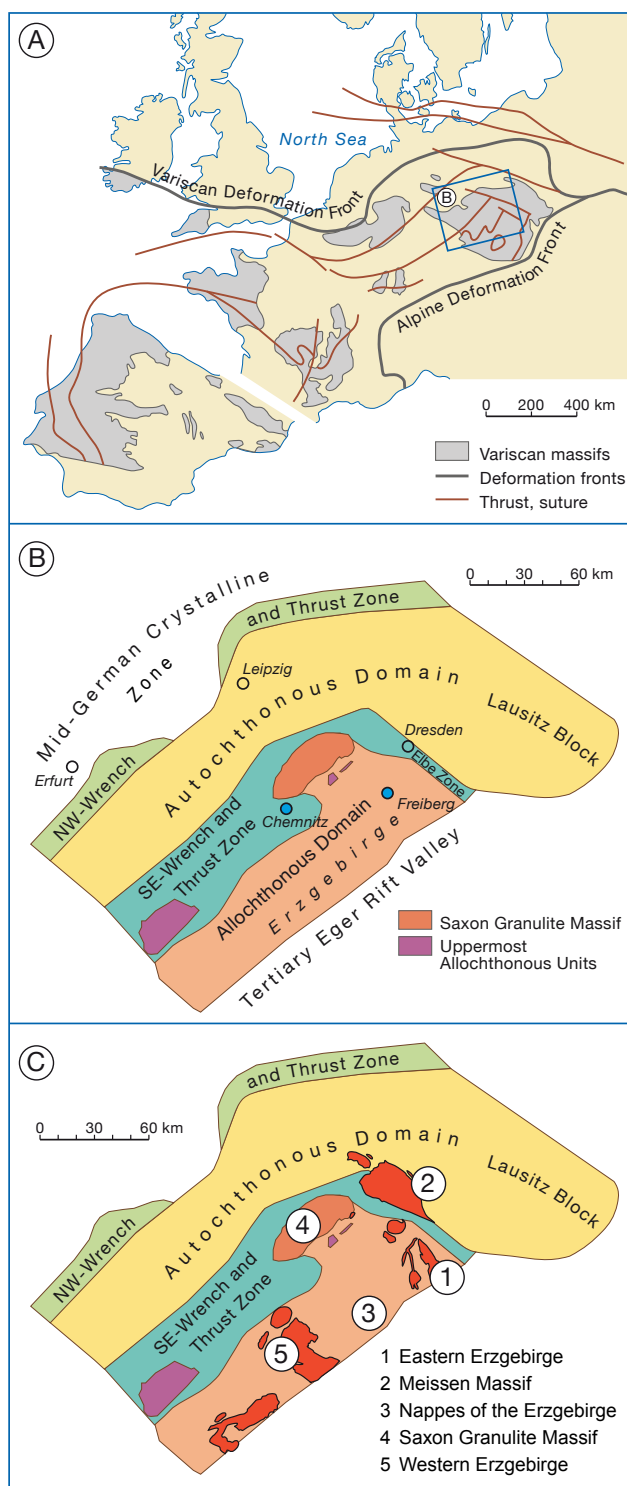
The Erzgebirge in the Saxo-Thuringian Zone of the Variscan orogen is a classical metallogenetic province known for its granite-related Sn-W mineralization, but also represents one of the largest U Provinces. After several hundred years of intense ore exploitation, mining stopped almost completely after 1990 and most mines are no longer accessible. Granitic magmatism in the Erzgebirge is geochemically highly diverse including I-, S-, and A-type granites that co-occur in the same region and have been emplaced within a relatively short period of only a few 10 Ma in the Carboniferous. To understand this diversity of magmatic rocks in the Erzgebirge and the factors that control their narrow age range and their spatial distribution, one has to see the Erzgebirge in a broader context, i.e., in relation with other Variscan metamorphic complexes (e.g., Saxon Granulite Massif) and the structures that control the emplacement of these metamorphic nappes (e.g., Elbe Fault Zone).

In a nutshell, both location and timing of granitic magmatism is related to different forms of reactivation of large-scale fault zones during the Variscan orogeny. The granites in the Erzgebirge represent crustal melts and their geochemical signatures are inherited from the volcano-sedimentary shelf deposits that form the protoliths of the metamorphic nappes. These mixed sources account for the chemical variability of coeval magmatism, but possibly also influence the spatial distribution of granitic intrusions.

The *Eurogranites 2012* field workshop focuses on the relation of different types of Late Palaeozoic granitic magmatism and the Variscan development of the Saxo-Thuringian Zone, i.e., (i) magmatism related to the nappe emplacement and exhumation of high-grade metamorphic crustal rocks, (ii) shallow-level magmatism post-dating the emplacement of the metamorphic nappes, and to a lesser extent (iii) felsic magmatism related to the post-Variscan reorganization of the stress field.

*Geological setting of the Erzgebirge in the Variscan orogen.* The Saxo-Thuringian Zone is structurally divided into three zones of contrasting Variscan overprint, i.e., an Autochthonous Domain with little or no Variscan overprint, an Allochthonous Domain with metamorphic nappes of contrasting P-T history (in part reaching UHT and UHP conditions), and a Wrench-and-Thrust Zone separating the Autochthonous and Allochthonous Domains. Variscan deformation in the Thrust-and-Wrench Zone allowed for the emplacement of rocks of the Allochthonous Domain from beneath the Bohemian Massif onto rocks of the Autochthonous Domain. The Erzgebirge and the Saxon Granulite Massif belong to the Allochthonous Domain. The Elbe Fault Zone is the structurally most distinct element of the Thrust-and-Wrench Zone.

*Granitic magmatism related to the emplacement of the Variscan nappes.* Emplacement of the nappes of the Erzgebirge and the Saxon Granulite Massif led to dextral strike-slip displacement along the deep-reaching Elbe



Fault Zone between c. 340 Ma and 325 Ma. During these movements, the huge sigmoidal Meissen Pluton was emplaced. The complex includes a magmatic suite that starts with a diorite monzodiorite-monzonite suite and evolves to increasingly stronger crustally influenced granites. A second group of granites related to nappe emplacement is exposed in the roof detachment of the Saxon Granulite Massif. Whereas the rocks of the Meissen Pluton carry an important mantle-derived component, the second group of granites represents crustal melts.

*Granitic magmatism post-dating metamorphism in the Variscan nappes.* The granites of the Erzgebirge are exposed along two zones, which are roughly parallel to the Elbe Fault Zone and strike at a high angle across the topographic trend, in the eastern and western Erzgebirge. They represent crustal melts and can be distinguished into five different types of magmatic suites that have been mostly emplaced between 327 and 318 Ma. The granites of the eastern Erzgebirge include a series of shallowly intruded I-, S-, and A-types granites. The most prominent feature of this magmatism is the Altenberg-Teplice complex, which includes volcanic and subvolcanic rocks and associated felsic dikes and highly evolved granite bodies of minor volume. The bulk of granites of the western Erzgebirge have been emplaced at a deeper level than those of the eastern Erzgebirge. Some of the western-Erzgebirge granites form larger composite plutons composed of texturally and geochemically distinct subintrusions. All these granites represent crustal melts and their large geochemical diversity within a small area reflects the lithological variability among the metamorphosed volcano-sedimentary rocks of the Variscan nappes that represent the granite source.

*Felsic magmatism related to the post-Variscan reorganization of the stress field.* With the erosion of the

Variscan orogen and the westward migration of the focus of collisional activity, reorganization of the stress field resulted in the Saxo-Thuringian Zone in the formation of numerous graben structures and basins whose position was largely controlled by old deep-reaching fault zones. These basins with their volcanosedimentary fill and minor granitic intrusions developed mainly between 300 and 285 Ma. This magmatism also involved mantle sources. Subordinate magmatism in the deeply eroded Erzgebirge with minor granite intrusions and volcanic and subvolcanic rocks may be related to this reorganization of the stress field.

*Metamorphic rocks of the Saxon Granulite Massif and the Erzgebirge.* The exhumation path of the felsic and mafic UHT rocks of the Saxon Granulite Massif gets close to the dry granite solidus, whereas the felsic UHP rocks of the Erzgebirge locally carry microdiamonds. Key locations from both metamorphic areas are shown to highlight the relation between tectono-metamorphic development and granitic magmatism.

The guidebook contains a thematic description and background information for each field day. The overall setting and development of the Saxo-Thuringian zone within the Variscan orogen is presented in Kroner and Romer (2010). This material is not included in this guide book (because of copyright reasons) and will be handed out to field trip participants as separate handout.

Kroner, U. & Romer, R.L. (2010) The Saxo-Thuringian Zone – tip of the Armorican spur and part of the Gondwana plate. In: Linnemann, U., Romer, R.L. (eds.) Pre-Mesozoic Geology of Saxo-Thuringia – From the Cadomian Active Margin to the Variscan Orogen. Schweizerbart Sci. Publ., Stuttgart, pp. 371-394.

| List of Contents  | Page |
|---|------|
| Rolf L. Romer<br>Geochronology of the Erzgebirge: a messy can of worms  | 1    |
| Axel Müller and Reimar Seltmann<br>The eastern Erzgebirge volcano-plutonic complex  | 13   |
| Thomas Wenzel<br>The plutonic rocks of the Meissen Massif (Germany):<br>evidence for subduction-modified mantle components<br>in a strike-slip related Variscan intrusion | 37   |
| Jochen Rötzler<br>The Erzgebirge  | 53   |
| Jochen Rötzler<br>The Saxon Granulite Massif  | 72   |
| Hans-Jürgen Förster<br>Late-Variscan felsic magmatism in the Erzgebirge–Vogtland  | 91   |
| Ronny Röbber<br>The petrified forest of Chemnitz – A snapshot of an<br>Early Permian ecosystem preserved by explosive volcanism   | 113  |



# Geochronology of the Erzgebirge: a messy can of worms

Rolf L. Romer  
 Inorganic and Isotope Geochemistry  
 GFZ German Research Centre for Geosciences  
 D-14473 Potsdam  
 romer@gfz-potsdam.de

Over the last 50 years an increasingly larger body of isotopic ages has been accumulated on magmatic and metamorphic rocks of the Erzgebirge. Quite some of these age determinations are not state of the art, largely because of (i) circular reasoning relying on incorrect lithologic correlations, (ii) concept-driven interpretation of the data, (iii) multiple reworking of material, and (iv) incompletely reset ages. This has led to a series of claims that entered literature and still are quoted despite of abundant evidence to the contrary.

Possibly most notorious among these incorrect claims are:

- \* there are two major phases of granitic magmatism in the Erzgebirge, an older and a younger one.
- \* granitic magmatism in the eastern Erzgebirge is generally younger than granitic magmatism in the western Erzgebirge.
- \* the high-grade metamorphic rocks of the Erzgebirge and the tectonically underlying Granulite Massif are old.
- \* vein-type mineralizations of U, Bi, Ni, Co, Pb, Ag, F, and Ba are genetically related to the granites.

In the following, I present a few examples for each type of mistake, explain which geological interpretations rely on this kind of problem, and present an internally consistent, simplified chronology of events in the Erzgebirge (note, there may still be some geochronological surprises lurking around the corner).

A second issue of confusion for decades is the source of the melts of the Erzgebirge granites, the extreme positions being (i) the granites represent crustal melts and (ii) the granites represent mantle-derived melts. With high-quality chemical and isotopic data becoming available, it was recognized that the I, S, and A type granites, which occur in essentially the same area, were emplaced at the same time. Furthermore, it was realized the  $\epsilon\text{Nd}$  values for all granite types fell in the same relatively narrow range, right in the middle between end values for the depleted mantle and the Palaeozoic rocks that form the protoliths of the metamorphic rocks of the Erzgebirge.

## 1. Lithological correlations and the age of magmatism in the Altenberg-Teplice Caldera

The volcanic and intrusive felsic rocks of the Altenberg area (rhyodacites, rhyolites, and granites) are part of a large volcanic complex (Fig. 1). The area has been intensely and multiply block-faulted after the emplacement of the volcanic rocks, has a rugged topography, and is relatively poorly exposed. The age

relations among the various units base on local contact relations and lithologic correlations. There are at least three generations of felsic dikes and two generations of lamprophyre dikes (e.g., Wetzel, 1984; Wetzel et al., 1985; von Seckendorff et al., 2004). Key units within this relative age sequence, however, are the calc-alkaline volcanic rocks of the Schönfeld area as these rocks are intercalated with sedimentary rocks that have been dated biostratigraphically (Westphal B-C or younger; Lobin, 1986; Schneider et al., 2005). In a drill-hole near Mikulow, about 30 km to the south of Schönfeld, calc-alkaline volcanic rocks have been found beneath the volcanic rocks of the Teplice Volcanic Complex (Breiter, 1995, 1997). Rocks from these two units have been correlated on basis of their calc-alkaline character and similar lithology (e.g., Breiter, 1995). If this correlation holds, the Teplice Rhyolite should be younger than c. 310 Ma, as are the felsic volcanic dikes and the lamprophyric dikes and the even younger granites and related Sn-ores. This relative age sequence is shown in Fig. 2 (left column). If the calc-alkaline volcanic rocks of the two areas are not correlated, some of the constraints on the age of magmatism fall away and an alternative age sequence is possible (Fig. 2, right column). This second interpretation is compatible with U-Pb and Re-Os dating of rocks from the Altenberg Sn-granite and Altenberg microgranite (Romer et al., 2007, 2010a), respectively, and is in line with the Ar-Ar age of a lamprophyre dike from Lauenstein (no exposed contact with the magmatic rocks of the Altenberg-Teplice Caldera; Werner and Lippolt 1998).

Direct dating of the various magmatic rocks *would be* the most straightforward approach to resolve the problem, but has encountered several problems. (i) Mineralization and multiple tectonic reactivation of the area have upset the Rb-Sr system of granites, yielding “isochrons” with too young ages and/or too low apparent initial  $^{87}\text{Sr}/^{86}\text{Sr}$  (e.g., Gerstenberger, 1989). (ii) Zircon extracted from the volcanic and intrusive rocks is generally dominated by inherited zircon (e.g., Hoffmann et al., 2012). Furthermore, as zircon of these granites typically is very uranium-rich, it accumulates radiation-damages and becomes metamict and, thus, a partially open system. Minor loss of Pb may not be apparent in low-resolution age determinations (e.g., LA-ICP-MS), but would result in inaccurate (generally too young) ages (see also section on *Analytical resolution and mixed ages*). Indirect dating approaches such as dating magmatic or hydrothermal ore minerals in mineralized granites may be a better way to go, although this approach is restricted to particular lithologies. This alternative approach, however, may resolve the geochronological ambiguity outlined in Fig. 2, in particular if the

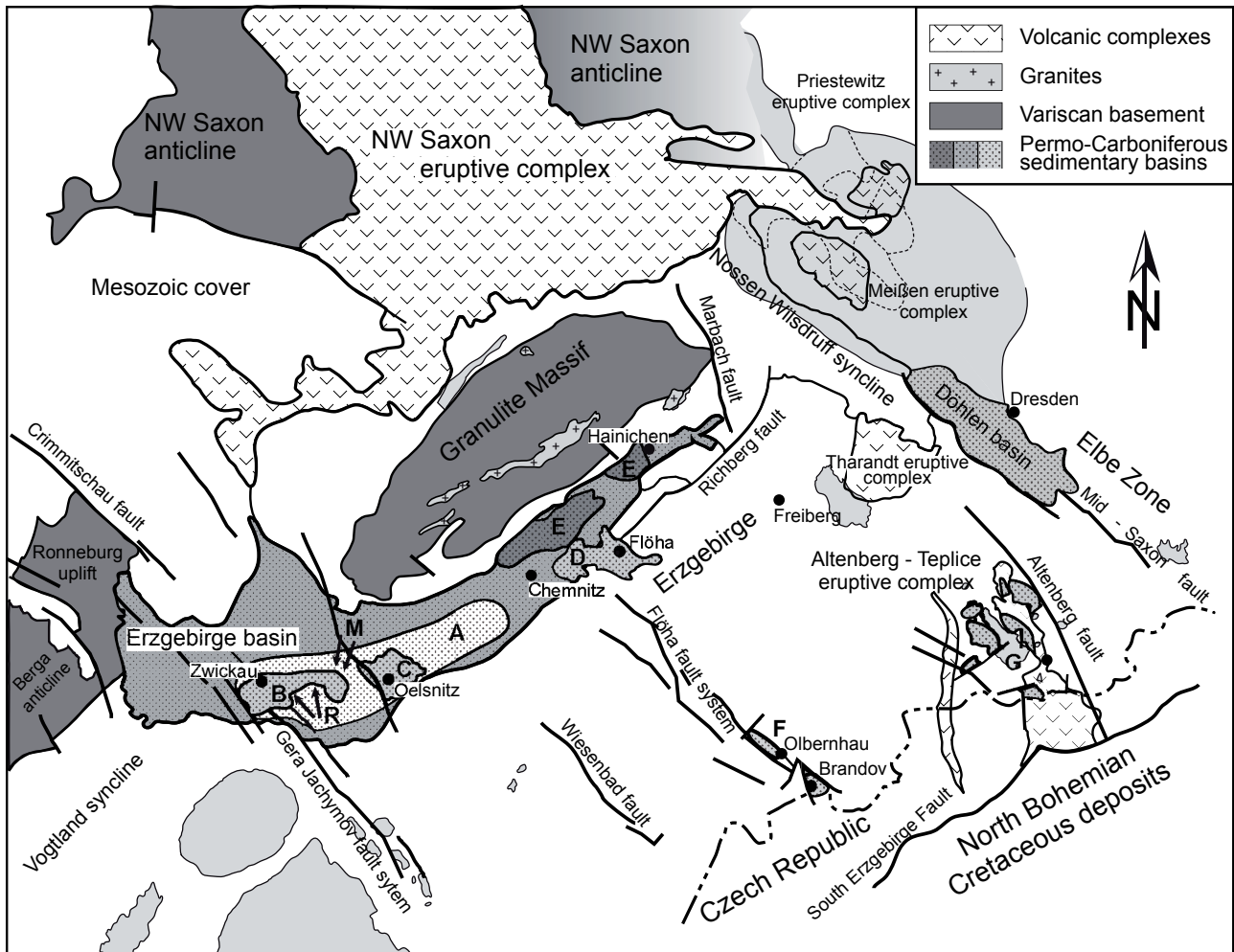


**Fig. 1.** Simplified geological map showing the distribution of early Carboniferous magmatic rocks and the late Carboniferous Saxon volcanosedimentary basins. Sedimentary basins: **A** – primary extend of the Westphalian D to ?Cantabrian Zwickau-Oelsnitz basin, **B** – erosional remnant of the Zwickau subbasin, **C** – remnant of the Oelsnitz subbasin, **D** – Westphalian B/C Flöha basin, **E** – remnants of the Visean Hainichen basin, **F** – remnants of the Westphalian B/C and Permian Olbernhau-Brandov basin; **G** – remnants of the Westphalian B-D Schönfeld-Altenberg basin, **R** – Reinsdorf fan of the Zwickau subbasin, **M** – Mülsen fan of the Zwickau subbasin. The thick line around the Erzgebirge basin marks the actual extent of the Rotliegend Chemnitz basin. Modified from Schneider and Romer (2010) and complemented with data from Förster and Romer (2010).

ore minerals are clearly older than expected by one of the models. Note, direct dating of the ore mineral has one big advantage: There is no inheritance. Potential candidates would be molybdenite for Re-Os dating and columbite-tantalite and hübnerite-ferberite for U-Pb dating.

Using different names for the calc-alkaline volcanic rocks from Schönfeld and Mikulow (e.g., Romer et al., 2010a; Hoffmann et al., 2012) only provides a partial relief from the problem. The earlier correlation of the volcanic rocks from both locations, calling both of them “Schönfeld volcanites”, brought along a problem that will stay: Some statements about the Schönfeld volcanic rocks base solely on data from the Mikulow location. In other words, some of the properties of the Mikulow volcanic rocks have been transferred to the Schönfeld volcanic rocks, most importantly among them statements about contact relations. This unfortunate connection of a lithologic name with properties of rocks from a different location may make it in continuation very difficult to distinguish in older literature between observation and interpretation-based inference. Even after introducing separate names for the two units: There may be plenty of misunderstanding waiting down the road.

## 2. Two events of late-Variscan granitic magmatism in the Erzgebirge?

Field evidence demonstrates that some granites have intruded in other granites, which led to the correct distinction in older and younger granites (e.g., Lange et al., 1972; Tischendorf, 1989). This distinction, however, does not tell how much time had elapsed between the emplacement of the older granite and the emplacement of the younger granite. Only with the first (“precise”) isotopic ages becoming available, it was possible to get a hold on this age difference and the problems started.

In the eastern Erzgebirge, the age of the Altenberg granite had been constrained by lithologic correlations and field-relations that defined a relative age sequence to the Schönfeld volcanic rocks that were biostratigraphically dated (see previous section). Rb-Sr WR dating gave an “isochron age” of  $305 \pm 3$  Ma, which apparently confirmed the earlier inference on the emplacement age of this granite. The forbiddingly low  $^{87}\text{Sr}/^{86}\text{Sr}$  initial (less than 0.700) was not taken as indication that this data set may not have fulfilled the requirements for an isochron. Instead, processes were modeled that would account for a too low initial without affecting

the age (for a discussion see Gerstenberger, 1989). In the western Erzgebirge, granites had been emplaced into metamorphic rocks. The age of these metamorphic rocks provides only a maximum age for the time of granite emplacement. Therefore, the emplacement age of these granites is only known from isotopic dating, including Rb-Sr WR dating and later U-Pb dating of accessory phases (zircon, monazite, uraninite). The Rb-Sr WR work on regionally sampled granites gave an age of  $332 \pm 5$  Ma to  $320 \pm 6$  for samples from the “older” granite and  $328 \pm 5$  Ma to  $323 \pm 1$  Ma for the “younger” granites (Gerstenberger et al., 1982). This overlap of ages agrees with later U-Pb dating (cf. Förster et al., 1999; Romer et al., 2007). These ages, however, are markedly older than the age constraints for the Altenberg granite, which represents the last major magmatic event in the Altenberg-Teplice caldera. These Rb-Sr data form the base for the incorrect idea that magmatism in the eastern Erzgebirge is younger than magmatism in the western Erzgebirge.

U-Pb dating did not confirm these age groups. Instead, granites fall predominantly in the age range from 318 to 327 Ma (Förster et al., 1999; Förster and Romer, 2010), the “younger” and “older” granites having essentially the same age. The U-Pb data imply that the age difference between granites with contact relations that allow to distinguish into an “older” and a “younger” one is considerably smaller than previously thought. This small time window, however, has additional implications: I-, S-, and A-type granites are essentially coeval. The range in contrasting granite types is not due to changes in tectonic setting, but in contrasting source lithologies, which in turn requires that these contrasting sources are available for melting at the same time. The simplest and most straightforward way to get such a diversity of granitoids is that the diversity is inherited from the source, which in the case of the Erzgebirge are the volcano-sedimentary shelf deposits of the Gondwana margin that are tectonically stacked in the metamorphic nappes of the Erzgebirge (for details see Förster and Romer, 2010).

Note, there are a few occurrences of granitic and felsic volcanic rocks with emplacement ages that correspond to the age range formerly assigned to the group of younger granites. These rocks form relatively small intrusions and include a high portion of volcanic and subvolcanic rocks. Similar volcanic and subvolcanic rocks of corresponding age occur also in the structurally controlled basins bordering the Erzgebirge and local remains of such basins atop of the metamorphic rocks of the Erzgebirge. In deeper eroded settings, where the post-Variscan sedimentary rocks have been eroded and only the deeper levels of the magmatic system are preserved, these “younger” subvolcanic and volcanic rocks commonly have not been linked to the coeval magmatic rocks in the basins bordering to the Erzgebirge. As the 318 to 327 Ma granitic rocks of the Erzgebirge and the 290 to 305 Ma old felsic rocks of the fault-bound sedimentary basins formed in different tectonic settings (e.g., Kroner and Romer, 2010), the “younger” felsic rocks of the Erzgebirge are unlikely to be related with the 318 to 327 Ma old magmatism.

### 3. Analytical resolution and mixed ages

The granitic rocks in the Erzgebirge are dominantly derived from crustal sources and, therefore, have a high potential for inherited zircon. Sources for inherited zircon include rocks of the Cadomian magmatic arc (570 to 540 Ma), which are now exposed in the gneiss domes of Freiberg, Reitzenhain, and Lauenstein (Fig. 1), and (ii) the Palaeozoic volcano-sedimentary cover that were deposited on the Cadomian basement and that are exposed in the Variscan nappes. Detrital zircon in the sedimentary rocks of

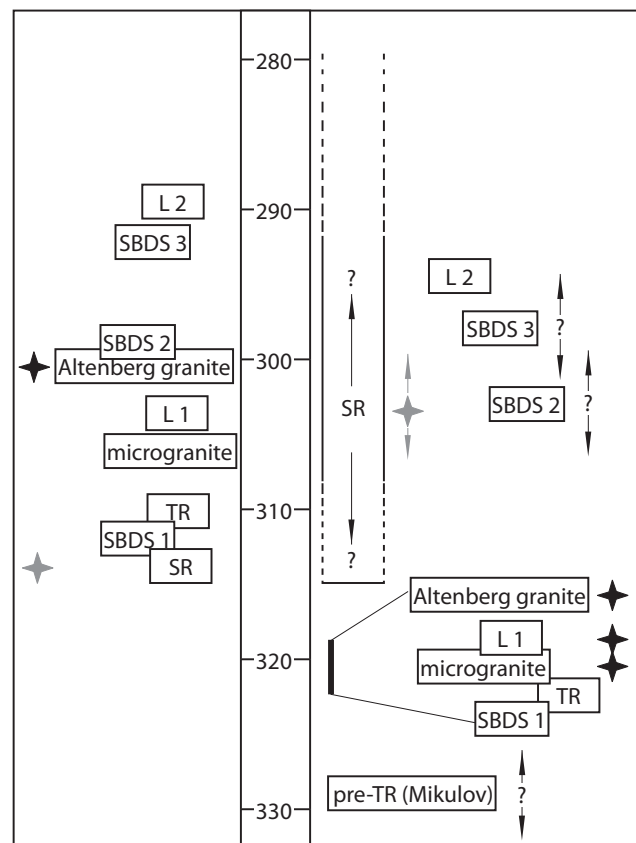


**Fig. 2.** Relative sequence of magmatic events in the Teplice-Altenberg area. The most fundamental difference between the two sequences is the interpretation of the calc-alkaline volcanic rocks as one event and as two events, respectively. The actual position of events on the absolute time scale basing on isotopic data in part differs due to contrasting interpretation of available data. Diagram from Romer et al. (2010a). For discussion and data sources of isotopic ages see Romer et al., (2010a). **SR** = Schöpfung Rhyolite sensu stricto; **TR** = Teplice Rhyolite; **SBDS** = Sayda-Berggießhübel Dike Swarm (three generations); **L** = lamprophyres (two generations); **pre-TR** (Mikulov) = volcanic rocks underlying TR at the Mikulov location; note, pre-TR and TR are geochemically unrelated. Black asterisks mark lithologic units that have been isotopically dated; the age for the Altenberg granites (left column) represents a Rb–Sr whole rock model age. Note, palaeobotanic data constrain the deposition age for the Putzmühle, Schöpfung, and Mühlwald formations to Westphalian or younger (pers. comm. J. Schneider to R.L. Romer, 2010). The earlier narrow bracketing to Westphalian B/C and Westphalian C/D, respectively, was largely influenced by then prevailing ideas about the age of the “younger” granites. Furthermore, SR and pre-TR are two separate events rather than one event.

the Palaeozoic cover are dominated by zircon from the Cadomian magmatic arc and subordinate zircon indicative for a derivation from the West African craton (e.g., Linnemann et al., 2004, 2010). In addition, there may be inherited zircon from the volcanic rocks related to the Ordovician rifting of peri-Gondwana. During the Variscan orogeny there may have been growth of new zircon and of rims on old zircon. Peak metamorphic conditions in the high-grade metamorphic nappes were reached at c. 340 Ma and the

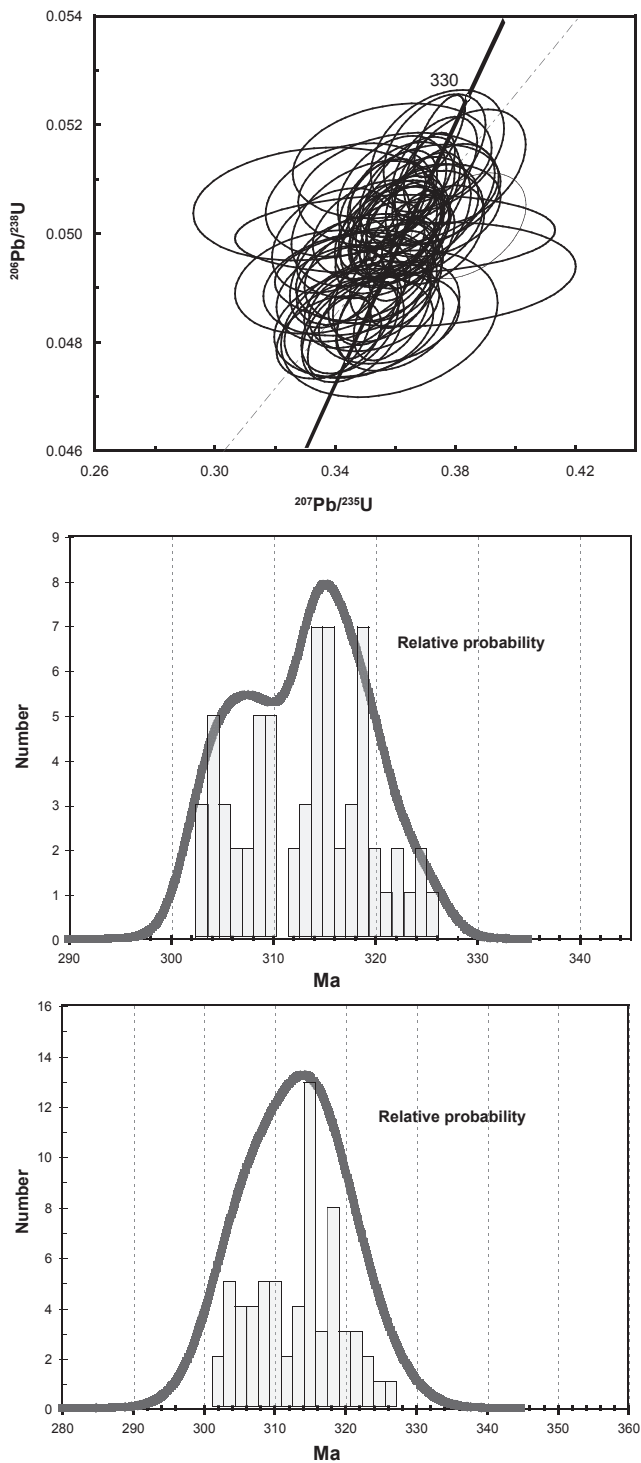


**Fig. 3.** Artificial U-Pb data set to illustrate the relation between analytical uncertainty and data heterogeneity. If the error ellipses shown correspond to  $2\sigma$  errors, the data correspond to a bimodal distribution. If the error ellipses, however, correspond to  $1\sigma$  errors, the data are compatible with one zircon population (at the  $2\sigma$  level). Thus, for the data with the smaller errors, a bimodal sample population is resolvable, for the data with the larger errors, the data do not show a bimodal distribution. Note, the analytical uncertainties used for the diagrams are in the range of published LA-ICP-MS and SHRIMP data (there are better ones and there are worse ones).

metamorphic rocks were rapidly exhumed (e.g., Willner et al., 1997; Rötzler et al., 1998).

The Variscan granites contain apart from newly formed zircon also inherited zircon with thin overgrowth zones or without overgrowth. Inherited zircon from these protoliths may cause significant problems in dating the emplacement of the granites in the Erzgebirge. Even at a low analytical precision – inherent to some fast dating methods – pre-metamorphic inherited zircon crystals will be readily recognized if their apparent age is forbiddingly old (i.e., older than the age of metamorphism) or the data fall distinctly to the right of the concordia (Fig. 3). The problem is entirely different for inherited zircon that formed during the Variscan orogeny. At an analytical uncertainty of 5%, each spot for zircon from Variscan granites or metamorphic rocks has an age uncertainty of  $\pm 16$ -17 Ma. Thus, the age spots of zircon from 325 Ma old granite and 340 Ma old metamorphic rocks can not be separated from each other, but overlap entirely. For large data sets with 30 to 50 analyses, it may be possible to demonstrate that the distribution of the apparent  $^{206}\text{Pb}/^{238}\text{U}$  ages does not correspond to a Gauß distribution, but corresponds to two overlapping Gauß distributions. Mathematical tools actually would allow to separate these two events by fitting two Gauß distributions to the data, with the mean and width of the distributions representing the best estimate for the age of the two events and their uncertainty. But at for data base of 8 to 15 spots, it is not possible to distinguish between one zircon population and two or more similarly aged zircon populations (Fig. 3).

The data reduction of U-Pb spot analyses (SHRIMP, LA-ICP-MS) involves the following assumptions: (i) there is only one population of zircon included in the calculation of the age; (ii) the data are not affected open system behavior (e.g., minor Pb-loss) or such samples have been recognized and, therefore, were omitted from the calculation; and (iii) the data scatter is entirely due to analytical uncertainties (i.e., not the samples) and, therefore, the data scatter about the true values. If these assumptions are fulfilled, the error is calculated as “error of the mean” ( $\sigma_m$ ) rather than the “standard deviation” ( $\sigma$ ). The two different kinds are related with each other by:  $\sigma_m = \sigma/\sqrt{n}$ , with  $n$  being the number of measurements. It is obvious that  $\sigma_m$  gets the smaller the more measurements are made. One important point is that for bimodal zircon populations of two events that are close in time (i.e., separated by a similar amount of time as the analytical uncertainty of the method) may yield apparently precise age data that are not accurate, as the average is between the two events. This point is illustrated in Fig. 3

#### 4. From ancient to Variscan metamorphism

Although nappes have been recognized in the Erzgebirge by Kossmat (1927), there was a return of the old and incorrect idea that (i) metamorphic grade and age are related with each other and (ii) the interpretation of the Erzgebirge as an essentially undisturbed lithostratigraphic profile. As a consequence thereof, many older maps and publications (pre-1990) refer to the metamorphic rocks of the Saxon Granulite Massif being Archaean and those of the Erzgebirge being Proterozoic to Palaeozoic. There are isolated Rb-Sr WR ages that seemed to support these claims. Rb-Sr work on the Saxon Granulite Massif giving an anomalous high apparent age bases on regionally sampled lithologies that are genetically not related with each other, are now known to have different age, and definitively to have had different initial  $^{87}\text{Sr}/^{86}\text{Sr}$  values, i.e., do not fulfill the basic requirement for dating. Palaeozoic Rb-Sr WR ages for regionally sampled lithostratigraphic units of the Erzgebirge most likely were obtained on samples from the metamorphosed volcanic and sedimentary rocks that had similar

initial  $^{87}\text{Sr}/^{86}\text{Sr}$  values and age. These local to regional Rb-Sr WR ages by and large correspond to later produced zircon ages. These ages, however, do not represent the age of metamorphism, but are “close” to the time of deposition of the volcanic and sedimentary rocks.

In the late 1980ies and early 1990ies, abundant geochronological evidence demonstrated that peak metamorphic conditions were reached in the Erzgebirge and the Saxon Granulite Massif essentially at the same time, at about 340 Ma. This age was obtained for zircon, monazite, and titanite using the U-Pb method (e.g., von Quadt, 1993; von Quadt and Günther, 1999; Kröner and Willner, 1998; Romer and Rötzler, 2001). Furthermore, Sm-Nd dating of garnet gave also late Palaeozoic ages for peak metamorphism, although the garnet ages ranged from 380 to 315 Ma (e.g., von Quadt, 1993; Schmädicke et al., 1995), i.e., in part were distinctly older than peak metamorphism or were younger than the deposition age of conglomerates containing fragment of the metamorphic rocks. The older Sm-Nd ages typically were interpreted to date prograde garnet growth, whereas the significance of the too young ages remained enigmatic, in part being speculatively interpreted that parts of the complex already were available for erosion when other parts still were at depth. These anomalous Sm-Nd ages, however, may represent an artefact from the metamorphic reaction history (Romer and Rötzler, 2011). Note, in other tectonostratigraphic units (e.g., the uppermost allochthonous units of the Münchberg Massif), peak metamorphism (and exhumation) occurred earlier, i.e., at c. 380 and c. 360 Ma. But these events are largely unrelated with the metamorphic development in the Erzgebirge and the Saxon Granulite Massif.

Thermal modeling of the P–T path of the various metamorphic units demonstrates that the UHP units could not remain at mantle depth for more than 3 Ma (otherwise they would reach higher peak temperatures), whereas the UHT rocks of the Saxon Granulite Massif had to reside at mantle depth for at least 20 Ma (cf. Kroner and Görz, 2010). After 340 Ma, the various units were exhumed rapidly and emplaced in mid-crustal level. This is known from the following observations: (i) shallow intrusions in the Saxon Granulite Massif and the Erzgebirge date at c. 333 Ma and 327–318 Ma, respectively. (ii) The synkinematic Berbersdorf granite was emplaced at c. 338 Ma into the middle crust. (iii) The oldest Rb-Sr ages (c. 338 Ma) of white mica from the Cordierite Gneiss Unit reflect the tectonic juxtaposition of the exhuming hot granulites against metamorphic rocks of lower grade. Zircon from a migmatite lens in the same unit yields the same age (Vavra and Reinhard, 1997), although the original interpretation (earlier migmatite event) is not maintained any longer (cf. Rötzler and Romer, 2010). (iv) The metamorphic nappes of the Erzgebirge contains rocks with very distinctive signatures, in particular highly radiogenic  $^{87}\text{Sr}/^{86}\text{Sr}$  (already at the time of metamorphism). This signature appears in the sediments in the foreland of the Erzgebirge at 339 Ma, indicating that the units with anomalous  $^{87}\text{Sr}/^{86}\text{Sr}$  became available for erosion (cf. Romer and Hahne, 2010). (v) Ar-Ar dating of white mica from the metamorphic nappes and deformation zones between them range from 330 to 340 Ma (Werner and Lippolt, 2000).

Whereas Sm-Nd ages younger than 340 Ma typically were considered to represent cooling or (if forbiddingly low) to have been affected by later disturbances, the Sm-Nd ages older than 340 Ma were interpreted to date garnet-growth on the prograde path of the metamorphic rocks. Romer and Rötzler (2001, 2011) discussed the possibility of initial isotopic disequilibrium between garnet and whole-rock sample as a result of the sequential nature of metamorphic reactions may account for both too young and too old Sm-Nd garnet ages. In particular, they pointed out that

the incorporation of Nd derived from consumed old xenotime (typically reflected in the high-Y cores of garnet) results in too old ages (for details see Fig. 4).

Extensive isotopic dating has shown: (i) the oldest protoliths for the metamorphic nappes are remains from the Cadomian magmatic arc (c. 570 to 540 Ma; Linnemann et al., 2004) and are preserved in the gneiss domes of Freiberg, Reitzenhain, and Lauenstein. (ii) The protoliths of the metamorphic nappes is dominated by Palaeozoic (500 to 415 Ma) volcanosedimentary rocks of the former Gondwana schelf (cf. Mingram, 1998; Rötzler and Plessen, 2010). (iii) Metamorphic mafic rocks in the Erzgebirge and the Saxon Granulite Massif dominantly have 500 to 485 Ma old protoliths, which possibly formed during the rifting of peri-Gondwana that eventually resulted in the opening of the Rheic ocean. (iv) Metamorphism in the Erzgebirge lasted only a few million years) and peaked at c. 340 Ma. The locally preserved “upper allochthonous units” (e.g., Münchberg Massif, Wildenfels, and Frankenberg) are related to an earlier event and experienced peak metamorphic conditions at c. 380 Ma. (v) There are no “old” (Archaean to Proterozoic) rocks in the Erzgebirge and the Saxon Granulite Massif.

## 5. Age relations between granites and ores in the Erzgebirge

There are two types of granite-related mineralization in the Erzgebirge: (i) mineralizations *genetically* related with the granites and (ii) mineralizations *spatially* related with the granites.

Mineralizations *genetically* related with the granites include high-temperature deposits of Sn, Mo, and W that occur in magmatic and greisen-type rocks. The formation of these deposits is directly related to the emplacement and crystallization of the associated granites. In particular if the dating of the granite is problematic, because of significant amounts of inherited zircon or later alteration, the direct dating of the ore minerals may provide an alternative dating approach.

Mineralizations *spatially* related with the granites include low- and medium-temperature vein-type deposits of Ag, U, F, and Ba. The typical feature of these deposits is that they are hosted by the metamorphic rocks in the vicinity of the granites. Traditionally, it was thought that the metal content of these deposits was brought by the granite and the formation of the deposits was triggered by the emplacement of the granites. This deep-rooted incorrect conception resulted in a marked criticism of isotopic ages that were younger than the granites rather than a reconsideration of the genetic model (e.g., Lippolt, 1984). Systematic dating of distinctive mineral assemblages of the Aue-Niederschlema uranium deposit (Förster, 1996) eventually demonstrated that the oldest mineral assemblages are more than 40 Ma younger than the granite and that different mineral assemblages show contrasting ages, spread over more than 200 Ma. Actually, the ages found in one single deposit are found throughout the entire Saxo-Thuringian Zone, indicating (i) the vein-type mineralizations are not coeval with granite emplacement, (ii) mineralization and metal redistribution is pulsed, and (iii) these pulses correlate with major tectonic events on the regional and even larger scale (for details see Romer et al., 2010b). For instance, the major pulse of mineralization around 280 Ma coincides with the post-Variscan reorganization of the regional stress field and the development of the Oslo Rift. Later pulses of metal redistribution correspond to the rifting of Tethys and North Atlantic and reorganizations in the system of spreading ridges (cf. Fig. 5). The spatial relation between granites and vein type mineralizations has rheological reasons. For instance, the vein type mineralizations of the Aue-Niederschlema district are located in deformation zones close to the outer margin of the

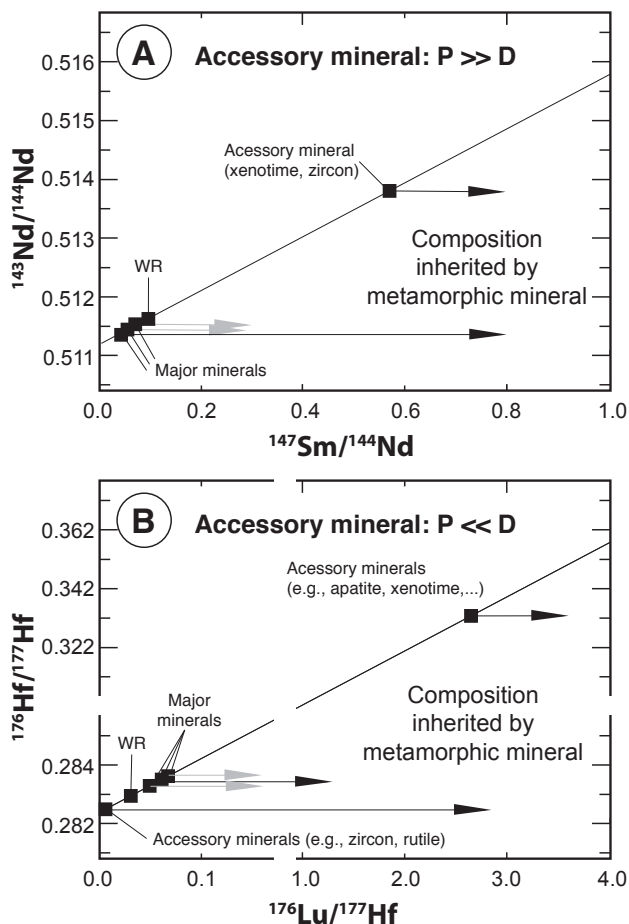


**Fig. 4.** Effect of pre-metamorphic accessory minerals that strongly enrich parent and daughter element, respectively, on the isotopic evolution of major minerals and the initial isotopic composition of metamorphic product minerals. The diagram shows the composition of the reactant minerals at the time of metamorphism. The slope of the line depends on the age of the precursor minerals. Fig. 4A shows a possible situation for the Sm-Nd dating of metamorphic garnet; Fig. 4B shows the situation in Lu-Hf dating of metamorphic garnet. A datable product mineral would acquire an initial isotopic composition that corresponds to the weighted average of the reactant minerals and a high parent-to-daughter ratio due to the strong preference for the parent element. Note, the horizontal arrows to the right schematically show the initial isotopic composition of Nd and Hf, respectively, if the daughter element of the product minerals is only derived from the reactant mineral at the rear end of the arrow. The initial slope of a two-point isochron between the whole rock sample and the product mineral (e.g., garnet for Lu-Hf or Sm-Nd dating) may encompass a wide range of values, depending on involved minerals and extent of parent-to-daughter element fractionation. Whether the metamorphic consumption of an accessory mineral sequestering parent or daughter element results in a too old or too young age depends on the relation between the parent-to-daughter ratios of the whole rock sample and the accessory mineral, i.e.,  $P/D_{Acc}$  and  $P/D_{WR}$ . From Romer and Rötzler (2011).

contact metamorphic aureole. The change in rock strength from the granites and its high-grade contact-metamorphic aureole to the low-grade regionally metamorphosed rocks is strongest at the outer margin of the contact metamorphic aureole and contributes in controlling the position of the deformation zone. The metal content of mineralizations in part may be derived from leaching/alteration of the granites. For instance, altered granite shows markedly lower U contents than unaltered granite and, thus, may have been acted as an U-source. Other elements such as Ni in some U-deposits, however, are derived from the wall rocks rather than from the granites.

## 6. An updated chronology of the Erzgebirge

The protoliths of the metamorphic rocks of the Erzgebirge and the Saxon Granulite Massif include (i) former Cadomian basement (580-540 Ma) and (ii) the volcano-sedimentary rocks that after the opening of the Rheic ocean were deposited on this Cadomian basement (Linnemann et al., 2004, 2010). After the opening of the Rheic Ocean, which was “heralded” in the Cambrian by the development of graben structures, in the Ordovician, the sedimentary material was derived from Gondwana. The volcanic material includes both mafic and felsic material and is dominantly of late Cambrian to Ordovician age. Locally, there were larger intrusive bodies were emplaced, such as the gabbros in the Vesser Zone (Kemnitz et al., 2002).

The late Cambrian and Ordovician extension of the peri-Gondwana margin introduced a rheological heterogeneity that largely influenced the development of the Variscan orogen, especially the distribution of high- and low-strain areas, low- and high-grade metamorphic belts, and the regional age variation of comparable rocks that obviously experienced similar P-T-D developments (cf. Kroner et al., 2007; Kroner and Romer, 2010). The thick blocks of Cadomian crust trapped between the colliding masses of Gondwana and Laurussia could not be subducted when they collided with Laurussia, which resulted in establishing a new subduction zone behind the block. Therefore, there are many subduction zones in Variscan Europe. The stretched continental crust – covered by the volcano-sedimentary shelf sequences – was subductable and became subducted. Some of these rocks are now preserved in the high-strain high-grade metamorphic belts, such as the Saxon Granulite Massif and Erzgebirge. The high-grade rocks to the east of the Bohemian Massif are related with the collision of Tépala-Barrandian Unit, whereas the high-grade rocks to the north, west, and south of the Bohemian Massif are related to the same subduction zone and reflect lateral escape and backflow, respectively, from beneath the Bohemian Massif (see Kroner et al., 2007; Kroner and Romer, 2010).

The metamorphic rocks of the Saxon Granulite Massif and the erzgebirge reached metamorphic peak condition at c. 340 Ma and thereafter were rapidly exhumed to mid-crustal levels (Rötzler and Romer, 2001, 2010). The stackig occurred between 340 and 330 Ma and the nappes contain rocks that reached widely different depth and peak temperatures. The rocks of the Saxon Granulite Massif and the Erzgebirge had been subducted at different time, as the ultra-high temperature rocks of the Saxon Granulite Massif needed a residence at depth of least 20 Ma to reach peak temperatures  $>1000^{\circ}\text{C}$ , whereas the ultra-high pressure rocks of the Erzgebirge reached their peak temperatures already after 3 to 4 Ma at depth (Kroner and Görz, 2010). The rocks of the Cadomian basement never reached high-pressure conditions and form now gneiss Domes.

The rapid exhumation of the metamorphic rocks of the Saxon Granulite Massif and the Erzgebirge was possible because of movements along the Central Saxon Lineament (forms the

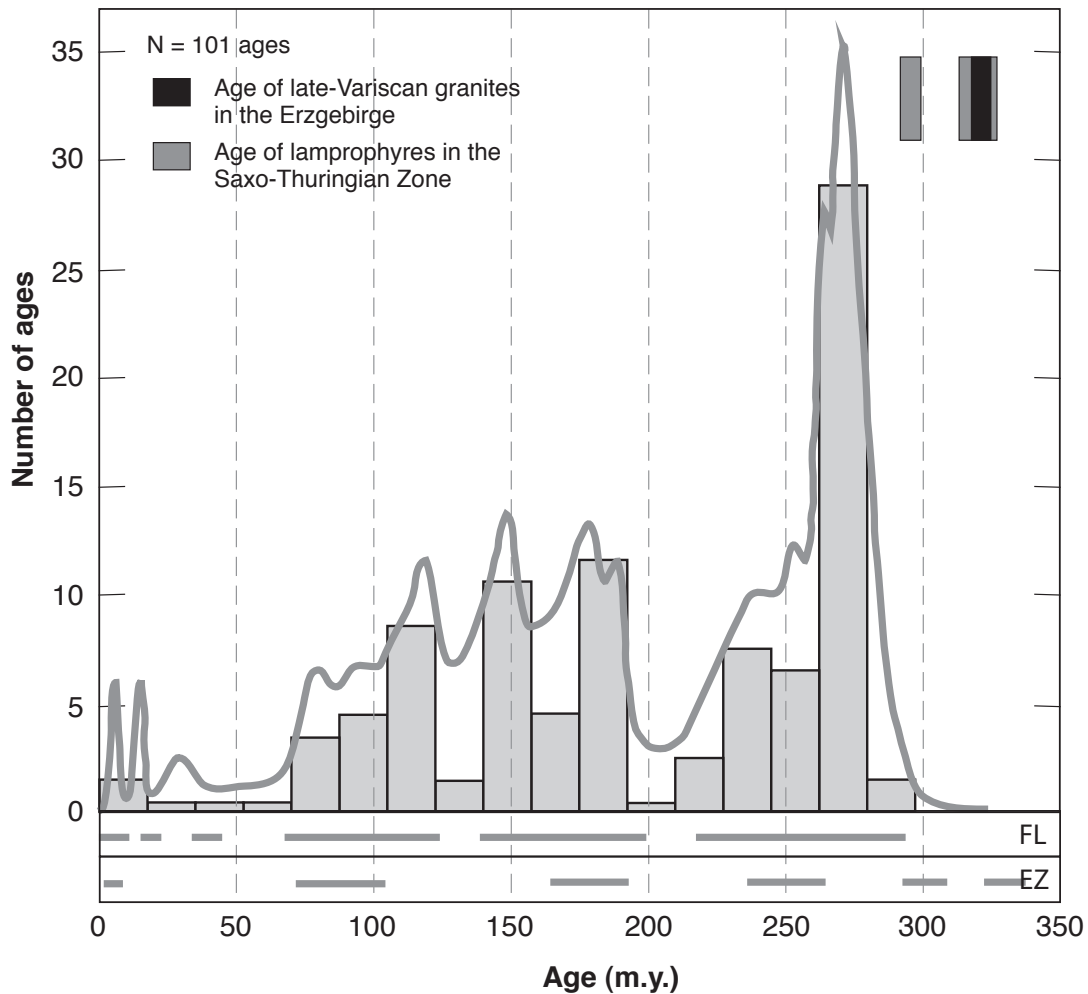


**Fig. 5.** Distribution of isotopic ages for post-Variscan hydrothermal activity in the Saxo-Thuringian Zone. Multiple datings of the same vein have been filtered away. EZ = Elbe Zone; FL = Franconian Line. For data source see Romer et al., (2010b).

footwall of the Saxon Granulite Massif) and along the Elbe Zone. The movements were associated and possibly faciliated by the emplacement of magmatic rocks, i.e., the monzonite-to-granites of the Meissen Massif (Elbe Zone) and the granites of, e.g., Berbersdorf in the margin of the Saxon Granulite Massif. Granites intruded during the emplacement of the Variscan metamorphic rocks of the Saxon Granulite Massif and the Erzgebirge to mid-crustal levels differ from the granites of the Erzgebirge in the following way: (i) The magmatic rocks of the Meissen Massif undoubtedly contain mantle material. Younger part of the complex show an increasingly stronger effect of crustal assimilation. (ii) The granites of the Saxon Granulite Massif have unusually high contents of  $K_2O$ , Ba, Sr, Pb, U, and Th (Förster and Romer, 2010) and may be closely related to the felsic ultra-high temperature rocks of the Saxon Granulite Massif, the UHT rocks having been too dry to melt, whereas the granites were derived from melting of the same rocks with slightly higher water content.

Vollbrecht et al. (1989) inferred from geophysical data a late Carboniferous indentation of a crustal block to the west or southwest of the Bohemian Massif. This collision of the Protoalps, another fragment of thick Cadomian crust, resulted in (i) the folding of the foreland (flysch-type) sedimentary rocks and the reactivation of fault zones transverse to the strike of the Erzgebirge. Although these folds in the foreland belong to the most spectacular

Variscan deformation structures, they post-date the main events of the Variscan orogen in the Saxothuringian Zone. The granites magmatism in the Erzgebirge (from 327 to 318 Ma) falls in the same age range the indentation of the Protoalps. The temporal coincidence of granite emplacement and collision of the Protoalps and the spatial association and similar orientation of granite intrusions and Erzgebirge-transverse fault zones indicates that these events and structures are closely related. The fault have facilitated the emplacement of the various types of Erzgebirge granites, whereas the duration of movements along these zones constrained the duration of granite emplacement.

With the onset of the reorganization of the stress field in central Europe, late Carboniferous to Permian fault bound basins and graben structures developed. The orientation and segmentation of these basins shows that old structures were reactivated, in particular structures being parallel to the Central Saxon Lineament and to the Elbe Zone and Erzgebirge-transverse faults (for a review see Schneider and Romer, 2010). The Variscan orogenic belt in the region of the Saxo-Thuringian Zone already was already deeply eroded at that time (cf. Schneider et al. 2006). This is in line with the chemical and Nd isotopic composition of shales – deposited in these basins – that indicate the major part of the sedimentary fill of the basins is derived from the volcanic centers (Romer and Hahne, 2010), which had developed locally at deep-reaching

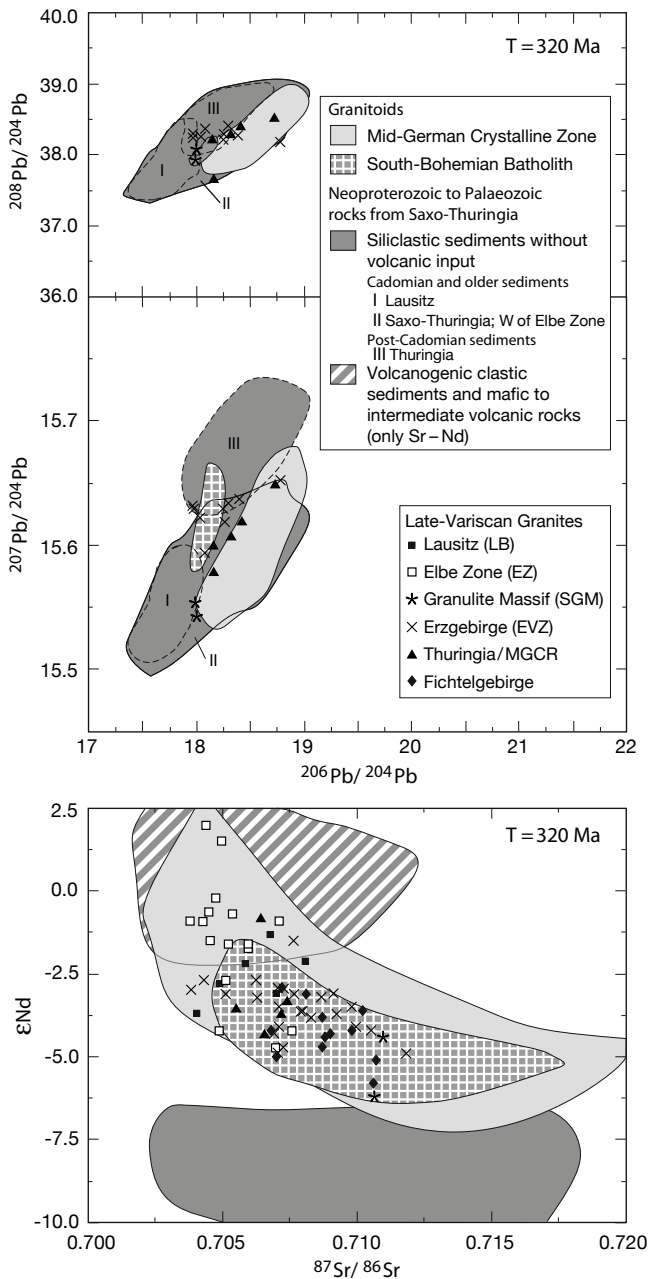


**Fig. 6.** The Variscan granites of the Erzgebirge plot in the  $^{87}\text{Sr}/^{86}\text{Sr}_{\text{init}}$  vs.  $\epsilon\text{Nd}_{\text{init}}$  diagram between the fields of Palaeozoic Saxo-Thuringian sedimentary rocks and mantle-derived magmatic rocks of the Meissen Massif. Although mass balance indicates that 30 to 50 of the Nd may be derived from the mantle and the rest from crustal rocks, the Nd data do not necessarily require direct mantle-input during the formation of these granites. Instead, the mantle contribution could be represented by older mantle-derived rocks that are associated with the sedimentary rocks (for discussion see text). Diagram from Förster and Romer (2010).

basin-bounding faults. These late Carboniferous to Permian basins occur in the foreland of the Erzgebirge, (Fig. 1) and only locally in Erzgebirge-transverse zones, where small erosional remains of them occur (Schönfeld, Olbernhau-Brandov, and possibly Döhlen). In the larger – or more completely preserved – basins, there occur in addition to the volcano-sedimentary sequences also

larger subvolcanic and minor granitic intrusions (e.g., Breitzkreuz and Kennedy, 1999; Romer et al., 2001). These magmatic rocks have a calc-alkaline character, which most likely is inherited from the assimilation of crustal rocks that already have this character (cf. Romer et al. 2001). It should be noted, that in areas where erosion completely removed the volcano-sedimentary fill of such a basin, deeper intrusions associated with the formation of the basin may from their field-relation only be defined as “post-metamorphic”, but not be related to this basin. It is quite possible that the late Carboniferous to Permian reactivation of Erzgebirge-transverse zones provided a pathway for the emplacement of magmatic rocks that because of the lack of young sedimentary rock are not associated with the formation of the basins, but because of their spatial distribution in the Erzgebirge rather are seen as late magmatism related to the bulk of the Erzgebirge granites. If these granites and rhyolites are dominated by crustal material, the ones in the Erzgebirge may geochemically not differ from the ones of the Erzgebirge even though they are related to entirely different and unrelated processes.

## 7. A geochronological outlook

Beyond any doubt, many of the problems associated with the dating of metamorphic and magmatic rocks in the Erzgebirge and various types of mineralizations will not be solved by more extensive dating using the same analytical approaches so far. The complex history of the area with a wide range of different processes that are closely spaced in time both lead to problems of inheritance, partial resetting, and mixed data populations.

A way to work around this problem may be the direct dating of magmatic and hydrothermal ore minerals, including (a) the Re-Os dating of sulfides and in particular molybdenite, (b) the Rb-Sr dating of sphalerite and related gangue minerals and of melt inclusions in quartz, and (c) the U-Pb dating of uraninite, columbite-tantalite, huebnerite-wolframite, and cassiterite. Among these minerals and dating approaches, only the Re-Os dating of molybdenite and to a lesser extent of other sulfide minerals has been widely used. The philosophical base for the different approaches is as follows:

- In most protoliths, the elements Mo, W, Nb, Ta, and Sn do not form phases of their own and, therefore, dating of sulfide and oxides of these elements avoids the problem of inheritance completely.
- The elements Mo, U, W, Nb, Ta, and Sn have a relatively high solubility in melt and tend to concentrate in late melts. For the unusual case that the protoliths contains sulfides or oxides of these elements, these minerals rapidly dissolve in the melt and are unlikely to be inherited.
- Uraninite and glass are readily altered and, therefore their chronological system gets disturbed. If uraninite or glass are trapped (completely enclosed!) in another mineral that prevents them from interacting with the surrounding, their chronological systems remains closed independent how much they recrystallize or exsolve separate phases. The host mineral forms a container for the dated phase and analyzing the container together with the inclusions leads to the correct age (cf. Romer et al., 2007).

## 8. Sources of the Erzgebirge granites

Disputes on the genesis of granites and associated mineralizations – not only the ones in the Erzgebirge – have been intimately associated with granites from the Erzgebirge for centuries, starting

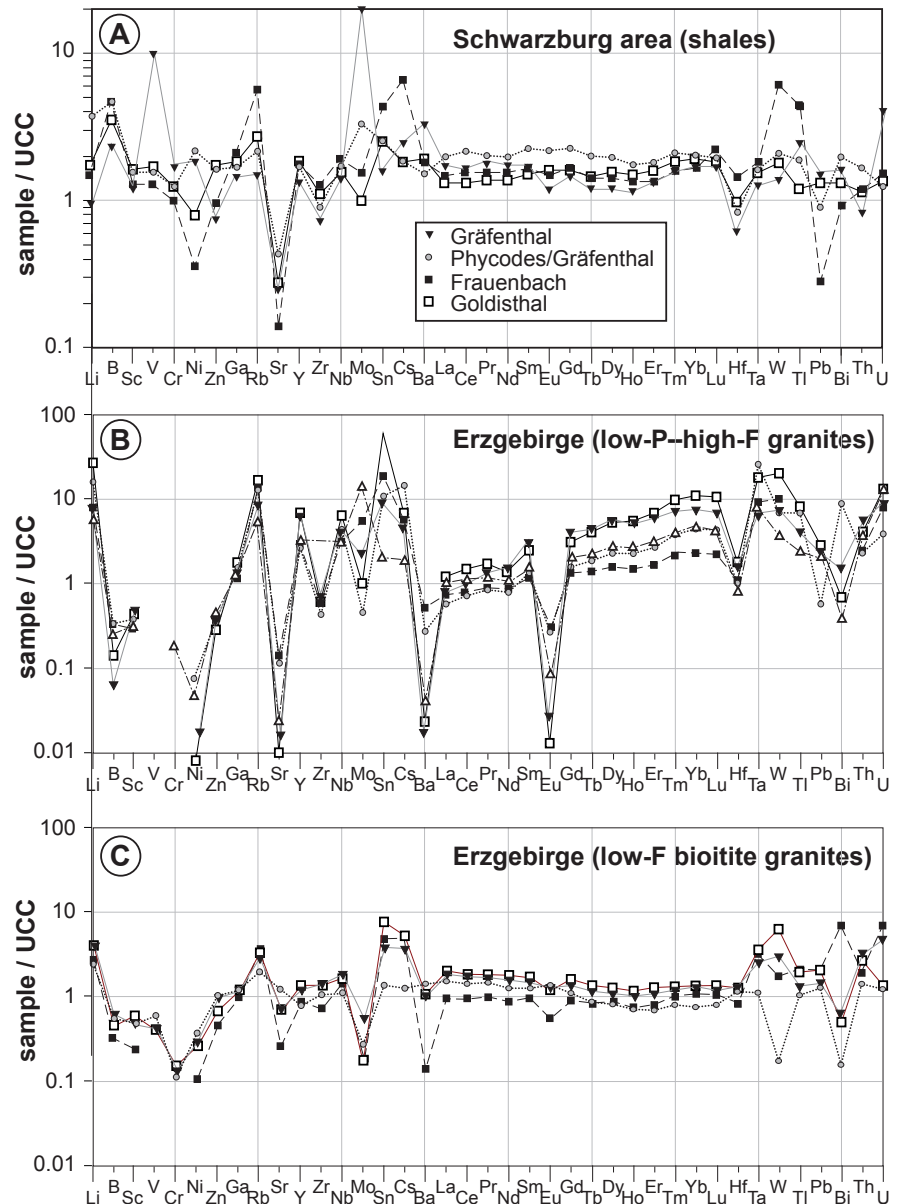


**Fig. 7.** Upper Continental Crust (UCC) normalized element pattern. **A.** Shales from the Schwarzburg area (averages for the various formations). Rocks with these compositions are the protoliths of the Variscan granites. **B.** Low-P high- and intermediate-F granites. **C.** Low-F biotite granites. Data from Romer and Hahne (2010), Förster and Romer (2010), and unpubl. Förster/Romer.

out with A.G. Werner, but being closely associated with names like Scheerer (dry fusion), Bunsen and von Cotta (granitic magma is a solution), and Zirkel and Rosenbusch (petrography) (cf. Young, 2003). The last major dispute centered around the source of the granitic magmas and polarized between “all” granites were derived from the mantle and “all” granites represent crustal melts. This dispute in part resulted in significant (and persisting) personal identification of the proponents and their students with one of the two end-member explanations.

Figure 7 shows the Sr, Nd, and Pb isotopic composition of granites from the Erzgebirge, the Saxon Granulite Massif, Thuringia, and the Meissen Massif. The rocks of the monzonitic, monzodioritic, and high Sr-Ba granitic rocks of the Meissen Massif are the only ones that show a distinct mantle signature in their Sr and Nd isotopic composition. The other granites have Sr and Nd isotopic compositions falling between the composition of depleted mantle and typical central European crust, indicating that mantle and crustal sources contribute in similar proportions to the Sr and Nd inventory of the granites. All granitoid rocks show crustal Pb isotopic compositions.

### 8.1. The problems.

- (i) Because of the contrasting Pb contents in mantle and average crust, it is expected (and observed) that the Pb isotopic composition of the granites is dominated by the crustal Pb isotope signature, independent of the source of the granitic melts. The Sr and Nd isotopic composition of the granites, however, reflects similar contributions from both sources, implying a high extent of assimilation for a mantle source. For a crustal source, the problem is to get a reservoir that provides the geochemical signature of the mantle reservoir.
- (ii) Why are there essentially only evolved granites?
- (iii) I, S, and A type granites occur in the same general area at the same time. This indicates that the variation in chemistry is inherited from the source rocks and is not related to changes in tectonic setting. How does a source look that yields such a broad range of different granites?
- (iv) There is a spatial and temporal association of lamprophyres (and rare lamproites) with granites and granite-related mineralizations.

## 8.2. Possible solutions.

- (i) The problem of a high extent of crustal assimilation through mantle-derived melts or the strong presence of mantle-derived material in crustal melts is an artificial problem, and is fueled by the incorrect perception that the crustal and mantle component must be mobilized at the same time. Yet, if the mantle component had been introduced earlier into the crust, simple crustal melting may result in melts that show the appropriate Sr and Nd isotopic composition and the I-type geochemical fingerprints. The protoliths of the metamorphic rocks of the Erzgebirge show a bipartite nature: (1) The rocks of the former Cadomian magmatic arc are dominantly preserved in the gneisses of the Cathrin-Reizenhain, Freiberg, and Lauenstein gneiss domes. (2) The dominantly Palaeozoic volcano-sedimentary rocks of the cover of the Cadomian basement makes up most of the metamorphic rocks of the nappes (beyond the gneiss domes) of the Erzgebirge. This Palaeozoic volcano-sedimentary cover contains mafic and felsic volcanic rocks of mainly Ordovician age.
- (ii) Crustal melting results in melts that are close to minimum melt composition, depending among others on melting depth, and the presence of F and B in the source. Thus, melting of metamorphosed Palaeozoic volcano-sedimentary rocks forming the nappes of the Erzgebirge removes the problem of missing large volumes of intermediate magmatic rocks, as they simply are not there. Because some of the protoliths have marked enrichments in, e.g., Li, K, Rb, Cs, and Sn (Fig. 7), partial melting of these rocks may introduce this enrichment into the melt, whereas melt evolution at lower pressure may result in additional enrichment (see Förster and Romer, 2010).
- (iii) The volcano-sedimentary cover of the Cadomian basement – and thus the metamorphic rocks of the Erzgebirge – are geochemically highly variable (Romer and Hahne, 2010). The entire range of I, S, and A type granites can be obtained by melting of different section of the metamorphosed volcano-sedimentary cover or by melting different units at different proportions (cf. Förster and Romer, 2010).
- (iv) Lamprophyres (and minor lamproites) occur throughout the entire Erzgebirge and are known especially from mineralized areas. They have a bimodal age distributions (c. 320-235 Ma and c. 300 Ma; e.g., von Seckendorf et al., 2004), i.e., by and large overlapping with the age of granite magmatism. Furthermore, some of them show mineralization. Therefore, the lamprophyres have been recurrently interpreted as evidence for a mantle-source of the granites and their ore content. The greater abundance of lamprophyres in mineralized areas may be an artefact as mining has provided a much better exposure of the rocks (continuous and in the third dimension) and, therefore, more lamprophyres have been recognized. Granites and lamprophyres exploited for their emplacement the same structures, which reached to the mantle. This co-occurrence, however, does not establish a genetic link between them. Finally, if a lamprophyre intrudes into a mineralized rock, mobilization of ore elements from the wall-rock may result in mineralization of the lamprophyres along contacts and altered zones. In such a scenario, the mineralized lamprophyres would represent a sink for the ore elements rather than a source.

## References

- Breiter, K. (1995) Geology and geochemistry of the Bohemian part of the Teplice rhyolite and adjacent post-rhyolite granite. *Terra Nostra* 95/7: 20–24.
- Breiter, K. (1997) The Teplice rhyolite (Krušné hory Mts., Czech Republic) – chemical evidence of a multiply exhausted stratified magma chamber. *Bull. Czech Geol. Surv.* 72: 205–213.
- Breitkreuz, C., Kennedy, A. (1999) Magmatic flare-up at the Carboniferous/Permian boundary in the NE German Basin revealed by SHRIMP zircon ages. *Tectonophysics* 302: 307–326.
- Förster, B. (1996) U/Pb Datierung an Pechblenden der U-Lagerstätte Aue-Niederschlema (Erzgebirge). PhD thesis Univ. Giessen, Germany, 212 pp + appendices
- Förster, H.-J., Tischendorf, G., Trumbull, R.B., Gottesmann, B. (1999) Late-Collisional Granites in the Variscan Erzgebirge, Germany. *J. Petrol.* 40: 1613–1645
- Förster, H.-J., Romer, R.L. (2010) Carboniferous magmatism. In: Linnemann, U. & Romer, R.L. (eds.) *Pre-Mesozoic Geology of Saxo-Thuringia – From the Cadomian Active Margin to the Variscan Orogen*. Schweizerbart, Stuttgart, pp. 287–308.
- Gerstenberger, H. (1989) Autometasomatic Rb enrichments in highly evolved granites causing lowered Rb/Sr isochron intercepts. *Earth Planet. Sci. Lett.* 93: 65–75.
- Gerstenberger, H., Kaemmel, T., Haase, G., Geisler, M. (1982) Zur Charakterisierung der Granite im Westerzgebirge: Rb/Sr-radiogeochronologische Untersuchungen und Spurenelementkonzentrationen. *Freib. F. H.* 389: 220–246
- Hoffmann, U., Breitkreuz, C., Breiter, K., Sergeev, S., Stanek, K., Tichomirowa, M., (2012) Carboniferous–Permian volcanic evolution in Central Europe—U/Pb ages of volcanic rocks in Saxony (Germany) and northern Bohemia (Czech Republic). *Int. J. Earth. Sci.* DOI 10.1007/s00531-012-0791-2.
- Kemnitz, H., Romer, R.L., Oncken, O. (2002) Gondwana breakup and the northern margin of the Saxothuringian belt (Variscides of Central Europe). *Int. J. Earth Sci.* 91: 246–259.
- Kossmat, F. (1927) Gliederung des varistischen Gebirgsbaues. *Abhandlungen des Sächsischen Geologischen Landesamtes*, 1: 1–39
- Kröner, A., Willner, A.P. (1998) Time of formation and peak of Variscan HP-HAT metamorphism of quartz-feldspathic rocks in the Central Erzgebirge, Saxony. *Contrib. Mineral. Petrol.* 132: 1–20
- Kroner, U., Goerz, I. (2010) Variscan assembling of the Allochthonous Domain of the Saxo-Thuringian Zone – a tectonic model. In: Linnemann, U. & Romer, R.L. (eds.) *Pre-Mesozoic Geology of Saxo-Thuringia – From the Cadomian Active Margin to the Variscan Orogen*. Schweizerbart, Stuttgart, pp. 271–286.
- Kroner, U., Romer, R.L. (2010) The Saxo-Thuringian Zone – tip of the Armorican spur and part of the Gondwana plate. In: Linnemann, U. & Romer, R.L. (eds.) *Pre-Mesozoic Geology of Saxo-Thuringia – From the Cadomian Active Margin to the Variscan Orogen*. Schweizerbart, Stuttgart, pp. 371–394.
- Kroner, U., Hahn, T., Romer, R.L., Linnemann, U. (2007) The Variscan orogeny in the Saxo-Thuringian zone – heterogeneous overprint of Cadomian / Palaeozoic Peri-Gondwana Crust. In: Linnemann, U., Nance, D., Kraft, P., and Zulauf, G. (Eds.) *The Evolution of the Rheic Ocean: From Avalonian-Cadomian active margin to Alleghenian-Variscan collision*. *Geol. Soc. Am. Spec. Pap.* 423: 153–172.
- Lange, H., Tischendorf, G., Pälchen, W., Kleim, I., Ossenkopf, W. (1972) Fortschritte der Metallogenie im Erzgebirge. *B. Zur*

- Petrographie und Geochemie der Granite des Erzgebirges. *Geologie* 21: 457–493.
- Linnemann, U., McNaughton, N.J., Romer, R.L., Gehmlich, M., Drost, K., Tonk, C. (2004) West African Provenance for Saxo-Thuringia (Bohemian Massif): Did Armorica ever leave pre-Pangean Gondwana? – U/Pb-SHRIMP zircon evidence and the Nd-isotopic record. – *Int. J. Earth Sci.* 93: 683–705.
- Linnemann, U., Romer, R.L., Gerdes, A., Jeffries, T.E., Drost, K., Ulrich, J. (2010) The Cadomian Orogeny in the Saxo-Thuringian Zone. In: Linnemann, U. & Romer, R.L. (eds.) *Pre-Mesozoic Geology of Saxo-Thuringia – From the Cadomian Active Margin to the Variscan Orogen*. Schweizerbart, Stuttgart, pp. 37–58
- Lippolt, H.J. (1984) Experimentelle Datierungen von postvaristischen Mineralisationen, Möglichkeiten und Grenzen. in *Postvariszische Gangmineralisation in Mitteleuropa. Alter, Genese und wirtschaftliche Bedeutung*. Schriftenr. GDMB 41: 305–359
- Lobin, M. (1986) *Aufbau und Entwicklung des Permosiles im mittleren und östlichen Erzgebirge*. Dissertation, Techn. Univ. Bergakademie Freiberg, 63 pp.
- Mingram, B. (1998) The Erzgebirge, Germany- a subducted part of northern Gondwana: geochemical evidence for repetition of early Paleozoic metasedimentary sequences in metamorphic thrust units. *Geol. Mag.* 135: 785–801
- Romer, R.L., Hahne, K. (2010) Life of the Rheic Ocean: Scrolling through the shale record. *Gondwana Res.* 17: 236–253.
- Romer, R.L., Rötzler, J. (2001) P-T-t evolution of ultrahigh-temperature granulites from the Saxon Granulite Massif, Germany. Part II: Geochronology. *J. Petrol.* 42: 2015–2032.
- Romer, R.L. and Rötzler, J. (2011) The role of element distribution for the isotopic dating of metamorphic minerals. *Eur. J. Mineral.* 23: 17–33.
- Romer, R. L., Förster, H.-J., Breitzkreuz, Chr. (2001) Intracontinental extensional magmatism with a subduction fingerprint: the late Carboniferous Halle Volcanic Complex (Germany). *Contrib. Mineral. Petrol.* 141: 201–221.
- Romer, R.L., Thomas, R., Stein, H.J., Rhede, D. (2007) Dating multiply overprinted Sn-mineralized granites – examples from the Erzgebirge, Germany. – *Mineral. Deposita* 42: 337–359.
- Romer, R.L., Förster, H.-J., Štemprok, M. (2010a) Age constraints for the late-Variscan magmatism in the Altenberg–Teplice Caldera (Eastern Erzgebirge/Krušné hory). *N. Jb. Mineral.* 187: 289–305.
- Romer, R.L., Schneider, J.C., Linnemann, U. (2010b) Post-Variscan deformation and hydrothermal mineralization in Saxo-Thuringia and beyond: a geochronological review. In: Linnemann, U. & Romer, R.L. (eds.) *Pre-Mesozoic Geology of Saxo-Thuringia – From the Cadomian Active Margin to the Variscan Orogen*. Schweizerbart, Stuttgart, pp. 347–360.
- Rötzler, J., Romer, R.L. (2001) P-T-t evolution of ultrahigh-temperature granulites from the Saxon Granulite Massif, Germany. Part I: Petrology. *J. Petrol.* 42: 1995–2013.
- Rötzler, J., Romer, R.L. (2010) The Saxon Granulite Massif: a key area for the geodynamic evolution of Variscan central. In: Linnemann, U. & Romer, R.L. (eds.) *Pre-Mesozoic Geology of Saxo-Thuringia – From the Cadomian Active Margin to the Variscan Orogen*. Schweizerbart, Stuttgart, pp. 233–252.
- Rötzler, K., Plessen, B. (2010) The Erzgebirge: a pile of ultrahigh- to low-pressure nappes of early Palaeozoic rocks. In: Linnemann, U., Kroner, U., Romer, R.L. (eds.) *From the Cadomian Active Margin to the Variscan Orogen: The pre-Mesozoic Geology of Saxo-Thuringia (NE Bohemian Massif)*. E. Schweizerbart Science Publishers, Stuttgart, pp. 253–270.
- Rötzler, K., Schumacher, R., Maresch, W.V., Willner, A.P. (1998) Characterization and geodynamic implications of contrasting metamorphic evolution in juxtaposed high-pressure units of the Western Erzgebirge (Saxony, Germany). *Eur. J. Mineral.* 10: 261–280
- Schmädicke, E., Mezger, K., Cosca, M.A., Okrusch, M. (1995) Variscan Sm-Nd and Ar-Ar ages of eclogite-facies rocks from the Erzgebirge, Bohemian Massif. *J. metamorphic Geol.* 13: 537–552
- Schneider, J.W., Romer, R.L. (2010) The Late Variscan Molasses (Late Carboniferous – Late Permian) of the Saxo-Thuringian Zone. In: Linnemann, U. & Romer, R.L. (eds.) *Pre-Mesozoic Geology of Saxo-Thuringia – From the Cadomian Active Margin to the Variscan Orogen*. Schweizerbart, Stuttgart, pp. 323–346.
- Schneider, J.W., Hoth, K., Gaitzsch, B.G., Berger, H.-J., Steinborn, H., Walter, H., Zeidler, M.K. (2005) Carboniferous stratigraphy and development of the Erzgebirge Basin, East Germany. *Z. Dt. Ges. Geowiss.* 156: 431–466
- Schneider, J. W., Körner, F., Roscher, M., Kroner, U. (2006) Permian climate development in the northern peri-Tethys area – the Lodève basin, French Massif Central, compared in a European and global context. *Palaeogeogr., Palaeoclimatol., Palaeoecol.* 240: 161–183.
- Tischendorf, G. (1989) Silicic Magmatism and Metallogenesis of the Erzgebirge. *Veröff. Zentralinst. Physik Erde* 107: 316 pp
- Vavra, G., Reinhardt, J. (1997) Which processes are dated by U/Pb zircon ages of high-grade metamorphic rocks? Zircon genesis in various lithologies and structural levels of the Saxonian Granulite Massif. *Terra Nostra* 97/5: 190–192
- Vollbrecht, A., Weber, K., Schmoll, J. (1989) Structural model for the Saxothuringian-Moldanubian suture in the Variscan basement of the Oberpfalz (Northeastern Bavaria, F.R.G.) interpreted from geophysical data. *Tectonophysics* 157: 123–133.
- von Quadt, A. (1993) The Saxonian Granulite Massif: new aspects from geochronological studies. *Geol. Rundsch.* 82: 516–530
- von Quadt, A., Günther, D. (1999) Evolution of Cambrian eclogitic rocks in the Erzgebirge: A conventional and LA-ICP-MS U-Pb Zircon and Sm-Nd study. *Terra Nostra* 99/1: 164
- von Seckendorff, V., Timmermann, M.J., Kramer, W., Wrobel, P. (2004) New  $^{40}\text{Ar}/^{39}\text{Ar}$  ages and geochemistry of Late Carboniferous–Early Permian lamprophyres and related volcanic rocks in the Saxothuringian Zone of the Variscan orogen, Germany. In: Wilson, M., Neumann, E.G., Davies, G.R., Timmermann, M.J., Heeremans, M. & Larsen, B.T. (eds.) *Permo–Carboniferous Magmatism and Rifting in Europe*. *Geol. Soc. London, Spec. Publ.* 223: 335–359
- Werner, O., Lippolt, H.J. (1998) Datierung von postkinematischen magmatischen Intrusionsphasen des Erzgebirges: Thermische und hydrothermale Überprägung der Nebengesteine. *Terra Nostra* 98/2: 160–163
- Werner, O., Lippolt, H.J. (2000) White mica  $^{40}\text{Ar}/^{39}\text{Ar}$  ages of Erzgebirge metamorphic rocks simulating the chronological results by a model of Variscan crustal imbrication. In: Franke, W., Haak, V., Oncken, O. & Tanner, D. (eds.) *Orogenic Processes: Quantification and Modelling in the Variscan Belt of Central Europe*. *Geol. Soc. London, Spec. Publ.* 179: 323–336
- Wetzel, H.-U. (1984) *Spätvariszische Bruchtektonik und subsequeute Gangmagmatite als Ausdruck der Krustenentwicklung im Osterzgebirge (Alteberger Scholle)*. Dissertation, Zentralinst. Phys. Erde Potsdam, Akademie der Wissenschaften der DDR

- Wetzel, H.-U., Lobin, M., Pälchen, W., Schilka, W. (1985) Eastern Erzgebirge (Upper Palaeozoic). In: Late Palaeozoic and Cenozoic continental sedimentation and magmatism in the southern part of the G.D.R., Multilateral Cooperation of the Academies of Sciences of the Socialist Countries. Acad. Sci. G.D.R., Guidebook of Excursions, pp. 56–85
- Willner, A.P., Rötzler, K., Maresch, V.W. (1997) Pressure-temperature and fluid evolution of quartzo-feldspathic metamorphic rocks with a relic high-pressure, granulite-facies history from the Central Erzgebirge (Saxony, Germany). *J. Petrol.* 38: 307–336
- Young, D.A. 2003. *Mind over magma. The story of igneous petrology.* Princeton University Press, Princeton, 685 pp.

# The eastern Erzgebirge volcano-plutonic complex

Axel Müller<sup>1,2</sup> and Reimar Seltmann<sup>2</sup>

<sup>1</sup> Geological Survey of Norway, Leiv Eirikssons vei 39, 7491 Trondheim, Norway

<sup>2</sup> Natural History Museum, Cromwell Road, London SW7 5BD, UK  
Axel.Muller@NGU.NO, r.seltmann@nhm.ac.uk

## Geological overview

The eastern Erzgebirge is the easternmost part of the Saxothuringian Fichtelgebirge–Erzgebirge antiform where late- to post-orogenic Variscan uplift and exhumation processes accompanied intense felsic (rhyolitic and granitic) magmatism that was controlled by brittle-fracture tectonics (Seltmann et al., 1996) and formed the eastern Erzgebirge volcano-plutonic complex (Štemprok et al., 2003). The crystalline basement of the area, referred to as the Krušné Hory/Erzgebirge Crystalline Complex, comprises various tectonic units of different metamorphic grades that received their last metamorphic and deformation imprint during Lower Carboniferous (e.g., Willner et al., 1997; Rötzler et al., 1998; Rötzler and Plessen, 2010). The orogenic collapse of the Saxothuringian zone as part of the Variscan orogenic belt contributed to the formation of volcano-tectonic intramontane depressions (Olbernhau and Schönfeld depressions) and strike-slip related pull-apart basins (Erzgebirge and Döhlen basins) in the marginal and central parts of the Erzgebirge. Caldera complexes developed in the Altenberg block (Altenberg–Teplice caldera) and in the Tharandter Wald (Fig. 1). The Tharandt Caldera (Benek, 1980) has been remapped recently and its magmatic rocks are under current geochemical and geochronological investigation (Hoffmann et al., 2012). The 630-km<sup>2</sup> Altenberg–Teplice caldera is a giant elliptical structure 18x35 km across and forms the main part of the eastern Erzgebirge volcano-plutonic complex. It is perhaps the best preserved Carboniferous caldera structure in Europe. The caldera collapse was triggered by the extrusion of at least 160 km<sup>3</sup> (630 km<sup>2</sup> x 250 m) Teplice volcanic rocks resulting in the formation of an eastward dipping trap door caldera with the maximal subsidence in its south-eastern part (Benek, 1991; Mlčoch and Skácelová, 2010). The chemical characteristics of the volcanic rocks resemble those of the Bishop Tuff (Hildreth, 1979). An idealised profile through the volcanic pile of the Altenberg–Teplice caldera has been compiled from the borehole Mikulov 4 in the southwestern part of the caldera (Jiránek et al., 1987; Breiter, 1997; Breiter et al., 2001) (Fig. 2).

Three major stages in respect to the formation of the Altenberg–Teplice caldera are distinguished:

(I) The pre-caldera granite intrusions of the Niederbobritzsch and Flaje massifs and the Telnice granite classified as low-F biotite granites of the Krušné Hory/Erzgebirge (Förster et al., 1998, 1999; Štemprok et al., 2003).

(II) The caldera stage comprising the extrusion of the rhyolitic/dacitic volcanics of the Mikulov beds (early caldera stage IIa), Teplice rhyolitic ignimbrites (main caldera stage IIb) and the intrusion of the Altenberg–Frauenstein microgranite into the caldera collapse structures (late caldera stage IIc).

(III) The post-caldera intrusions of topaz-bearing rare metal granites comprising the Schellerhau granite complex and several small intrusions (Sadisdorf, Altenberg, Hegelshöhe, Schenkenshöhe, Zinnwald-Cínovec, Loupený, Preiselberk, Knötel). These granites belong to the high-F, low-P<sub>2</sub>O<sub>5</sub> Li-mica granites of the Krušné Hory/Erzgebirge (Štemprok et al., 2003). This is followed by volcanic rocks of the Schönfeld Formation.

The magmatic phases forming the three stages have principally the following characteristics:

(I) The post-kinematic, late-collisional Niederbobritzsch massif (Fig. 1) forms a multiphase intrusion consisting of four intrusive phases of low-F biotite monzogranites with a transitional I- to S-type character (Förster et al., 1999). Phase-Two granitic rocks (NB2) contain mafic enclaves and are interpreted as hybrid granites, resulting from mingling and mixing with mafic magma (Rösler and Bothe, 1990). The more felsic Phase-Three rocks (NB3) form the main part of the Niederbobritzsch massif. The most silicic rocks (Phase Four, NB4) are represented by aplite dikes.

The Flaje massif (Fig. 1) consists of medium- to coarse-grained low-F biotite monzogranites with local occurrences of subordinate two-mica granites. The granites are rather primitive, moderately peraluminous and relatively rich in CaO (up to 2.5 wt.%) that decreases with rising silica content.

The Telnice biotite monzogranite forms a small intrusion about 15 km east of Zinnwald/Cínovec.

(IIa) In the Czech part of the Altenberg–Teplice caldera, the early caldera stage is represented by the Mikulov beds, which are completely cored in the drilling Mikulov 4 (Breiter, 1997). The Mikulov beds comprise 320 m of volcanic rocks covering metamorphic basement and underlying 600 m thick Teplice ignimbrite. The Mikulov beds have been suggested to be equivalent to the volcanic rocks of Schönfeld Formation (Breiter et al., 2001), which is controversially discussed (cf. Romer et al., 2010; Hoffmann et al., 2012).

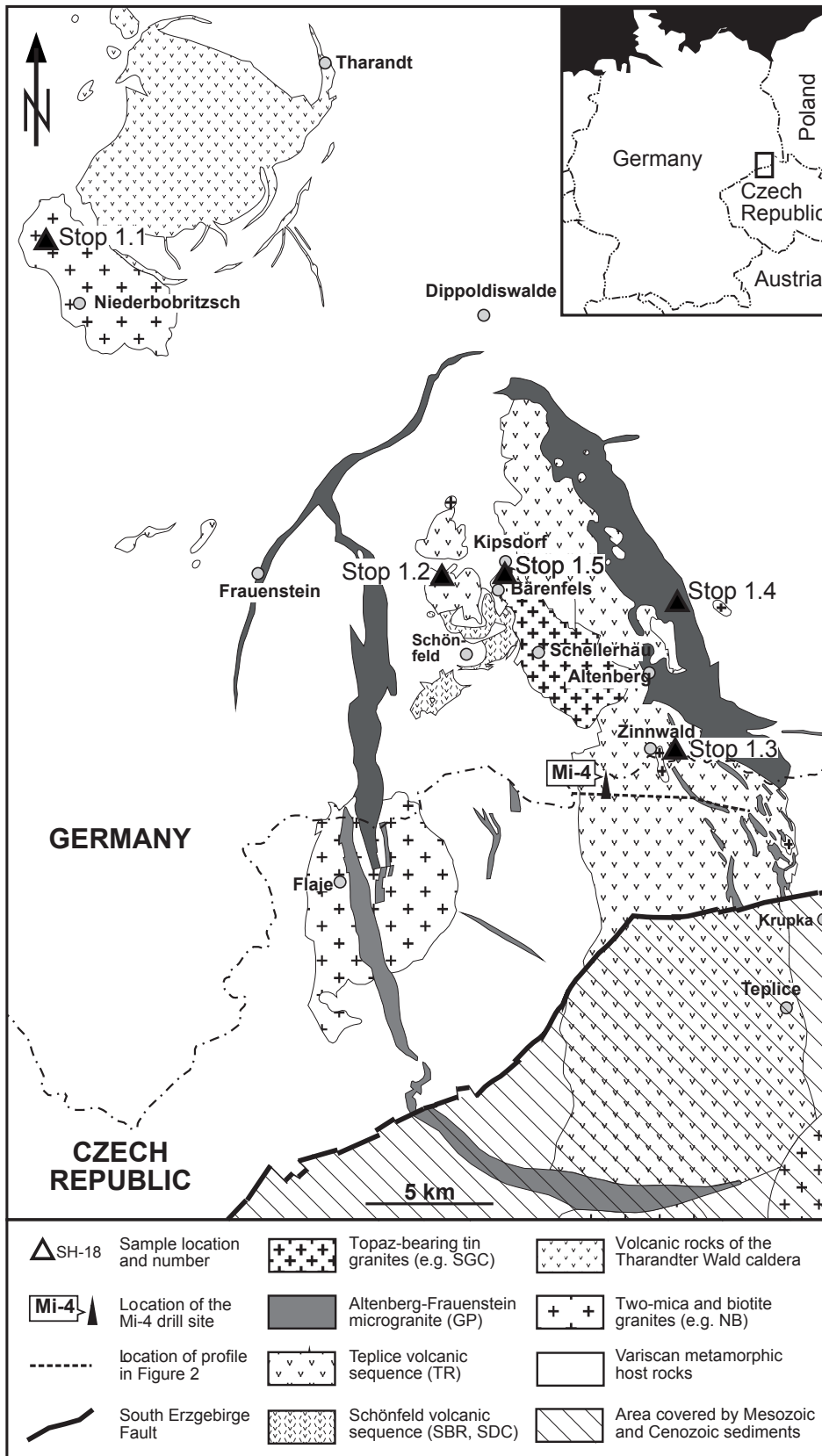


**Fig. 1.** Geological map (after various sources) of the Eastern Erzgebirge volcano-plutonic complex with the Altenberg-Teplice Caldera framed by the Altenberg-Frauenstein microgranite (dark grey).

(IIb) The rhyolitic volcanic to subvolcanic rocks of the Teplice formation and ignimbrites are much more evolved than the older Schönfeld rocks and are high-K calc-alkaline in character (Breiter, 1997; Breiter et al., 2001). They can be subdivided into three phases (TR1, TR2, TR3) and several subphases. Each of the three phases shows a reverse

geochemical evolution from highly evolved to less evolved rocks, which is explained by a step-by-step deflation of a stratified magma chamber (Breiter, 1997).

(IIc) The eruption of up to 120 km<sup>3</sup> Teplice volcanic rocks led to the collapse of the Altenberg-Teplice caldera with N-S elongated, pear-shaped ring fractures that were filled by

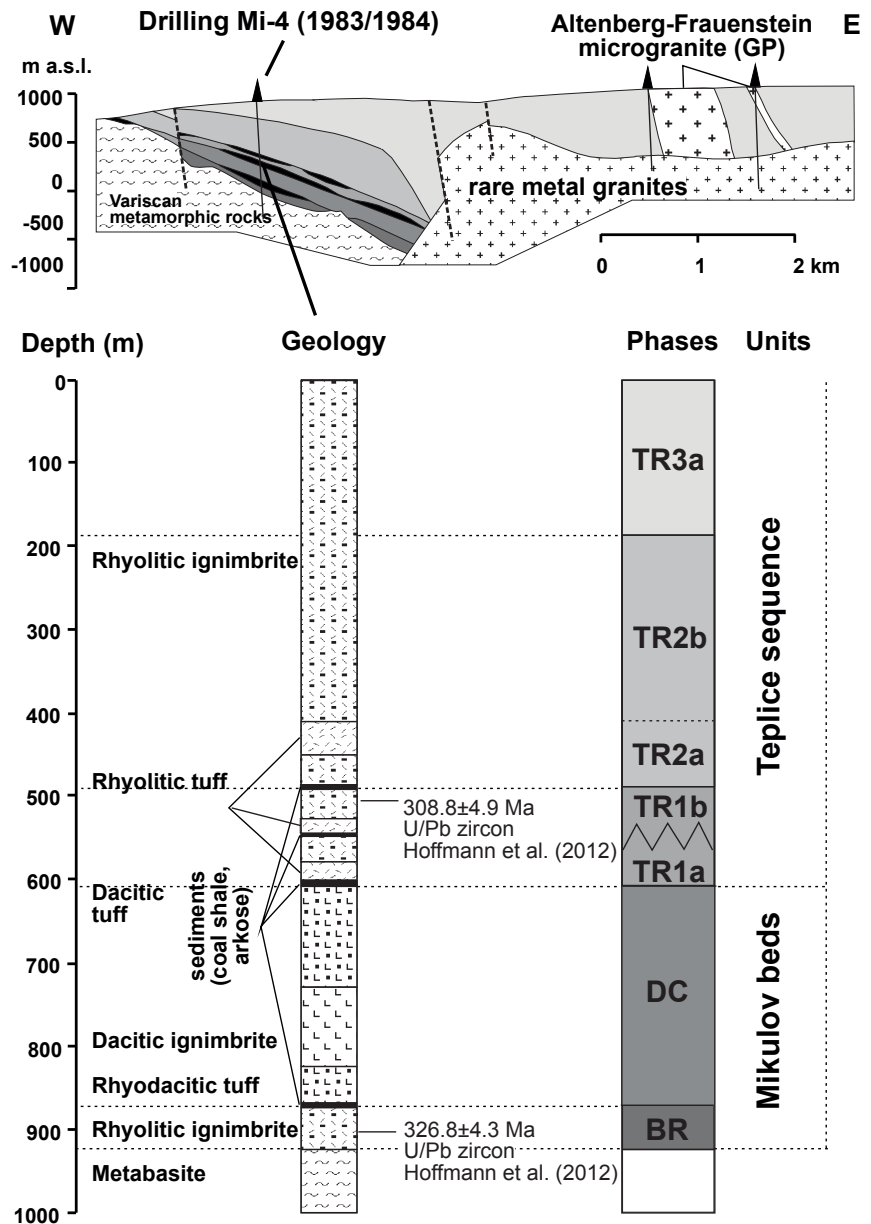


**Fig. 2.** Geological cross section of the central part of the Altenberg-Teplice caldera and schematic log of borehole Mikulov 4 and its division into volcanic phases and subphases (events) according to Jiránek et al. (1987) and Breiter (1997). The U-Pb SHRIMP age for the Mikulov beds bases on 13 grains and supersedes earlier age estimates that place this unit into the Namurian, whereas plant fossils in the Schönfeld Formation were assigned to Westphal B/C (Lobin, 1986) and the overlaying volcanic rocks were assigned to Westphal C/D, which corresponds to an age of 305–311 Ma (for a discussion see Romer et al., 2011). The U-Pb SHRIMP age for TR1b rocks is less constrained as it bases only on two spots (cf. Hoffmann et al., 2012).

multiple intrusions of the rapakivi-textured porphyritic microgranite of Altenberg-Frauenstein (GP) (Müller and Seltmann, 2002). The ring dyke complex is dominated by the older acid microgranite GP1, with less common occurrence of intermediate batches of microgranite GP2.

- (III) The topaz-bearing rare metal granites are represented by the Schellerhau granite complex and several small intrusions (Sadisdorf, Altenberg, Schenkenshöhe, Hegelshöhe, Zinnwald-Cinovec, Loupený, Preiselberk, and Knötel). The Schellerhau granite complex is characterised by porphyritic (SG1) to weakly porphyritic (SG2) biotite syeno- to monzogranites and seriate albite granites (SG3) (Müller et al., 2000). The SG1, SG2 and SG3 rocks are P-poor and Li-F-enriched and show some A-type traits (Förster et al., 1995; Breiter et al., 1999).

In the German part of the Altenberg-Teplice caldera, the Schönfeld Formation consisting of rhyolitic ignimbrites at the base (max. 130 m thick), a rhyodacitic to dacitic lava with max. 160 m thickness followed by up to 105 m thick volcanoclastic

sediments with anthracitic hard coal horizons (Pälchen, 1968; Lobin, 1986; Breiter, 1997; Breiter et al., 2001). Plant fossils from the Schönfeld Formation in combination with lithologic correlations for a long time provided the sole constraints on the age of the rocks in the Altenberg-Teplice caldera and represent the base for later controversies. The Schönfeld rhyodacite represents a relatively primitive calc-alkaline magma with relatively high contents of Fe, Mg, Ca, P, and Sr, low contents of Rb, Th and heavy REE and insignificant Eu anomaly (Breiter, 1997; Breiter et al., 2001). The older Schönfeld rhyolite is more evolved than the younger Schönfeld rhyodacite.

A number of igneous rocks of the eastern Erzgebirge volcano-plutonic complex display textural and chemical evidence for multiple interaction of mafic and silicic magmas. Mixing textures include mafic micro enclaves, rounded quartz phenocrysts with smudged pre-resorption growth zoning and post-resorption quartz overgrowth with high Ti, plagioclase-mantled K-feldspar (rapakivi texture), sieve-textured plagioclase, and patchy zones in plagioclase. In addition, concentration steps of trace and minor

elements in quartz (Ti) and feldspar (anorthite content, Ba, Sr) support magma mixing. The heterogeneous nature of mixing is indicated by the varying distribution of textures between and within the magmatic stages.

Mainly based on the classification of quartz phenocrysts using their growth patterns, Müller et al. (2005) presented a magma chamber model for the evolution of the eastern Erzgebirge volcano-plutonic complex. Considering thermobarometric melt inclusion studies of quartz (Thomas, 1992), two levels of magma storage may be distinguished: deep reservoirs between 17 and 24 km and shallow reservoirs between 13 and 6 km. The deep magma reservoir of the eastern Erzgebirge volcano-plutonic complex served as a source for the Teplice rhyolite, Altenberg-Frauenstein microgranite, and the Schellerhau granites, which are associated with the Altenberg-Teplice caldera. The reservoir was strongly stratified, as the phases show a wide chemical variation but contain the same quartz phenocryst population. The older Niederbobritzsch granites, the Schönfeld volcanic rocks and the Mikulov beds represent temporally and spatially separate magma sources. The deep magma reservoir of these magmatic rocks is assumed to have been at a depth between 17 and 24 km.

The relative temporal relationships between the different intrusion stages are well constrained by surface and subsurface (mines) outcrops and numerous drill holes performed in the 1970/80's for Sn-W exploration in the former German Democratic Republic. However, for a number of igneous stages the absolute ages are not well constrained mainly due to large populations of inherited zircon and intense late- to post-magmatic hydrothermal overprint. However, the igneous rocks of the Eastern Erzgebirge volcano-plutonic complex intruded and extruded at least over a period of about 25 Ma (e.g., Förster et al., 1999; Breiter et al., 1999), beginning with the intrusion of the Niederbobritzsch granites at  $320 \pm 6$  Ma (Tichomirowa, 1997) and ending with the emplacement of the volcanic rocks of the Schönfeld complex. These time relationships imply the presence of a long-standing, partly interconnected magma stockwork in the Erzgebirge region - a matter of debate since Watznauer (1954). Hoffmann et al. (2012) acquired a U/Pb zircon age of  $326.8 \pm 4.3$  Ma for the Mikulov ignimbrite (Mikulov beds) which overlaps with the age of the pre-caldera stage monzogranites of Niederbobritzsch and Flaje.

## Eurogranites 2012

### Stop 1-1

Quarry Buchberg, Naundorf

Niederbobritzsch granite

Coordinates: UTM 33U 389470 m E/ 5642880 m N, 370 m a.s.l.

Road 173 from Freiberg to Naundorf and from Naundorf road S208 to Bobritzsch

Guide: Axel Müller/Reimar Seltmann

The post-kinematic Niederbobritzsch massif, which intruded into the Freiberg gneiss dome, is about 7 km ESE of Freiberg and extends 9 km in NW-SE direction and 3 km in NE-SW direction. The massif belongs to a group of late-collisional low-F, low- $P_2O_5$  biotite monzogranites and forms a multiphase intrusion and consists of four intrusive phases (NB1–NB4) – three granitic phases and one aplitic phase – with a transitional I- to S-type character (Förster et al., 1999). The three granite phases are distinguished basically by their geochemistry, namely the  $Al_2O_3$ ,  $SiO_2$ ,  $TiO_2$ , CaO, MgO and  $P_2O_5$  content (Table 1). Phase NB1 in the south and phase NB2 in the north represent the older generations of the Niederbobritzsch massif. NB2 is more heterogeneous in texture and chemistry than NB1 and is interpreted as a hybrid granite, resulting from mingling and mixing with more mafic magma (Rösler and Bothe, 1990). Mafic enclaves in NB2 correspond texturally to lamprophyre dikes that are associated with NB3 (Rösler and Budzinski, 1994). Phase NB3 (“Normalgranit”) forms the main central part of the Niederbobritzsch massif. The most silicic Phase (NB4) is represented by aplite dikes occurring predominantly at the margin of the massif. In addition, up to 1 m large pegmatite pockets, up to several meters large lamprophyric enclaves, and hydrothermal sulfide mineralizations occur within the granites. In the quarry Buchberg both the NB2 and NB3 phases are exposed.

The major phase NB3 contains 30 wt.% quartz, 32 wt.% plagioclase with an anorthite content around  $An_{25}$ , 30 wt.% K-feldspar and 6 wt.% biotite. The hybrid granite NB2 contains 30 wt.% quartz, 33 wt.% plagioclase with c.  $An_{28}$ , 25 wt.% K-feldspar, and 13 wt.% biotite. Common accessories are apatite, allanite, zircon, monazite, and xenotime. The mafic enclaves show a relative wide chemical and mineralogical variety. Beside the major minerals plagioclase, K-feldspar, and biotite, there occur minor hornblende and diopsidic pyroxene in enclaves (Rösler and Bothe, 1990). The interaction/reaction zone between the mafic enclaves and the host granite is enriched in allanite. The origin of the mafic enclaves is still under debate.

**Table 1.** Average compositions of the Niederbobritzsch granites NB1 to NB4 according to Rösler and Budzinski (1994) and Rösler and Bothe (1990). Concentrations are given in wt.% for major elements and in ppm for trace elements. stdv – standard deviation

|                                | NB1     |       | NB2     |       | NB3     |       | NB4     |       | mafic enclaves |      |
|--------------------------------|---------|-------|---------|-------|---------|-------|---------|-------|----------------|------|
|                                | average | stdv  | average | stdv  | average | stdv  | average | stdv  | average        | stdv |
|                                | N=12    |       | n=9     |       | n=20    |       | n=11    |       | n=2            |      |
| SiO <sub>2</sub>               | 66.73   | 1.47  | 67.98   | 2.17  | 69.00   | 1.30  | 74.26   | 0.89  | 60.89          | 2.39 |
| TiO <sub>2</sub>               | 0.29    | 0.06  | 0.38    | 0.15  | 0.47    | 0.07  | 0.27    | 0.06  | 0.49           | 0.11 |
| Al <sub>2</sub> O <sub>3</sub> | 18.24   | 0.74  | 17.30   | 1.00  | 14.69   | 0.72  | 12.59   | 0.90  | 17.97          | 0.90 |
| FeO                            | 2.49    | 0.30  | 2.53    | 0.56  | 2.24    | 0.32  | 1.35    | 0.50  | 6.88           | 1.12 |
| MnO                            | 0.06    | 0.01  | 0.05    | 0.02  | 0.06    | 0.01  | 0.03    | 0.01  | 0.20           | 0.00 |
| CaO                            | 2.16    | 0.58  | 0.95    | 0.51  | 2.30    | 0.51  | 0.86    | 0.26  | 4.16           | 1.00 |
| MgO                            | 1.20    | 0.13  | 0.74    | 0.35  | 1.00    | 0.28  | 0.53    | 0.24  | 3.18           | 0.00 |
| K <sub>2</sub> O               | 3.96    | 0.23  | 4.87    | 0.54  | 4.00    | 0.39  | 5.28    | 0.61  | 3.33           | 0.18 |
| Na <sub>2</sub> O              | 3.56    | 0.17  | 3.16    | 0.19  | 3.54    | 0.26  | 2.87    | 0.55  | 3.44           | 0.48 |
| P <sub>2</sub> O <sub>5</sub>  | 0.40    | 0.03  | 0.36    | 0.09  | 0.16    | 0.03  | 0.15    | 0.08  | 0.51           | 0.05 |
| H <sub>2</sub> O               | 0.12    | 0.06  | 0.10    | 0.08  | 0.26    | 0.10  | 0.25    | 0.11  | 0.66           | 0.06 |
| LOI                            | 0.75    | 0.14  | 0.85    | 0.46  | 0.96    | 0.24  | 0.80    | 0.21  | 0.09           | 0.04 |
| sum                            | 99.95   | 0.73  | 99.26   | 1.26  | 98.66   | 0.33  | 99.26   | 0.58  | 100.10         | 0.81 |
| B                              | 19.1    | 7.9   | 3.3     | 0.7   | 12.8    | 2.8   | 14.1    | 4.3   | -              | -    |
| Ba                             | 1111.6  | 316.2 | 530.8   | 221.2 | 709.2   | 235.1 | 579.2   | 380.1 | -              | -    |
| Be                             | 5.6     | 0.9   | 5.2     | 1.8   | 4.8     | 0.8   | 5.0     | 1.2   | -              | -    |
| Co                             | 10.5    | 6.9   | 5.5     | 1.6   | 6.1     | 1.6   | 4.7     | 2.3   | -              | -    |
| Cu                             | 6.1     | 4.9   | 11.5    | 11.1  | 12.5    | 6.9   | 11.5    | 6.4   | -              | -    |
| Cr                             | 92.2    | 20.6  | 111.9   | 31.5  | 26.4    | 10.6  | 33.8    | 37.7  | -              | -    |
| Ga                             | 14.3    | 2.0   | 14.6    | 2.1   | 18.3    | 2.8   | 16.6    | 3.2   | -              | -    |
| Li                             | 63.9    | 11.7  | 68.4    | 19.0  | 64.1    | 9.5   | 41.8    | 20.8  | -              | -    |
| Mo                             | 0.8     | 0.2   | 1.1     | 0.9   | 1.1     | 0.5   | 1.0     | 0.7   | -              | -    |
| Ni                             | 10.0    | 1.8   | 5.9     | 4.4   | 5.3     | 1.3   | 3.6     | 1.9   | -              | -    |
| Pb                             | 19.9    | 4.7   | 27.2    | 10.8  | 25.6    | 5.5   | 35.7    | 7.4   | -              | -    |
| Rb                             | 211.9   | 26.8  | 262.6   | 60.7  | 206.5   | 26.6  | 221.7   | 37.2  | -              | -    |
| Sn                             | 3.5     | 1.2   | 2.6     | 0.8   | 4.5     | 1.7   | 3.2     | 1.9   | -              | -    |
| Sr                             | 260.8   | 102.9 | 178.9   | 96.5  | 409.6   | 180.5 | 141.5   | 98.3  | -              | -    |
| V                              | 43.6    | 10.3  | 27.7    | 12.7  | 31.7    | 10.5  | 17.5    | 13.0  | -              | -    |
| Zr                             | 223.3   | 70.0  | 145.7   | 49.2  | 183.4   | 59.6  | 129.6   | 37.7  | -              | -    |

## Eurogranites 2012

### Stop 1-2

Harter Stein, SE Ammeldorf

Teplice rhyolite TR3

Coordinates: UTM 33U 403850 m E/5628250 m N, 710 m a.s.l.

Road S208 from Bobritzsch to Hartmannsdorf-Reichenau; from there road 171 to Hennersdorf; from there road K9050 and K9042 to Ammeldorf and continuing to Schönfeld

Guide: Axel Müller/Reimar Seltmann

The Harter Stein is situated in the forest southwest of the road between Schönfeld and Ammeldorf. Harter Stein means hard rock and is the western offset of a Teplice rhyolite (TR) flow. Rapid cooling of the flow caused the formation of five- to six-edged columns. The phenocryst-rich rhyolite with dense groundmass belongs to the youngest effusive TR3 stage of the Teplice ignimbrite sequence.

The volcanic to subvolcanic rocks of the Teplice rhyolite are high-K calc-alkaline in character (Breiter, 1997; Breiter et al., 2001; Fig. 3). They are relatively enriched in K, Zr, Th, Y, and HREE, and depleted in Al, Ti, Mg, and Sr and can be subdivided into three phases (TR1, TR2, TR3) and several subphases (Table 2). Each of the three phases shows a reverse geochemical evolution from highly evolved to less evolved which is explained by a step-by-step deflation of a stratified magma chamber (Breiter, 1997). The three phases show similar chemical trends from rocks

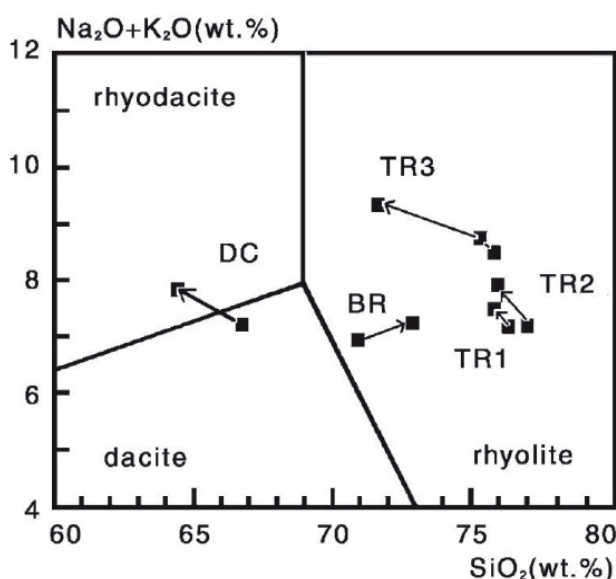


**Fig. 3.** TAS classification of the igneous rocks of the Mikulov beds (BR, DC) and the younger Teplice sequence (TR1-TR3) according to Breiter et al. (2001). The analyzed samples are from the drill core Mikulov 4.

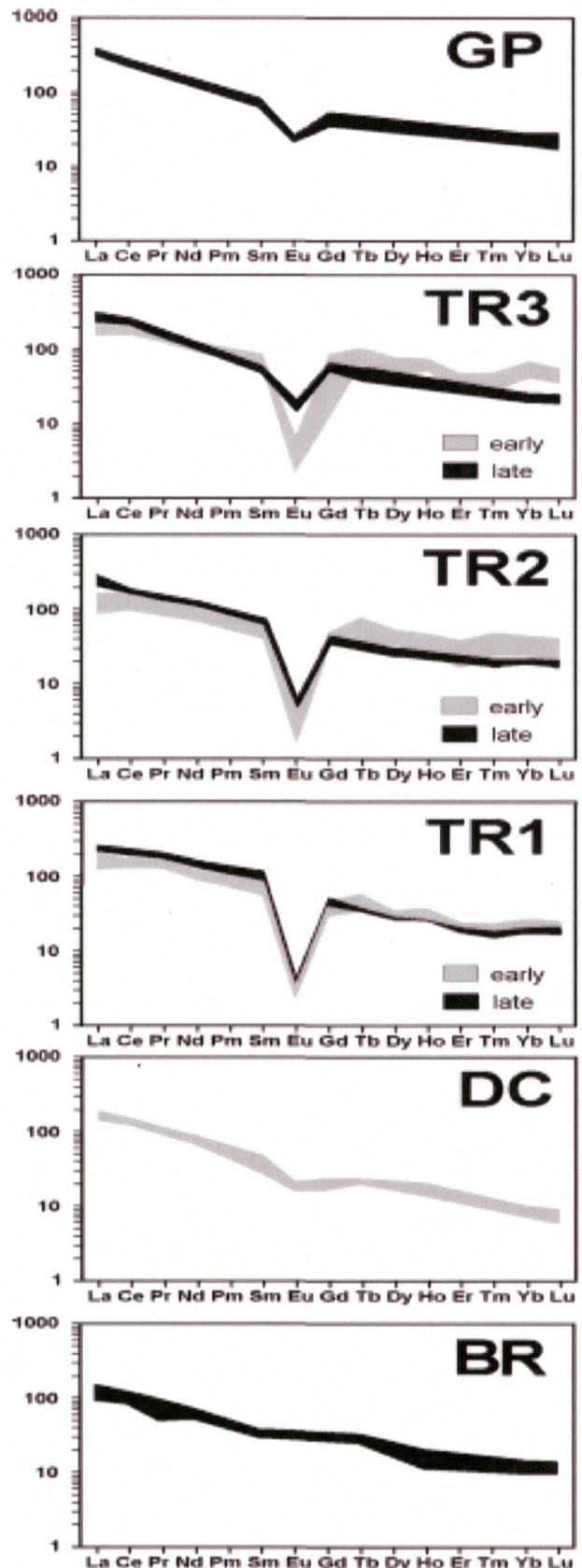


**Fig. 4.** Chondrite normalised REE-patterns of igneous rocks of the Mikulov beds (BR, DC), Teplice sequence (TR1-TR3) and Altenberg-Frauenstein microgranite (GP) according to Breiter et al. (2001).

**Table 2.** Concentrations of major (wt.%) and trace (ppm) elements of igneous rocks of Mikulov beds (BR, DC), Teplice sequence (TR1-TR3) and Altenberg-Frauenstein microgranite (GP) according to Breiter et al. (2001).

|                                    | BR            | DC            | TR1            | TR2                           | TR3              | GP                  |                         |      |
|------------------------------------|---------------|---------------|----------------|-------------------------------|------------------|---------------------|-------------------------|------|
|                                    | early -> late | early -> late | early -> late  | early -> late<br>TR2a -> TR2b | Pramenáč<br>TR3a | Vlčí, Kámen<br>TR3b | Přední, Cínovec<br>TR3c |      |
| n                                  | 9             | 13            | 6              | 16                            | 7                | 8                   | 8                       | 4    |
| SiO <sub>2</sub>                   | 71 -> 73      | 67.1 -> 64.5  | 76             | 77.0 -> 76.4                  | 75.9             | 75.6                | 72.1                    | 70.1 |
| TiO <sub>2</sub>                   | 0.33 -> 0.25  | 0.64 -> 0.65  | 0.07 -> 0.12   | 0.06 -> 0.13                  | 0.1              | 0.15                | 0.28                    | 0.51 |
| Al <sub>2</sub> O <sub>3</sub>     | 15.2 -> 14.0  | 15.0 - 16.0   | 12.2 -> 11.8   | 11.5 -> 12.4                  | 12.3             | 12.2                | 13.4                    | 14.1 |
| Fe <sub>2</sub> O <sub>3</sub> tot | 2.1 -> 1.5    | 3.1 - 3.8     | 0.8 -> 1.4     | 0.5 - 1.5                     | 1.65             | 1.63                | 2.47                    | 3.65 |
| MgO                                | 0.8 -> 0.7    | 1.5 - 1.9     | 0.08 -> 0.14   | 0.1                           | 0.1              | 0.14                | 0.31                    | 0.54 |
| CaO                                | 0.7 - 1.1     | 1.0 - 2.0     | 0.8 -> 0.4     | 0.1 - 1.1                     | 0.57             | 0.56                | 0.70                    | 0.62 |
| Na <sub>2</sub> O                  | 1.9 -> 2.5    | 2.3 - 4.2     | 2.4 -> 1.2     | 1.6 - 2.6                     | 3.34             | 2.98                | 3.32                    | 3.3  |
| K <sub>2</sub> O                   | 5.0 -> 4.7    | 3.6 - 4.8     | 5.0 -> 6.3     | 5 -> 6                        | 5.18             | 5.57                | 5.94                    | 5.9  |
| P <sub>2</sub> O <sub>5</sub>      | 0.09 - 0.07   | 0.23 - 0.25   | 0.011 -> 0.017 | 0.01 - 0.03                   | 0.03             | 0.05                | 0.09                    | 0.17 |
| Rb                                 | 240           | 175           | 350 -> 250     | 330 -> 265                    | 296              | 285                 | 229                     | 210  |
| Sr                                 | 150 - 225     | 325           | 25 -> 50       | 17 -> 30                      | 49               | 48                  | 84                      | 91   |
| Zr                                 | 100           | 75            | 100 -> 200     | 95 -> 145                     | 168              | 152                 | 244                     | 319  |
| U                                  | 8 - 10        | 6 - 8         | 10 -> 5        | 5 -> 30                       | 20               | 12                  | 10                      | 7    |
| Th                                 | 15            | 17            | 60 -> 30       | 43 -> 33                      | 75               | 45                  | 38                      | 30   |
| Y                                  | 24 - 18       | 16 -> 18      | 46 -> 24       | 72 -> 42                      | 75               | 45                  | 38                      | 55   |
| Ce                                 | 77 - 54       | 88 -> 92      | 84 -> 128      | 59 -> 113                     | 106              | 135                 | 140                     | 160  |
| Yb                                 | 2.3 - 1.7     | 1.55 -> 1.60  | 4.3 -> 2.7     | 7.4 -> 4.25                   | 6.2              | 4                   | 3                       | 4    |

Remarks: 24 - 18 .... variation of the element content (elements without distinct vertical evolution).

84 -> 128 .... changes in the element content from the early to the late rocks within the individual unit (elements with distinct vertical evolution).

relatively rich in Rb (Th, HREE) and poor in Sr and Zr (LREE) at the bottom of each unit to the rock depleted in Rb (Th, HREE) and enriched in Sr (LREE) in the upper part of each unit (Fig. 4).

According to the model of Hildreth (1979) and Fridrich and Mahood (1984) the step-by-step exhaustion of stratified magma chambers can be explained as follows. The melt produced in the deeper crust interrupted its ascent in a transitional reservoir. This gave rise to gravitational stratification - with relatively heavy crystals of feldspars, dark minerals and most accessories concentrated in the deeper part of the reservoir and light melt enriched in the upper part. Chemically, the stratification is reflected by higher content of Si, Na, and incompatible trace elements (Rb, Th, Y) in the melt in the upper part of the reservoir, while the deeper part is enriched in K, Fe, Mg, Sr, and Zr. The subsequent eruption deposited first acid tuffs, then intermediate ignimbrites rich in phenocrysts and later the ignimbrites rich in accessories (see also Breiter, 1997). The content of fluid in the melt stepwise decreased from the TR1 to the TR3 and the explosive style of the TR1 eruption changed to the more extrusive style of TR2 and to the extrusive to subvolcanic style of TR3 (Breiter et al., 2001).

The maximal thickness of the Teplice rhyolite in borehole TP-39 near Teplice is 1033 m and the assumed maximum thickness

may be up to 1200 m (Mlčoch and Skácelová, 2010). In the western part of the caldera, the rhyolitic/ignimbritic cover was only 30-50 m thick (Mlčoch and Skácelová, 2010). The volume of extruded Teplice volcanic was at least 160 km<sup>3</sup> assuming a minimum average thickness of the Teplice rhyolite of 250 m within the caldera structure. For comparison, during the Novarupta (Katmai, Alaska) in 1912, which was the largest eruption of the last century, 12.5 km<sup>3</sup> ignimbrites and ashes were erupted.

The Mikulov beds consisting of basal rhyolites (BR) and dacites (DC) form the bottom of the Teplice sequence (Fig. 2). They are relatively primitive calc alkaline in character with relative high contents of Fe, Mg, Ca, P, and Sr, low contents of Rb, Th, and HREE, and none or a small Eu-anomaly. Thus, they are chemically very different from the Teplice rhyolites. The different chemical compositions imply that the volcanic rocks of the Mikulov beds originated from different magma sources and reservoirs. The recent published U-Pb zircon age of 326.8±4.3 Ma by Hoffmann et al. (2012) suggest that the rocks of the Mikulov beds are significantly older than the Teplice ignimbrites. However, the 308.8±4.9 Ma age for the Teplice ignimbrite TR1 is not well constrained (Hoffmann et al., 2012).

## Eurogranites 2012

### Stop 1-3

Tourist mine „Vereinigt Zwitterfeld“  
(Tiefer Bünaustolln)

Zinnwald/Cínovec granite

Coordinates: UTM 33U 412925 m E/5621754 m N,  
760 m a.s.l.

Road K9090 and S183 from Schönefeld to Bärenfels via Oberpöbel; from there road K9045 to road 170 via Schellerhau; road 170 to Zinnwald

Guide: Axel Müller/Reimar Seltmann

The Tiefer Bünaustolln (Deep Bünau Adit) was developed at about 1550 under the name Tiefer Zinnwalder Erbstollen to exploit the Sn-W greisen mineralization hosted by the Zinnwald/Cínovec granite beneath the village Zinnwald (Figs. 5 and 6). However, tin mining goes back at least until 1378 when for the first time the name Zinnwald (Tin Forest) was recorded. Since that time primary tin ores have been mined with various intensity in the Cínovec/Zinnwald district until 1990, when the last mine in the Czech Cínovec was closed down. Until 1852 the Bünaustolln drained the German part of the mining district. In 1910 the adit was widened for the construction of mining rail. The most active period of mining was during the World War I and II. After the Second World War mining in the Bünaustolln was abandoned and continued only in the Czech part of district. The amount of extracted tin from the Cínovec/Zinnwald district was about 40,000 t. Between 1990 and 1992 the mine was secured and upgraded for tourism.

The deposit was investigated scientifically since the end of the 18th century. Mainly variegated mineralogy of the deposit attracted the attention of many mineralogists. Almost 450 papers have been published on the deposit. The deposit was described in detail by Štemprok (1960, 1961), Bolduan et al. (1967), and Čada and Novák (1974). Between 1962 and 1965 a 1596 m deep drilling (CS-1) was carried out in the center of the deposit (Rub et al., 1983).

The Czech and German side of the deposit were explored by drilling for Sn-W-Li vein and greisen ores in recent time revealing reserves on the Czech side of approximately 550 mill t of low-grade ore with 0.18 wt.% Rb, 0.26 wt.% Li and 0.01 wt.% Cs in zinnwaldite. From this amount, ca 55 mill t of ore contain in addition 0.2 % Sn and 0.045 wt.% W in cassiterite, wolframite, and scheelite. Apart from this, the Sn and W concentrates from Cínovec contain considerable contents of Nb, Ta, and especially Sc, by which they differ distinctly from greisens ores in the western part of the Erzgebirge/Krušné Hory area.

The Zinnwald/Cínovec granite forms a multiple composed, elliptical granite cupola outcropping 1.3 km in N-S direction between the German village Zinnwald and the Czech village Cínovec (Fig. 7). The W contact of the intrusion is steep whereas

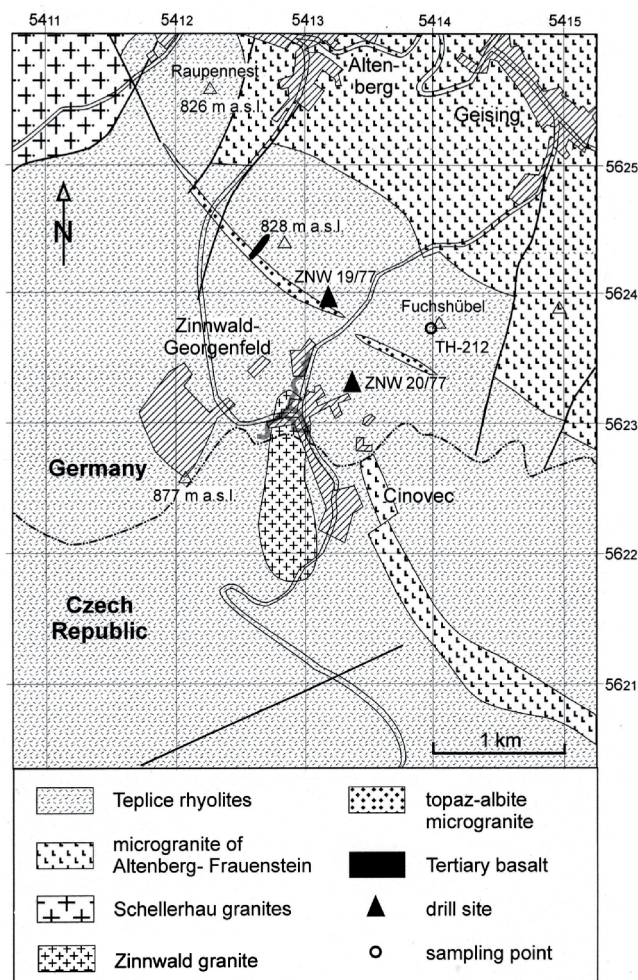


**Fig. 5.** Geological map of the area Cínovec/Zinnwald (after various sources). The approximate location surface projection of the Tiefer Bünaustolln is indicated by the grey line in the northern part of the Zinnwald granite.

the S, SE and E contact plunges gently with 10 to 30°. The upper part of the intrusion is formed by lithium-albite granite that is underlain by medium-grained protolithionite granite at a depth of 730 m (beneath Cínovec; Štemprok and Šulcek, 1969; Rub et al., 1983). In the cupola, the lithium-albite granite consists of two textural varieties: an older porphyritic and younger medium-grained seriate granite which encloses the relicts of the porphyritic granite. Zinnwaldite is the predominant mica in the lithium-albite granite. Minor dykes of aplite lithium-albite granite, marginal pegmatite (Stockscheider) separate the granite from its host rocks (Figs. 8 and 9).

The lithium-albite granites contain on average 0.11 wt.%  $\text{Li}_2\text{O}$  and 4.62 wt.%  $\text{K}_2\text{O}$  (Tables 3 and 4). According to the IUGS classification, they are classified as alkali feldspar granites. Plagioclase is absent, sodium feldspars are represented by albite with a low (<3 wt.%) anorthite content. Main accessories are cassiterite, fluorite, topaz, and columbite-tantalite in addition to rare bastnaesite, uranpyrochlor, uranmicrolite, strueverite, and synchisite (Johan and Johan, 1993; Rub et al., 1998). The protolithionite granite contains on average 0.05 wt.%  $\text{Li}_2\text{O}$  and 5.34 wt.%  $\text{K}_2\text{O}$ . Main accessories are zircon, columbite, monazite, xenotime and rutile. Apatite is very rare.

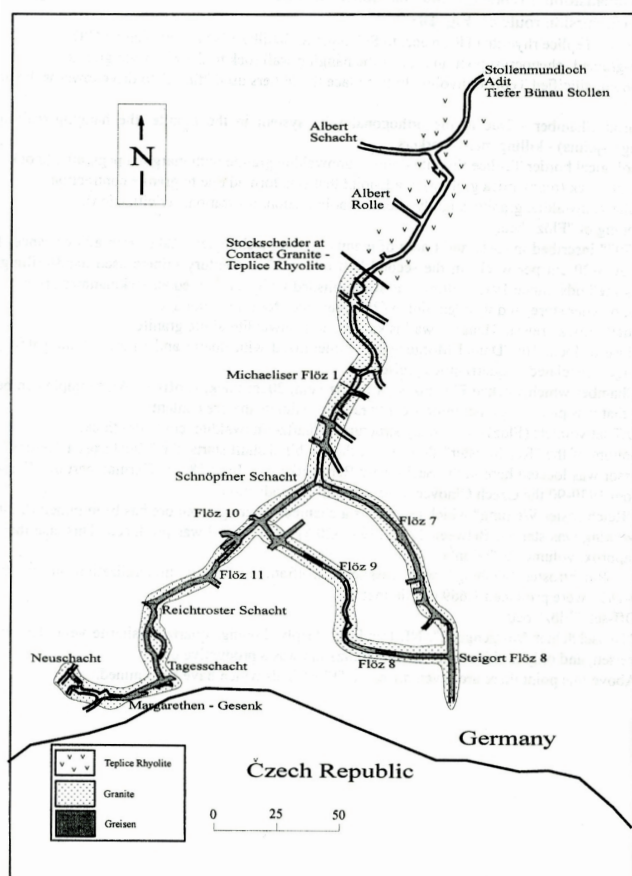


Fig. 6. Mine plan of the Tiefer Bünaustolln.

The chemical composition of the rocks exposed in the Tiefer Bünaustolln is shown in Table 5.

The Sn-W-Li deposit is spatially associated with the granite cupola. The deposit consists of two morphological types of ores:

- (I) Irregular, metasomatic greisens, several tens of meters wide, follow the morphology of the granite contact. There are several types of greisen and greisenized granites. The predominant greisen consist of quartz and zinnwaldite or zinnwaldite-quartz-topaz. The greisen contain irregular admixtures of sericite, fluorite, and potash feldspar of adularia type. Some of the greisen are intensely hematitized.
- (II) Flat thin greisen zones (called Flöze) and quartz veins with a thickness of up to 2 m in the centre of the granite cupola. The quartz veins are accompanied by irregular wall rock greisenization. The main ore minerals are cassiterite, wolframite, and scheelite. Cassiterite commonly contains inclusions of tapiolite, columbite, tantalite, and Nb-Ta rutile (Hoffmann et al., 1965).

The form of the ore bodies is highly irregular depending on the intersection of steep and flat fissures and the development of late stage greisen in three principal zones: (a) Saxony zone (N) with greisen and vein systems, (b) Central zone with flat-plunging quartz veins and wall rock greisen, and (c) Southern zone with large irregular greisen bodies (Štemprok et al., 1994). A strong „intravenous“ metasomatism was postulated by Štemprok (1960) supposing preferential migration of fluids in a fissured vein system in the granite and neighboring Teplice rhyolite. In the veins, the mineralization can be differentiated

**Table 3.** Average compositions of the two major Zinnwald/Cínovec granite phases. Analysed samples are from drill hole CS-1 (1596 m deep; Štemprok and Šulcek, 1969; Rub et al., 1983; Štemprok, 1989; Cocherie et al., 1991).

|                                | lower protolithionite granite (n= 11) | upper zinnwaldite granite (n = 7) |
|--------------------------------|---------------------------------------|-----------------------------------|
| SiO <sub>2</sub> %             | 75.95                                 | 75.09                             |
| TiO <sub>2</sub>               | 0.10                                  | 0.07                              |
| Al <sub>2</sub> O <sub>3</sub> | 12.19                                 | 13.61                             |
| Fe <sub>2</sub> O <sub>3</sub> | 0.54                                  | 0.31                              |
| FeO                            | 0.71                                  | 0.54                              |
| MnO                            | 0.03                                  | 0.04                              |
| MgO                            | 0.14                                  | 0.17                              |
| CaO                            | 0.60                                  | 0.29                              |
| Na <sub>2</sub> O              | 2.81                                  | 3.86                              |
| K <sub>2</sub> O               | 5.34                                  | 4.62                              |
| Li <sub>2</sub> O              | 0.05                                  | 0.11                              |
| P <sub>2</sub> O <sub>5</sub>  | tr.                                   | tr.                               |
| H <sub>2</sub> O <sup>+</sup>  | 1.07                                  | 0.84                              |
| F                              | 0.52                                  | 0.68                              |
| H <sub>2</sub> O <sup>-</sup>  | 0.18                                  | 0.20                              |
| As ppm                         | 9 (n=87)                              | 29 (n=73)                         |
| Ba                             | 59                                    | 49                                |
| Be                             | 21                                    | 11                                |
| Bi                             | 5                                     | 22                                |
| Cu                             | 9                                     | 9                                 |
| Mo                             | 4                                     | 3                                 |
| Nb                             | 48                                    | 74                                |
| Pb                             | 28                                    | 22                                |
| Rb                             | 771                                   | 1677                              |
| Sb                             | 3                                     | 5                                 |
| Sn                             | 29                                    | 92                                |
| U                              | 31                                    | 29                                |
| W                              | 36                                    | 54                                |
| Zn                             | 27                                    | 45                                |
| Zr                             | 130                                   | 37                                |
| Cs                             | 26.8 (n=2)                            | 31.7 (n=1)                        |
| Hf                             | 6.6                                   | 5.6                               |
| Sr                             | 14                                    | 12                                |
| Ta                             | 7.61                                  | 47.6                              |
| Th                             | 67.6                                  | 14.5                              |
| Y                              | 102                                   | ~6                                |
| La                             | 41 (n=9)                              | 28 (n=6)                          |
| Ce                             | 83                                    | 65                                |
| Sm                             | 9.92                                  | 6.33                              |
| Eu                             | 0.13                                  | ~0.005                            |
| Tb                             | 2.2                                   | 1.3                               |
| Yb                             | 17.2                                  | 19.0                              |
| Lu                             | 2.23                                  | 2.16                              |

n = number of samples; for elements with a larger or smaller number of samples, this is indicated behind the respective element.

~ = indicates contents of elements with data below detection limit.

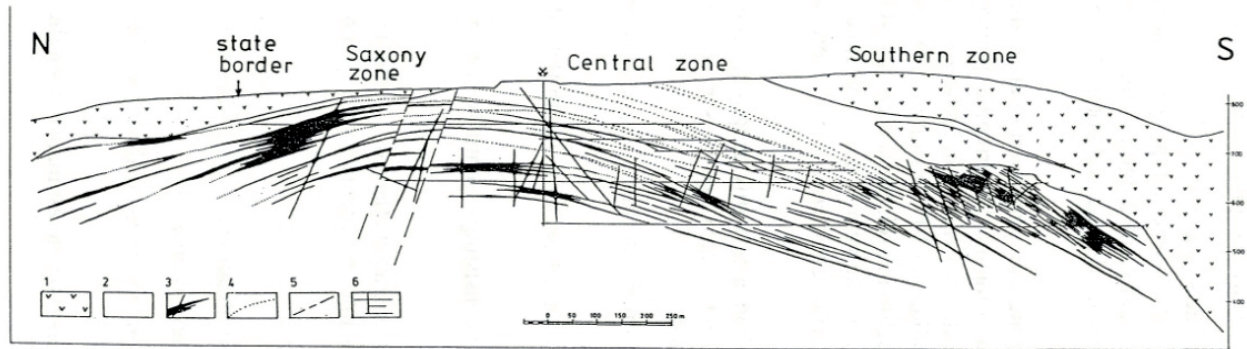


Fig. 7. North-south geological cross section from the German into the Czech part of the Zinnwald/Cínovec granite cupola (Štemprok et al., 1994). 1 – Teplice rhyolite, 2 – lithium-albite granite, 3 – greisen, 4 – quartz veins, 5 – faults, 6 – schematic representation of the mine levels on the Czech side of the deposit.

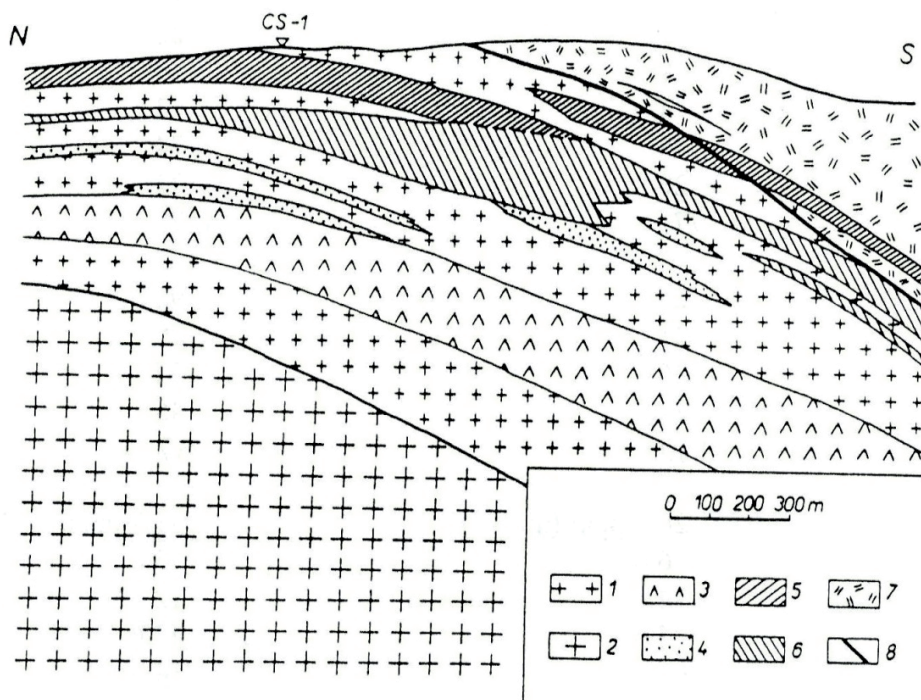


Fig. 8. Schematic cross section of the Zinnwald/Cínovec granite intrusion according to Štemprok and Šulcek (1969). 1 – medium-grained lithium-mica granite, 2 – lower, porphyritic medium-grained granite and microgranite, 3 – porphyritic lithium-mica microgranite, 4 – feldspatites, 5 – upper vein and greisen zone, 6 – lower greisen zone, 7 – Teplice rhyolite, 8 – marginal pegmatite (Stockscheider).

into four stages: (I) quartz/barren quartz veins, (II) greisen with zinnwaldite, topaz, cassiterite, and wolframite, (III) K-feldspar (adularia) metasomatism with pegmatite-like textures, and (IV) minor sulfide mineralization with arsenopyrite, galena, sphalerite, tennantite, chalcopyrite, bismuth, bismuthinite, wittichenite, pyrite, and opal. The deposition of sulfides was accompanied by sericitization and kaolinization. Supergene alteration affected the sulphide mineralization in the upper part of the cupola resulting in the formation of malachite, philipsbornite, mimetite, olivenite, and some rare supergene oxide minerals.

In general, the deposit was formed by repeated introduction of ore-bearing solutions into the mainly flat fissures of the granite which were formed apparently by the contraction of the granite in its upper part. The solutions moved to the place of ore deposition from lower levels of the intrusion as indicated by greisen in the deep parts of the granite body (about 1200 m). There was an effective interplay of metasomatism and repeated tectonic movements, which led to the zoning of the deposit and the manifestations of post-magmatic alteration down to the deepest known parts of the

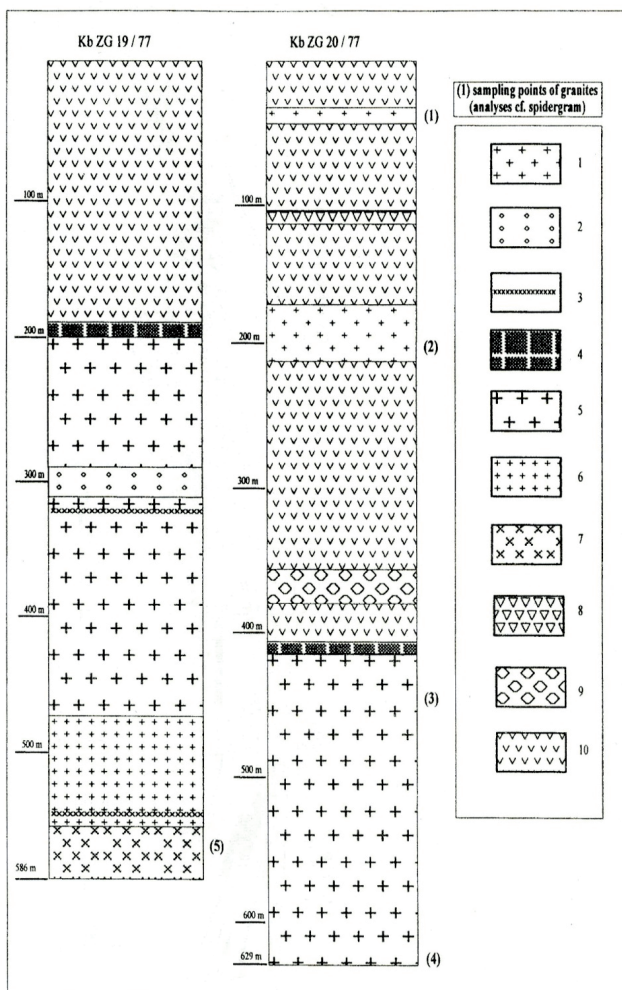
**Table 4.** Composition of representative granite samples from Zinnwald deep drillings. Data from Seltmann et al. (1998).

| Albite granite type            | zinnwaldite (lepid)      | zinnwaldite (lepid)      | zinnwaldite                 | zinnwaldite              | protolithionite                |
|--------------------------------|--------------------------|--------------------------|-----------------------------|--------------------------|--------------------------------|
| Texture                        | fine-grained porphyritic | fine-grained porphyritic | medium-grained equigranular | medium-grained (seriate) | fine-grained seriate (altered) |
| SiO <sub>2</sub> , wt. %       | 73.87                    | 72.95                    | 74.01                       | 74.36                    | 75.01                          |
| TiO <sub>2</sub>               | 0.01                     | 0.01                     | 0.01                        | 0.01                     | 0.02                           |
| Al <sub>2</sub> O <sub>3</sub> | 14.02                    | 14.73                    | 13.86                       | 13.69                    | 13.31                          |
| Fe <sub>2</sub> O <sub>3</sub> | 0.93                     | 0.82                     | 0.87                        | 0.97                     | 1.82                           |
| MnO                            | 0.04                     | 0.05                     | 0.05                        | 0.04                     | 0.08                           |
| MgO                            | 0.03                     | 0.04                     | 0.03                        | 0.04                     | 0.01                           |
| CaO                            | 0.24                     | 0.33                     | 0.43                        | 0.36                     | 0.38                           |
| Na <sub>2</sub> O              | 4.18                     | 4.00                     | 4.22                        | 4.17                     | 4.98                           |
| K <sub>2</sub> O               | 4.42                     | 4.77                     | 4.34                        | 4.67                     | 2.36                           |
| P <sub>2</sub> O <sub>5</sub>  | 0.01                     | 0.01                     | 0.01                        | 0.01                     | 0.01                           |
| H <sub>2</sub> O+              | 1.20                     | 1.30                     | 0.95                        | 0.87                     | 0.58                           |
| CO <sub>2</sub>                | 0.04                     | 0.11                     | 0.11                        | 0.12                     | 0.09                           |
| F                              | 0.39                     | 0.60                     | 0.87                        | 0.52                     | 1.49                           |
| F=O <sub>2</sub>               | 0.164                    | 0.253                    | 0.366                       | 0.219                    | 0.627                          |
| Total                          | 99.21                    | 99.46                    | 99.39                       | 99.60                    | 99.51                          |
| Ba, ppm                        | 37                       | 44                       | 55                          | 64                       | 14                             |
| Be                             | 5.1                      | 7.3                      | 8.1                         | 7.8                      | 11.0                           |
| Cs                             | 62.3                     | 90.4                     | 36.0                        | 25.5                     | 56.1                           |
| Ga                             | 39                       | 41                       | 43                          | 36                       | 35                             |
| Hf                             | 7.0                      | 6.6                      | 9.3                         | 7.3                      | 11.3                           |
| Li                             | 341                      | 912                      | 1057                        | 710                      | 1078                           |
| Mo                             | 1.0                      | <1                       | 2.9                         | 0.6                      | 44                             |
| Nb                             | 107                      | 104                      | 103                         | 95                       | 82                             |
| Pb                             | 26                       | 31                       | 54                          | 42                       | 42                             |
| Rb                             | 2005                     | 2537                     | 1967                        | 1479                     | 1327                           |
| Sb                             | 1.6                      | 2.2                      | 0.2                         | 0.4                      | 0.3                            |
| Se                             | 8.4                      | 8.6                      | 6.9                         | 6.3                      | 9.2                            |
| Sn                             | 153                      | 158                      | 152                         | 74                       | 62                             |
| Sr                             | 11                       | 11                       | 4.0                         | 4.8                      | 3.6                            |
| Ta                             | 33                       | 34                       | 49                          | 22                       | 19                             |
| Th                             | 21.2                     | 20.1                     | 20.9                        | 24.2                     | 39.9                           |
| U                              | 13.2                     | 11.0                     | 27.4                        | 28.6                     | 27.0                           |
| W                              | 13                       | 18                       | 9                           | 18                       | 81                             |
| Y                              | 17.1                     | 14.7                     | 25.4                        | 32.8                     | 127                            |
| Zn                             | 22                       | 21                       | 40                          | 31                       | 64                             |
| Zr                             | 49                       | 46                       | 61                          | 62                       | 131                            |
| La                             | 14.6                     | 16.4                     | 18.3                        | 26.3                     | 33.7                           |
| Ce                             | 40.0                     | 43.7                     | 51.7                        | 71.5                     | 89.6                           |
| Pr                             | 4.86                     | 5.11                     | 6.76                        | 8.89                     | 11.7                           |
| Nd                             | 11.7                     | 12.5                     | 18.5                        | 24.6                     | 36.8                           |
| Sm                             | 3.09                     | 3.09                     | 5.32                        | 7.31                     | 11.2                           |
| Eu                             | <0.006                   | 0.010                    | 0.008                       | 0.012                    | 0.013                          |
| Gd                             | 2.28                     | 2.19                     | 3.77                        | 6.04                     | 11.6                           |
| Tb                             | 0.65                     | 0.60                     | 0.95                        | 1.45                     | 2.73                           |
| Dy                             | 5.05                     | 4.59                     | 6.76                        | 9.39                     | 19.8                           |
| Ho                             | 1.08                     | 0.96                     | 1.47                        | 1.82                     | 4.32                           |
| Er                             | 4.29                     | 3.70                     | 5.77                        | 6.35                     | 15.2                           |
| Tm                             | 1.01                     | 0.89                     | 1.33                        | 1.34                     | 2.92                           |
| Yb                             | 8.85                     | 8.05                     | 11.5                        | 11.6                     | 22.0                           |
| Lu                             | 1.35                     | 1.26                     | 1.72                        | 1.80                     | 3.32                           |
| A/CNK                          | 1.16                     | 1.19                     | 1.12                        | 1.09                     | 1.17                           |
| 1/TiO <sub>2</sub>             | 143                      | 143                      | 111                         | 83                       | 48                             |

intrusion (about 1600 m; Seltmann et al., 1998).

**Table 5.** Geochemical characteristics of rocks exposed in the Tiefer Bünaustolln. Data from Seltmann et al. (1998).

| Rock                                  | Albite granite ZG 19/77, 20/77 | Altered granites              | Greisen   | Teplice rhyolite                                       |
|---------------------------------------|--------------------------------|-------------------------------|---|--|
| SiO <sub>2</sub> , wt.%               | 72.5 – 74.5                    | enriched, 73 – 76             | qtz-mica- and top- mica greisen >74; qtz- / topaz greisen <60                           | unaltered 74 – 76; altered and greisenized: 76 – 80    |
| A/CNK                                 | 1.0 – 1.1                      | 1.0 – 1.4                     | wt.-% Al <sub>2</sub> O <sub>3</sub> : top greisen >20; quartz-/top-mica greisen 7 – 13 | 1.0 – 1.1  |
| Na <sub>2</sub> O, wt.%               | 4.0 – 4.2                      | <4                            | depleted, < 2   | <3   |
| K <sub>2</sub> O, wt.%                | 4.2 – 4.7                      | 3-4                           | depleted, < 3   | > 4  |
| P <sub>2</sub> O <sub>5</sub> , wt.-% | poor, < 0.01                   | poor, < 0.1                   | poor, < 0.1   | poor, < 0.1  |
| F, wt.%                               | 0.2 – 0.8                      | enriched, 0.5 – 1.7           | enriched, 3.4 – 5.4   | F-rich: 0.4 – 1.5                                      |
| Rb, ppm                               | 1400 – 2500                    | mostly enriched: 1800 – 3000  | enriched: >2000; but low in topaz greisen: <1600  | unaltered: < 600; altered and greisenized: 1280 – 1700 |
| Li, ppm                               | 300 – 1100                     | high, 500 – 3000              | high, 140 – 4800  | low, 115 – 140; altered: 450 – 1365                    |
| Sn, ppm                               | 60 – 160                       | enriched, 50-320              | mica greisen: >100; topaz greisen 30 – 50   | high, 20 – 50, altered: up to 180                      |
| Y, ppm                                | 15 – 30                        | low, < 10                     | < 10  | 40 – 60  |
| Ba, Sr, Ni, Cu, Zr, Sc contents       | low                            | low                           | low   | low  |
| LREE vs.HREE REE pattern              | flat, wing-shaped REE pattern  | flat, wing-shaped REE pattern | flat, wing-shaped REE pattern   | LREE > HREE, steep pattern                             |
| Tetrad effect                         | slightly                       | weak                          | significant   | fresh rocks: none                                      |
| Eu anomaly                            | negative                       | negative                      | negative  | slightly   |
| K/Rb                                  | 15 – 25                        | low, < 10                     | low, varying  | low, < 10  |
| Rb/Sr                                 | 200 – 500                      | high, >50                     | varying, 130 – 300  | high, > 50   |

**Fig. 9.** Lithology of drill cores Kb ZG 19/77 and Kb ZG 20/77 (see Fig. 5 for location) modified after Grunewald (1978).

1 – dikes of albite-zinnwaldite(-lepidolite) granite, 2 – greisen derived from albite-Li-mica granites, 3 – fine-grained aplitic dikes, 4 – marginal pegmatite (Stockscheider), 5 – equigranular medium-grained albite-zinnwaldite granite with greisen veinlets, 6 – fine-grained porphyritic albite-zinnwaldite granite with enclaves of (5), 7 – sequence of albite-protolithionite granites and medium- to coarse-grained albite-zinnwaldite granites, 8 – tectonic breccias within Teplice rhyolite cut by greisen veinlets, 9 – dike of phenocryst-rich Teplice rhyolite TR3b, 10 – Teplice rhyolite TR3a with greisen veinlets.

# Eurogranites 2012

## Stop 1-4

### Quarry Bärenstein

#### Altenberg-Frauenstein microgranite

Coordinates: UTM 33U 413470 m E/5627500 m N, 570 m a.s.l.

Road K9033 from Zinnwald to Geising; from Geising road S178 (Dresdner Strasse, Müglitztalstrasse) to junction with road K9061 (Bielatalstrasse), continuing on road K9061 to branch to the Quarry Bärenstein

#### Guide: Axel Müller/Reimar Seltmann

The quarry Bärenstein is operated by the company *ProStein GmbH & Co. KG* for gravel production. It is located on the north-western flank of the hill Kesselshöhe (657 m a.s.l.), about 3 km NNE of Altenberg and exposes the Altenberg-Frauenstein microgranite.

The eruption of the enormous volume of the Teplice rhyolites of at least 160 km<sup>3</sup> led to the collapse of the Altenberg-Teplice caldera, forming a trap-door caldera, with N–S elongated pear-shaped ring fractures with multiple intrusions of the Altenberg-Frauenstein porphyritic microgranite dike complex (Benek, 1991; Fig. 1).

The microgranites show wide textural and geochemical variations (Müller and Seltmann, 2001; Seltmann et al., 2001; Müller and Seltmann, 2002; Fig. 10). Field documentation allowed the reconstruction of the age relations and the classification of chemically and texturally distinct GP I and GP II intrusive phases that are characterized by sharp intrusive contacts. The granite porphyries intruded in the sequence: 1) K-feldspar phenocryst-poor porphyritic feldspar-quartz microgranite with fine-grained matrix (GP I), 2) porphyritic feldspar-quartz-hornblende microgranite with granophyric matrix (GP II). The latter may locally contain

mafic schlieren (GP II<sub>hbl</sub>) and phenocryst-free miarolitic zones (GP II<sub>m</sub>). The most acid medium- to coarse-grained microgranite (GP I<sub>cum</sub>) occurs as enclaves in GP I and GP II. The ring dyke complex is dominated by GP I, with less common occurrences of more mafic batches of GP II. The varieties GP I<sub>cum</sub>, GP II<sub>hbl</sub>, and GP II<sub>m</sub> are rare and occur mapable only in the eastern dike in the vicinity of Altenberg. Pegmatite and aplite schlieren, several meters large, coarse-grained phenocryst-rich porphyritic varieties (apparently forming a marginal facies of GP II), and phenocryst-free microgranitic varieties (with sharp contact to GP II and interpreted as GP III, Seltmann et al., 2001) seem to be local phenomena and occupy only a minor volume. They were observed predominantly in the quarry Bärenstein NNE of Altenberg, along with all other textural varieties. The petrographic characteristics of the different microgranite facies are summarized in Table 6.

The most interesting petrographic feature is the common occurrence of rapakivi-type plagioclase-mantled K-feldspar phenocrysts in most of the microgranite varieties. The plagioclase mantles have oligoclase composition but are commonly strongly hematitized and altered to albite (Fig. 11a).

Other specific petrographic features are the occurrence of sieve-textured plagioclase phenocrysts, resorbed quartz phenocrysts mantled by microcrystalline plagioclase, biotite and titanomagnetite, and nests (globules) of mafic minerals with biotite, plagioclase, ferro-tremolites, and rare pyroxene. The resorbed quartz phenocrysts are overgrown by Ti-rich granophyric quartz (Figs. 11b and 11a) indicating that the magma temperature increased at least 82°C after the resorption event (Müller et al., 2008). These textural features indicated mixing and mingling with mafic magmas prior to emplacement of the microgranites.

The chemical evolution pattern of the microgranite intrusion sequence correlates well with its textural and mineralogical characteristics. Chemical compositions of representative samples are given in Table 7. The varieties of the microgranites represent two major intrusion stages evolving from acid, more fractionated rocks (GP I), to less acid rocks (GP II). In the REE plot, GP I and GP II show similar degrees of fractionation, with a pronounced LREE enrichment over HREE and pronounced Eu minimum. The Eu minimum for GP II<sub>hbl</sub> is less deep than for its precursors GP I and GP II because the mafic schlieren are rich in hornblende, plagioclase, and REE-bearing accessory minerals.

**Table 6.** Petrographic characteristics of the main varieties of the porphyritic microgranite of Altenberg-Frauenstein. Data from Müller and Seltmann (2002).

| Variety<br>(sample #)         | Phenocryst content (vol.%) |     |                  |    |     | Matrix   | Mafic minerals               | Main accessories   |
|-------------------------------|----------------------------|-----|------------------|----|-----|--|------------------------------|--|
|                               | qz                         | kfs | kfs <sub>m</sub> | pi | sum |  |                              |  |
| GP I <sub>qz</sub> (20/2000)  | 18                         | 34) | 1                | 6  | 59  | fine-grained                                   | biotite, epidote             | zircon, apatite, titanomagnetite                               |
| GP I (18/2000)                | 9                          | 23  | 2                | 7  | 41  | fine-grained                                   | biotite, epidote             | zircon, apatite, titanomagnetite                               |
| GP I <sub>fs</sub> (19/2000)  | 8                          | 37  | 2                | 9  | 56  | fine-grained                                   | biotite, epidote             | zircon, apatite, titanomagnetite                               |
| GP I <sub>cum</sub> (93)      | 24                         | 28  | 0                | 3  | 55  | medium-grained                                 | biotite                      | zircon, apatite  |
| GPII (23/2000)                | 1                          | 28  | 6                | 13 | 48  | fine-grained, qtz-kfs intergrowth              | biotite, hornblende, epidote | zircon, apatite, titanomagnetite, allanite, monazite, xenotime |
| GP II <sub>hbl</sub> (113)    | 2                          | 6   | 7                | 20 | 35  | fine-grained, qtz-kfs intergrowth              | biotite, hornblende, epidote | zircon, apatite, titanomagnetite, allanite, monazite, xenotime |
| GP II <sub>gs</sub> (22/2000) | 2                          | 32  | 5                | 16 | 55  | fine-grained, qtz-kfs intergrowth, greisenized | biotite, hornblende, epidote | zircon, apatite, titanomagnetite, allanite, monazite, xenotime |

**Table 7.** Composition of the main varieties of the Altenberg-Frauenstein microgranite. Data from Müller and Seltmann (2002).

| Type<br>Sample                  | GP I <sub>qz</sub><br>20/2000 | GP I <sub>fs</sub><br>19/2000 | GP I<br>18/2000 | GP I <sub>cum</sub><br>GP 93 | GP II <sub>gs</sub><br>22/2000 | GP II<br>23/2000 | GP II <sub>hbl</sub><br>GPI 13 | GP II <sub>m</sub><br>GP98 |
|---------------------------------|-------------------------------|-------------------------------|-----------------|------------------------------|--------------------------------|------------------|--------------------------------|----------------------------|
| SiO <sub>2</sub> %              | 73.8                          | 68.8                          | 68.7            | 72.9                         | 66.1                           | 65.8             | 64.1                           | 74.5                       |
| TiO <sub>2</sub>                | 0.21                          | 0.45                          | 0.48            | 0.18                         | 0.59                           | 0.55             | 0.75                           | 0.15                       |
| Al <sub>2</sub> O <sub>3</sub>  | 12.8                          | 14.5                          | 14.3            | 13.2                         | 14.1                           | 14.4             | 15.3                           | 13.1                       |
| tFe <sub>2</sub> O <sub>3</sub> | 1.38                          | 3.61                          | 3.73            | 1.67                         | 4.96                           | 3.92             | 5.53                           | 0.97                       |
| MnO                             | 0.016                         | 0.038                         | 0.046           | 0.055                        | 0.068                          | 0.074            | 0.107                          | 0.033                      |
| MgO                             | 0.11                          | 0.54                          | 0.74            | 0.25                         | 0.66                           | 0.83             | 1.24                           | 0.17                       |
| CaO                             | 0.21                          | 0.77                          | 0.62            | 1.06                         | 1.95                           | 1.31             | 2.23                           | 0.42                       |
| BaO                             | 0.044                         | 0.082                         | 0.079           | 0.048                        | 0.083                          | 0.098            | 0.122                          | 0.04                       |
| Na <sub>2</sub> O               | 2.77                          | 3.32                          | 3.38            | 2.56                         | 3.09                           | 3.07             | 3.71                           | 2.28                       |
| K <sub>2</sub> O                | 6.76                          | 6.57                          | 6.59            | 6.75                         | 6.35                           | 6.73             | 5.07                           | 7.66                       |
| H <sub>2</sub> O <sup>+</sup>   | 0.72                          | 1.05                          | 1.11            | 0.48                         | 0.85                           | 1.04             | 1.44                           | 0.49                       |
| P <sub>2</sub> O <sub>5</sub>   | 0.07                          | 0.15                          | 0.15            | 0.05                         | 0.21                           | 0.21             | 0.30                           | 0.01                       |
| CO <sub>2</sub>                 | n.d.                          | n.d.                          | 0.03            | 0.53                         | 0.09                           | 0.03             | 0.2                            | 0.27                       |
| F                               | 0.022                         | 0.029                         | 0.060           | 0.042                        | 1.380                          | 0.070            | 0.082                          | 0.019                      |
| 0=F                             | -0.011                        | -0.013                        | -0.026          | -0.018                       | -0.581                         | -0.030           | -0.035                         | -0.008                     |
| Sum                             | 99.0                          | 99.9                          | 100.0           | 99.8                         | 99.9                           | 98.2             | 100.1                          | 100.1                      |
| Zn ppm                          | 35                            | 65                            | 65              | 34                           | 120                            | 80               | 160                            | 54                         |
| Rb                              | 305                           | 229                           | 217             | 313                          | 933                            | 241              | 186                            | 329                        |
| Sr                              | 52                            | 117                           | 127             | 90                           | 94                             | 176              | 208                            | 56                         |
| Y                               | 46.8                          | 35.2                          | 40.5            | 26.4                         | 46.7                           | 34.3             | 37.7                           | 22.9                       |
| Zr                              | 227                           | 330                           | 367             | 172                          | 338                            | 309              | 430                            | 167                        |
| Nb                              | 13                            | 15                            | 16              | <10                          | 17                             | 14               | 13                             | <10                        |
| Sn                              | <=20                          | <20                           | n.d.            | 5                            | <20                            | n.d.             | 4                              | 7                          |
| Cs                              | 11.4                          | 7.8                           | 13.9            | 8.8                          | 21.9                           | 7.6              | 10.4                           | 7.8                        |
| La                              | 75.2                          | 75.9                          | 81.6            | 60.4                         | 67.4                           | 68.9             | 78.4                           | 37.7                       |
| Ce                              | 153                           | 149                           | 155             | 115                          | 138                            | 135              | 155                            | 72                         |
| Pr                              | 17.6                          | 16.8                          | 18.1            | 12.2                         | 16.2                           | 15.3             | 17.6                           | 7.6                        |
| Nd                              | 61.7                          | 59.3                          | 63.4            | 41.4                         | 57.9                           | 54.2             | 63.6                           | 26.0                       |
| Sm                              | 11.9                          | 10.6                          | 11.2            | 7.0                          | 11.3                           | 9.7              | 11.3                           | 4.8                        |
| Eu                              | 0.76                          | 1.32                          | 1.37            | 0.79                         | 1.31                           | 1.41             | 1.98                           | 0.65                       |
| Gd                              | 10.24                         | 8.31                          | 9.29            | 5.53                         | 9.62                           | 8.09             | 9.04                           | 4.12                       |
| Tb                              | 1.55                          | 1.242                         | 1.35            | 0.83                         | 1.50                           | 1.16             | 1.27                           | 0.64                       |
| Dy                              | 9.10                          | 7.22                          | 7.87            | 4.74                         | 9.17                           | 6.72             | 7.46                           | 3.86                       |
| Ho                              | 1.71                          | 1.36                          | 1.48            | 0.92                         | 1.75                           | 1.27             | 1.45                           | 0.77                       |
| Er                              | 4.88                          | 3.87                          | 4.26            | 2.65                         | 5.04                           | 3.61             | 4.06                           | 2.32                       |
| Tm                              | 0.66                          | 0.53                          | 0.58            | 0.39                         | 0.72                           | 0.49             | 0.55                           | 0.34                       |
| Yb                              | 4.23                          | 3.52                          | 3.75            | 2.56                         | 4.77                           | 3.23             | 3.71                           | 2.38                       |
| Lu                              | 0.61                          | 0.53                          | 0.55            | 0.37                         | 0.68                           | 0.49             | 0.56                           | 0.36                       |
| Hf                              | 7.05                          | 8.69                          | 9.62            | 5.75                         | 8.49                           | 7.97             | 9.99                           | 5.49                       |
| Pb                              | 40.1                          | 30.4                          | 32.3            | 28.3                         | 38.4                           | 30.1             | 43.2                           | 50.2                       |
| Th                              | 43.5                          | 25.2                          | 26.6            | 27.5                         | 20.6                           | 22.7             | 24.2                           | 22.7                       |
| U                               | 8.4                           | 4.9                           | 6.2             | 8.0                          | 4.7                            | 5.2              | 5.1                            | 7.2                        |
| Be                              | 3.8                           | 4.0                           | 3.8             | n.d.                         | 31                             | 3.7              | n.d.                           | n.d.                       |
| Co                              | <5                            | 7                             | 8               | n.d.                         | 9                              | 11               | n.d.                           | n.d.                       |
| Cr                              | <20                           | <20                           | <20             | 39                           | <20                            | <20              | 34                             | 32                         |
| Cu                              | <5                            | <5                            | <5              | n.d.                         | <5                             | 7                | n.d.                           | n.d.                       |
| Li                              | 23                            | 24                            | 51              | n.d.                         | 179                            | 32               | n.d.                           | n.d.                       |
| Ni                              | <20                           | <20                           | <20             | <10                          | <20                            | n.d.             | <10                            | <10                        |
| Sc                              | 4                             | 7                             | 7               | n.d.                         | 11                             | 9                | n.d.                           | n.d.                       |
| V                               | 40                            | 85                            | 95              | <10                          | 165                            | 180              | 27                             | <10                        |
| Zr/Hf                           | 32.3                          | 38.0                          | 38.1            | 29.9                         | 39.8                           | 38.7             | 43.0                           | 30.4                       |
| Y/Ho                            | 27.4                          | 26.0                          | 27.3            | 28.7                         | 26.7                           | 27.0             | 26.0                           | 29.6                       |
| Th/U                            | 5.17                          | 5.18                          | 4.33            | 3.45                         | 4.36                           | 4.37             | 4.77                           | 3.14                       |

n.d. - not detected

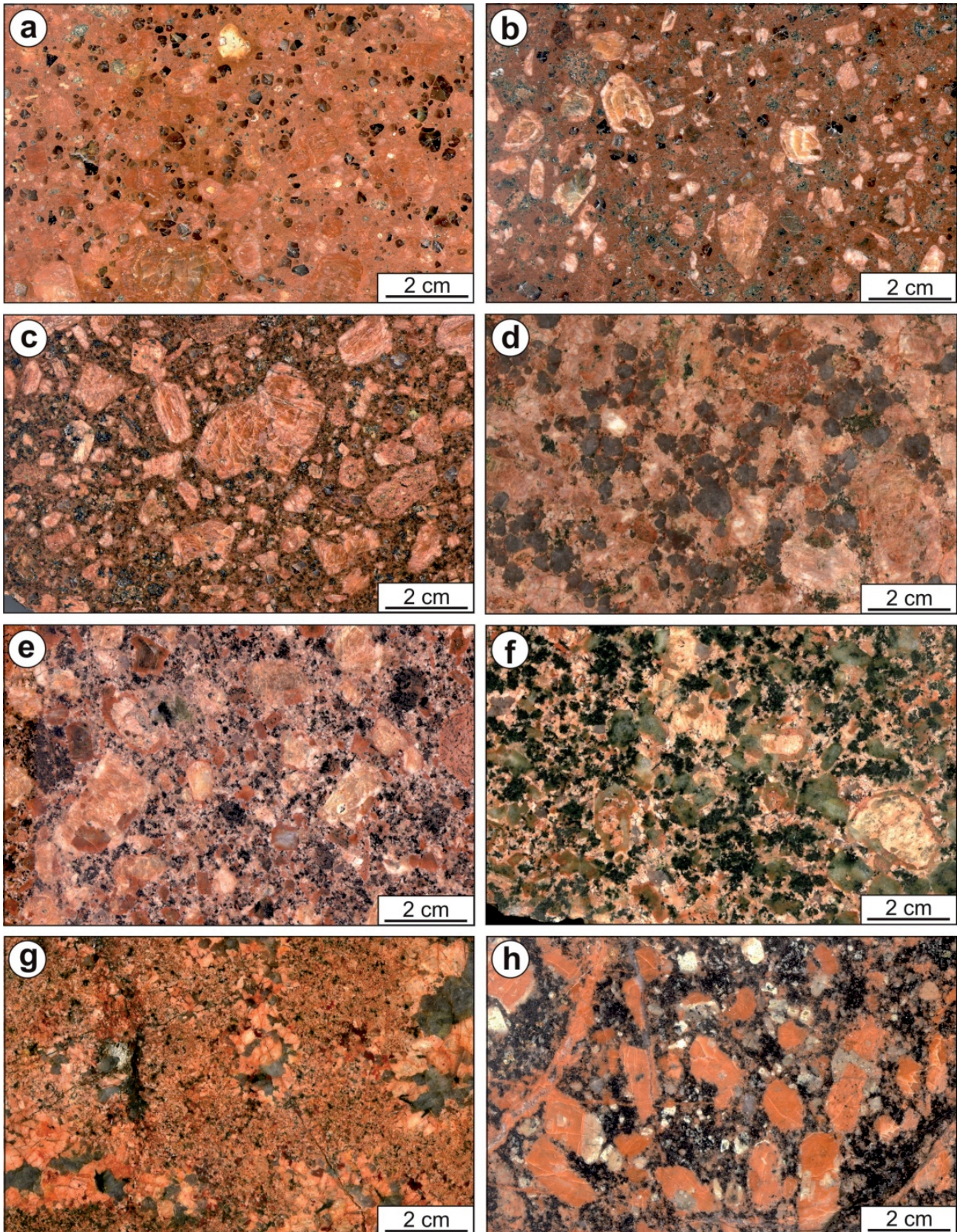


**Fig. 10.** Textural varieties of Altenberg-Frauenstein microgranite of the intrusion phases GP I and GP II. a – quartz-phenocryst-rich porphyritic feldspar-quartz microgranite GP I<sub>qz</sub> (20/2000). b – porphyritic feldspar-quartz microgranite GP I (18/2000). c – K-feldspar-rich porphyritic feldspar-quartz microgranite GP I<sub>fs</sub> (19/2000). d – medium- to coarse-grained microgranite GP I<sub>cum</sub> (GP 93). e – porphyritic feldspar-quartz-hornblende microgranite GP II with granophyric matrix (23/2000). f – mafic schlieren within the feldspar-quartz-hornblende microgranite GP II<sub>hbl</sub> (GP 113). g – miarolitic microgranite GP II<sub>m</sub> (GP 98). h – greisenized feldspar-quartz-hornblende microgranite GP II<sub>gs</sub> (22/2000). From Müller and Seltmann (2002).

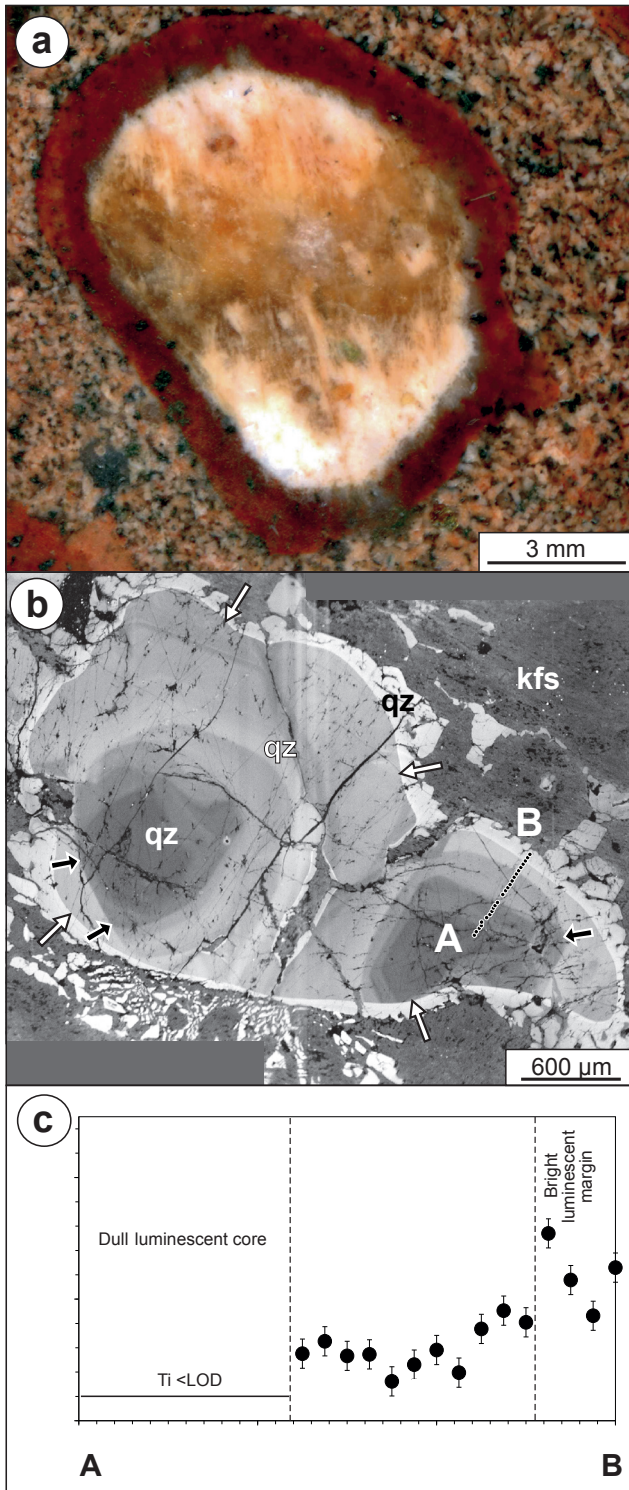


**Fig. 11.** (a) Plagioclase-mantled K-feldspar phenocryst in the GP I microgranite. The plagioclase (originally of oligoclase composition) mantle is strongly hematitized and altered to albite. (b) Scanning electron microscope cathodoluminescence image of a resorbed quartz phenocryst. The resorption surface indicated by the arrows is overgrown by bright luminescent granophyric quartz. (c) Electron microprobe profile showing the Ti content in the quartz phenocryst shown in (b) along the A-B line. From Müller et al. (2008).

Similar to the classic Precambrian rapakivi granites, which are A-type granites (Haapala and Rämö, 1992), the studied Upper Carboniferous porphyritic microgranite exhibits A-type characteristics, as shown in Fig. 12. Furthermore, the rocks show some interesting chemical similarities, e.g. the I-type tendency of GP I<sub>cum</sub>, with the intrusions of the nearby Niederbobritzsch and Flaje I-(S) type granite massifs (Förster and Tischendorf, 1994).

The detailed textural and geochemical investigations of the porphyritic microgranites permit the establishment of a schematic sequence of crystallization (Fig. 13). Preserved pre-mixing crystals representing the early magmatic stage are divided into a silicic stratum and a mafic stratum. The first is represented by quartz phenocrysts ( $q_1$ ), oligoclase ( $o_1$ ), K-feldspar phenocrysts ( $k_1$ ) with  $o_1$  inclusions, and the latter by andesine ( $an$ ). The mixing-mingling stage first causes the resorption (rounding) of pre-mixing crystals ( $q_{1r}$ ) and second the formation of new crystals due to equilibration ( $b_1$ ,  $h$ ,  $al_1$ ) some of them mantling the pre-existing crystals ( $o_2$ ). The formation of sieve-textured plagioclase phenocrysts ( $o_{2d}$ ) is explained as a result of rapid textural adjustment in the contact of silicic and mafic magmas causing strong local undercooling. Different crystal habits and textural relationships of allanite indicate two stages of allanite crystallisation: an early crystallization which may be associated with magma mixing ( $al_1$ ), and a late-magmatic crystallization after emplacement ( $al_2$ ). Textural relationships of the hornblende crystals such as euhedral habit, Fe-rich and Ti-poor rims, and reaction coronas of biotite indicate that hornblende was present before the magma intruded and re-equilibrated at the emplacement level.

Graphic quartz intergrowths ( $q_2$ ) in K-feldspar ( $k_3$ ) around phenocrysts developed in GP II are typically found in dike granites (e.g., Walker 1975) formed in highly undercooled melts. Beside the quartz-K-feldspar intergrowth, subhedral albite ( $ab$ ), fine-crystalline biotite ( $b_2$ ), anhedral allanite ( $al_2$ ), and epidote ( $e$ ) crystallised in the last stage. Finally, a widespread albitization caused an overprint of older feldspar generations.

Because of the abundant magma mixing features in the porphyritic quartz-feldspar-hornblende microgranite (GP II), the rock is interpreted as a hybrid granite. The mixing features are less discrete in the early phase (GP I) and not obvious in the acid enclaves (GP I<sub>cum</sub>). This trend seems to reflect a continuous deflation of the magma chamber from the top to the bottom. According to the definition of rapakivi granites after Haapala and Rämö (1992), the porphyritic microgranite of Altenberg-Frauenstein may be considered as rapakivi granite. Due to its Carboniferous age and being the only known granite with rapakivi texture in the German-Czech part of the Variscan belt, the microgranite of Altenberg-Frauenstein is exceptional.

**Fig. 12.** Zr+Nb+Ce+Y versus tFeO/MgO plot after Whalen et al. (1987) for characteristic samples of the main varieties of the porphyritic microgranite of Altenberg-Frauenstein. The diagram shows fields for A-type granites and also for fractionated felsic granites and unfractionated M-, I- and S-type granites.

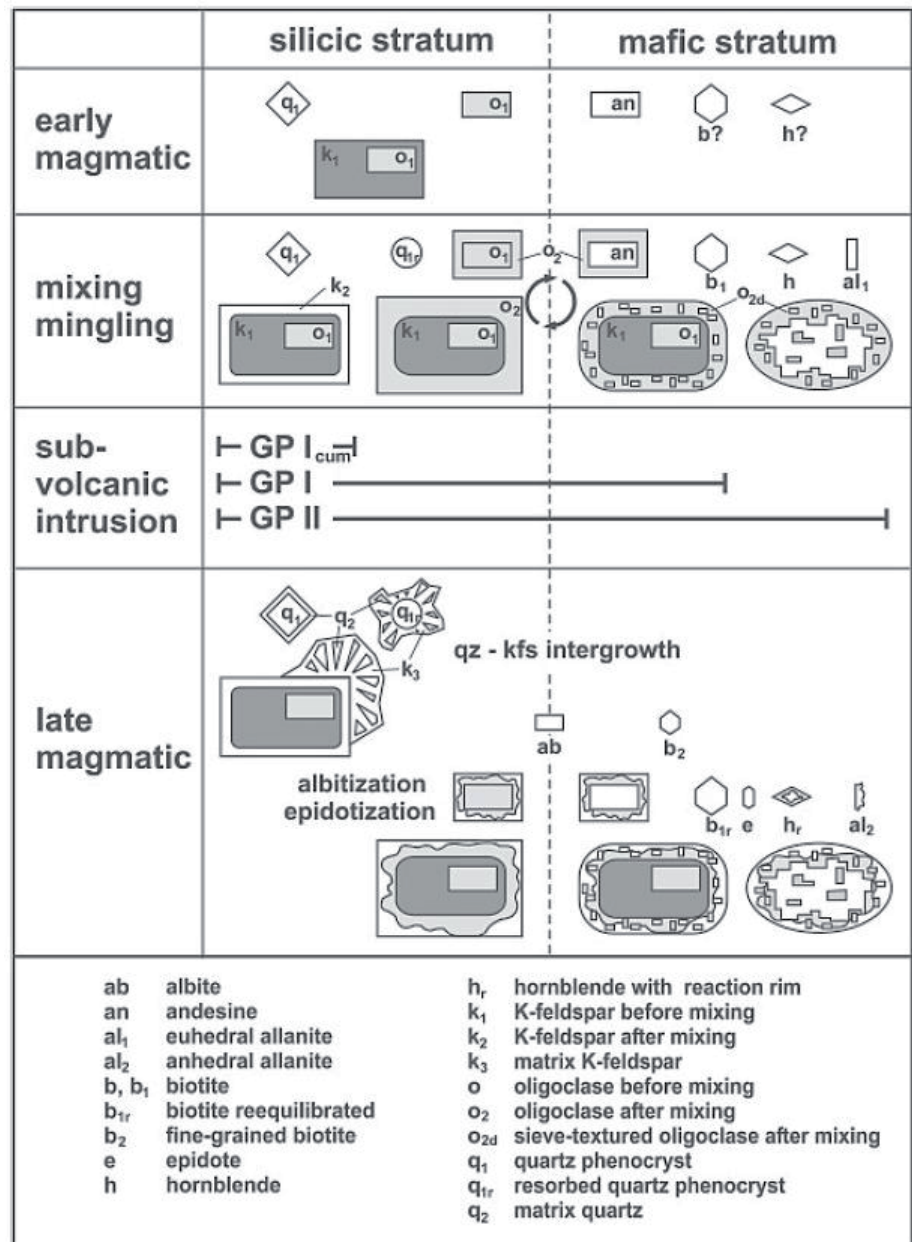
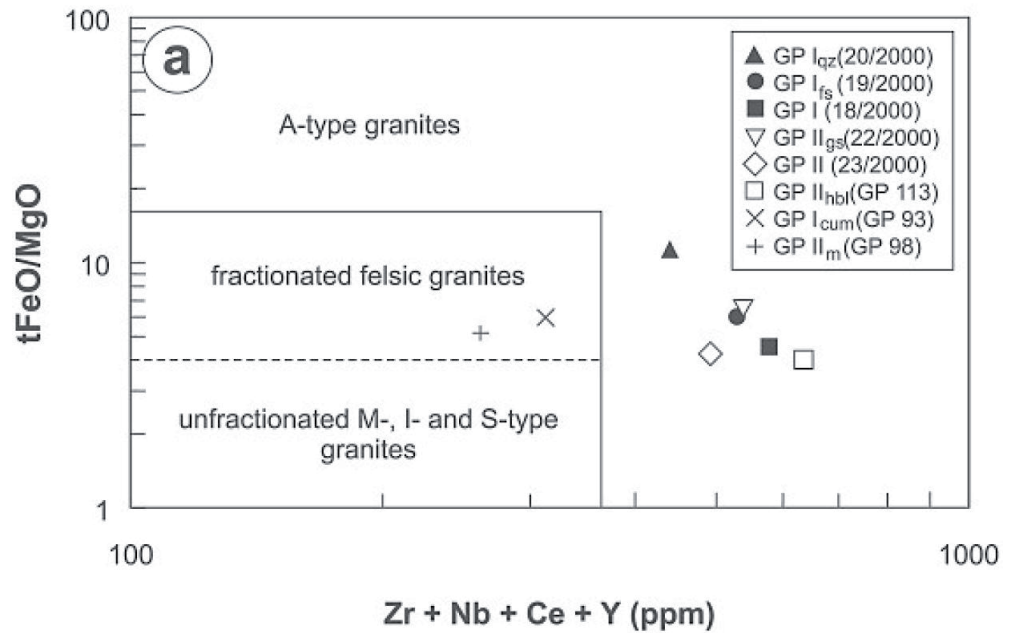


**Fig. 13.** Interpretative sequence of crystallisation. The textural variety of minerals found in the intrusion stages GP I<sub>cum</sub>, GP I and GP II is indicated by bars. Data from Müller and Seltmann (2002).

## Eurogranites 2012

### Stop 1-5

Kipsdorf railway station

Schellerhau granites

Coordinates: UTM 33U 406700 m E/5628900 m N, 550 m a.s.l.

Road from quarry Bärenstein back to Bielatalstrasse continuing to Altenberg via road S182. From Altenberg road 170 to Kipsdorf

Guide: Axel Müller/Reimar Seltmann

The outcrop next to the railway station Kipsdorf exposes granites of the Schellerhau granite complex (SGC). The Schellerhau granite complex belongs to the group of highly evolved rare metal granites of the Erzgebirge (Tischendorf and Förster, 1990; Štemprok, 1993; Förster and Tischendorf, 1994; Seltmann, 1994). Gneisses of the metamorphic basement and volcano-sedimentary rocks of the Altenberg-Teplice caldera form the host rocks (Figs. 1, 14).

Late-collisional extensional tectonics and collapse of the Variscan orogen controlled during the Upper Carboniferous the block and graben tectonics in the area, caldera formation with pre-dominantly ignimbritic rhyolites and porphyritic microgranites, and finally the post-tectonic multiple intrusion of tin granites of the Schellerhau granite complex into a subvolcanic level. Uplift, faulting, block tilting and erosion took place mostly in the Upper Carboniferous to Permian and in the Cenozoic and formed the recent morphology. NW- and NE-striking faults with vertical dislocations of several hundred meters. The Schellerhau granite complex is part of a horst and as a result thereof deeper parts of the pluton are locally exposed. The Schellerhau granite complex crops out on a surface of about 13 km<sup>2</sup>, forming a NW-SE elongated body roughly bound by the Weisseritztal fault to the northeast and by the Pöbelbach fault to the southwest. These marginal fault zones indicate – within the structural pattern of the Altenberg-Teplice caldera – that NW-striking sinistral strike-slip movement and northeast-directed extension controlled the intrusion of the post-tectonic Schellerhau granite complex in the post-caldera stage. Faults intersecting the Schellerhau granite complex are either post-intrusively reactivated or newly formed as indicated by hydrothermal mineralizations ranging in age from the Upper Carboniferous to the Cenozoic.

According to gravimetric data and geochemical studies of drill cores, granites of the Schellerhau granite type form the eastern Erzgebirge partial pluton, which is mostly hidden (Tischendorf, 1964). This NNW-striking hidden granite ridge extends from Dippoldiswalde in the north to Zinnwald in the south with an approximately 10 km east-west extension. To the south, in the Czech part of the Erzgebirge, the chemically and texturally similar Preisselberg-Cinovec granite (Štemprok et al., 1994) forms the continuation of this granite ridge.

The Schellerhau granite complex is characterized by the intrusion sequence of porphyritic (SG1) to weakly porphyritic (SG2) biotite syeno- to monzogranites, and mostly seriate albite granites (SG3). The SG1, SG2, and SG3 rocks of the SGC represent individual stages (phases) of a multiple granite intrusion. The SG1 forms the central and upper part of the Schellerhau granite complex and occupies about 2/3 of the complex at the recent surface. The SG2 intruded the SG1 along its margins probably due to cauldron subsidence effects in the post-caldera stage of the Altenberg-Teplice crustal unit. The SG2 occupies about one third of the SGC surface. The albite granites (SG3) occur as fine- to medium-grained porphyritic and seriate varieties. They were found in most of the drillings as flat igneous layers of up to several tens of meters thick, intercalated with SG1 and SG2 units characterizing the SGC as a sheeted laccolite body. Small SG3 dykes cross-cutting the earlier granite phases SG1 and SG2 provide evidence for the magmatic origin of SG3 and against its interpretation as a metasomatic zone.

The SG1, SG2, and SG3 rocks represent a suite of P-poor, Li-F-enriched leucogranites that exhibit distinct A-type tendencies (Förster et al., 1995; Breiter et al., 1999). The latter are weakly peraluminous ( $A/CNK \leq 1.2$ ), enriched in HREE, Y, Th, Hf, Zr, Sc, Nb, Ta, and U and display elevated abundances of Rb, Li, F, and Sn (Förster et al., 1996) increasing from SG1 to SG3. There is only a moderate chemical contrast between SG1 and SG2 rocks. The SG3 granites, however, exhibit – in contrast to SG1 and SG2 granites – the chemical and petrographic features of alkali feldspar leucogranites (Table 8). The SG3 rocks are more highly evolved as also shown by low Zr/Hf and Y/Ho values. Due to feldspathization, the modal composition of SG3 rocks (Table 9) differs from the one of SG1 and SG2 rocks. Topaz occurs mostly poikiloblastic and was classified to be of secondary nature, although primary magmatic topaz exists in a few cases in rocks of the Schellerhau granite complex (Table 9).

The SG1, SG2, and SG3 rocks are interpreted as products of in-situ fractionation of a magma derived from a common deep-crustal parental magma. Chemical and textural features of SG3 rocks dominantly reflect the deuteric alteration of the rocks. Primary textural and chemical features are preserved in only few cases (drill cores). Chemically, the Schellerhau granites are related to the Teplice rhyolites and the Altenberg-Frauenstein microgranites. Using cathodoluminescence-contrasted growth pattern and trace element signature of the phenocrysts (Fig. 15), Müller et al. (2005) showed that the quartz phenocrysts occurring in the Teplice rhyolites, the Altenberg Frauenstein microgranites, and the Schellerhau granites grew in the same magma chamber.

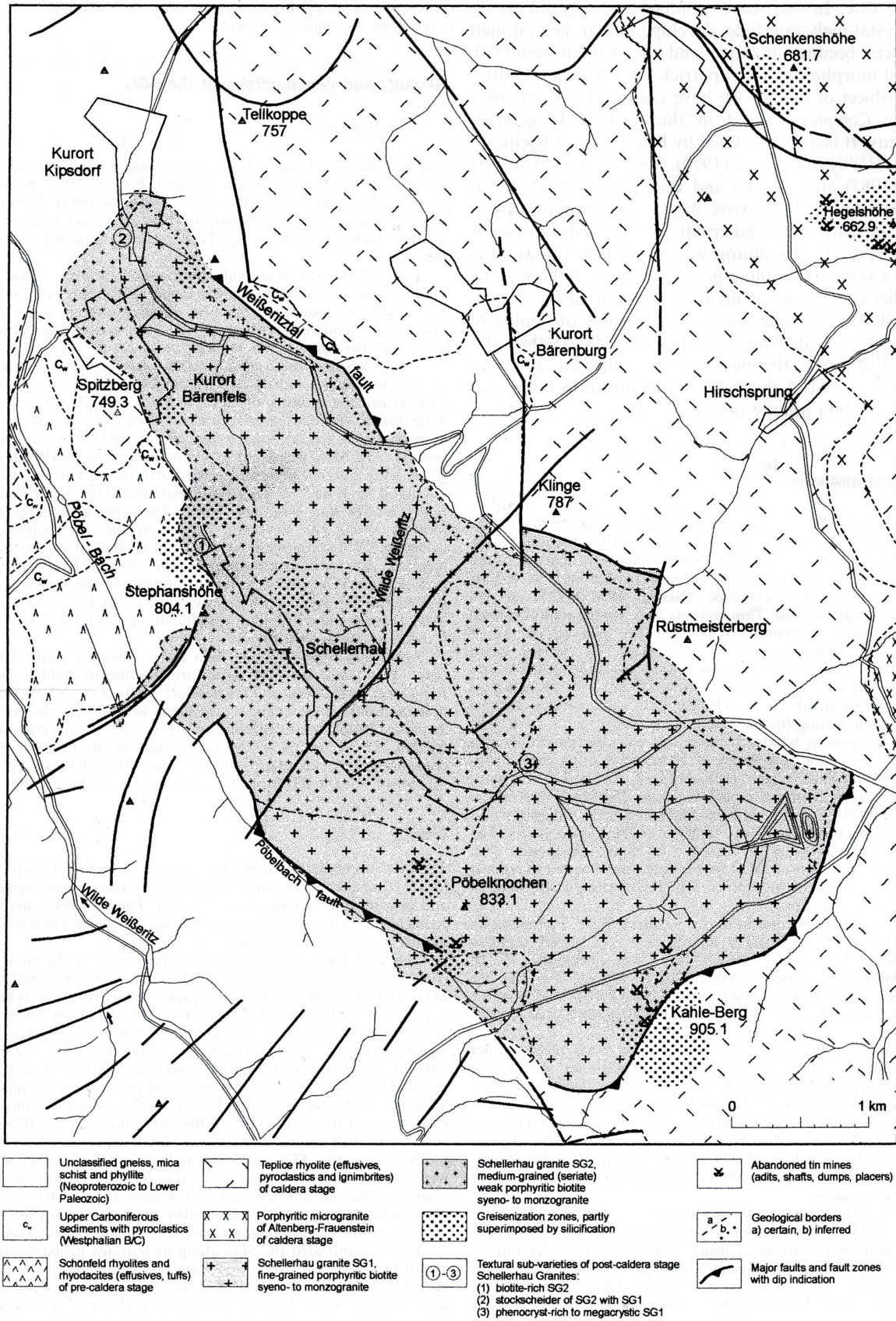


**Fig. 14.** Geological sketch map of the Schellerhau granite massif and its geological setting in the Altenberg-Teplce caldera (without Cenozoic cover). From Müller et al. (2000).

**Table 8.** Chemical analyses of major and trace elements of representative Schellerhau granite samples. Data from Müller et al. (2000).

| Granite                        | Sh-22 (SG1)  | 16 (SG2)  | Sh-32 (SG2)                                    | Sh-18 (SG3)                                |
|--------------------------------|--|---|--|--|
| Locality                       | Abandoned mine Paradies-Fdgr.                          | Abandoned mine Paradies-Fdgr.                         | Drill core near Kipsdorf                       | 295 m depth, drill core at Kipsdorf        |
| Texture                        | Very fine-grained, weakly porphyritic, phenocryst-poor | Medium-grained (altered), seriate, weakly porphyritic | Medium-grained equigranular (slightly altered) | Fine- to medium-grained seriate, albitized |
| SiO <sub>2</sub> wt%           | 75.13  | 72.93   | 71.91  | 69.29                                      |
| TiO <sub>2</sub>               | 0.057  | 0.094   | 0.068  | 0.022                                      |
| Al <sub>2</sub> O <sub>3</sub> | 12.60  | 13.84   | 14.64  | 16.97                                      |
| Fe <sub>2</sub> O <sub>3</sub> | 0.89   | 1.69  | 1.25   | 0.74                                       |
| MnO                            | 0.02   | 0.05  | 0.033  | 0.09                                       |
| MgO                            | 0.06   | 0.17  | 0.07   | 0.02                                       |
| CaO                            | 0.50   | 0.71  | 0.92   | 0.11                                       |
| Na <sub>2</sub> O              | 3.31   | 3.47  | 3.91   | 6.96                                       |
| K <sub>2</sub> O               | 5.33   | 5.09  | 4.64   | 4.09                                       |
| P <sub>2</sub> O <sub>5</sub>  | 0.02   | 0.04  | 0.036  | 0.03                                       |
| H <sub>2</sub> O               | 0.86   | 0.72  | 0.98   | 0.87                                       |
| C <sub>2</sub> O               | 0.05   | 0.10  | 0.12   | 0.15                                       |
| Li <sub>2</sub> O              | 0.037  | 0.075   | 0.164  | 0.016                                      |
| F                              | 0.51   | 0.82  | 1.41   | 0.12                                       |
| O=F                            | -0.21  | -0.34   | -0.59  | -0.05                                      |
| Total                          | 99.16  | 99.45   | 99.56  | 99.43                                      |
| Sn, ppm                        | 1.8  | 402   | 164  | 42   |
| Nb                             | 5.1  | 40  | 75   | 72   |
| Rb                             | 782  | 929   | 1295   | 1115                                       |
| Sr                             | 8.53   | 34.0  | 32.1   | 19.2                                       |
| Ba                             | 86.9   | 798   | 105  | 83.8                                       |
| Cs                             | 29.7   | 40.2  | 62.4   | 16.7                                       |
| Zr                             | 140  | 121   | 84.2   | 40.1                                       |
| Hf                             | 8.11   | 7.53  | 6.71   | 8.28                                       |
| Pb                             | 39   | 413   | 1.8  | 6.9  |
| Th                             | 58.1   | 39.5  | 24.9   | 9.29                                       |
| U                              | 15.0   | 17.6  | 20.8   | 3.33                                       |
| Y                              | 103  | 89.6  | 44.5   | 1.55                                       |
| La                             | 15.8   | 35.5  | 26.1   | 1.14                                       |
| Ce                             | 32.4   | 85.3  | 69.0   | 2.44                                       |
| Pr                             | 5.22   | 11.2  | 8.55   | 0.26                                       |
| Nd                             | 19.0   | 37.4  | 25.3   | 0.70                                       |
| Sm                             | 6.11   | 10.3  | 6.85   | 0.24                                       |
| Eu                             | 0.063  | 0.195   | 0.12   | <0.02                                      |
| Gd                             | 8.47   | 10.7  | 6.01   | 0.24                                       |
| Tb                             | 1.94   | 2.27  | 1.36   | 0.06                                       |
| Dy                             | 14.3   | 15.4  | 9.54   | 0.38                                       |
| Ho                             | 3.24   | 3.25  | 1.99   | 0.08                                       |
| Er                             | 10.6   | 10.5  | 6.95   | 0.30                                       |
| Tm                             | 1.73   | 1.89  | 1.42   | 0.08                                       |
| Yb                             | 12.0   | 12.8  | 11.4   | 0.93                                       |
| Lu                             | 1.80   | 1.97  | 1.71   | 0.15                                       |
| Y/Ho                           | 31.7   | 27.5  | 22.4   | 20.7                                       |
| Zr/Hf                          | 17.2   | 16  | 12.5   | 4.8  |

Notes on analytical methods: Oxides, Nb, Sn by XRF. Li by ICP-AES, F by ISE, other trace elements by ICP-MS. Details on analytical conditions and accuracy are available on request from RS. H<sub>2</sub>O<sup>-</sup> not determined. Sample 16 bears little galena

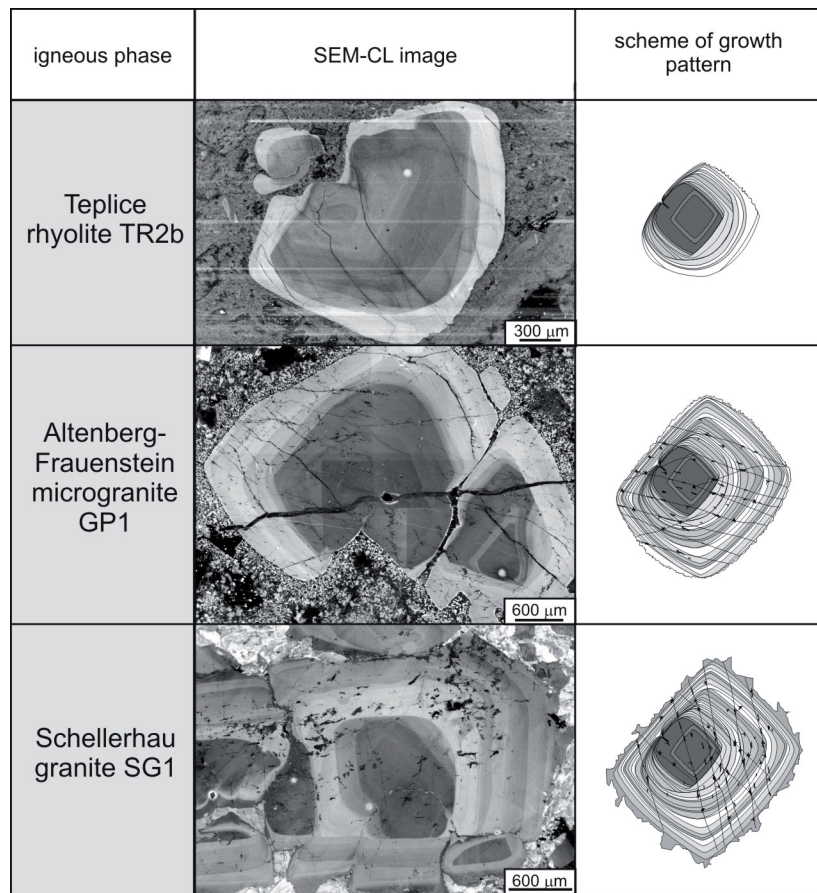


**Fig. 15.** Textures of quartz phenocrysts from the Teplice rhyolite, the Altenberg-Frauenstein microgranite, and the Schellerhau granite of the Altenberg-Teplice caldera. All three phases contain the same population of quartz phenocrysts as indicated by the comparable growth pattern. From Müller et al. (2005).

**Table 9.** Modal mineral composition of representative Schellerhau granite samples. Data from Müller et al. (2000).

| Samples  | Sh-22 (SG1)  | 16 (SG2)   | Sh-32 (SG2)                                     | Sh-18 (SG3)                                |
|--|--|--|---|--|
| Characteristics  | Very fine-grained, weakly porphyritic, phenocryst-poor | Fine- to medium-grained (altered), seriate, weakly porphyritic | Medium-grained, equigranular (slightly altered) | Fine- to medium-grained seriate, albitized |
| Primary minerals: phenocrysts and groundmass, vol%                     |  |  |   |  |
| Quartz   | 31.7   | 30.7   | 23.6  | 19.7                                       |
| K-feldspar   | 35.8   | 32.2   | 30.3  | 15.3                                       |
| Albite (An < 5 vol%)   | 6.3  | 5.0  | 13.0  | 14.9                                       |
| Albite-oligoclase (An > 5 vol%)  | 14.2   | 15.0   | 13.9  | —  |
| Li-mica (protolithionite to zinnwaldite)                               | 3.4  | 3.0  | 9.0   | 4.9  |
| Accessories (titanite, rutile, monazite, zircon, thorite, apatite,...) | 0.1  | 0.8  | 0.1   | 0.1  |
| Opaque minerals: ilmenite, sulfides                                    | 0.1  | 0.1  | 0.1   | 0.1  |
| Secondary minerals, vol%   |  |  |   |  |
| Albite (An < 5 vol%)   | 3.3  | 6.3  | 3.0   | 38.1                                       |
| Mica from vein lets  | —  | 0.6  | —   | —  |
| Sericite (± hydrosericite)   | 4.4  | 3.6  | 2.5   | 6.3  |
| Muscovite  | 0.1  | 0.5  | —   | —  |
| Kaolinite  | 0.1  | 1.6  | 1.5   | —  |
| Fluorite   | 0.3  | 0.7  | 0.8   | 0.6  |
| Topaz  | 0.2  | 0.2  | 2.1   | —  |
| Carbonate  | —  | 0.4  | —   | —  |
| Sum, vol%  | 100.0  | 100.1  | 99.9  | 100.0                                      |

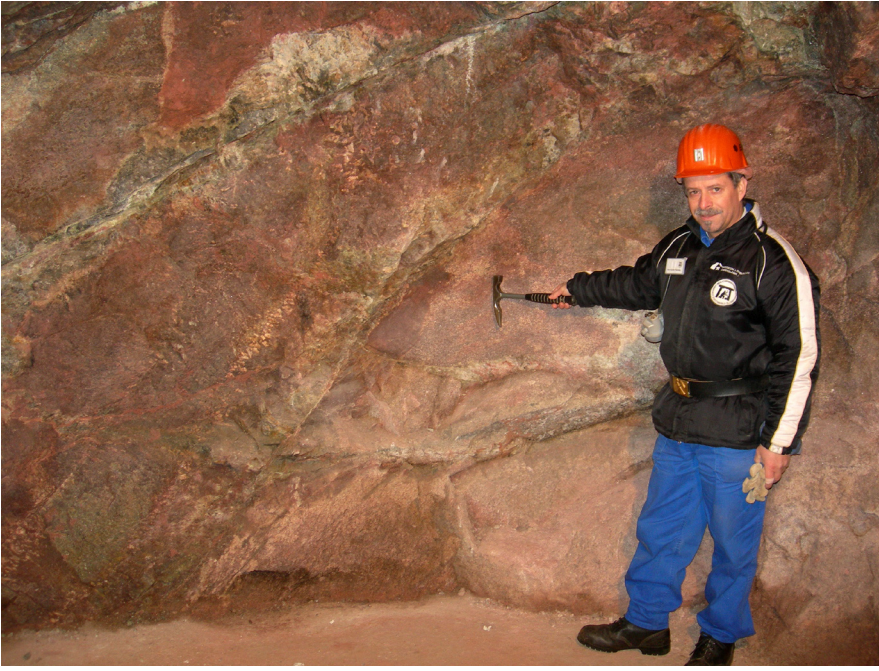


**Fig. 16.** Steep-dipping contact between the Teplice rhyolite (left) and the Zinnwald granite (right) with transecting, flat-dipping greisen veins. The contact is marked by megacrystic K-feldspar comb crystals up to 10 cm in size. Mine staff member Gunter Herklotz for scale.



**Fig. 18.** Sub-horizontal topaz-albite-zinnwaldite greisen vein with megacrystic zinnwaldite after Zinnwaldite granite.

## References

- Benek, R. (1980) Geologisch-strukturelle Untersuchungen im Tharandter Vulkanitkomplex (Südteil DDR). *Z. Geol. Wiss.* 8: 627–643.
- Benek, R. (1991) Aspects of volume calculation of paleovolcanic eruptive products—the example of the Teplice rhyolite (east Germany). *Z. Geol. Wiss.* 19: 379–389.
- Bolduan, H., Lächelt, A., Malasek, F. (1967) Zur Geologie und Mineralisation der Lagerstätte Zinnwald (Cinovec). *Freib. Forsch.-H. C* 218: 35–52.
- Breiter, K. (1997) The Teplice rhyolite (Krušné Hory Mts., Czech Republic) - chemical evidence of a multiply exhausted stratified magma chamber. *Věstník Českého geologického ústavu* 72: 205–213.
- Breiter, K., Förster, H.-J., Seltmann, R. (1999) Variscan silicic magmatism and related tin–tungsten mineralization in the Erzgebirge-Slavkovsky les metallogenic province. *Mineralium Deposita* 34: 505–531.
- Breiter, K., Novák, J.K., Chulpáčová, M. (2001) Chemical evolution of volcanic rocks in the Altenberg-Teplice Caldera (Eastern Krušné Hory Mts. Czech Republic, Germany). *Geolines* 13: 17–22.
- Čada, M., Novák, J.K. (1974) Spatial distribution of greisen types at the Cinovec-South tin deposit. In: Štemprok, M. (ed.) *Metallization associated with acid magmatism 1*. Ústř. úst. geol., Praha, pp. 383–388.
- Cocherie, A., Johan, V., Rossi, P., Štemprok, M. (1991) Trace



**Fig. 19.** Vertical offset of a quartz-zinnwaldite vein in greisenised Zinnwald granite.

- element variations and lanthanide tetrad effect studied in a Variscan lithium albite granite: Case of the Cínovec granite (Czechoslovakia). In: Pagel, M., Leroy, J.-L. (eds.) *Source, transport and deposition of Metals*. Balkema, Rotterdam, pp. 745–749.
- Förster, H.-J., Tischendorf, G. (1994) Evolution of the Hercynian granite magmatism in the Erzgebirge metallogenic province. *Min. Mag.* 58A: 284–285.
- Förster, H.-J., Seltmann, R., Tischendorf, G. (1995) High-fluorine, low phosphorus A-type (post-collision) silicic magmatism in the Erzgebirge. 2nd Symp. Permocarboiferous Igneous Rocks. *Terra Nostra* 7: 32–35.
- Förster, H.-J., Tischendorf, G., Seltmann, R., Gottesmann, B. (1998) Die variszischen Granite des Erzgebirges: neue Aspekte aus stofflicher Sicht. *Z. Geol. Wiss.* 26: 31–60.
- Foerster, H.-J., Seltmann, R., Tischendorf, G. (1996) Post-collisional A-type silicic magmatism in the Variscan Erzgebirge. *J. Conference Abstr.* 1: 174.
- Förster, H.-J., Tischendorf, G., Trumbull, R.B., Gottesmann, B. (1999) Late-collisional granites in the Variscan Erzgebirge, Germany. *J. Petrol.* 40: 1613–1645.
- Fridrich, C.J., Mahood, G.A. (1984) Reverse zoning in the resurgent intrusions of the Grizzly Peak cauldron, Sawatch Range, Colorado. *Geol. Soc. Am., Bull.* 95: 779–787.
- Grunewald, V. (1978) Metallogenie und Prognose Zinnwald. Teil I Metallogenie. Unpubl. Report ZGI Berlin, 166 pp.
- Haapala, I., Rämö, O.T. (1992) Tectonic setting and origin of the Proterozoic rapakivi granites of southeastern Fennoscandia. *Transactions of the Royal Society of Edinburgh, Earth Sciences* 83: 165–171.
- Hildreth, W. (1979) The Bishop Tuff: evidence for the origin of compositional zonation in silicic magma chambers. *Geol. Soc. Am., Spec. Pap.* 180: 43–75.
- Hoffmann, V., Trdlička, Z. (1965) Die Geochemie des Li, Rb, Cs und Be in den Greisen der Cínovec-Lagerstätte. *Z. Angew. Geol.* 12: 41–46.
- Hoffmann U., Breikreuz C., Breiter K., Sergeev S., Stanek K., Tichomirowa M. (2012) Carboniferous-Permian volcanic evolution in Central Europe – U/Pb ages of volcanic rocks in Saxony (Germany) and northern Bohemia (Czech Republic). *Int. J. Earth Sci.*, doi: 10.1007/s00531-012-0791-2
- Jiránek, J., Kríbek, B., Mlčoch, B., Procházka, J., Schovánek, P., Schováňková, D., Schulmann, K., Šebesta, J., Šimůnek, Z., Štemprok, M., (1987) The Teplice rhyolite. MS Czech Geological Survey Praha. (in Czech).
- Johan, V., Johan, Z. (1993) Accessory minerals of the Cínovec (Zinnwald) granite cupola, Czech Republic, part 1. Nb-, Ta-, and Ti-bearing oxides. *Mineral. Petrol.* 49: 1–21.
- Lobin, M. (1986) Aufbau und Entwicklung des Permosiles im östlichen und mittleren Erzgebirge. PhD thesis, Bergakademie Freiberg, Freiberg, 63 pp.
- Mlčoch, B., Skácelová Z. (2010) Geometry of the Altenberg-Teplice caldera revealed by the borehole and seismic data in its Czech part. *J. Geosci.* 55: 217–229.
- Müller, A., Seltmann, R. (2001) Textural and mineralchemical evidence of an Upper Carboniferous rapakivi granite in the Erzgebirge/Krušné Hory. In: Piestrzynski, A. et al. (eds.) *Mineral Deposits at the Beginning of the 21st Century. Proceedings of the Joint Sixth Biennial SGA–SEG Meeting*, Krakow. Lisse: Swets & Zeitlinger Publ., pp. 461–464.
- Müller, A., Seltmann, R. (2002) Plagioclase-mantled K-feldspar in the Carboniferous porphyritic microgranite of Altenberg-Frauenstein, Eastern Erzgebirge/Krušné Hory. *Bull. Geol. Soc. Finl.* 74: 53–79.
- Müller, A., Seltmann, R., Behr, H.-J. (2000) Application of cathodoluminescence to magmatic quartz in a tin granite case study from the Schellerhau Granite Complex, Eastern Erzgebirge, Germany. *Miner. Dep.* 35: 169–189.
- Müller, A., Breiter, K., Seltmann, R., Pécskay, Z. (2005) Quartz and feldspar zoning in the eastern Erzgebirge volcano-plutonic complex (Germany, Czech Republic): evidence of multiple magma mixing. *Lithos* 80: 201–227.

- Müller, A., Seltmann, R., Kober, B., Eklund, O., Jeffries, T., Kronz, A. (2008) Compositional zoning of rapakivi feldspars and coexisting quartz phenocrysts. *Can. Miner.* 46: 1417–1442.
- Pälchen, W. (1968) Zur Geochemie und Petrologie der postorogenen variszischen Granitoide des sächsischen Osterzgebirges. PhD thesis, Bergakademie Freiberg, Freiberg, 142 pp.
- Romer, R.L., Förster, H.-J., Štemprok, M. (2010) Age constraints for the late-Variscan magmatism in the Altenberg–Teplice Caldera (Eastern Erzgebirge/Krušné hory). *N. Jb. Mineral.* 187: 289–305.
- Rösler, H.J., Bothe, M. (1990) Bemerkungen zur Petrologie des Granits von Niederbobritzsch bei Freiberg und zur Bildung der Allanite. *Abh. Staatl. Museum Miner. Geol. Dresden* 37: 73–101.
- Rösler, H.J., Budzinski, H. (1994) Das Bauprinzip des Granits von Niederbobritzsch bei Freiberg (Sa.) auf Grund seiner geochemischen Analyse. *Z. Geol. Wiss.* 22: 307–324.
- Rötzler, K., Plessen, B. (2010) The Erzgebirge: a pile of ultra-high- to low-pressure nappes of Early Palaeozoic rocks and their Cadomian basement. In: Linnemann, U., Romer, R.L. (eds.) *Pre-Mesozoic Geology of Saxo-Thuringia – from the Cadomian Active Margin to the Variscan Orogen*. Schweizerbart Sci. Publ., Stuttgart, pp. 253–270.
- Rötzler, K., Schumacher, R., Maresch, W.V., Willner, A.P. (1998) Characterization and geodynamic implications of contrasting metamorphic evolution in juxtaposed high-pressure units of the Western Erzgebirge (Saxony, Germany). *Eur. J. Mineral.* 10: 261–280.
- Rub, M. G., Pavlov, V.A., Rub, A. K., Štemprok, M., Drábek, M., Drábková, E., (1983) Elements of vertical zoning in the Cínovec massif of lithium fluorine granites (Czechoslovakia). In: *Correlation of magmatic rocks of Czechoslovakia and some districts of the USSR* Izd. Nauka, 108–137, Moskva (in Russian).
- Rub, A.K., Štemprok, M., Rub, M.G. (1998) Tantalum mineralization in the apical part of the Cínovec (Zinnwald) granite stock. *Mineral. Petrol.* 63: 199–222.
- Seltmann, R. (1994) Subvolcanic minor intrusions in the Altenberg caldera and their metallogeny. In: Seltmann, R., Möller, P., Kämpf, H. (eds.) *Metallogeny of collisional orogens*, Czech Geological Survey Prague, p. 198–206.
- Seltmann, R., Breiter, K., Schilka, W., Benek, R. (1996) The Altenberg–Teplice caldera: reversed zonation of a stratified magma chamber. *J. Conf. Abstr.* 1: 556.
- Seltmann, R., Förster, H.-J., Gottesmann, B., Sala, M., Wolf, D., Štemprok, M. (1998) The Zinnwald greisen deposit related to post-collisional A-type silicic magmatism in the Variscan Eastern Erzgebirge/Krušné Hory. In: Breiter, K. (ed.) *Genetic significance of phosphorus in fractionated granites*. Excursion guide. *Geol. Surv. Prague*, p. 33–50.
- Seltmann, R., Müller, A., Schilka, W. (2001) Geochemical characteristics of the rapakivi-textured porphyritic microgranites in the Altenberg–Teplice caldera. In: Piestrzynski, A. et al. (eds.) *Mineral Deposits at the Beginning of the 21st Century*. Proceedings of the Joint Sixth Biennial SGA-SEG Meeting Krakow. Lisse: Swets & Zeitlinger Publ., pp. 481–484.
- Štemprok, M. (1960) On the genesis of the ore deposit of Cínovec (Zinnwald). *Int. Geol. Congr., Rep. 21 st. Sess., Part XVI*, pp. 43–52.
- Štemprok, M. (1961) Genetische Untersuchungen der flach fallenden Gänge auf der Erzlagerstätte Cínovec (Zinnwald) im Erzgebirge. *Sbor. Ústř. úst. geol.* 26: 455–527.
- Štemprok, M. (1989) Rare earth elements in the rocks of the Cínovec cupola (Czechoslovakia). *Bull. Geol. Surv. Prague* 64: 1–16
- Štemprok, M. (1993) Magmatic evolution of the Krusne Hory-Erzgebirge batholith. *Z. Geol. Wiss.* 21: 237–245.
- Štemprok, M., Šulcek, Z. (1969) Geochemical profile through an ore-bearing lithium granite. *Econ. Geol.* 64: 392–404.
- Štemprok, M., Novák, J.K., David, J. (1994) The association between granites and tin-tungsten mineralization in the Krušné hory (Erzgebirge), Czech Republic. *Monogr. Series Mineral Deposits* 31: 97–129
- Štemprok, M., Holub, F.V., Novák, J.K. (2003) Multiple magmatic pulses of the Eastern Erzgebirge Volcano-Plutonic Complex, Krušné hory/Erzgebirge batholith, and their phosphorus contents. *Bull. Geosci.* 78: 277–296.
- Thomas, R. (1992) Results of investigations on melt inclusions in various magmatic rocks from the northern border of the Bohemian Massif. In: Kukul, Z. (ed.) *Proceedings of the 1st International Conference about the Bohemian Massif, Prague 1988*. *Czech Geol. Surv., Prague*, pp. 298–306.
- Tichomirowa, M. (1997) 207Pb/206Pb-Einzel-zirkondatierungen zur Bestimmung des Intrusionsalters des Niederbobritzscher Granites. *Terra Nostra* 8: 183–184.
- Tischendorf, G. (1964) Stand der Kenntnisse bei der Suche nach Zinnlagerstätten im Osterzgebirge. *Z. Angew. Geol.* 10: 225–238.
- Tischendorf, G., Förster, H.J. (1990) Acid magmatism and related metallogenesis in the Erzgebirge. *Geol. J.* 25: 443–454.
- Walker, M. (1975) Origin of quartz-feldspar, graphic intergrowth. Thesis, Michigan State University., 65 pp.
- Watznauer, A. (1954) Die erzgebirgischen Granitintrusionen. *Geologie* 3: 688–706.
- Whalen, J.B., Currie, K.L., Chappell, B.W. (1987) A-type granites: geochemical characteristics, discrimination and petrogenesis. *Contr. Miner. Petrol.* 95: 405–419.
- Willner, A.P., Rötzler, K., Maresch, V.W. (1997) Pressure-temperature and fluid evolution of quartzo-feldspathic metamorphic rocks with a relic high-pressure, granulite-facies history from the Central Erzgebirge (Saxony, Germany). *J. Petrol.* 38: 307–336.

# The plutonic rocks of the Meissen Massif (Germany): evidence for subduction-modified mantle components in a strike-slip related Variscan intrusion

Thomas Wenzel  
 Fachbereich Geowissenschaften  
 Universität Tübingen  
 thomas.wenzel@uni-tuebingen.de

## 1. Introduction

This overview on geological, petrological, geochemical, and geochronological aspects of the plutonic rocks from the Meissen Massif is based on the results of a detailed re-investigation accomplished between 1988 and 2000 (see below). Earlier investigations of this interesting intrusion, which is assumed to be genetically related to the so-called „Elbe lineament“, have been summarized by Pfeiffer (1964, and references therein). In a comprehensive geochemical investigation of the granitoid rocks of the south-eastern part of Germany (Tischendorf et al., 1987), it was documented and concluded that in particular the „lineament-bound“ pyroxene- and amphibole-bearing plutonic rocks of the Meissen Massif have a „deep-crustal to sub-crustal origin“ and contrast in their formation from granitoid rocks of the Erzgebirge, the Lausitz, and the Harz that were interpreted to represent products of anatectic remelting of crustal precursors. However, data on the composition of rock-forming minerals and whole rock samples, including trace elements of special petrological interest such as Nb, Th, and the REEs, were not available at that time. High-quality age data on rocks of the Meissen Massif were completely lacking, as was a modern reconstruction of the geological evolution of the units in contact with the Meissen intrusion, i.e., the geological context of this type of magmatism was not understood. Therefore, it is not surprising that the first identification of a „subduction signature“ in the trace element pattern of Meissen monzonites in 1993 provoked a controversy as a late-Paleozoic subduction was not supported (or even excluded) by the geodynamic models that were used to interpret the Variscan orogenic processes in the early 1990s. Today it is widely accepted that the Variscan orogeny is characterized by plate convergence including oceanic and crustal subduction (e.g., Kroner et al., 2007) that led to the enrichment of mantle domains. Such metasomatically enriched domains were the source for the shoshonitic and ultrapotassic melts that formed monzonitic rocks and lamprophyres of the Meissen Massif as well as of many other occurrences of the mid-European Variscides (Wenzel et al., 1997; Becker et al., 1999).

## 2. Geological situation

The Meissen Massif is situated in the eastern part of Germany between the geological units of the Erzgebirge, Granulitgebirge, and the Lausitz (Lusatia). It represents an integral part of the Elbe Zone (Pietzsch, 1956; see Fig. 1). The massif forms a longitudinal lens parallel to the Variscan NW–SE direction of the Elbe Zone. A

tectonic boundary (Westlausitzer Störung) separates the Meissen Massif from Lusatia in the east. Intrusive contacts are developed between the plutonic rocks and the metasedimentary rocks of the Nossen-Wilsdruffer Schiefergebirge (NWS) and the Elbtal-Schiefergebirge (ES) in the west.

Based on shape and distribution in the field, the Meissen plutonic complex traditionally has been subdivided in a northern, a central, and a southern part. The rocks of the central part take up most of the volume of the intrusion. Lithological variations define a nearly concentric structure that is built up by the following rock types (Fig. 1):

- \* pyroxene+biotite-bearing diorites and monzodiorites, grading into amphibole-bearing monzonites at the southwestern rim
- \* monzonites and quartz-monzonites, locally with varying amounts of pyroxene+biotite in the outer parts, and amphibole-bearing monzonites in the inner parts
- \* biotite- and in part muscovite-bearing granodiorites and monzogranites of the Hauptgranit in the center
- \* a biotite+hornblende-bearing granodiorite developed only in the east-central part between monzonite and the Hauptgranit
- \* a late leucomonzogranite, the so-called Riesensteingranit, at Meissen.

According to field geological evidence, the plutonic rocks of the Meissen Massif were emplaced *during* the Variscan orogeny (Reichert, 1926; Pietzsch, 1956).

## 3. Petrography and mineral chemistry

### 3.1. Diorite-monzodiorite-monzonite rocks

Rock types more primitive than the dominating monzonites were exposed in a quarry near Freital at the outwestern margin of the intrusion. Transitions between diorite, monzodiorite, and monzonite are gradual within some tens of meters. Typical fabric patterns as well as mineral-chemical compositions of the Freital rocks are given in Fig. 2.

The primary mineral association with diopside + Mg-rich biotite + labradorite + magnetite is quite similar to those of shoshonite lavas from, e.g., Fiji (compare [www.gabbrosoft.org](http://www.gabbrosoft.org)). The mineral chemistry indicates transitional to alkaline affinities of the parental melt (cf. Bergman, 1987). The crystallization of biotite in the diorite refers to a high potassium activity in the magma. Both the diorite and monzodiorite are characterized by accumulations of diopside, magnetite, and plagioclase, and the whole rocks probably do not represent true melt compositions.

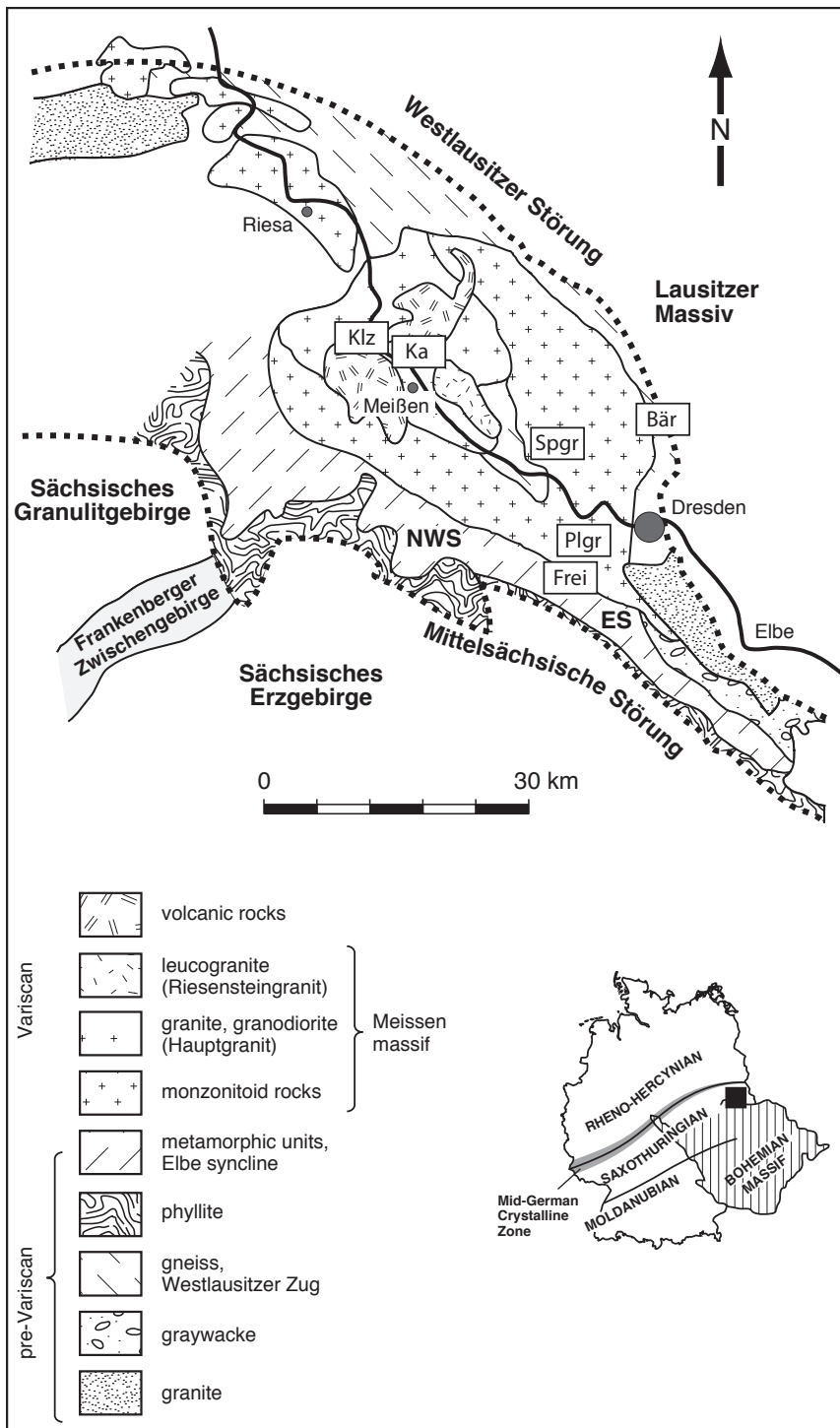


**Fig.1.** Geological map of the Meissen massif and adjacent units (modified from Pietzsch, 1956) with selected sample locations discussed in the text. ES = Elbtal-Schiefergebirge, NWS = Nossen-Wilsdruffer Schiefergebirge. Bär = Bärwalde, Frei = Freital, Ka = Karpfenschänke, Klz = Klein-Zadel, Plgr = Plauenscher Grund, Spgr = Spitzgrund.

Monzonite from Freital is composed of edenitic amphibole, oligoclase-andesine, and K-feldspar with growth zonation. Locally, in monzonite with heterogeneous textures, mineral relics of the „dioritic to monzodioritic stage“ can be observed which are converted to actinolite, chlorite, and titanite (Wenzel et al., 1991). Dark-blue luminescing zoned K-feldspar is partly corroded by a second generation of K-feldspar showing light-blue cathodoluminescence (Wenzel and Ramseyer, 1992).

Monzonites and quartz-monzonites from the inner parts of the Massif (Heidenschanze/Plauenscher Grund and Spitzgrund – stop 2-2) are weakly oriented rocks that have more homogeneous fabric characteristics than the rocks of the outer parts (stop 2-1). They contain edenite, oligoclase, K-feldspar, quartz, and titanite.

Along the eastern rim near the castle of Moritzburg (village of Bärwalde), lenses of strongly deformed rocks occur that originally were classified as „metamorphic rocks of Proterozoic to Lower Paleozoic age“ on the geological map of Saxony (1994). However, they are composed of edenite, oligoclase-andesine, K-feldspar, quartz and biotite and correspond to deformed monzonites from the Meissen massif. Using the least deformed parts of these rocks, crystallization pressures were estimated using the  $Al^{IV}$  content of amphibole to range from  $5.5 \pm 0.6$  to  $6.2 \pm 0.6$  kbar (after the calibration of Schmidt, 1992) and from  $4.1 \pm 0.6$  to  $4.7 \pm 0.6$  kbar assuming equilibration with  $H_2O-CO_2$  fluids (Johnson and Rutherford, 1989). Consequently, the Bärwalde amphibole composition equilibrated at mid-crustal levels (Wenzel et al.,

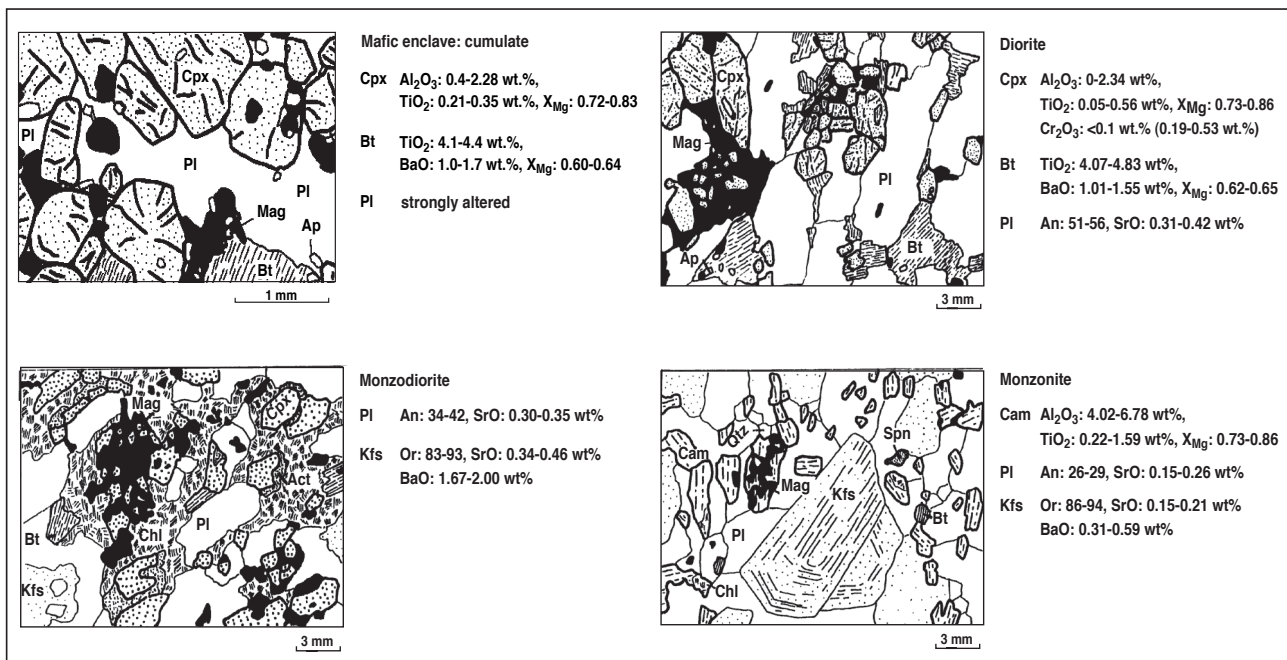


**Fig. 2.** Fabric pattern of the Freital rock suite and concentrations of the most important components in the different minerals. Cpx – clinopyroxene, Bt – biotite, PI – plagioclase, Kfs – alkali feldspar, Cam – calcium amphibole, Act – actinolite, Chl – chlorite, Qtz – quartz, Mag – magnetite, Ap – apatite, Spn – titanite (modified from Wenzel et al., 1991).

2000). Pre- to syntectonic growth of amphibole (Frischbutter, 1982) points to a syntectonic emplacement of the monzonitic crystal mush.

Under CL, apatite crystals from diorite, monzodiorite, and monzonite show blue-violet luminescing growth zonation caused by  $\text{Sm}^{3+}$ ,  $\text{Dy}^{3+}$ ,  $\text{Eu}^{2+}$  and  $\text{Ce}^{3+}$  contents (Wenzel and Ramseyer, 1992). Such CL colors are typical in apatite from alkaline igneous rocks and carbonatites (e.g., Fleischer and Altschuler, 1969). About 5% of the crystals contain yellow-luminescing cores. They are interpreted as relics of contaminants since apatite from several crustal rocks shows this  $\text{Mn}^{2+}$ -activated CL color (Mariano, 1978).

The investigation of internal structures of zircon separated from diorites, monzodiorites, and monzonites reveals cores (Wenzel and Wolf, 1992). According to single-zircon age determinations (Wenzel et al., 1993; Nasdala et al., 1999), however, only a part of these cores represent xenocrysts whereas other seem to reflect reworked zircon grains that crystallized during the „dioritic to monzodioritic stage“ of the magmatic evolution.

### 3.2. Lamprophyres

A suite of lamprophyre dikes (minette and kersantite) occurs in the inner part of the monzonite intrusion (Plauenscher Grund). The investigation of these lamprophyres was of special interest since at least some of the minette dikes appear to have synmagmatically intruded into monzonite, and there several models that invoke a genetic relation between lamprophyres and monzonitic rocks (for an overview see Wenzel et al., 1997, 2000).

The minette dikes trend approximately N-S, perpendicular to the maximum extension direction, and may have used strike-slip tension fractures for their ascent (cf. Mattern, 1996). Minette dikes are composed of phlogopite and diopside phenocrysts embedded in a groundmass of alkali feldspar, magnetite, apatite, calcite, and very fine-grained Zr-Th-U-LREE-bearing minerals. Olivine is completely altered to serpentine, talc, and iron oxide. Diopside contains up to 5800 ppm Cr. The cores of phlogopite crystals are

relatively poor in  $\text{TiO}_2$  (2.1 wt %) and enriched in Cr (up to 18000 ppm) and Ni (up to 2000 ppm). In general, the minette phlogopite composition from Plauenscher Grund (Meissen Massif) is quite similar to the phlogopite chemistry from other K-rich magmatic rocks interpreted to be derived from metasomatically enriched mantle sources (Wenzel, 1997).

A NE-SW trending kersantite dike contains Cr-poor (up to 3300 ppm) Ti-augite phenocrysts showing sector-zonation, and pseudomorphs after olivine. Ti-augite, kaersutite, Mg-biotite, andesine, and Fe-oxide form microphenocrysts. Alkali feldspar, apatite, titanite, and zircon are restricted to the groundmass. Sector-zoned Ti-augite and kaersutite reflects a tendency towards alkaline lamprophyres (cf. Tröger, 1922).

### 3.3. Granites (Hauptgranit, Riesensteingranit)

The monzogranites from several outcrops of the Hauptgranit are weakly to non-oriented and differ mainly in their content of biotite, ranging from 3 to 8 wt %. The occurrence of intergranular and intracrystalline white mica, especially in some samples from Klein-Zadel (Klz in Fig. 1), is a local peculiarity of this rock type (Wenzel et al., 1991). For typical fabric characteristics and mineral chemical data see description to Stops 2-4 and 2-5. Based on the position in the  $\text{TiO}_2$ - $\text{Fe}_2\text{O}_3$ -MgO space (Speer, 1984), intergranular muscovite is of magmatic origin, whereas the intracrystalline generation corresponds to post-magmatic muscovite. About 87 % of the zircon crystals from Hauptgranit samples contain voluminous cores surrounded by small zoned rims (Wenzel and Wolf, 1992). Only 13 % of the zircon grains are completely zoned and, thus, entirely grown in the Hauptgranit melt. The important role of crustal sources is supported by single-zircon  $^{207}\text{Pb}/^{206}\text{Pb}$  evaporation relic ages scattering between 570 and 2220 Ma (Wenzel et al., 1993).

Samples of the Riesensteingranit are non-oriented and biotite-poor. In comparison to the Hauptgranit, plagioclase and alkali feldspar are depleted in Sr and Ba, respectively. For typical fabric characteristics and mineral chemical data see description to Stop

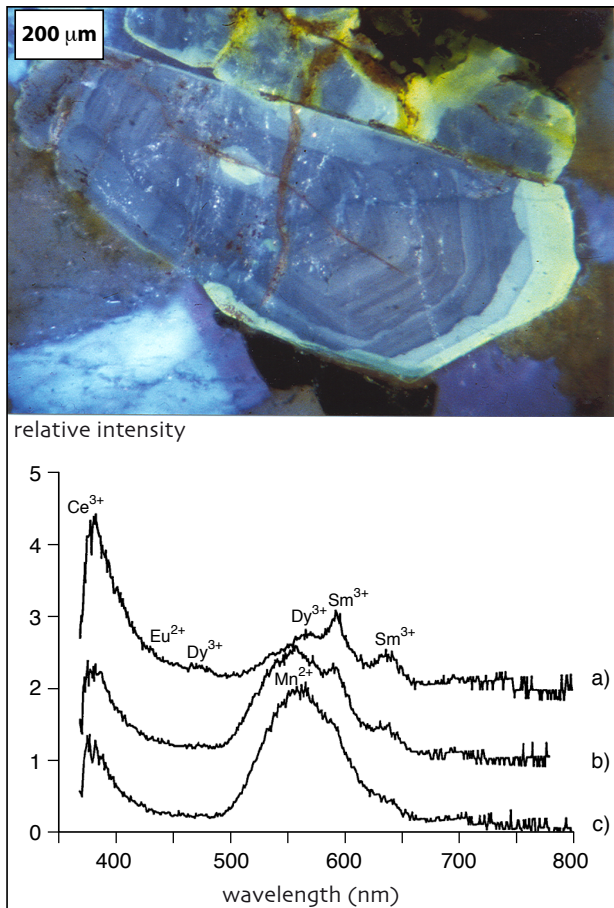


**Fig. 3.** CL image of a large apatite crystal from the Heidenschanze monzonite showing growth zonation, and a yellow core and rim. CL spectra of a) a zoned apatite displaying violet luminescence, b) a yellow luminescing core, and c) a yellow luminescing rim (apatite from Freital; after Wenzel and Ramseyer, 1992).

2-4. The majority of zircon crystals from the Riesensteingranit is completely, but often irregularly, zoned. Only 20 % of the zircon grains contain partly recrystallized cores probably indicating relics of crustal precursors or contaminants (Wenzel and Wolf, 1992).

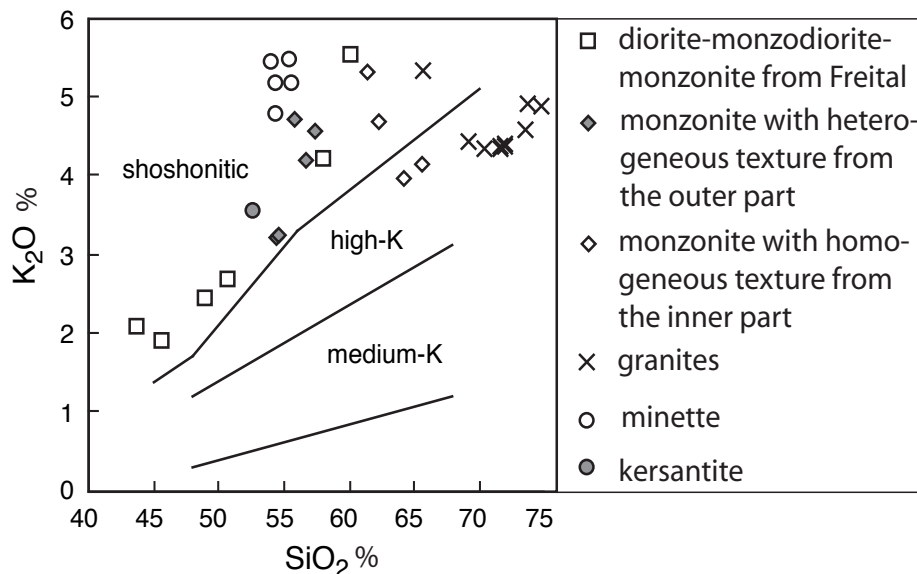


**Fig. 4.**  $K_2O^*$  versus  $SiO_2^*$  for the plutonic rocks and lamprophyres from the Meissen Massif, recalculated to LOI-free compositions (after Wenzel et al., 2000).

## 4. Geochemical characteristics

### 4.1. Monzonitoid rocks and lamprophyres

The shoshonitic character of the diorites, monzodiorites, and most of the monzonites is documented in a  $K_2O$  vs.  $SiO_2$  diagram (Fig. 4). The decrease in  $K_2O$  for samples with  $SiO_2 > 60$  wt % is also known to be typical of shoshonite associations (Morrison, 1980). Additional similarities include  $K_2O/Na_2O$  ratios between 0.7 and 1.4,  $TiO_2$  contents lower than 1.5 wt %,  $Al_2O_3$  contents ranging from 11.9 to 18.1 wt %, a flat trend in an AFM plot, and the change from slightly silica-undersaturated diorites to quartz-bearing monzonites (Wenzel and von Quadt, 1993; Wenzel, 1997; Wenzel et al., 2000).

Based on their  $K_2O$  contents, the kersantite and minette dikes are classified as shoshonitic lamprophyres. Compared to monzonite samples with similar  $SiO_2$  of about 55 wt %, the minettes are more enriched in  $K_2O$ . The most primitive minette samples have  $K_2O/Na_2O$  ratios of 2 and 2.7, thus indicating a tendency toward ultrapotassic rocks (cf. Foley et al., 1987). Regarding the low  $Al_2O_3$  contents (c. 12.5 wt %) and  $K_2O/Al_2O_3$  ratios (c. 0.42), the most primitive minette dikes are similar to „plagiocleucites“. The  $K_2O/Na_2O$  ratio of 1.2 for the kersantite is lower than for the minette dikes.

Major element systematics demonstrate that the diorite-monzodiorite-monzonite rocks and the lamprophyres do probably not belong to a single magmatic series (Fig. 5).

Low Cr (<145 ppm) and Ni contents (<46 ppm) provide evidence that the Meissen monzonitoid rocks crystallized from evolved melts. The monzonitoid rocks are generally enriched in Ba (up to 2940 ppm), Sr (up to 2270 ppm), La (up to 130 ppm), Ce (up to 221 ppm) and Nd (up to 112 ppm). The trends of some immobile trace elements vs.  $SiO_2$  and  $P_2O_5$ , as fractionation index are shown in Fig. 6.

Compared to the decrease in Ce from the orthocumulate sample (mafic enclave) towards monzodiorite sample Frei 12, probably caused by fractional crystallization of apatite, the Ce concentration of the monzonites Frei 10 and Frei 38 increase abruptly from 162 ppm to >200 ppm although  $P_2O_5$  is decreasing. Increasing Th and Zr concentrations from monzodiorite to the monzonite samples are similar to Ce. The 10- to 14-fold increase in, e.g. Th, cannot be exclusively produced by fractional crystallization of a gabbroic parental magma.

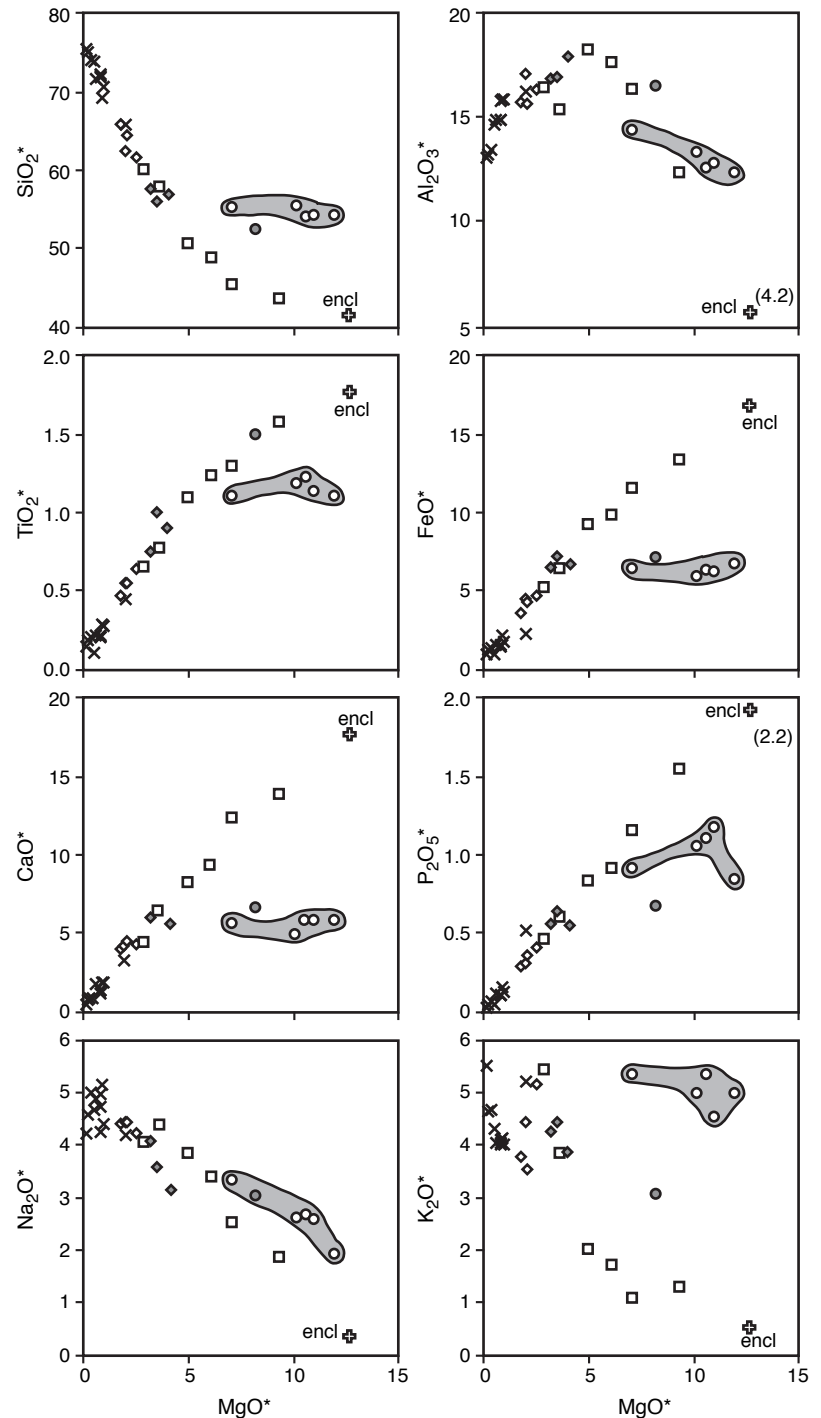


**Fig. 5.** Major element trends versus  $MgO^*$  for Meissen plutonic rocks and lamprophyres; symbols as in Fig. 4. Data recalculated to LOI-free compositions. encl = orthocumulate from Freital.

Mantle-normalized trace element pattern of Freital diorites and monzodiorites are characterized by strongly enriched LILE and LREE contents, and relative depletions in Th, U, Nb, Zr, and Ti, similar to less contaminated diorites and syenites from the Scottish Caledonides (Thompson and Fowler, 1986; Fig. 7a). Most of the Scottish diorites and syenites are thought to be related to the subduction of oceanic crust. The chemical signatures of the Meissen monzonites, however, are similar to those Scottish syenites that crystallized from crustally contaminated lithospheric mantle magmas. These syenites as well as the Meissen monzonites show enrichments in Th, U, Pb, and Zr compared to the more primitive rocks (Fig. 7b). Gneiss xenoliths and wall rocks from the Meissen monzonitoid intrusion, however, do not contain enough Th, U, and LREEs to explain the corresponding element enrichments in the monzonites by bulk assimilation (Fig. 7c).

The minette dikes contain up to 633 ppm Cr and up to 390 ppm Ni, suggesting that they must be very primitive mantle-derived magmas. They are highly enriched in Ba (up to 4660 ppm), Sr (up to 1230 ppm), Th (up to 91 ppm), U (up to 23 ppm), La (up to 206 ppm), Ce (up to 373 ppm), Nd (up to 173 ppm), and Zr (up to 1690 ppm). The kersantite dike, which has a different trace element composition than the minette dike, has lower Cr (225 ppm) and Ni (153 ppm) contents than the most evolved minette dikes, i.e., the kersantite is less primitive. The kersantite also has lower Ba, Th, U, LREE, Sr, and P contents, whereas Rb, Nb, Pb, Zr, and HREE concentrations are similar in kersantite and minette (Fig. 8). Higher Cr and Ni concentrations than in the diorites indicate the more primitive character of the kersantite.

The Sr-Nd isotopic compositions of the Meissen diorite-monzodiorite-monzonite suite and the lamprophyres is presented

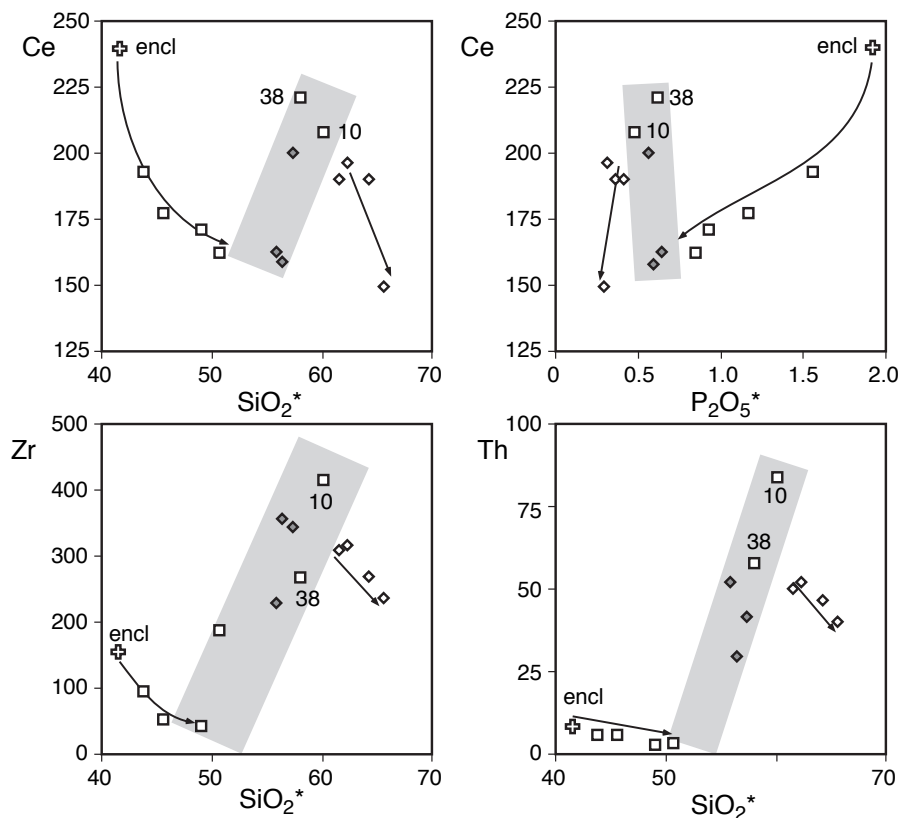


**Fig. 6.** Trends of Ce, Zr, and Th versus  $\text{SiO}_2^*$ , and of Ce versus  $\text{P}_2\text{O}_5^*$  for the Freital rocks and the more evolved monzonites; symbols as in Fig. 4. Major elements recalculated to LOI-free compositions. Note the drastic increase in the trace element contents from Freital monzodiorites to monzonite samples Frei 10 and Frei 38 (modified from Wenzel et al., 2000).

in Fig. 9 (the results for the granites will be discussed below). In addition, the Sr-Nd isotopic compositions of the most important wall rocks and a gneiss xenolith are shown.

The  $^{87}\text{Sr}/^{86}\text{Sr}_{(330\text{Ma})}$  ratios and  $\epsilon_{\text{Nd}(330\text{Ma})}$ -values of the diorites, monzodiorites and monzonites from the outer parts as well as their mafic enclaves (Group I in Fig. 9) range from 0.7047 to 0.7055 and -1.9 to -0.5, respectively. These data indicate slightly enriched isotopic signatures. In contrast, the most evolved monzonites ( $\text{SiO}_2 > 60$  wt%) and mafic enclaves from the inner part of the intrusion (Group II in Fig. 9) show characteristics of isotopically depleted melts ( $^{87}\text{Sr}/^{86}\text{Sr}_{(330\text{Ma})} = 0.7044$  to 0.7050;  $\epsilon_{\text{Nd}(330\text{Ma})} = +0.1$  to +2.2). In agreement with petrographic and geochemical results, the observed isotopic heterogeneity supports the conclusion that the diorite-monzodiorite-monzonite sequence cannot be explained by closed system fractional crystallization. The wall rock and xenolith samples included by our investigation have too radiogenic  $^{87}\text{Sr}/^{86}\text{Sr}_{(330\text{Ma})}$  ratios and too unradiogenic  $\epsilon_{\text{Nd}(330\text{Ma})}$ -values and, therefore, cannot have caused the trend from Group I to Group II samples.

The lamprophyres are heterogeneous in their isotopic compositions (Fig. 9). The kersantite has a  $\epsilon_{\text{Nd}(330\text{Ma})}$ -value of -0.7 similar to Group I of the plutonic rocks. The minette samples are characterized by significantly lower  $\epsilon_{\text{Nd}(330\text{Ma})}$ -values (-3.8 to -4.9) and higher  $^{87}\text{Sr}/^{86}\text{Sr}_{(330\text{Ma})}$  ratios (0.7068-0.7078 compared to the kersantite and the monzonitoid rocks. Despite the primitive character of the minettes based on high Cr and Ni contents, they show „crustal“ isotopic signatures.

#### 4.2. Granites

Most of the Hauptgranit samples can be characterized as high-K calc-alkaline rocks (Fig. 4). Only the least evolved Hauptgranit sample has shoshonitic features similar to those of some monzonites. A/CNK values vary from 0.88 to 1.12 for the Hauptgranit, thus indicating transitions from metaluminous to

peraluminous rocks. The least evolved, metaluminous Hauptgranit sample is strongly enriched in Ba (2341ppm), Sr (1384ppm), and Th (52ppm) similar to monzonitic rocks. Although decreasing concentrations of Th, U, the LREEs, P, and Zr theoretically may be caused by fractionation of accessory minerals such as orthite, apatite, zircon and titanite, such an interpretation disagrees with the discontinuous trends in some trace element plots vs. MgO (used as fractionation index), as seen in the figures to Stop 2-4. AFC processes are also reflected by varying  $\delta^{18}\text{O}$  values (+8.5 to +10.5 per mill) of whole rock samples from the Hauptgranit, as well as the shift in the Sr-Nd isotopic composition towards lower  $\epsilon_{\text{Nd}(330\text{Ma})}$ -values (-2.7 to -4.3) and to higher  $^{87}\text{Sr}/^{86}\text{Sr}_{(330\text{Ma})}$  ratios (c. 0.7057) than for the monzonitoid rocks (Fig. 9).

In comparison to the Hauptgranit, Riesensteingranit samples have lower  $\text{Al}_2\text{O}_3$ , FeO, MgO, and CaO contents that are typical for leucogranites.  $\text{K}_2\text{O}/\text{Na}_2\text{O}$  ratios vary from 1.3 to 1.6, and A/CNK values from 1.03 to 1.06, the latter indicating slightly peraluminous characteristics.  $\epsilon_{\text{Nd}(330\text{Ma})}$  of -6.2 and  $^{87}\text{Sr}/^{86}\text{Sr}_{(330\text{Ma})}$  of 0.7053 indicate crustal additions to the Riesensteingranit magma.

#### 5. Geochronology

SHRIMP analyses on zircon rims with magmatic growth zoning gave concordant  $^{238}\text{U}/^{206}\text{Pb}$  ages of 326.5 $\pm$ 6.3 Ma (monzonite from Leuben) and 330.5 $\pm$ 4.6 Ma (monzonite from Heidenschanze; Nasdala et al., 1999). The zircon ages are indistinguishable from laser step heating  $^{40}\text{Ar}/^{39}\text{Ar}$  plateau as well as total gas ages determined on amphiboles from both localities ranging from 329.1 $\pm$ 1.4 to 330.4 $\pm$ 1.4 Ma and from 330.4 $\pm$ 2.1 to 330.6 $\pm$ 1.8 Ma, respectively (Wenzel et al., 1997). The results indicate intrusion into the middle crust during the uppermost Viséan.

A mean integrated  $^{40}\text{Ar}/^{39}\text{Ar}$  age of five single biotite grains from different minette samples (Plauenscher Grund) of 326.8 $\pm$ 3.6

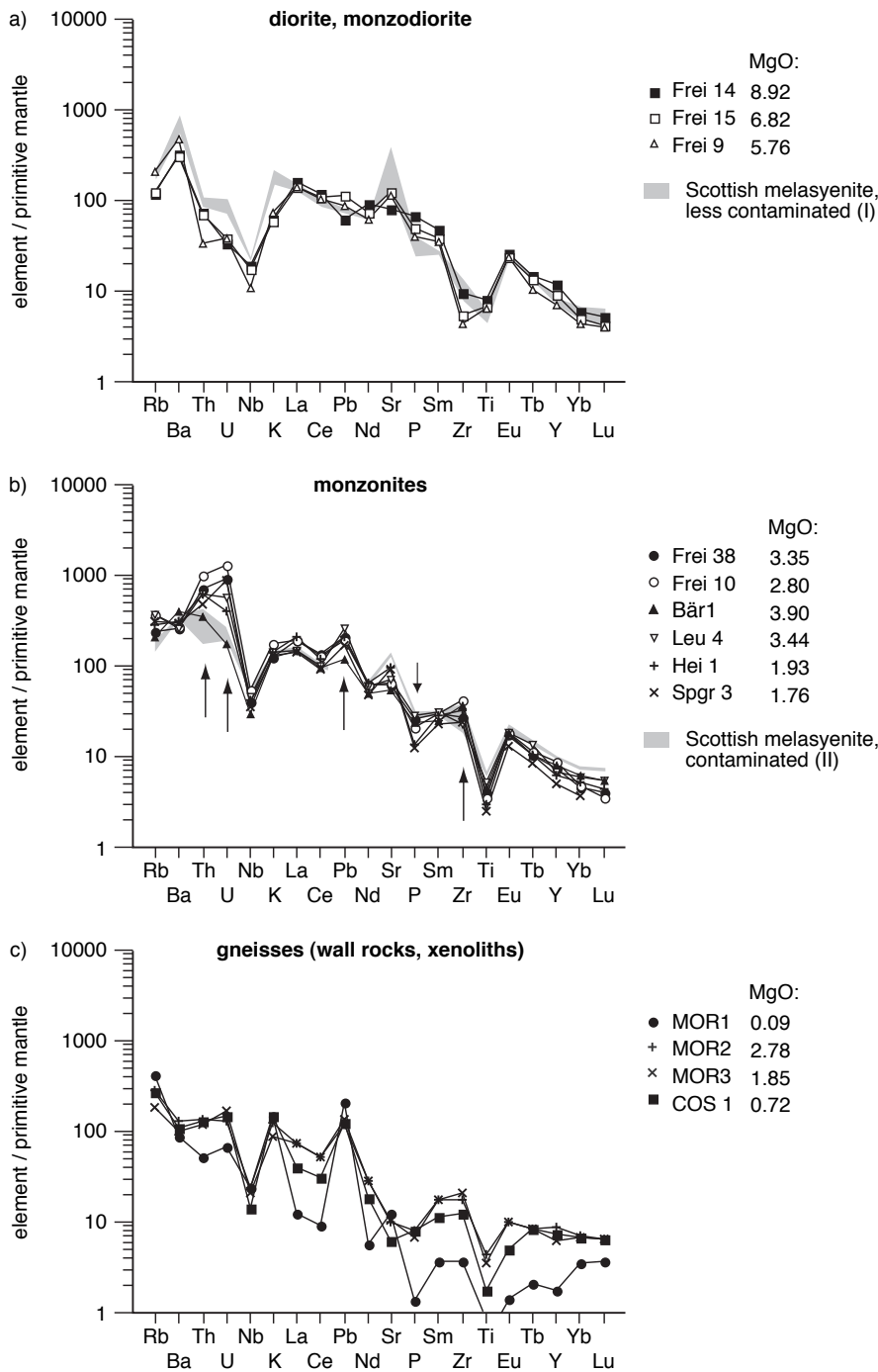


**Fig.7.** Multi-element variation diagrams for (a) diorites-monzodiorites, (b) monzonites, and (c) wall rocks and xenoliths of the monzonitoid intrusion. Element concentrations were normalized to primitive mantle values (Hofmann, 1988). For comparison, the fields for K-rich rocks derived from a subduction-modified continental lithospheric mantle source is shown (Scottish Caledonides; Thompson and Fowler, 1986). Arrows emphasize important petrogenetic features of the monzonite signatures. Note, the chemical similarities between „normal“ monzonite samples and the strongly foliated rock Bär1 in (b).

Ma is interpreted as the minimum age of the minette dikes (Sharp et al., 1997).

Attempts to get intrusion ages for the Hauptgranit by using the single-zircon evaporation technique were not successful since voluminous cores predominate in the zircon population from the Hauptgranit (Wenzel et al., 1993). The Hauptgranit has been dated by the K-Ar method using biotite and muscovite fractions from four locations with ages ranging between  $322\pm 6$  and  $336\pm 6$  Ma with an average of  $326\pm 6$  Ma (Wenzel et al., 1993).  $^{40}\text{Ar}/^{39}\text{Ar}$  plateau ages of two white mica fractions of  $323.4\pm 1.0$  and  $323.6\pm 1.0$  Ma are in agreement with these older age data (Sharp et al., 1997). The intrusion ages of the kersantite dike and the Riesensteingranit remain unconstrained.

## 6. Discussion

A comparison between shoshonitic plutonic rocks from the Meissen Massif and the composition of experimental melts of various crustal lithologies shows that especially the mafic K-rich diorites and monzodiorites cannot be produced by crustal anatexis (Wenzel et al., 2000). Modeling indicates that (i) hybridization of asthenospheric basalt by gneiss from the upper crust or granulite from the lower crust or (ii) interaction of asthenospheric basalt and ultrapotassic melts similar to minette do not yield these compositions. The parental melt of the diorite from Freital possibly is derived from the continental lithospheric mantle (CLM). The LILE- and LREE-enrichment of the diorite is interpreted to reflect mainly source enrichment. High Sr concentrations and small negative to absent Eu anomalies of the diorite samples agree with

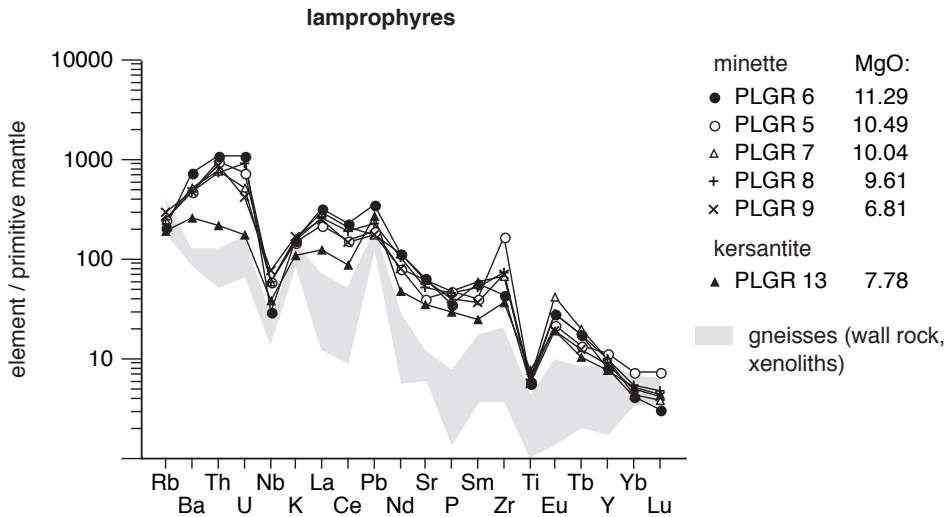


**Fig. 8.** Multi-element variation diagram of the lamprophyre samples from Meissen; normalization as in Fig. 7. Field for wall rocks and a gneiss xenolith is shown for reference and illustrates that the strong enrichment of the lamprophyres cannot be due to bulk crustal contamination (after Wenzel et al., 2000).

derivation from a plagioclase-free source.  $K_2O/Na_2O$  ratios of 0.8 to 1.1 in the diorites probably indicate the presence of amphibole or higher amounts of clinopyroxene besides minor amounts of phlogopite in the source (cf. Foley, 1994). Similarities of the trace element patterns of Freital diorites and of less contaminated diorites and syenites from Scotland (see Fig. 7) may reflect a similar mantle enrichment caused by subduction of oceanic crust.

Fig. 10 summarizes the geodynamic evolution of the Elbe Zone and adjacent units (Wenzel et al., 1997). Of particular interest is the temporal relation between the development of the Elbe Zone and its magmatic rocks and the high-grade metamorphic rocks of the Erzgebirge and Saxon Granulite Massif and their exhumation.

\* In the Elbe Zone, the Lower Carboniferous was characterized by the deposition of flysch-type sediments. The continuous transition from fine- to coarse-grained sedimentation is related

to increasing compression and steepening of relief (Linnemann, 1994). The sedimentary basin of the Elbe Zone was folded and the different units were stacked in SW direction (Kurze et al., 1992).

\* Lusatia to the east of the Elbe Zone is interpreted to represent a Cadomian terrane that largely escaped Variscan deformation and that was accreted during late stages of the Variscan orogeny (Kröner et al., 1994).

\* Eclogite-facies rocks of the Erzgebirge are thought to have reached c. 100 km depth during the collisional event (Schmädicke et al., 1992). Based on  $^{40}Ar/^{39}Ar$  phengite ages and Sm-Nd ages for garnet-whole-rock pairs, Schmädicke et al. (1995) suggested an age for the corresponding high-pressure metamorphism in the Erzgebirge at around 350Ma. Later work indicated that peak metamorphic conditions in the Erzgebirge most likely were reached at 341-340 Ma (see compilation in Rötzler and Plessen, 2010)

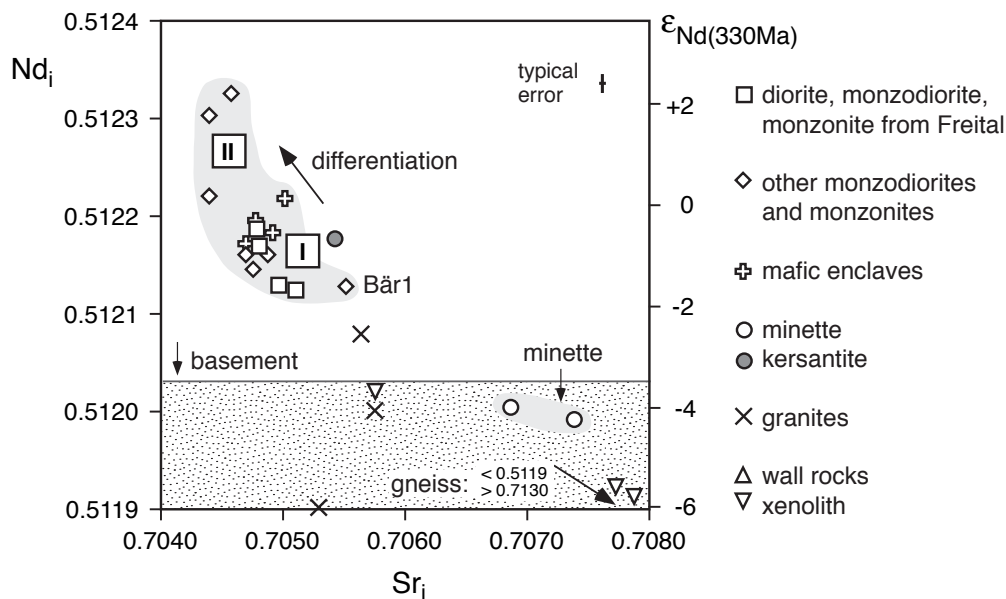


**Fig. 9.** Nd and Sr initial isotope ratios (calculated for 330 Ma) of different whole rock samples from the Meissen Massif (after Wenzel and von Quadt, 1993; Wenzel et al., 2000). Rocks from the Variscan basement plot below the „basement“ line (Liew and Hofmann, 1988). Please, note the similarities between „Group I“ monzonitoid samples and the strongly foliated rock Bär1.

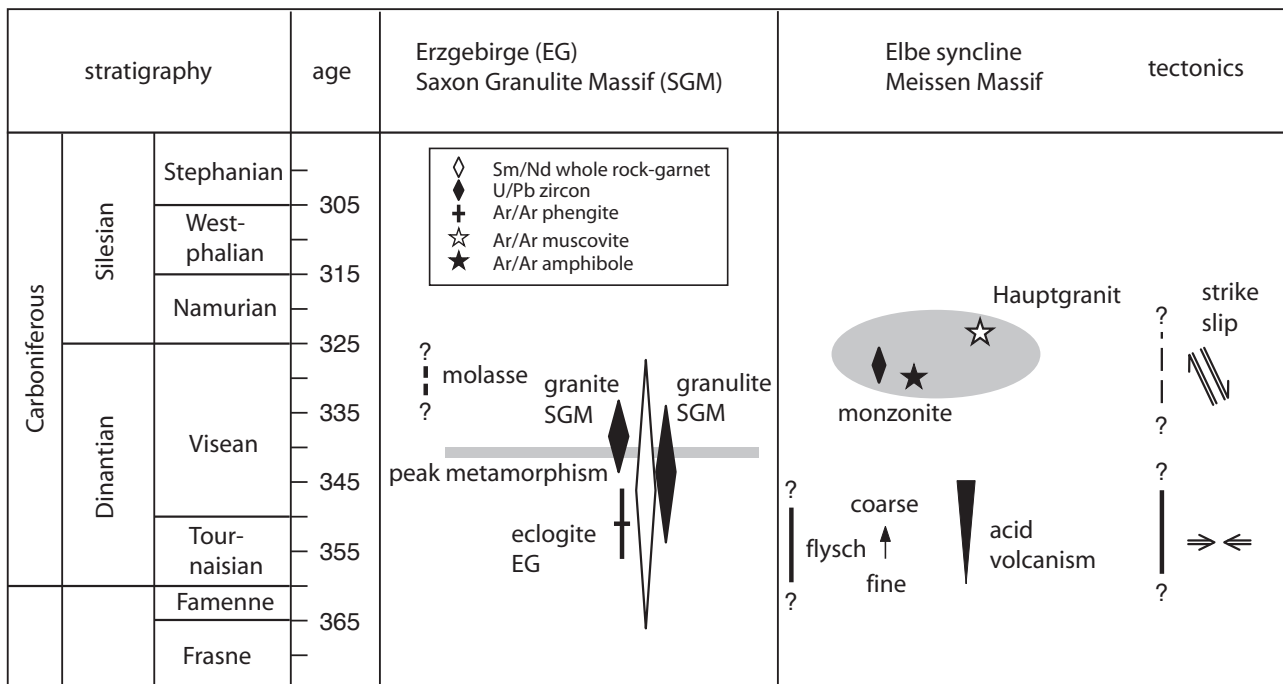


**Fig. 10.** Geodynamic setting of the Meissen Massif and adjacent crustal units (modified after Wenzel et al., 1997). Note Sm-Nd garnet-whole-rock ages show a higher age range than the U-Pb zircon, monazite, and titanite ages, which may reflect initial Nd-isotopic disequilibrium between garnet and whole-rock sample (for discussion see Romer and Rötzler, 2001, 2011).

\* Ultrahigh-temperature-high-pressure metamorphism in the Saxon Granulite Massif reached peak conditions at about 341-340 Ma (cf. Rötzler and Romer, 2010). The rocks were rapidly exhumed to middle crustal levels. A time marker for the development of shear zones is given by the synkinematic intrusion of the Berbersdorf granite at  $338 \pm 5$  Ma (von Quadt, 1993) and the occurrence of granite boulders in uppermost Visean molasse-type deposits.

There is no indication for active subduction and related calc-alkaline magmatism at 330 Ma. The  $^{40}\text{Ar}/^{39}\text{Ar}$  amphibole ages and the  $^{238}\text{U}/^{206}\text{Pb}$  zircon ages demonstrate that the monzonitoid intrusion from Meissen Massif postdates Upper Devonian/Lower Carboniferous subduction and collision by at least 20 Ma. The enrichment of the mantle sources may be of Upper Devonian/Lower Carboniferous ages or older, the intrusion of the Meissen Massif, however, is directly related to strike-slip movements along the Elbe zone (e.g., Mattern, 1996) as reflected by the strongly foliated monzonite at Bärwalde.

The trace element patterns of the minettes (Fig. 8) resemble those of the monzonites (Fig. 7b), whereas the Sr-Nd isotope signatures differ (Fig. 9) and, thus, exclude a common origin of both rock types. Similar  $\epsilon_{\text{Nd}(330\text{Ma})}$ -values of kersantites and Group I monzonitoid rocks do not exclude derivation from a common source, but a direct relation between them is not supported by the major element systematics (Fig. 5). For a heterogeneously enriched veined mantle source, these discrepancies are readily resolved by different relative contributions from the vein material (carrying the metasomatic geochemical signature and Nd-Sr isotopic compositions shifted toward crustal values) by different extent of melting. The minette and kersantite dikes reflecting a smaller degree of melting have a higher contribution of vein material, whereas the more voluminous magmatic rocks of the Meissen Massif reflect a higher extent of melting and thus a smaller

contribution of vein-type material. Zircon relics demonstrate that the K-rich parental magma of the monzonite additionally was affected by intermingling and assimilation of crustal material. Mixing of monzonite-like and crustal melt fractions is responsible for the formation of the Hauptgranit whereas the Riesensteingranit represents a dominantly crustal origin.

**Acknowledgements.** I greatly appreciate technical support by T. Fußwinkel and M. Marks and helpful comments by P. Bons, G. Markl, and K. Pfaff.

## 7. References

- Becker, H., Wenzel, Th., Volker, F. (1999) Geochemistry of glimmerite veins in peridotites from Lower Austria - implications for the origin of K-rich magmas in collision zones. *Geochim. J. Petrol.* 40: 315-338.
- Bergman, S.C. (1987) Lamproites and other potassium-rich igneous rocks: a review of their occurrence, mineralogy and geochemistry. In: Fitton, J.G., Upton, B.G.J. (eds.) *Alkaline Igneous Rocks*. Geol. Soc. Spec. Publ. 30: 103-190.
- Fleischer, M., Altschuler, Z.S. (1969) The relationship of rare-earth composition of minerals to geological environment. *Geochim. Cosmochim. Acta* 33: 725-732.
- Foley, S.F. (1994): *Geochemische und experimentelle Untersuchungen zur Genese der kalireichen Magmatite*. N. Jb. Miner. Abh. 167: 1-55.
- Foley, S.F., Venturelli, G.; Green, D.H., Toscani, L. (1987) The ultrapotassic rocks: characteristics, classification, and constraints for petrogenetic models. *Earth-Science Rev.* 24: 81-134.
- Frischbutter, A. (1982) Zur präkambrischen Entwicklung der Elbezone. *Z. angew. Geol.* 28: 359-366.

- Hofmann, A.W. (1988): Chemical differentiation of the Earth: the relationship between mantle, continental crust, and oceanic crust. *Earth Planet. Sci. Lett.* 90: 297–314.
- Johnson, M.C., Rutherford, M.J. (1989): Experimental calibration of the Aluminium-in-hornblende geobarometer with application to Long Valley caldera (California) volcanic rocks. *Geology* 17: 837–841.
- Kroner, U., Hahn, T., Romer, R.L., Linnemann, U. (2007) The Variscan orogeny in the Saxo-Thuringian zone – Heterogeneous overprint of Cadomian/Paleozoic Peri-Gondwana crust. *Geol. Soc. Am., Spec. Paper* 423: 153–172.
- Kröner, A., Hegner, E., Hammer, J., Haase, G., Bielicki, K.-H., Krauss, M., Eidam, J. (1994) Geochronology and Nd-Sr systematics of Lusatian granitoids: significance for the evolution of the Variscan orogen in east-central Europe. *Geol. Rundsch.* 83: 357–376.
- Kurze, M., Linnemann, U., Tröger, K.-A. (1992) Weesensteiner Gruppe und Altpaläozoikum in der Elbtalzone (Sachsen). *Geotekt. Forsch.* 77: 101–167.
- Liew, T.C., Hofmann, A.W. (1988) Precambrian crustal components, plutonic associations, plate environment of the Hercynian Fold Belt of central Europe: Indications from a Nd and Sr isotopic study. *Contrib. Mineral. Petrol.* 98: 129–138.
- Linnemann, U.G. (1994) Geologischer Bau und Strukturentwicklung der südlichen Elbezone. *Abh. Staatl. Museum Mineral. Geol. Dresden* 40: 7–36.
- Mariano, A.N. (1978) The application of cathodoluminescence for carbonatite exploration and characterization. In: Braga, C.J. (ed.) *Proceedings of the 1st. Intern. Symp. on Carbonatites, Pocos de Caldas, Minas Gerais, Brazil*, pp. 39–57.
- Mattern, F. (1996) The Elbe zone at Dresden - a Late Paleozoic pull-apart intruded shear zone. *Z. dt. geol. Ges.* 147: 57–80.
- Morrison, G.W. (1980) Characteristics and tectonic setting of the shoshonite rock association. *Lithos* 13: 97–108.
- Nasdala, L., Wenzel, Th., Pidgeon, R.T., Kronz, A. (1999) Internal structures and dating of complex zircons from Meissen Massif monzonites, Saxony. *Chem. Geol.* 156: 331–341.
- Pfeiffer, L. (1964): Beiträge zur Petrologie des Meißener Massivs. *Freiberger Forsch.-H. C* 179: 222 pp.
- Pietzsch, K. (1956): Die Elbtalzone. *Ber. Geol. Ges. DDR* 1(2): 117–135.
- Reichert, H. (1926): Tektonik des Meißener Syenit-Granitmassivs. *Abh. Sächs. Akad. d. Wiss., Math.-phys. Kl.* 39: 16 pp.
- Romer, R.L., Rötzler, J. (2001) P-T-t evolution of ultrahigh-temperature granulites from the Saxon Granulite Massif, Germany. Part II: Geochronology. *J. Petrol.* 42: 2015–2032.
- Romer, R.L. and Rötzler, J. (2011) The role of element distribution for the isotopic dating of metamorphic minerals. *Eur. J. Mineral.* 23: 17–33.
- Rötzler, J., Romer, R.L. (2010) The Saxon Granulite Massif: a key area for the geodynamic evolution of Variscan central. In: Linnemann, U. & Romer, R.L. (eds.) *Pre-Mesozoic Geology of Saxo-Thuringia – From the Cadomian Active Margin to the Variscan Orogen*. Schweizerbart, Stuttgart, pp. 233–252.
- Rötzler, K., Plessen, B. (2010) The Erzgebirge: a pile of ultrahigh- to low-pressure nappes of early Palaeozoic rocks. In: Linnemann, U., Kroner, U., Romer, R.L. (eds.) *From the Cadomian Active Margin to the Variscan Orogen: The pre-Mesozoic Geology of Saxo-Thuringia (NE Bohemian Massif)*. E. Schweizerbart Science Publishers, Stuttgart, pp. 253–270.
- Schmädicke, E., Okrusch, M., Schmidt, W. (1992) Eclogite-facies rocks in the Saxonian Erzgebirge, Germany: high pressure metamorphism under contrasting P-T conditions. *Contrib. Mineral. Petrol.* 110: 226–241.
- Schmädicke, E., Mezger, K., Cosca, M.A., Okrusch, M. (1995) Variscan Sm-Nd and Ar-Ar ages of eclogite facies rocks from the Erzgebirge, Bohemian Massif. *J. metamorphic Geol.* 13: 537–552.
- Schmidt, M.W. (1992) Amphibole composition in tonalite as a function of pressure: an experimental calibration of the Al-in-hornblende barometer. *Contrib. Mineral. Petrol.* 110: 304–310.
- Sharp, W.D., Wenzel, Th., Nasdala, L., Mertz, D.F., Becker, T. (1997) Geochronology of Hercynian Meissen Massif magmatic rocks based on <sup>40</sup>Ar/<sup>39</sup>Ar (amphibole, mica) and <sup>206</sup>Pb/<sup>238</sup>U SHRIMP (zircon) data. *Schriftenreihe dt. Geol. Ges.* 2: 108–109.
- Speer, J.A. (1984) Micas in igneous rocks. In: Bailey, S.W. (ed.) *Micas. Rev. Mineral.* 13: 299–356.
- Thompson, R.N., Fowler, M.B. (1986) Subduction-related shoshonitic and ultrapotassic magmatism: a study of Siluro-Ordovician syenites from the Scottish Caledonides. *Contrib. Mineral. Petrol.* 94: 507–522.
- Tischendorf, G., Pälchen, W., Röllig, G., Lange, H. (1987) Formationelle Gliederung, petrographisch-geochemische Charakteristik und Genese der Granitoide der Deutschen Demokratischen Republik. *Chem. Erde* 46: 7–23.
- Tröger, E. (1922) Neues zum Gangfolge des Meißener Massivs. *Cbl. Mineral.* 451-457.
- von Quadt, A. (1993) The Saxonian Granulite Massif: new aspects from geochronological studies. *Geol. Rundsch.* 82: 516–530.
- Wenzel, T. (1997) Magmenquellen und tektonische Stellung variscischer K-reicher Plutonite und Lamprophyre des Meißener Massivs (Sachsen) und Vergleiche mit anderen K-reichen Intrusionen in den mitteleuropäischen Varisciden. *Unpubl. Habilitationsschrift, Universität Mainz*.
- Wenzel, T. (1999) Mantel- und Krustenkomponenten in den Granitoiden des Meißener Massivs (Elbezone). *Z. geol. Wiss.* 27: 417–426.
- Wenzel, Th., Hengst, M., Pilot, J. (1993) The plutonic rocks of the Elbe valley-zone (Germany): evidence for the magmatic development from single-zircon evaporation and K-Ar age determinations. *Chem. Geol.* 104: 75–92.
- Wenzel, Th., Mercolli, I., Oberhänsli, R. (1991) The plutonic rocks of the Meißener Massif (Germany): evidence for open and closed system fractionation processes. *Schweiz. Mineral. Petrogr. Mitt.* 71: 371–390.
- Wenzel, Th., Mertz, D.F., Oberhänsli, R., Becker, T., Renne, P.R. (1997) Age, geodynamic setting, and mantle enrichment processes of a K-rich intrusion from the Meissen Massif (Northern Bohemian Massif) and implications for related occurrences from the Mid-European Hercynian. *Geol. Rundsch.* 86: 556–570.
- Wenzel, Th., Oberhänsli, R., Mezger, K. (2000) K-rich plutonic rocks and lamprophyres from the Meissen Massif (Northern Bohemian Massif): Geochemical evidence for variably enriched lithospheric mantle sources. *N. Jb. Miner. Abh.* 175: 249–293.
- Wenzel, Th., Ramseyer, K. (1992) Mineralogical and mineral-chemical changes in fractionation-dominated diorite-monzodiorite-monzonite sequence: evidence from cathodoluminescence. *Eur. J. Mineral.* 4: 1391–1399.
- Wenzel, Th., von Quadt, A. (1993) The intrusion of the Meissen pluton (Elbe valley-zone): evidence from geochemical and isotopic data. *Isotopenpraxis* 28: 251–262.
- Wenzel, Th., Wolf, D. (1992) The plutonic rocks of the Elbe valley zone (Germany): evidence for different fractionation processes from morphology and internal structure of zircons. *Schweiz. Mineral. Petrogr. Mitt.* 72: 307–314.

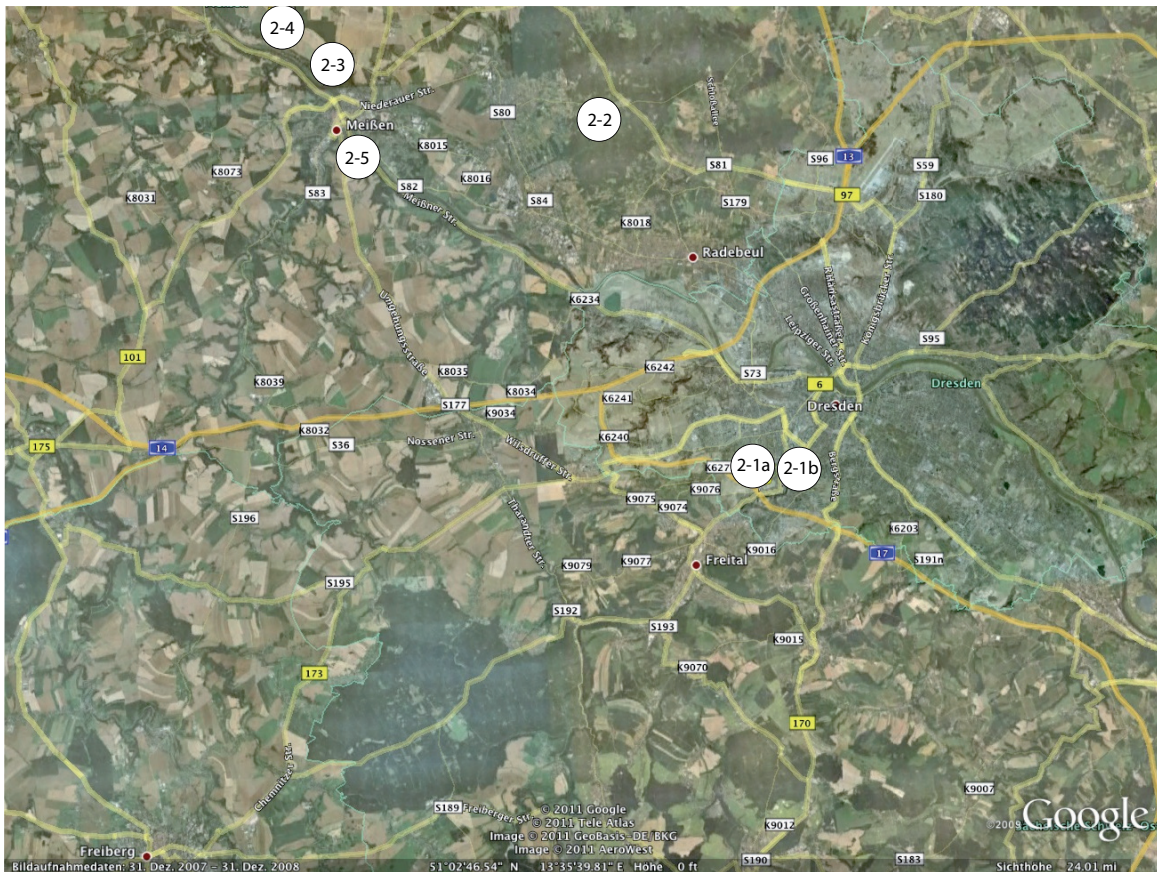


Fig. 11: Field exposures 1-5 in the Meissen Massif; (Google Map)

## Eurogranites 2012

### Stops 2-1a and 2-1b

Plauenscher Grund below the „Begerburg“ at Highway A 17, former quarry „Begerbruch“ and Plauenscher Grund, parking at the „Felsenkeller Brauerei“

Monzonite

Coordinates:

51°01'23"N, 13°41'18"E, 170 m a.s.l.

51°01'28"N, 13°42'03"E, 149 m a.s.l.

Guide: Thomas Wenzel

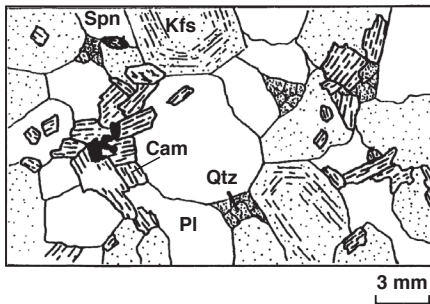
The monzonite of this outcrop belongs to the inner part of the monzonitoid intrusion (Plgr in Fig. 1). Typical petrographic characteristics as well as the local occurrence of mafic enclaves can be observed.

Monzonite of this area is composed of 42.2% plagioclase (oligoclase), 33.4% alkali feldspar, 5.1% quartz, 15.2% amphibole (edenite), 1.2% clinopyroxene+biotite, and 2.9% accessory+ore minerals (zircon, apatite, orthite, titanite, magnetite) on average (Pfeiffer, 1964). The composition of mafic enclaves

from the former Begerbruch is highly variable ranging from amphibole- (37% amphibole, 4.5% clinopyroxene, 3% biotite) to clinopyroxene+biotite-dominated (16% amphibole, 22.1% clinopyroxene, 32.3% biotite; Pfeiffer, 1964). Fabric patterns and mineral chemistry of the monzonite and mafic enclaves are presented in Fig. 12. Feldspar crystals are aligned into foliation that dips moderately to steeply to the NE (cf. Pfeiffer, 1964).

At this place, one can nicely observe the discordance between the monzonite and Cretaceous sandstones.

- \* The trends of some incompatible trace elements from clinopyroxene+biotite-dominated diorites-monzodiorites to amphibole-dominated monzonites (Fig. 6) argue against a simple fractionation scheme and point to a multi-phase intrusion.
- \* Textural and mineral chemical characteristics of clinopyroxene+biotite-dominated enclaves in the monzonite from Plauenscher Grund reflect the presence of early dioritic-monzodioritic precipitates (similar to the Freiberg suite) that are dispersed in a highly differentiated „syenite-like“ groundmass (compare Fig. 2 and Fig 12). This process is also reflected by monzonites with heterogeneous textures from the outer part of the intrusion whereas the monzonite from Plauenscher Grund shows a more equilibrated and homogenized texture.
- \* Amphibole-dominated enclaves from the central monzonites (see Fig. 12) which represent early stages of the differentiation process of the monzonite magma are characterized by isotopic signatures similar to Group I samples and different to their host rocks (Group II in Fig. 9). The process which introduced isotopically depleted components apparently occurred during late evolutionary stages of the monzonite magma (Wenzel et al., 2000).



**monzonite Plauenscher Grund/  
Heidenschanze**

**Cam** Al<sub>2</sub>O<sub>3</sub>: 6.55-6.91 wt%,  
TiO<sub>2</sub>: 0.98-1.43 wt%  
X<sub>Mg</sub>: 0.56

**Pl** An: 19-27, SrO: 0.10-0.36 wt%

**Kfs** Or: 87-93, SrO: 0.24-0.32 wt%  
BaO: 0.78-1.07 wt%

**mafic enclave: Bt - Cpx - rich**

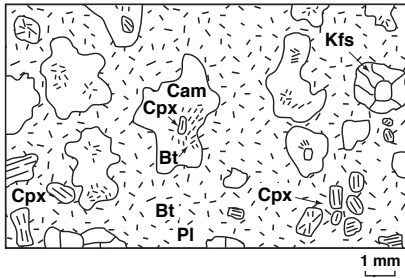
**Cpx** Al<sub>2</sub>O<sub>3</sub>: 1.38-2.17 wt%,  
TiO<sub>2</sub>: 0.26-0.40 wt.%  
Cr<sub>2</sub>O<sub>3</sub>: 0.1-0.55 wt.%, X<sub>Mg</sub>: 0.80-0.88

**Bt** TiO<sub>2</sub>: 1.72-3.78 wt.%,  
BaO: 0.17-0.30 wt.%, X<sub>Mg</sub>: 0.59-0.66

**Cam** Al<sub>2</sub>O<sub>3</sub>: 7.29 - 7.88 wt.%,  
TiO<sub>2</sub>: 1.08 - 1.60 wt.%  
X<sub>Mg</sub>: 0.60 - 0.62

**Pl** An: 26-31

**Kfs** Or: 88-92, BaO: 1.17-1.36 wt.%



**mafic enclave: Cam - rich**

**Cam** Al<sub>2</sub>O<sub>3</sub>: 1.49 - 7.06 wt.%,  
TiO<sub>2</sub>: 0.06 - 0.98 wt.%  
X<sub>Mg</sub>: 0.63 - 0.72

**Pl** An: 25-34

**Kfs** Or: 84-98, BaO: 1.21-2.12 wt.%

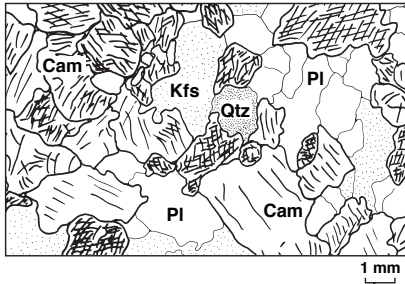


**Fig. 12.** Fabric pattern of monzonite and mafic enclaves from Plauenscher Grund (Plgr in Fig. 1) and concentrations of the most important components in the different minerals (after Wenzel et al., 1991; Wenzel, 1997). Mineral abbreviations as in Fig. 2

- \* A pure crustal origin of the hypothetical contaminant, i.e. the „syenite-like“ melt fraction, seems to be at least not obvious as the most fractionated monzonite samples with >60wt% SiO<sub>2</sub> tend towards depleted ε<sub>Nd(330Ma)</sub>-values of c. +2 (Group II in Fig. 9; see also Fig. 13) which is in contrast to the isotopic signatures of many Variscan basement rocks.
- \* Assuming a contamination scenario, basalts and basaltic tuffs of Upper Devonian ages are the only known wall rocks of the K-rich intrusion showing depleted Sr and Nd isotopic characteristics (Wenzel et al., 2000). However, bulk contamination of monzonite by these basaltic rocks cannot simultaneously explain isotopic, major and trace element compositions of the central monzonites. Models assuming contamination by partial melts of altered basalt that are slightly enriched in Rb, Ba, Sr, and the LREE compared to the original basalt also fail.
- \* Markedly zoned, metamict zircons from several monzonite outcrops are probably associated with the „syenite-like“ contaminant (Wenzel & Wolf, 1991; Wenzel et al., 1993). Zircon

cores of this type from the Heidenschanze monzonite were analysed by SHRIMP (Nasdala et al., 1999). Unfortunately, the age of their source(s) could not be determined since the cores have experienced complete resetting of their U-Pb system during the 330Ma event or they were additionally affected by recent lead loss. Little disordered, low U and Th cores gave discordant U-Pb SHRIMP data corresponding to Proterozoic relic ages (Nasdala et al., 1999).

- \* Similar ε<sub>Nd(330Ma)</sub>-values of group I monzonitoid rocks and the kersantite dike (Fig. 9) demonstrate that these rock types can be derived from similar sources probably enriched by subduction of oceanic crust. In contrast, minette dikes originated from CLM sources modified by subduction of upper continental crust (Wenzel et al., 2000).

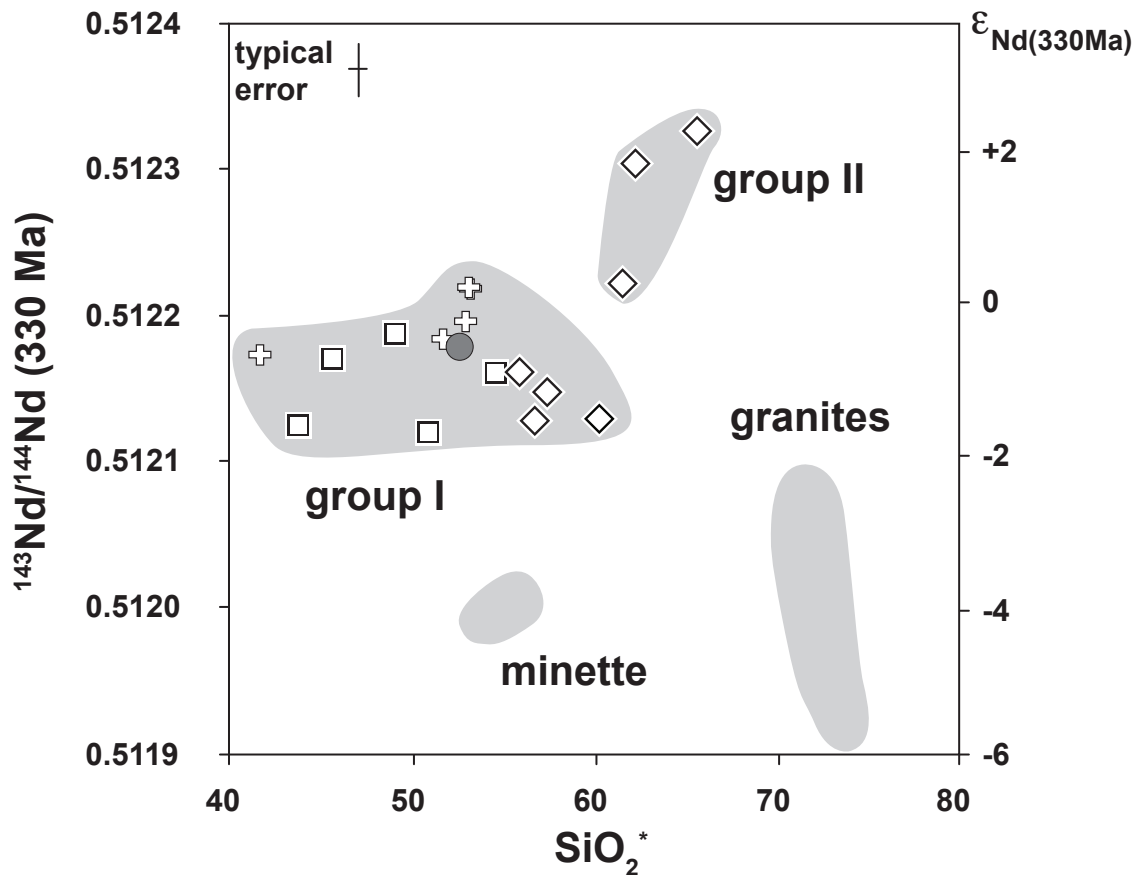


Fig. 13: Nd initial isotopic composition versus  $\text{SiO}_2^*$  content of Meissen Massif rocks; \* - recalculated to LOI-free, symbols as in Fig. 9 (from Wenzel et al., 2000). The monzonite of this outcrop belongs to the inner part of the monzonitoid intrusion (Plgr in Fig. 1). Typical petrographic characteristics as well as the local occurrence of mafic enclaves can be observed.

## Eurogranites 2012

### Stop 2-2

Spitzgrund near Coswig, former quarry

Monzonite

Coordinates:

51°08'51"N, 13°36'35"E, 181 m a.s.l.

Continue through Dresden toward the highway A4-Moritzburg-Auer-Spitzgrund

Guide: Thomas Wenzel

The monzonite of this outcrop belongs to the inner part of the monzonitoid intrusion (Spgr in Fig. 1) where monzonite with homogeneous texture is exposed. Compared to the monzonite from Plauenscher Grund, the local monzonite is slightly enriched in quartz and nearly depleted in pyroxene. A peculiarity is the occurrence of reddish rock varieties adjacent to greyish ones.

While the grey samples contain pyrite and to a lesser amount magnetite, the red ones contain magnetite and hematite.  $\delta^{34}\text{S}$  values of pyrite group around 0 per mill, supporting a magmatic origin (Wenzel et al., 1991). The Nd and Sr isotopic composition of the Spitzgrund monzonite samples is heterogeneous. The  $^{87}\text{Sr}/^{86}\text{Sr}_{(330\text{Ma})}$  ratios and  $\epsilon_{\text{Nd}(330\text{Ma})}$ -values range from 0.7044 to 0.7046 and from +0.1 to +2.2, respectively.

## Eurogranites 2012

### Stop 2-3

East of parking space at the hotel „Knorre“

Biotite-hornblende granodiorite

Coordinates:

51°10'29"N, 13°27'39"E, 103 m a.s.l.

Continue toward Coswig and Meissen, drive along Elbtalstraße toward Riesa to hotel „Knorre“ (the hotel is on the left side, the parking is on the right side).

The so-called „biotite-hornblende granodiorite“ (quartz monzodiorite) is only exposed at the eastern central part of the Meissen massif between monzonite and Hauptgranit. Mainly coarse-grained feldspar is enclosed by a medium- to fine-grained groundmass. On average, the rock consists of 46.4% plagioclase, 27.5% alkali feldspar, 16.7% quartz, 3.7% amphibole, 4.1% biotite, and 1.6% accessory and ore minerals. Based on optical characteristics, amphibole is similar to the amphibole from monzonite, and biotite is similar to biotite from the Hauptgranit (Pfeiffer, 1964). Therefore, this rock type has been interpreted to represent a (metasomatic) reaction product between Hauptgranit and the previously intruded monzonite (Pfeiffer, 1964, and references therein). Based on field evidence, the „biotite-hornblende granodiorite“ is restricted to areas where the monzonite is overlaying the Hauptgranit.

The biotite-hornblende granodiorite contains about 65.5 % SiO<sub>2</sub>, 16.5 % Al<sub>2</sub>O<sub>3</sub>, 3.7 % Fe<sub>2</sub>O<sub>3</sub>, 1.8 % MgO, 2 % CaO, 3.8 % Na<sub>2</sub>O and 5.4 % K<sub>2</sub>O (Romer, unpublished data). It shows shoshonitic affinities and strong enrichments in Sr (c. 1500 ppm) and Ba (c. 2170 ppm). The whole rock composition of the biotite-hornblende granodiorite is very similar to the most evolved monzonite from Spitzgrund and also to the most primitive Hauptgranit sample from Karpfenschänke. Similarities to monzonite and the Hauptgranit are also demonstrated by the SrO contents of alkali feldspar phenocrysts that vary between 0.07 and 0.25 wt%, and BaO concentrations ranging from 0.46 to 0.83 wt% (Wenzel, unpublished data; Wenzel et al., 1991).

The isotopic characteristics of the biotite-hornblende granodiorite ( $\epsilon_{\text{Nd}}(330\text{Ma}) = -0.7$ ;  $^{87}\text{Sr}/^{86}\text{Sr}(330\text{Ma}) = 0.7049$ ; Romer, unpublished data) overlap with those of Group I monzonites (see Fig. 9).

According to the geochemical data, the interpretation of the biotite-hornblende granodiorite as a result of interactions between monzonite and the Hauptgranit magma (Pfeiffer, 1964) may be possible.

## Eurogranites 2012

### Stop 2-4

Northwest of Karpfenschänke, former quarry behind the sewage disposal plant

Granodiorite

Coordinates:

51°11'33"N, 13°26'13"E, 109 m a.s.l.

Continue along Elbtalstraße toward Riesa to Karpfenschänke (on the right side).

The local granodiorite (Ka in Fig. 1) belongs to the so-called Hauptgranit. Granodiorite of this outcrop is composed of 46.7% plagioclase (oligoclase), 26.2% alkali feldspar (microcline), 17.2% quartz, 8% biotite, and 1.9% accessory and ore minerals (Pfeiffer, 1964). Amphibole-bearing mafic enclaves that contain sphene and orthite are less frequently observed. Adjacent to such enclaves, feldspar is aligned into foliation that dips moderately to steep to the NE (Pfeiffer, 1964).

A few sample locations of the Hauptgranit such as Klein-Zadel (Klz in Fig. 1) contain biotite intergrown with intercrystalline white mica. Fabric patterns and mineral chemistry of the Hauptgranite are presented in Fig. 15 (the data for the Riesensteingranit are given for information).

Hauptgranit samples are generally enriched in Rb, Ba, Th, U, Pb, and Sr indicating certain petrogenetic relationships to the monzonite (see Fig. 16). The concentrations of LREE, P, Zr and Ti are significantly lower than those in the monzonite.

However, a simple fractionation model can be excluded on the basis of different  $^{87}\text{Sr}/^{86}\text{Sr}_{(330\text{Ma})}$  ratios and  $\epsilon_{\text{Nd}(330\text{Ma})}$ -values of monzonites and granites (see Fig. 9). Further arguments for open system processes are presented in Fig. 14 showing discontinuous trends in plots of Th, Sr and  $\delta^{18}\text{O}$  vs. MgO as fractionation index.

An important role of crustal sources in the formation of the Hauptgranit is also reflected by almost 90% of zircons with voluminous cores (Wenzel & Wolf, 1991) that yield Precambrian  $^{207}\text{Pb}/^{206}\text{Pb}$  single-grain evaporation ages (Wenzel et al., 1993). Mixing of monzonite-like and crustal melt fractions is at last supported by isotope and trace element modelling results.

It is concluded that lithospheric mantle melts partially melted crustal rocks, and the interaction of mantle and crustal melts produced various degrees of coexistence and hybridization in the Meissen massif (Wenzel, 1999).

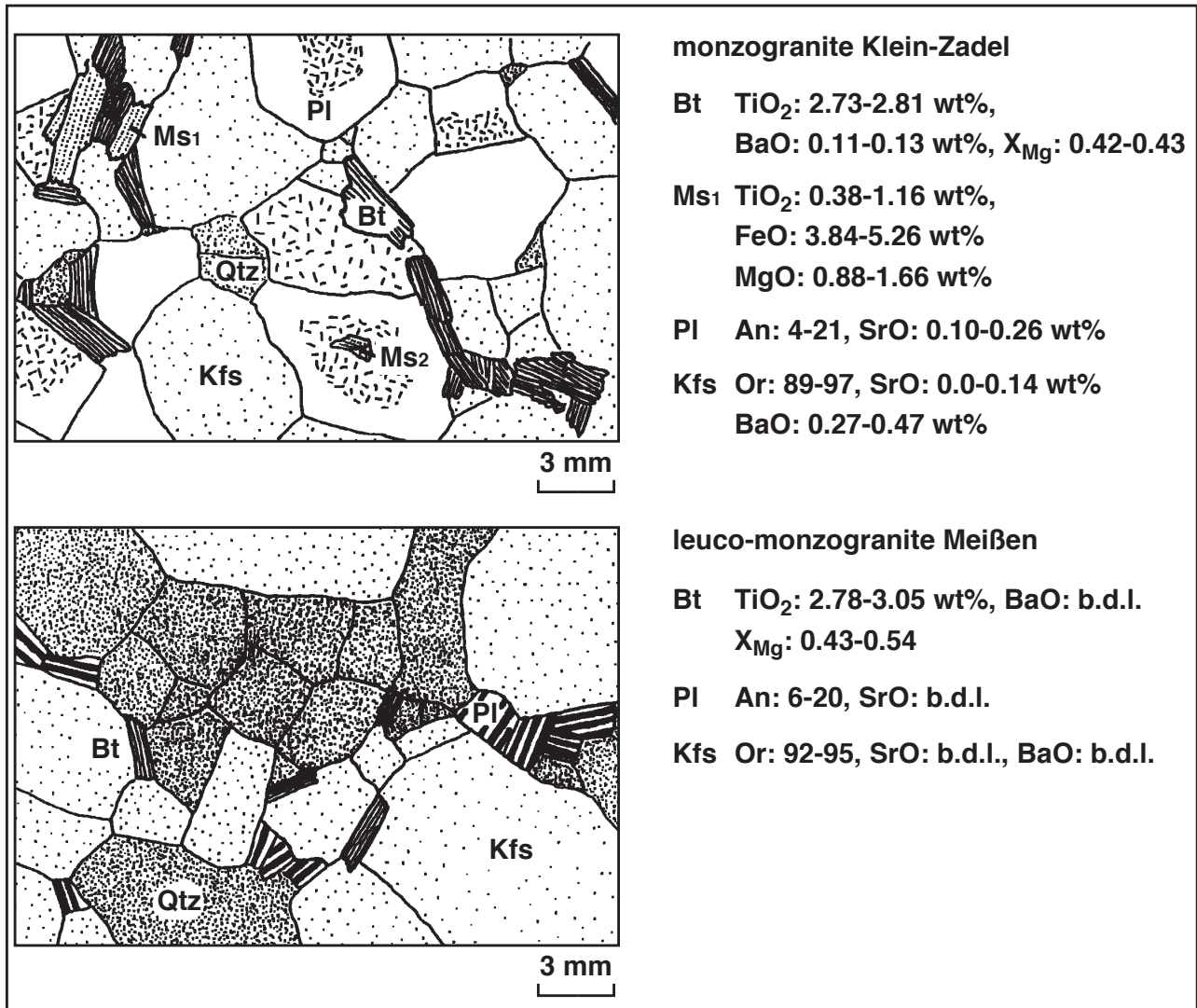


**Fig. 14.** Fabric patterns of the monzogranite from Klein-Zadel (Klz in Fig. 1) and concentrations of the most important components, analyzed by electron-microprobe, in the different minerals (after Wenzel et al., 1991; Wenzel, 1997). Mineral abbreviations as in Fig. 2. Data for the Riesensteingranit are given for comparison (see also Stop 2-5).

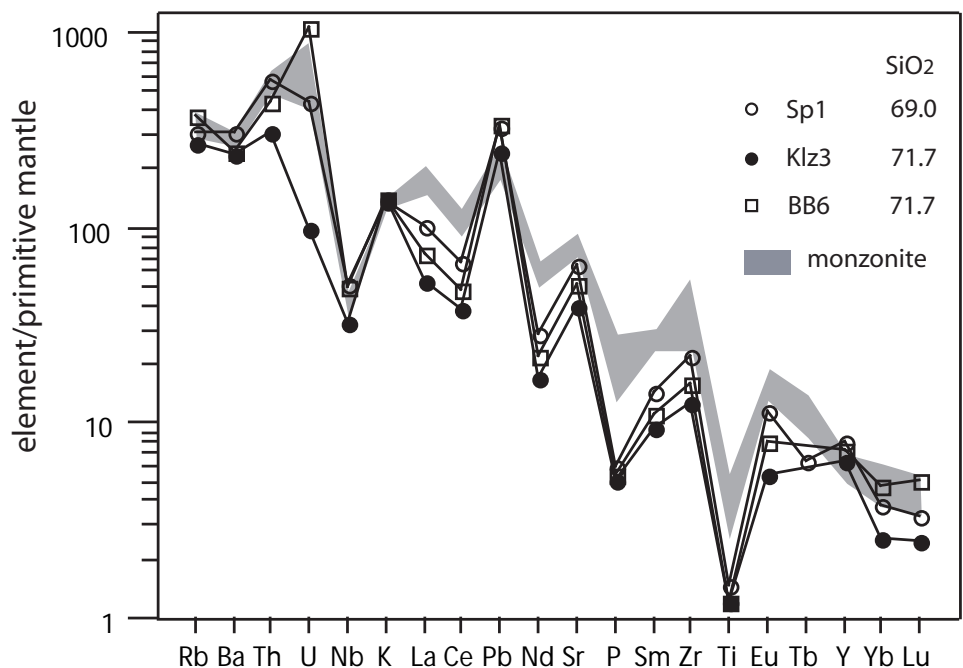


**Fig. 15.** Multi-element variation diagram of the Hauptgranit samples; normalization as in Fig. 7. Field for monzonite is given for comparison (after Wenzel, 1999).

## Eurogranites 2012

## Stop 2-5

Meissen, Riesensteingranite (optional)

Granite

Coordinates:

51°09'41"N, 13°29'58"E, 107 m a.s.l.

Meissen.

Guide: Thomas Wenzel

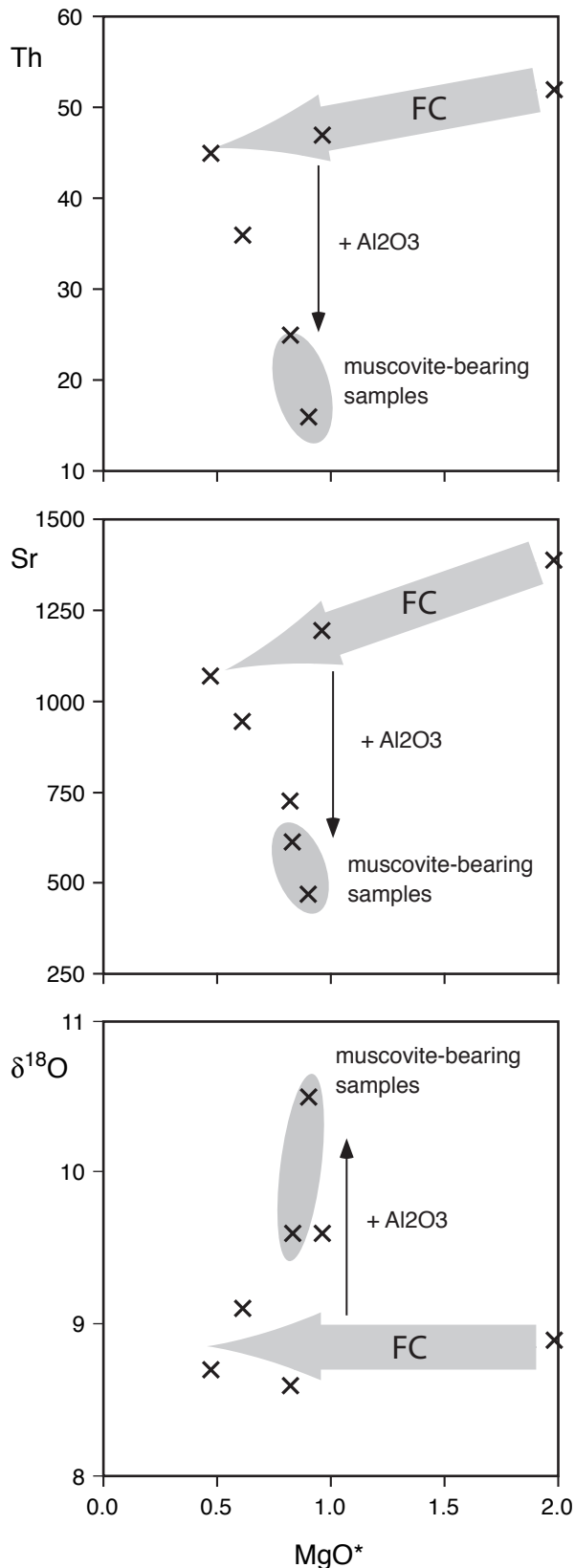


**Fig. 16.** Th and Sr (in ppm) and  $\delta^{18}O$  (in per mill) versus  $MgO^*$  for the Hauptgranit samples; \* - recalculated to LOI-free compositions. FC – fractional crystallization trend; addition of  $Al_2O_3$ -rich crustal material depleted in Th and Sr and enriched in  $^{18}O$  is probably responsible for the local formation of muscovite-bearing granites (after Wenzel, 1999).

The Riesensteingranit consists of 34.2 % plagioclase, 33.1 % alkali feldspar, 29.9 % quartz, 2 % biotite and 0.7 % accessory and ore minerals on average (Pfeiffer, 1964). Typical fabric patterns of this non-foliated rock and mineral chemical data are given in Fig. 14.

In contrast to the Hauptgranit, the Riesensteingranit is probably of crustal origin. This is supported by a typical crustal  $\epsilon Nd$  (330Ma) -value of c.  $-6.2$  (Wenzel and von Quadt, 1993). The leucogranites show low  $Al_2O_3$  (13.1-13.5 %),  $Fe_2O_3$  (1.1-1.5 %), MgO (0.1-0.3 %) and CaO contents (0.4-0.9 %). The chemical composition and  $K_2O/Na_2O$  ratios of 1.3-1.6 are similar to post-collisional leucogranites of the French Massif Central which are believed to be generated by melting of metasediments (Wenzel, 1999, and references therein). However, in contrast to the S-type French leucogranites the Riesensteingranit has lower A/CNK ratios  $<1.1$  and a lower content of CIPW-normative corundum (0.5-0.8 %) what may be related to different melting conditions.

# The Erzgebirge

Jochen Rötzer<sup>1</sup>, with contributions (Stops 3/2 and 3/3) by Uwe Kroner<sup>2</sup>

<sup>1</sup> GFZ German Research Centre for Geosciences,  
Telegrafenberg, D-14473 Potsdam, Germany  
rtzlr@gfz-potsdam.de

<sup>2</sup> TU Bergakademie Freiberg, Dept. of Geology,  
Bernhard-v.-Cotta-Str. 2, D-09599 Freiberg, Germany  
kroner@geo.tu-freiberg.de

Apatite fission-track ages (Ventura and Lisker, 2003) indicate that the Erzgebirge mountain range owes its topography to two episodes of Mesozoic-Cenozoic block faulting and denudation, which brought metamorphic rocks to the surface of an area about 120 km long and 45 km wide (Fig. 1). The north-eastern and south-eastern margins of the uplifted area slope steeply down to graben structures in the Elbe fault zone and the Eger rift, respectively. The topography is less severe across the north-western boundary to the Erzgebirge basin, and is smooth along the south-westerly continuation of the metamorphic rocks into the Fichtelgebirge region. The variable vertical offset comes from tilting of the Erzgebirge block to the northwest, consistent with south-eastward deepening of the erosion level and the south-easterly position of the mountain crest, rising 1244 metres above sea level on the highest point.

The Erzgebirge has traditionally received attention as one of the world's classical mining districts, but since the 1990's when high- to ultrahigh-pressure rocks were recognized, the focus has shifted. Up until then, the Erzgebirge was interpreted to be an autochthonous complex formed in a subsiding basin during continuous Neoproterozoic to early Palaeozoic deposition and concomitant low- to medium-pressure metamorphism, followed by weak overprinting during the Variscan orogeny (e.g., Lorenz and Hoth, 1990, and references therein). Quartzite, metacarbonate, and meta-igneous intercalations in the siliciclastic metasedimentary sequence served as marker horizons for correlating isolated outcrops and drill cores, and for dividing the crustal section into successive stratigraphic units. This method was applied because neither paleontologic nor reliable isotopic age data existed at that time, except for low-grade rocks at high structural levels. From inception, the autochthonous concept raised various problems, such as insufficient overhead load on the metasediments even in relation to unrealistic low pressure estimates. It was also obvious that the peak-pressure conditions assumed for the metasediments were too low to account for the eclogites intercalated within them. Ductile contacts between rocks of indisputably distinct metamorphic grade, such as gneiss and phyllite, were problematic as well.

Petrologic investigations aimed at determining the P-T evolution of the eclogites were a first step towards solving these problems. Schmädicke et al. (1992) have divided the eclogites into three regional groups marked by an increase in grain size and a concomitant decrease in schistosity from the western to the central Erzgebirge. Two of these groups, occurring in the western Erzgebirge, do not differ strongly in mineral assemblages and reaction textures. The peak assemblages consist of omphacite, garnet, quartz, and rutile, and locally kyanite and

phengite. Actinolitic hornblende and zoisite are additional peak minerals in the eclogites of the south-western Erzgebirge. In the eclogites of the north-western Erzgebirge, amphibole is not part of the peak assemblages but reappeared during early post-peak metamorphism, forming poikiloblastic overgrowths of pargasitic hornblende or edenite. Another difference between both groups is in the chemical zoning of garnet, which in the south-western Erzgebirge defines a well-preserved growth zoning pattern, with Ca-Mn rich cores and Mg-rich rims, whereas in the north-western Erzgebirge the zoning trends vary, suggesting that retrograde diffusive zoning has partially overprinted the growth zoning. Omphacite and phengite from the eclogites of the south-western and north-western Erzgebirge, respectively, have maximum jadeite contents of 50 mol % and 40 mol %, and Si contents of 3.40 and 3.45 atoms per formula unit (apfu). In the south-western Erzgebirge, inclusions of actinolite, epidote, plagioclase, and paragonite in garnet indicate that the eclogites passed through the stability field of paragonite before reaching the metamorphic peak. In the north-western Erzgebirge the only mineral found included in garnet is pargasite or pargasitic hornblende, with little implications on prograde metamorphism. Both eclogite groups largely resemble each other in their retrograde reaction textures, which include, in order of formation: i) plagioclase-clinopyroxene symplectites replacing omphacite, ii) plagioclase-biotite symplectites, locally associated with barian K-feldspar or barite, replacing phengite, iii) amphibole coronas on omphacite and garnet, partly involving plagioclase and epidote, and iv) margarite pseudomorphic after kyanite. Peak temperature estimates based on garnet-clinopyroxene thermometry are 630-700 °C in the south-western Erzgebirge, and 700-760 °C in the north-western Erzgebirge. The omphacite-kyanite forming breakdown reaction of paragonite sets a lower limit of 2.0-2.4 GPa on the peak pressure in the eclogites of the south-western Erzgebirge. For these rocks, the sequence of mineral assemblages constrains a tight clockwise P-T path, with only about 100 °C difference in temperature between burial and exhumation path. The eclogites of the north-western Erzgebirge preserve a similar, though less well-constrained, P-T path because prograde mineral relics are absent. The decompression-cooling paths in both eclogite groups reached the margarite-quartz stability field at P-T conditions <600 °C and <0.8 GPa (Fig. 2). Both eclogite groups occur also in the Czech part of the western Erzgebirge, where Klápová et al. (1998) have distinguished three eclogite types. The first two types showing varying modal proportions of minerals but also a gradual transition into each other correspond to the eclogite group of the south-western Erzgebirge. However, some features, such as the presence of paragonite and, locally,

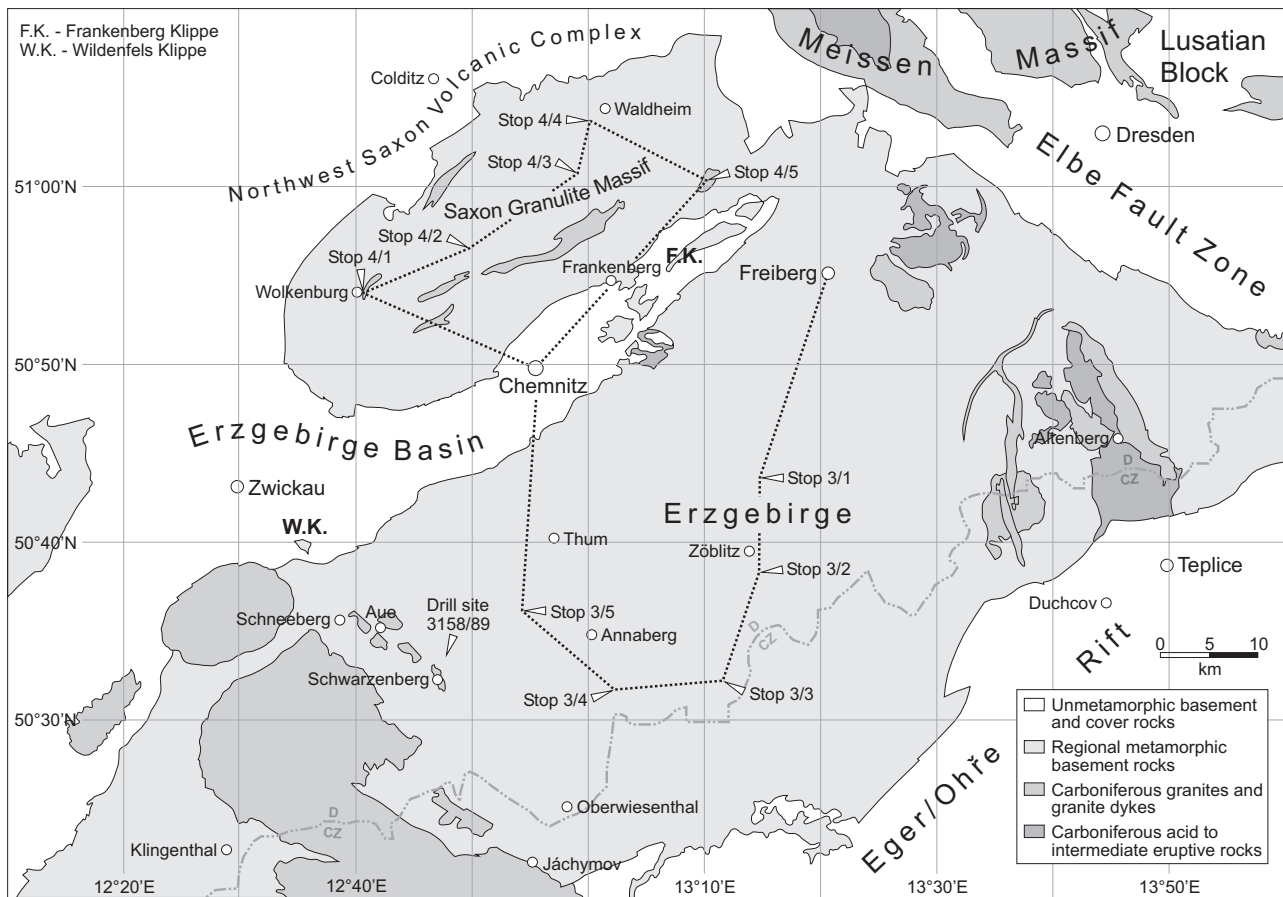


**Fig. 1.** Route map for Field Trips 3 and 4 showing major crustal units, the extent of regional metamorphism, and outcrops of late- to post-orogenic magmatic rocks in the south-eastern Saxo-Thuringian Zone of the Variscan Orogen. Note the location of borehole 3158/89 drilled by Wismut Corporation.

talc as peak metamorphic minerals, differ from those described above, as does the occurrence of peak metamorphic carbonate in the third rock type representing the eclogite group of the north-western Erzgebirge. Kláková et al. (1998) have grouped these rocks into a single unit by explaining variation of the peak-temperature estimates within the wide range from 550 °C to 730 °C as an artefact of erroneous assumptions on the  $\text{Fe}^{2+}$  content in omphacite. Peak-pressure estimates near 2.6 GPa derived by these authors from garnet-omphacite-phengite equilibria are far above the reaction across which paragonite – reported to be a stable peak metamorphic mineral – reacts to form the observed omphacite composition, kyanite, and vapour. With this exception, the exhumation path established by Kláková et al. (1998) for their eclogite type 1 is identical to the decompression-cooling path for the eclogites of the south-western Erzgebirge from Schmädicke et al. (1992).

The eclogites of the central Erzgebirge are particular in that their peak assemblages originally contained coesite, apart from omphacite, garnet, rutile, and locally kyanite. Occasionally developed amphibole, corresponding to pargasite or pargasitic hornblende, likely originated during post-peak eclogite facies overprinting. Phengite is present in places, mostly exhibiting disequilibrium textural relations with the peak assemblages. The Si contents of phengite reach 3.35 apfu, consistent with formation or re-equilibration of phengite at a post-peak stage. Phengite-phlogopite intergrowths suggest that at peak or near-peak pressure conditions the temperature overstepped the stability limit of phengite, which reacted partially with garnet to produce phlogopite, kyanite, and coesite/quartz. High-temperature

metamorphism is also evident from polycrystalline inclusions in omphacite and garnet formed of quartz pseudomorphs after coesite in association with K-feldspar and orthopyroxene. The compositions of omphacite and garnet are nearly homogeneous on an outcrop scale but vary between outcrops, with jadeite contents of omphacite up to 50 mol % and pyrope or grossular contents of garnet up to 40 mol %. Retrograde reaction textures are similar to those in the Western Erzgebirge eclogites. Garnet-clinopyroxene thermometry indicates that the metamorphism culminated at temperatures of 840-910 °C, which, considering the stability limit of coesite, require a peak pressure not below 2.9 GPa. After initial near-isothermal decompression to pressures of 1.4-1.6 GPa, the ascending rocks started to cool substantially, reaching the margarite-quartz stability field, where the P-T paths for the three eclogite groups coincided (Fig.2).

The above results did not disclose the relationship of the eclogites to their country rocks as a key issue in understanding the structure and evolution of the Erzgebirge. Rötzer et al. (1998) have shown based on petrologic and structural evidence from major rock types that the upper part of the Erzgebirge crustal section is not, as previously assumed, a continuous metamorphic sequence but a stack of metamorphic units, each with a different P-T path. From top to bottom, these units include the Phyllite, the Garnet-Phyllite, and the Mica-Schist/Eclogite Units. However, the latter one flanking the central Erzgebirge to the west and the northwest comprises two or more different parts (Gross et al., 2008; Rötzer and Plessen, 2010) whose boundaries are concealed within similar rock associations. The widespread mica schists and concordant intercalations of paragneiss, orthogneiss, quartzite,

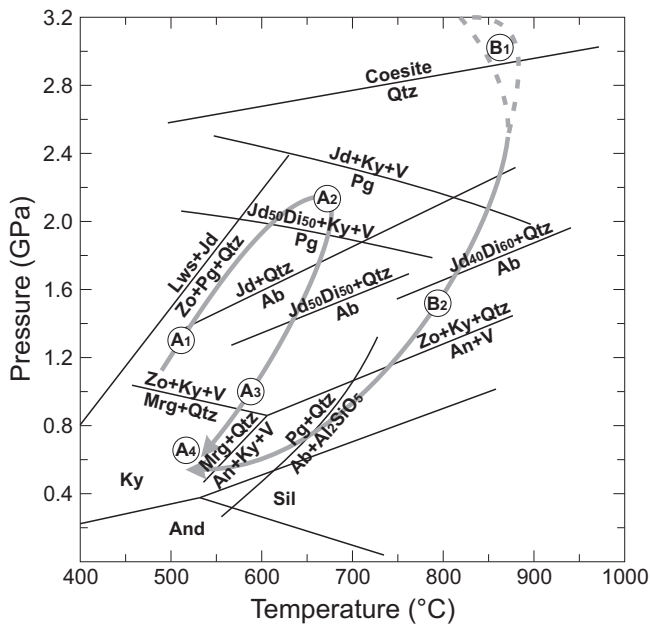


**Fig. 2.** P-T paths for the Erzgebirge eclogites (Schmädicke et al., 1992). South-western Erzgebirge: A1, garnet appears and plagioclase disappears; A2, paragonite is absent in the matrix, but has survived as inclusions in garnet; A3, Cpx-Pl symplectite grows on omphacite; A4, kyanite reacts to margarite. Central Erzgebirge: B1, coesite-bearing peak assemblage; B2, formation of Cpx-Pl symplectite.

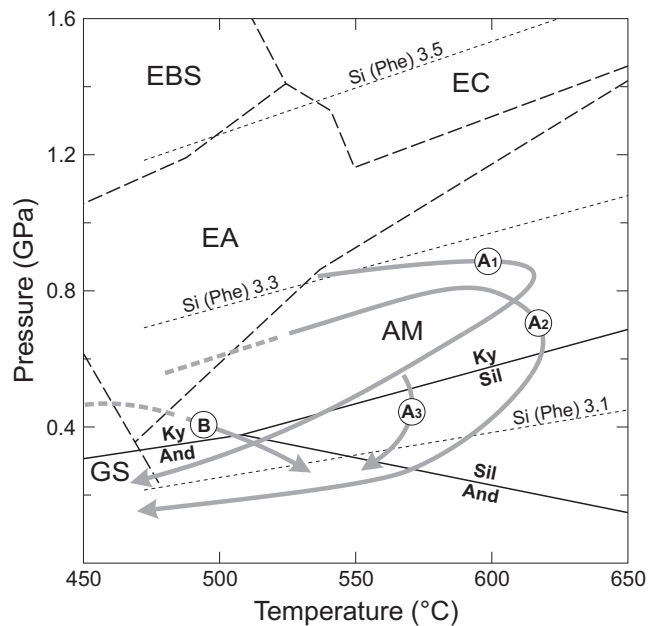


**Fig. 3.** P-T paths for garnet-staurolite-bearing schists and gneisses exposed in a band running from the north-western flank of the Erzgebirge to the Elbe Fault Zone east of the Saxon Granulite Massif (Reich, 1996). The paths labelled with A1 to A3 represent either different parts of the same metamorphic unit or different units, in which kyanite, sillimanite, and andalusite have successively replaced each other. Path B describes heating of a low-pressure unit resulting in replacement of chloritoid by staurolite.

marble, and metabasite thus appear to form a coherent unit, the Mica-Schist/Eclogite Unit. The mica schists are partly feldspar-bearing, semipelitic to variably aluminous pelitic types, and partly feldspar-free Fe-Al rich metapelites (Rötzler et al., 1998). The feldspar-bearing types involve graphite-mica schists. Typical country rocks for the eclogites of the Mica-Schist/Eclogite Unit are light-coloured phengitic mica schists with local chloritoid, whereas staurolite-K-feldspar-bearing light and dark-coloured mica schists with highly variable proportions of white mica and primary biotite enclose epidote amphibolites that lack evidence of eclogite facies metamorphism. This change in rock association and mineral assemblage may arise from heterogeneous re-equilibration of a coherent unit during successive metamorphic stages but rather indicates different metamorphic units. Rötzler and Plessen (2010) have pointed out that staurolite-mica schists originally considered part of the Mica-Schist/Eclogite Unit may instead be coherent with staurolite-bearing medium-pressure rocks extending along the north-western flank of the Erzgebirge (Fig. 3).

The Mica-Schist/Eclogite and Garnet-Phyllite Units show a similar sequence of structural features, starting with a crenulated S1 foliation preserved within garnet porphyroblasts and relic domains, a subhorizontal main S2 foliation carrying an E-W trending stretching lineation, and a local S3 foliation produced by low-angle normal faulting (Rötzler et al., 1998). The mica schists enclosing eclogite represent the entire above-mentioned range of metapelitic lithologies. Their S1 assemblages invariably consist of phengite, quartz, rutile, and ilmenite, and may involve albite, chloritoid, graphite, and tourmaline, depending on bulk-rock composition (Fig. 4a). Chlorite and biotite are likely also part of the S1 assemblages, but are difficult to distinguish from subsequent, more common, generations of these minerals, which

grew at the expense of garnet and phengite, respectively (Fig. 4b). Ilmenite of the S1 assemblage is partially included in rutile, and that, in turn, is included in garnet, suggesting the formation of rutile from ilmenite during D1. The S1 assemblages are present as crenulated inclusion trails in garnet, with fold axes parallel to the stretching lineation on S2. Consequently, garnet porphyroblast growth was syn-D2 (Rötzler et al., 1998). The minerals defining S1 occur also in S2, except for albite from feldspar-bearing assemblages, which is replaced by oligoclase, partially in association with K-feldspar. Mica schist from borehole 3158/89 sunk by the Wismut Corporation into the contact aureole of an unexposed granite body at Beierfeld (Fig. 1) is exceptional as the S1 and S2 assemblages have been reported to contain kyanite and staurolite, respectively (Rötzler et al., 1998). The intrusive granite contact, at a depth of 877 m, is 555 m below the sample locality. A re-examination of the sample during preparation of this excursion guidebook did not find kyanite but disclosed overgrowths of contact-metamorphic andalusite and biotite on the regional metamorphic minerals (Fig. 4c). A single grain of staurolite observed adjacent to the andalusite-biotite assemblage likely is part of the contact-metamorphic overprint (Fig. 4d). This assumption is consistent with mineral reactions in contact-metamorphic metapelites by which staurolite gives way to andalusite and biotite as temperature increases (e.g., Mezger et al., 2001). The local staurolite occurrence therefore developed rather in the contact aureole than during regional metamorphism. A typical feature of the Mica-Schist/Eclogite and Garnet-Phyllite Units are albite porphyroblasts overprinting S2. Rötzler et al. (1998) have invoked a model established by Jamieson and O'Beirne-Ryan (1991) to put these porphyroblasts down to decompression-related ionic reactions that enlarge the stability field of albite relative to white mica. They inferred further that the

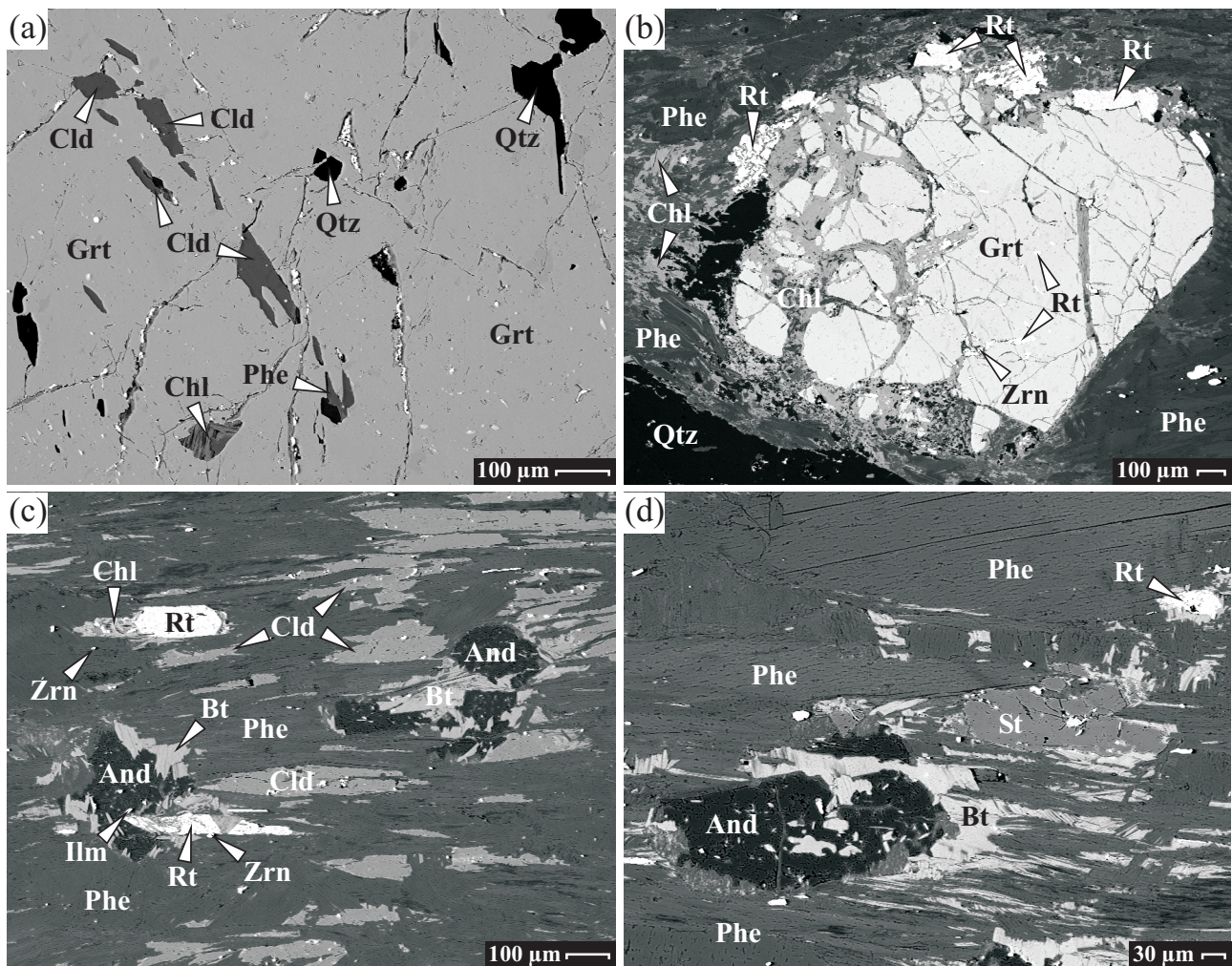


**Fig. 4.** BSE images of mineral textures in mica schist penetrated by the 3158/89 drilling at 322.4 m depth: (a) chloritoid, phengite, chlorite, and quartz are part of the S1 assemblage preserved in porphyroblastic garnet; (b) garnet with inclusions of rutile and zircon is rimmed by rutile and is cut by chlorite; (c) the contact-metamorphic andalusite-biotite assemblage grows on regional-metamorphic phengite and chloritoid; (d) contact-metamorphic andalusite and biotite associated with local staurolite grow on phengite.

late-D2 albite porphyroblasts and euhedral inclusion-free garnet rims grew roughly coevally. Muscovite and quartz aligned in S3, and chlorite penetrating and pseudomorphing garnet indicate D3 retrogression, which caused Ca release from garnet and related corona growth of syn-D3 oligoclase on the late-D2 albite porphyroblasts.

Garnet of the feldspar-bearing mica schists essentially is a grossular-almandine solid solution, with compositional variation corresponding to growth zoning. A decrease in grossular content from up to 44 mol % in the core down to 6 mol % in the rims compensates for a simultaneous increase in almandine content from 50 mol % to up to 80 mol %. Garnet of the feldspar-free mica schists, however, is different, showing a relatively homogeneous almandine-rich (>90 mol %) composition. The garnet core compositions manifest a first metamorphic stage when initially formed minor garnet has equilibrated with the S1 assemblages. Garnet porphyroblast growth during a second stage produced most of the garnet in equilibrium with the S2 assemblages (Rötzler et al., 1998). The Si contents of white mica decrease across the generations, from 3.5 apfu for S1 phengite through 3.3-3.2 apfu for S2 phengite to 3.15-3.05 apfu for S3 muscovite. S1 phengites included in garnet and those present in the matrix

or in the core of S2 phengites show contrasting zoning trends with rimward increasing and decreasing Si contents, respectively. P-T estimates for the successive garnet-phengite equilibria of the mica schists constrain a decompression-heating path through metamorphic stages at 1.2 GPa, 500-520 °C and 0.7 GPa, 540-580 °C (Fig. 5). However, the pressure estimate for the first stage sets only a lower limit on the peak pressure because K-feldspar as a product of the phengite barometer reaction does not occur in the S1 assemblages. Garnet-phengite equilibria from intercalations of orthogneiss within the mica schists have yielded slightly lower temperature estimates of 470 °C and 525 °C for the first and second stage, respectively. The real peak pressure could again not be determined from these rocks because their S1 assemblages lack biotite as another product of the phengite barometer reaction. Additional P-T data for the S2 assemblages obtained using multi-equilibrium calculations suggest equilibration at little variable pressures near 0.8 GPa but at widely scattered temperatures within the interval between the first and second stages as inferred from conventional thermometry. Syn-D3 feldspar recrystallization textures and phengite barometry of S3 white mica constrain the third metamorphic stage to the P-T range of 0.2-0.3 GPa and 400-500 °C, consistent with entrapment conditions of secondary

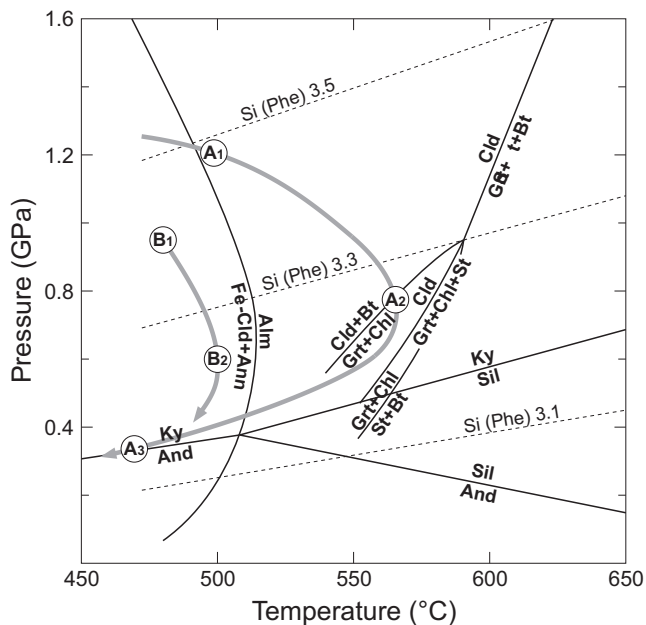


**Fig. 5.** P-T paths for the Mica-Schist/Eclogite and Garnet-Phyllite Units (Rötzler et al., 1998) in relation to reactions in the KFMASH grid from Spear & Cheney (1989), and to Si isopleths for KMASH phengite in equilibrium with phlogopite, K-feldspar, and quartz at  $a_{\text{H}_2\text{O}} = 1$  from Massonne (1991). The deformation stages D1 to D3 and simultaneous re-equilibration stages are marked A1 to A3 for the Mica-Schist/Eclogite Unit, and B1 to B2 for the Garnet-Phyllite Unit (B3 coincides with A3).

fluid inclusions. This retrograde stage is in evidence not only in the Mica-Schist/Eclogite Unit but also in the deeper part of the Erzgebirge crustal section.

The uncertain peak-pressure conditions for the major rock types of the Mica-Schist/Eclogite Unit leave open whether these rocks and the eclogites followed the same P-T path. Contrasting decompressional heating and cooling paths, respectively, for the country rocks and the eclogites, i.e. those eclogites ascribed above to the south-western Erzgebirge, argue against a common metamorphic evolution (cf. Figs. 2 and 5). However, multi-equilibrium P-T estimates for the country rocks indicate a range from constant to variably elevated temperatures during decompression (Rötzler et al., 1998). The decompression-heating path might thus be an artefact of combining non-coherent units. Gross et al. (2008) tackled this problem by studying a calc-silicate reaction zone separating marble from an intercalated eclogite body. The 15-20 m wide reaction zone shows ubiquitous small-scale heterogeneities that attend across-strike variation in composition and texture. A marble-rich layer with fragments of calc-silicate and metabasic rocks fringing the marble contact grades into a metabasite layer in which carbonate penetration declines towards the eclogite contact. The study focussed on the metabasite layer since there, garnet and pyroxene are less strongly symplectitized than in the marble-rich mixing layer. Despite the heterogeneity of this layer, the constituent minerals vary little in composition. These minerals include, in order of decreasing average modal content: garnet, clinopyroxene, amphibole, quartz, clinozoisite, and phengite. Symplectite replacing pyroxene and amphibole as well as carbonates are additional major constituents. Biotite, feldspar, and chlorite replacing phengite as well as titanite, rutile, and hematite are accessories. Importantly, both the country-rock marble and the marble-rich layer of the reaction zone contain dispersed fluorite. A sharp decrease in whole-rock

fluorine content from 0.9 wt. % in the marble, on through 0.7 wt. % in the carbonatic layer and 0.3 wt. % in the metabasite layer, to negligible contents in the eclogite monitors fluorine mobility across the reaction zone.

The metabasite layer contains two types of garnet different in grain size. Garnets up to one millimetre in diameter have little variable contents of almandine, grossular, and pyrope in the core that increase slightly outwards within the core to balance a significant gradual decrease in spessartine content. The rims do not differ from the core in almandine content but the grossular content decreases and the pyrope content increases strongly near the rims. A spatially related reversal in the Mn zoning trend slightly increases the spessartine content in the outer rims. The garnets of the second type are smaller by about one order of magnitude and resemble in composition the outer core and rim of the large garnets. A crucial point for determining the evolution common to the country rocks and eclogites is the sequestration of fluorine in the outer core of the large garnets (up to 0.1 apfu) and the core of the smaller ones (up to 0.26 apfu). The clinopyroxenes in the matrix and in inclusions in garnet represent omphacite, those from symplectitic intergrowths with amphibole and plagioclase are omphacite to diopside. The textural relationships suggest four types of amphiboles: matrix, porphyroblastic, symplectitic, and inclusion amphiboles. The matrix and porphyroblastic amphiboles are Mg-rich and correspond in composition to calcic and transitional calcic to sodic-calcic amphiboles, respectively. The fluorine content averages 0.2 apfu in matrix amphibole and may rise to 0.4 apfu in porphyroblastic amphibole. The symplectitic amphiboles represent calcic amphiboles low in Mg and F. The amphibole inclusions in garnet vary widely in composition. All feldspar is symplectitic and either plagioclase overgrown on matrix omphacite and amphibole, or plagioclase and K-feldspar overgrown on phengite. Phengite inclusions in amphibole porphyroblasts have Si contents near 3.5 apfu, with a slight increase towards the rims, whereas matrix phengites display an inverse trend at similar or slightly lower Si contents. The garnet zoning pattern records growth stages, which along with correlated mineral inclusions and matrix minerals define three equilibration stages that preceded symplectite formation during a fourth stage. The inclusion assemblage in the core of the large garnets has yielded P-T estimates of 1.1 GPa and 300-400 °C. Hence, garnet growth either began at very low temperatures or the garnet mixing models used for calculation do not meet the activity-composition relationships in this particular composition and the real temperature was higher at this early stage. The inner garnet rims have equilibrated with matrix omphacite, the highest-Si phengite, and the most Na-rich amphibole. This assemblage constrains the metamorphic peak to P-T conditions of 2.3-2.7 GPa and 530-640 °C. P-T estimates for the outermost garnet rims and the rims of matrix minerals indicate final garnet growth during isothermal decompression to 2.0-2.3 GPa. The symplectites developed when the rocks passed through the P-T range of 1.0-1.3 GPa and 450-600 °C (Fig. 6). Striking evidence that the low-grade precursors of eclogite and marble must have already been in contact comes not only from carbonate-derived fluorine but also calcium sequestration in early metamorphic mineral relics, as shown by more calcic core compositions of garnet in the reaction zone metabasite compared to the adjoining unaltered eclogite. Gross et al. (2008) have concluded from these results that the Mica Schist/Eclogite Unit consists of a high-pressure part affected by the same metamorphism as the intercalated eclogites, and a less deeply subducted part that merged with the partially exhumed first part upon reaching its peak-pressure stage at 1.1-1.3 GPa. However, decompressional heating inferred from the second part is not in evidence either in the eclogites or the studied reaction zone.

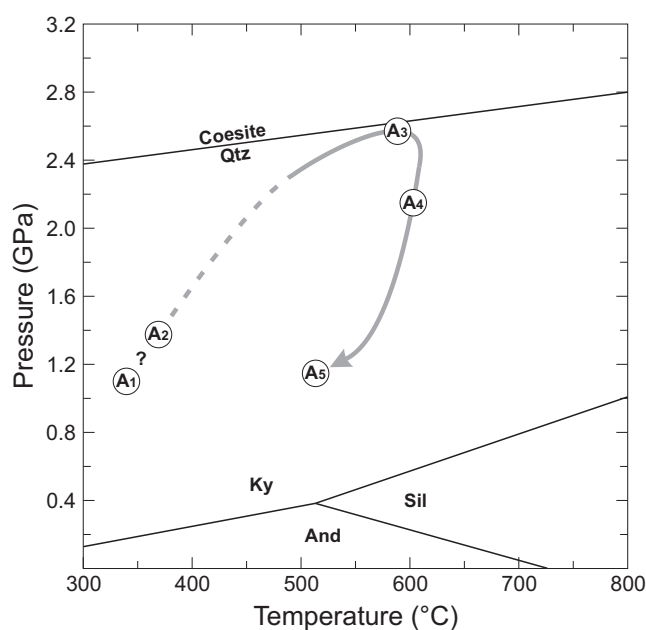


**Fig. 6.** P-T path for the metabasite layer of a calc-silicate reaction zone separating marble and eclogite in the Mica-Schist/Eclogite Unit (Gross et al., 2008): A1, possible P-T conditions for the equilibration of the inner garnet core composition with inclusions of omphacite, amphibole, quartz, clinozoisite, and dolomite; A2, sequestration of marble-derived fluorine in garnet of the metabasite layer; A3, peak of metamorphism, equilibration of the inner garnet rims with omphacite, high-Si phengite (3.5 apfu), and porphyroblastic amphibole corresponding in composition to winchite and barroisite; A4, equilibration of the outer garnet rims with rims of matrix minerals; A5, formation of clinopyroxene-amphibole-plagioclase symplectite.

Major metamorphic discontinuities discovered by Rötzler (1994) below the above-described crustal section have led to divide the Erzgebirge into another three structural units, named from top to bottom: the Gneiss/Eclogite Units I and II, and the Gneiss/Amphibolite Unit (Fig. 7). Inferences as to whether the eclogites from the Gneiss/Eclogite Units I and II, above referred to as the eclogite groups of the north-western and central Erzgebirge, respectively, were contiguous with their host rocks throughout the metamorphism remained ambiguous because the studied predominant rock types record only part of the decompression paths derived from the eclogites. Willner et al. (1997) have focussed on felsic mylonite gneiss and garnet-phengite-quartz schist from localities representing all but one the Gneiss/Eclogite Unit II. These rock types preserve early mineral assemblages and textures useful for assessing the extent to which they, the surrounding rocks, and intercalated eclogites have a common history. According to the geological map of Saxony at scale 1:25 000, nearly anhydrous felsic mylonite gneiss forms a 10 kilometre-long tract as well as lenses up to one kilometre in length surrounded by phengite-bearing felsic gneiss of similar composition, but with a higher degree of retrogression. The geological map, surveyed between 1872 and 1907, classifies these rocks as granulite gneiss and muscovite gneiss, respectively. Both rock types are associated and intercalated with eclogite and locally diamondiferous garnet-phengite-quartz schist. The felsic high-temperature mylonites show relic granoblastic domains, but also gradations into more retrogressed country-rock gneisses defined by biotitization, grain coarsening, and decreasing shape-

preferred orientation. A relic migmatitic texture predating the mylonitisation is present in places (Fig. 8a). The mylonitic layering is concordant with the main S2 foliation of the country rocks in which a relic S1 foliation is evident from rare, rootless intrafolial folds deforming quartz-feldspar layers. The structural features of the Gneiss/Eclogite Units I and II, including an E-W trending stretching lineation on S2 and a locally developed ductile S3 foliation, are consistent with those in the structurally higher units of the Erzgebirge.

Willner et al. (1997) have distinguished the felsic mylonite gneisses by their peak mineral assemblages. The peak assemblage of weakly foliated felsic gneiss observed in low-strain domains between the high-temperature mylonites consists of quartz, K-feldspar, plagioclase, garnet, kyanite, and rutile, and may have originally involved local omphacite, as inferred from the pseudomorphing of a granoblastic mineral by clinopyroxene-plagioclase symplectite. Accessories are rutile, magnetite, pyrite, apatite, zircon, and monazite. Large K-feldspar and plagioclase grains show lamellar or patchy exsolution in the core. Polycrystalline inclusions in garnet surrounded by radial cracks consist of quartz and K-feldspar, partly joined by plagioclase. Prograde white mica and biotite occur as rare inclusions in garnet, kyanite, and in part also in zircon. White mica growing on kyanite and K-feldspar, and biotite growing on white mica and garnet indicate the reappearance of both minerals during retrogression. The second type of felsic mylonite gneiss exhibits a stronger mylonitisation, as indicated by more strongly deformed feldspars with largely obliterated exsolution textures. The major difference with the first type, however, is the presence of phengite, but not kyanite, in the peak assemblage. This primary white mica grown along S2 has partially reacted to form coronitic biotite, biotite-K-feldspar symplectite, or quartz-white mica symplectite. Titanite grows on rutile. The associated garnet-phengite-quartz schist (Fig. 8b) is an unfoliated to weakly foliated, K-feldspar-free metapelite with a larger grain size than the felsic mylonite gneisses (Willner et al., 1997). The matrix assemblage is quartz, phengite, garnet, rutile, and either kyanite or plagioclase. However, the rock at the later-discovered microdiamond locality contains both kyanite and plagioclase. Phengite is partly unaligned, or is S2-parallel as is kyanite. It has inclusions of rutile and ilmenite and displays a mutual inclusion relationship with kyanite. Plagioclase, if present, is a matrix mineral like quartz. Tourmaline, monazite, and zircon are accessories. Garnet occurs as variably sized, mm to cm large, poikiloblasts, which enclose all other matrix mineral phases as well as apatite, pyrite, and rarely biotite and magnetite, partly concentrated in the core and/or aligned along an internal foliation. Rutile included in garnet is more abundant and larger in grain size than matrix rutile. Willner et al. (1997) have interpreted oriented rutile needles embedded in sharply bounded zones of garnet as due to a topotaxial relationship with a Ti-rich precursor mineral. Oriented rutile needles found enclosed in some garnet crystals from the diamondiferous schist are at variance with that, as they are unevenly distributed and spatially associated with inclusions of microdiamond. For the origin of these rutile needles, Hwang et al. (2007) have considered several models, such as i) inheritance from sagenitic biotite, ii) simultaneous growth with the garnet host from Ti-rich biotite, iii) solid-state precipitation from the garnet host and iv) deposition in garnet cleavings during melt infiltration. Since transmission electron microscopy has shown that there is no specific crystallographic relationship between the rutile needles and either a possible biotite precursor or the host garnet, and because the rutile needles do not coexist with pyroxene lamellae required by reaction stoichiometry in case of solid-state precipitation from the garnet host, the preferred model is deposition in garnet cleavings during melt infiltration. The garnet cleavings may have developed during a high strain rate event

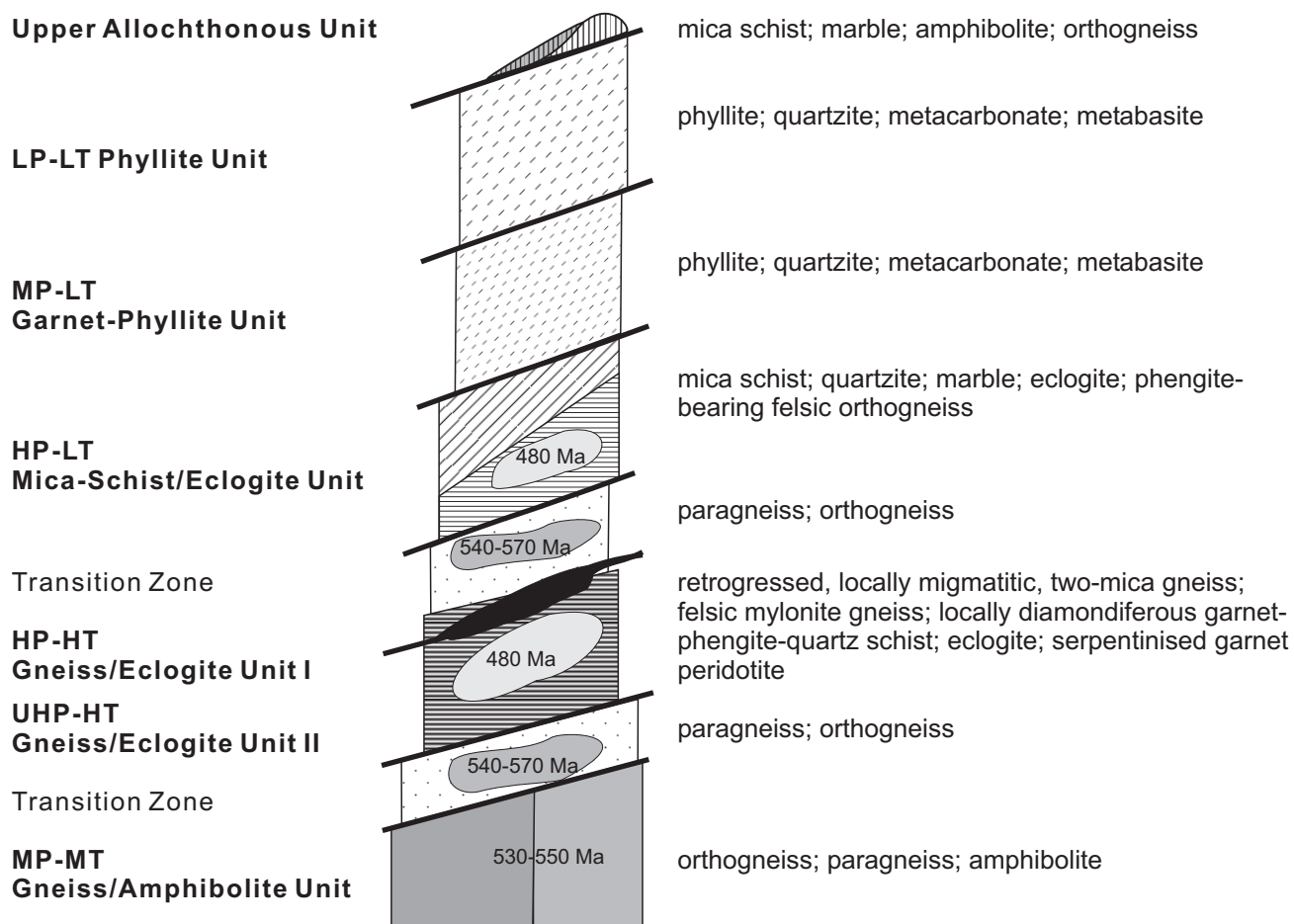


Fig. 7. Schematic cross-section through the crustal stack of the Erzgebirge (Mingram, 1998; Rötzler & Plessen, 2010).

at peak or near-peak metamorphic conditions related with minor partial melting, for instance during formation of pseudotachylite. However, the diamondiferous schist exposed at the Saldenbach Reservoir is conspicuously homogeneous and devoid of any macroscopic partial melts or pseudotachylites (Fig. 8b). Retrograde minerals of the garnet-phengite-quartz schist are biotite produced from phengite or garnet, white mica replacing kyanite, and ilmenite growing on rutile. Retrograde white mica is locally oriented along S3.

Both types of felsic mylonite gneiss and the plagioclase-bearing garnet-phengite-quartz schist have garnet compositions consisting, in order of abundance, of almandine, grossular, and pyrope components. Element X-ray mapping of this garnet has revealed an irregular patchy zoning with a decrease in Ca and an increase in Mg from core to rim at little variable Fe content. The element zoning contours are roughly parallel to the resorbed garnet rims, suggesting diffusion zoning. The feldspar-free garnet-phengite-quartz schist contains garnet with a different, relatively almandine-rich composition (80-92 mol %). Small euhedral grains of a second garnet generation reported to be local overgrowths on the early garnet correspond to a sharp increase in Ca and decrease in Fe contents at constant Mg content compared to the adjacent early garnet (Willner et al., 1997). However, the depicted X-ray maps do not show a second garnet generation, but indicate rather marginal re-equilibration of garnet. Garnet from the diamondiferous schist is similar in composition and zoning to that described above from plagioclase-bearing garnet-phengite-quartz schist, except that pyrope prevails over grossular. Massonne (1999) has distinguished between inner core, outer core, intermediate zone, and rim of this garnet because the core-

rim trend towards lower Ca and higher Mg contents reverses in locally developed garnet rims. The Ti content reaches a maximum in the outer garnet core, whereas microdiamond inclusions, partially pseudomorphed by graphite, occur exclusively in the intermediate zone. Massonne (1999) has interpreted this zoning and inclusion pattern as reflecting growth stages of garnet during pre-peak, syn-peak, and post-peak metamorphism, followed by marginal re-equilibration (Fig. 9). White mica of the felsic mylonite gneisses and the garnet-phengite-quartz schist is mostly phengitic in composition, with Si contents decreasing from maximum values of 3.4-3.3 apfu in inclusion phengite to 3.3-3.2 apfu in the core of matrix phengite and further to 3.15 apfu at the rims of matrix phengite. White mica aligned in S3 has Si contents close to 3.1 apfu. White mica of the diamondiferous schist falls within the same compositional range. Plagioclase shows a core-to-rim increase in anorthite content from albite to sodic oligoclase, and in outermost rims and small matrix grains may have andesine compositions. Plagioclase included in garnet is albite and rarely oligoclase. Based on these mineral assemblages and compositions, Willner et al. (1997) have inferred the following metamorphic evolution: i) Phengite, paragonite, oligoclase, and rutile enclosed in garnet, kyanite, and zircon define a prograde metamorphic stage at P-T conditions of about 1.5 GPa and 650 °C in anhydrous felsic mylonite gneiss. ii) Anhydrous and phengite-bearing felsic mylonite gneisses have yielded maximum P-T estimates of 2.2-2.3 GPa, 830 °C and 1.8-2.1 GPa, 780 °C, respectively. Their different peak assemblages are a result of different water activities estimated at <0.15 and 0.15-0.40, respectively. Peak pressure estimates for garnet-phengite-quartz schist obtained using Ti-muscovite barometry on core compositions of matrix phengite



**Fig. 8.** Rock types and fabrics found in outcrop but mainly in loose blocks at the Saldenbach Reservoir: (a) Garnetiferous felsic mylonite gneiss has thin, isoclinally folded leucosomes (arrows) with axial planes parallel to the main S2 foliation; (b) Medium-grained diamondiferous garnet-phengite-quartz schist is enclosed in felsic mylonite gneiss; (c) Medium-grained, compositionally layered eclogite forms a few large bodies up to 100 m in length and a greater number of thin intercalations within anhydrous mylonitic and more retrogressed types of felsic gneiss; (d) Felsic mylonite gneiss is intercalated with thin eclogite layers that are deformed into pinch-and-swell structures and local boudins. The extensional structures are asymmetric S-C fabrics indicating top-to-the-W shearing (S and C plane orientations shown by white bars); (e) Dark grey quartz lenses up to 1 cm in size are oriented parallel to the C planes of an S-C fabric in felsic mylonite gneiss; (f) Two-mica country-rock gneiss of the high-temperature mylonite area shows a network of leucosomes that formed along the shear planes of an S-C fabric when invading fluids had lowered the solidi for the granitic to tonalitic melts below the ambient temperature. Phengite disseminated in the leucosomes indicates decompression to 0.8-0.9 GPa at this stage (Willner et al., 1997).

are in the wide range of 1.2-2.4 GPa at assumed temperatures of 700-800 °C. This rock type maintained a high water activity  $>0.4$  during peak metamorphism. iii) Clinopyroxene-plagioclase symplectite found in anhydrous felsic mylonite gneiss developed after decompression to 1.5-1.7 GPa at temperatures of 745-780 °C. iv) Retrograde phengite grown during fluid influx into the felsic mylonite gneisses has yielded pressure estimates of 1.2-1.3 GPa at an assumed temperature of 700 °C. At this stage the water activity had risen to  $>0.5$ , reaching values as high as 0.8-1.0 in strongly retrogressed rocks, where granitic to tonalitic partial melts (Fig. 8f) appeared when the solidi for these melts, increasingly lowered by the invading fluids, had fallen below the ambient temperature. The wet granite and tonalite solidi intersect the Si isopleth for phengite from the leucosomes at P-T conditions of 0.8-0.9 GPa and 650-700 °C. v) The S3 mineral assemblages of the felsic mylonite gneisses and fluid inclusions trapped therein indicate cooling through 500 °C at pressures in the range of 0.25-0.4 GPa. These P-T data match those for the S3 assemblages in the Mica-Schist/Eclogite Unit (see above), suggesting that the contrastingly metamorphosed ultrahigh- to high-pressure units had arrived in the upper crust and were juxtaposed against each other.

The discovery of diamond in garnet-phengite-quartz schist of the Gneiss/Eclogite Unit II has turned the question as to whether the country rocks underwent the same peak metamorphism as the enclosed eclogites upside down because the diamondiferous schist indicates higher pressure conditions than the associated eclogite. In an attempt at determining burial and exhumation rates as constraints for tectonic inferences, Massonne et al. (2007) used SHRIMP U-Pb zircon and monazite geochronology for dating the metamorphic stages of the diamondiferous schist (Fig. 9). The diamond inclusions averaging 10  $\mu\text{m}$  in size and reaching a maximum size near 30  $\mu\text{m}$  are most plentiful in zircon, followed by garnet, kyanite, and rarely rutile and monazite (Nasdala and Massonne, 2000). Cathodoluminescence (CL) images and Th/U ratios show that the zircon consists of three distinct zones: i) the low-CL core zone with  $\text{Th}/\text{U} \leq 0.023$ , ii) the diamondiferous intermediate zone with moderate CL intensity and  $\text{Th}/\text{U} \geq 0.037$ , and iii) the high-CL rim zone with  $\text{Th}/\text{U} = 0.015\text{-}0.038$ . In addition, there are rare oscillatory zoned zircon cores with  $\text{Th}/\text{U} \geq 0.8$ , i.e. far above 0.3-0.4 typically considered as lower limit for magmatic zircon. These cores have slightly discordant ages near 400 Ma interpreted as dating magmatism in the provenance area of the sedimentary protolith. Striking evidence that the diamondiferous schist is metasedimentary in origin comes from the diamond  $\delta^{13}\text{C}$  value of -28 ‰ (relative to the PDB standard) indicating formation from biogenic carbon (Massonne, 2005). The detrital zircon cores constrain a Lower Devonian or younger protolith age of the diamondiferous schist. The metamorphic low-CL zircon cores contain inclusions of prograde low-Ti garnet and jadeitic clinopyroxene. Hence, their age of  $337 \pm 2.7$  Ma corresponds to a pre-peak metamorphic stage. Phengite dehydration melting during peak metamorphism at P-T conditions  $\geq 5$  GPa and  $>1050$  °C produced voluminous silicate melt or supercritical COH silicate fluid that corroded the pre-existing zircon and ascended rapidly, thereby cooling adiabatically. The intermediate zircon zone dated at  $336.8 \pm 2.8$  Ma crystallised from the ascending crystal-melt mush/fluid still at ultrahigh-pressure conditions, as shown by microdiamond inclusions, but did not develop oscillatory zoning or Th/U ratios  $>0.3$  typical for magmatic zircon. Diamond floating free in the magma or, after solidification, occurring free in the matrix likely changed into graphite once the pressure had dropped below ultrahigh-pressure conditions. The thin, locally developed, high-CL zircon rims dated at  $330.2 \pm 5.8$  Ma and monazite dated at  $332.4 \pm 2.1$  Ma formed from invading or internally derived fluid concurrent with re-equilibration of the matrix assemblage

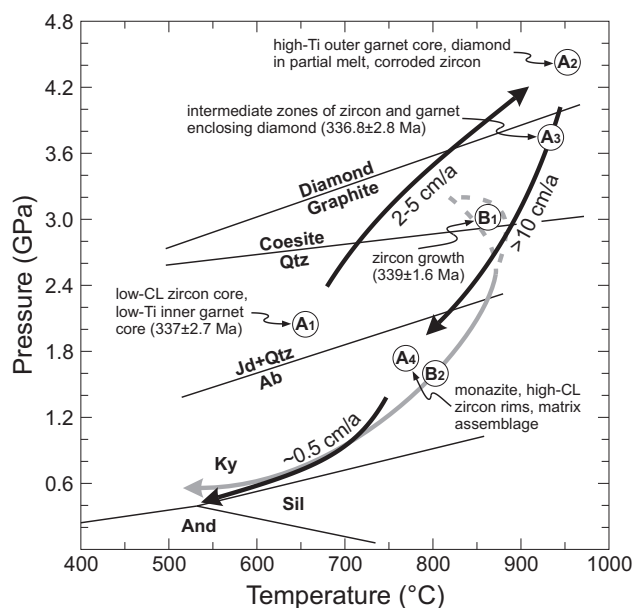


**Fig. 9.** P-T paths proposed for diamondiferous garnet-phengite-quartz schist and eclogite from the Gneiss/Eclogite Unit II. The metamorphic stages of the diamondiferous schist (path A; Massonne, 1999; Massonne et al., 2007) are: A1, approximate equilibration conditions for the inclusion assemblage in the inner garnet core and the zircon core, correlated with the age of  $337 \pm 2.7$  Ma obtained from metamorphic zircon cores; A2, growth of outer garnet core at highest attained Ti solubility in garnet, phengite dehydration melting, formation of diamond from partial silicate melt or supercritical COH silicate fluid, and corrosion of zircon during peak metamorphism; A3, crystallisation of phengite, minor K-feldspar, and the intermediate zircon zone from rapidly ascending ( $>10$  cm/year) crystal-melt mush at  $336.8 \pm 2.8$  Ma, along with introduction of diamond inclusions into the simultaneously growing intermediate zones of zircon and garnet; A4, re-equilibration of the matrix assemblage after solidification of melt, accompanied by growth of zircon rims ( $330.2 \pm 5.8$  Ma) and monazite ( $332.4 \pm 2.1$  Ma) from invading or internally derived fluid. For the metamorphic stages of the eclogite (path B; Schmädicke et al., 1992), see Fig. 2. Eclogite enclosed in the same body of anhydrous felsic mylonite gneiss as the diamondiferous schist underwent peak metamorphism at  $339.0 \pm 1.6$  Ma (von Quadt & Günther, 1999).

at P-T conditions of 1.5-1.8 GPa and 700-750 °C. The burial is assumed at rates of 2-5 cm/year, whereas exhumation as crystal-melt mush occurred at rates  $>10$  cm/year until the melt solidified after decompression to 1.5 GPa. Final exhumation from the base of thickened orogenic crust occurred at an estimated rate of about 0.5 cm/year (Fig. 9).

The crustal structure of the Erzgebirge is further complicated in that the stack of Variscan low- to ultrahigh-pressure units overlies reworked Cadomian basement rocks that underwent Variscan medium-pressure metamorphism at P-T conditions of 0.6-0.8 GPa and 620-650 °C (Rötzler, 1994; Rötzler and Plessen, 2010). This lowermost unit, referred to as the Gneiss/Amphibolite Unit, represents the deepest exposed structural level not only in the Erzgebirge but also in the wider Saxothuringian Zone. It consists of granodioritic, locally garnet-bearing, two-mica orthogneiss, and minor paragneiss. Some intercalated bodies

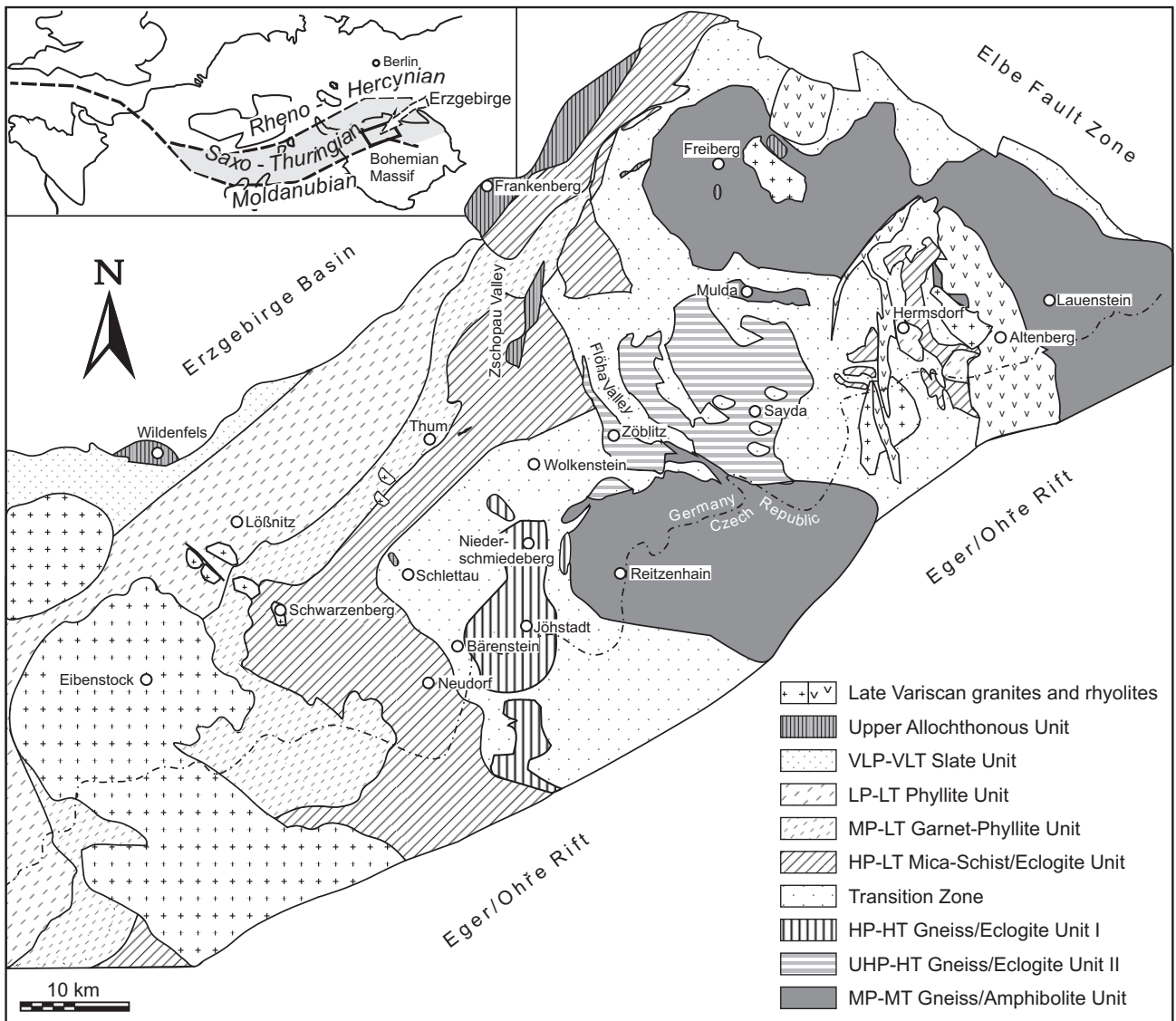


**Fig. 10.** Schematic geological map of the Erzgebirge (Rötzler & Plessen, 2010).

of garnet amphibolite are mostly difficult to allocate to one or another structural unit, as they occupy the shear zone between the Gneiss/Amphibolite Unit and the overlying ultrahigh- to high-pressure units, thus representing either prograde metamorphosed medium-pressure amphibolites of the Gneiss/Amphibolite Unit or retrogressed eclogites of the hanging-wall units. Figure 10 shows a schematic geological map outlining the outcrop areas of all structural units of the Erzgebirge.

Mingram (1998) analysed the major, trace, and rare-earth element compositions of 250 representative outcrop and drill-core samples taken from siliciclastic metasediments in all structural units of the Erzgebirge. The sample set included aluminous to siliceous metapelites, quartzites, and metagreywackes. The study aimed to identify typical geochemical signatures of the variably metamorphosed rocks in order to establish a chemostratigraphic correlation with non- to weakly metamorphosed rocks of a reference section and to gain information regarding geotectonic setting and environmental conditions in the source area of the protoliths. The reference section from the Schwarzburg Anticline, about 80 kilometres to the west of the Erzgebirge, exposes mainly siliciclastic sedimentary rocks, which document a transition from Neoproterozoic syn-orogenic deposition at an active continental margin to Cambro-Ordovician rift-related deposition on a passive

continental shelf. The Neoproterozoic greywacke-shale turbidite sequence contrasts with the highly mature and, thus, chemically distinct Cambro-Ordovician shale-sand sequence. The modal and chemical compositions of the rocks change systematically through the section, with a reversal corresponding to extreme sediment maturity in the Tremadocian-Arenigian Frauenbach Group, where detrital feldspar has totally vanished and heavy minerals are most abundant. The conspicuous modal composition of the Frauenbach Group rocks translates into high  $K_2O/Na_2O$  ratios (~30), high  $Al_2O_3/Na_2O$  ratios (~80), and high Rb/Sr ratios (~12). The Tremadocian to Arenigian sediments, piled up to a thickness of about 3200 metres, record fast subsidence and deposition in the Lower Ordovician. The sedimentation rate subsequently slowed down, as indicated by a thickness of only 600 metres for Arenigian to Ashgillian black shale intercalated with sand and chamositic iron ore. These rocks and the variably metamorphosed metasediments of the Erzgebirge show a statistically significant correlation of their geochemical fingerprints, which allows identifying the stratigraphic units from the reference section in the Erzgebirge crustal stack. The feldspar-free, feldspar-bearing, and graphite-bearing metapelites recurring in all structural units of the Erzgebirge from the Phyllite Unit down section to the Gneiss/Eclogite Unit II correspond, respectively, to the Tremadocian-

Arenigian Frauenbach Group, the Arenigian Phycodes Group, and the Arenigian-Ashgillian Gräfenenthal Group of the reference section. The proved multiple recurrence of stratigraphic section within the stack of contrastingly metamorphosed structural units makes the former stratigraphic correlation chart for the Erzgebirge and the lithostratigraphic units defined therein (Lorenz and Hoth, 1990) obsolete.

Isotopic dating has yielded the following age constraints on the above evolution: i) The orthogneiss protoliths from the Gneiss/Amphibolite Unit reflect continental arc magmatism at the Cadomian active margin of Gondwana ca. 550-530 Ma ago (Tichomirowa et al., 2001). ii) Felsic and mafic meta-igneous rocks occurring in all units from the Mica-Schist/Eclogite Unit down section to the Gneiss/Amphibolite Unit (Fig. 7) document Cambro-Ordovician rift-related magmatism in the continental shelf of Gondwana ca. 495-458 Ma ago (Kröner and Willner, 1998; Mingram and Rötzler, 1999; von Quadt and Günther, 1999; Tichomirowa et al., 2001; Mingram et al., 2004). iii) U-Pb and Pb-Pb zircon ages on felsic mylonite gneiss, garnet-phengite-quartz schist, and eclogite constrain the time of peak metamorphism in the Gneiss/Eclogite Unit II to ca. 344-337 Ma (Kröner and Willner, 1998; Mingram and Rötzler, 1999; von Quadt and Günther, 1999; Massonne et al., 2007). Ar-Ar and Rb-Sr mica ages on metamorphic rocks correspond to two clusters of ages around 340 Ma and 330 Ma (Tikhomirova et al., 1995; Werner, 1998; Werner and Lippolt, 2000). These age clusters alternate through the crustal section, dividing it into four zones. The older ages come from the first zone, represented by the Phyllite Unit, and the third zone. The latter comprises the Mica-Schist/Eclogite Unit and the Gneiss/Eclogite Unit I, which have yielded both clusters of ages. The second zone (Garnet-Phyllite Unit) and the fourth zone (Gneiss/Eclogite Unit II and Gneiss/Amphibolite Unit) show the younger ages. Werner (1998) and Werner and Lippolt (2000) have related this age distribution pattern to a crustal indenter with cooling age of ca. 340 Ma that invaded, at ca. 330 Ma, a crustal segment in which reheating prior to 330 Ma obscured an identical early cooling history. A different interpretation proposed by Rötzler and Plessen (2010) takes into account that white mica, due to the difference in peak temperature between the metamorphic units, was stable in the high-pressure units, but had disappeared in the ultrahigh-pressure unit during peak metamorphism at ca. 340 Ma (cf. Schmädicke et al., 1992; Willner et al., 1997; Massonne et al., 2007). As a result, the ultrahigh-pressure unit has only exhumation-related retrograde white mica dated at ca. 330 Ma, whereas the high-pressure units preserve both peak-metamorphic and retrograde white micas. The coexistence of different white mica ages in the same unit as well as the overlap in age between peak-metamorphic white mica and metamorphic zircon from different units argue that the mica ages refer to formation rather than cooling (cf. Romer and Rötzler, 2011). Werner (1998) has found also significantly older apparent Ar-Ar ages of up to 383 Ma, which suggest either the presence of older metamorphic rocks or mixing of metamorphic with relic inherited Ar components. For instance, orthogneiss from the Gneiss/Amphibolite Unit may retain inherited Ar components because a comparison with unmetamorphic equivalents from the Lusatian Block suggests that the protoliths had primary magmatic muscovite (Hammer, 1996). This would have implications for the disputed intrusive (Kröner et al., 1995) or subautochthonous anatectic (Tichomirowa et al., 2001) nature of the rocks. Muscovite can crystallise from H<sub>2</sub>O-saturated granitoid melt only in the pressure range above 0.4 GPa, where the temperature of muscovite-forming reactions is above the wet granite solidus, but does not form at lower pressures, where a cooling granitoid magma solidifies before muscovite can grow (Spear et al., 1999). Primary magmatic muscovite in Cadomian granitoids surrounded by country rocks that lack evidence of Ca-

domian regional metamorphism necessarily implies an intrusive nature of the granitoids.

## Eurogranites 2012

### Stop 3-1

Forchheim – Saidenbach Reservoir

Gneiss/Eclogite Unit II

Coordinates: lat.: 50°43'36"N, long.: 13°14'43"E,  
455 m a.s.l.

Guide: Jochen Rötzer

This stop examines rocks from the Gneiss/Eclogite Unit II exposed in outcrop and as boulders at the Saidenbach Reservoir to the west of Forchheim. The Saidenbach Reservoir covers an area of ca. 1.5 square kilometres, which makes it the largest artificial lake in the central Erzgebirge. The reservoir was constructed be-

tween 1929 and 1933 at a cost of Reichsmark 21.5 million (ca. Euro 88 million) to supply raw water to waterworks delivering the city of Chemnitz and southern Saxony with drinking water. It also reduces the danger of floods and serves for hydro-electricity generation. The reservoir has a catchment area of about 61 square kilometres, where land use is restricted to avoid contamination. Bathing and water sports are strictly prohibited in the reservoir, as is public access to the waterside. However, the reservoir management has granted us permission to enter the protected zone, reminding all participants to take care not to pollute the area. A reservoir officer will accompany us to supervise the compliance with the regulation. The water level in the reservoir changes depending on seasonal precipitation rate and surplus discharge, with the result that boulders widely present along the shoreline that provide most of the insight the area holds can submerge for extended periods of time. We will walk over a distance of 3 km (way there and back again) from the crossroads in Forchheim to the Haselbach Bay of the reservoir. The walking route passing boulders, clearance cairns, and a large crag enables us to observe major rock types and structures independent of the flow conditions in the reservoir. When climbing the large crag sticking out into the water, please mind the steep faces and take care of other persons.

On our way to the reservoir, we will encounter the first small boulders along a forest road that begins west of two small auxil-

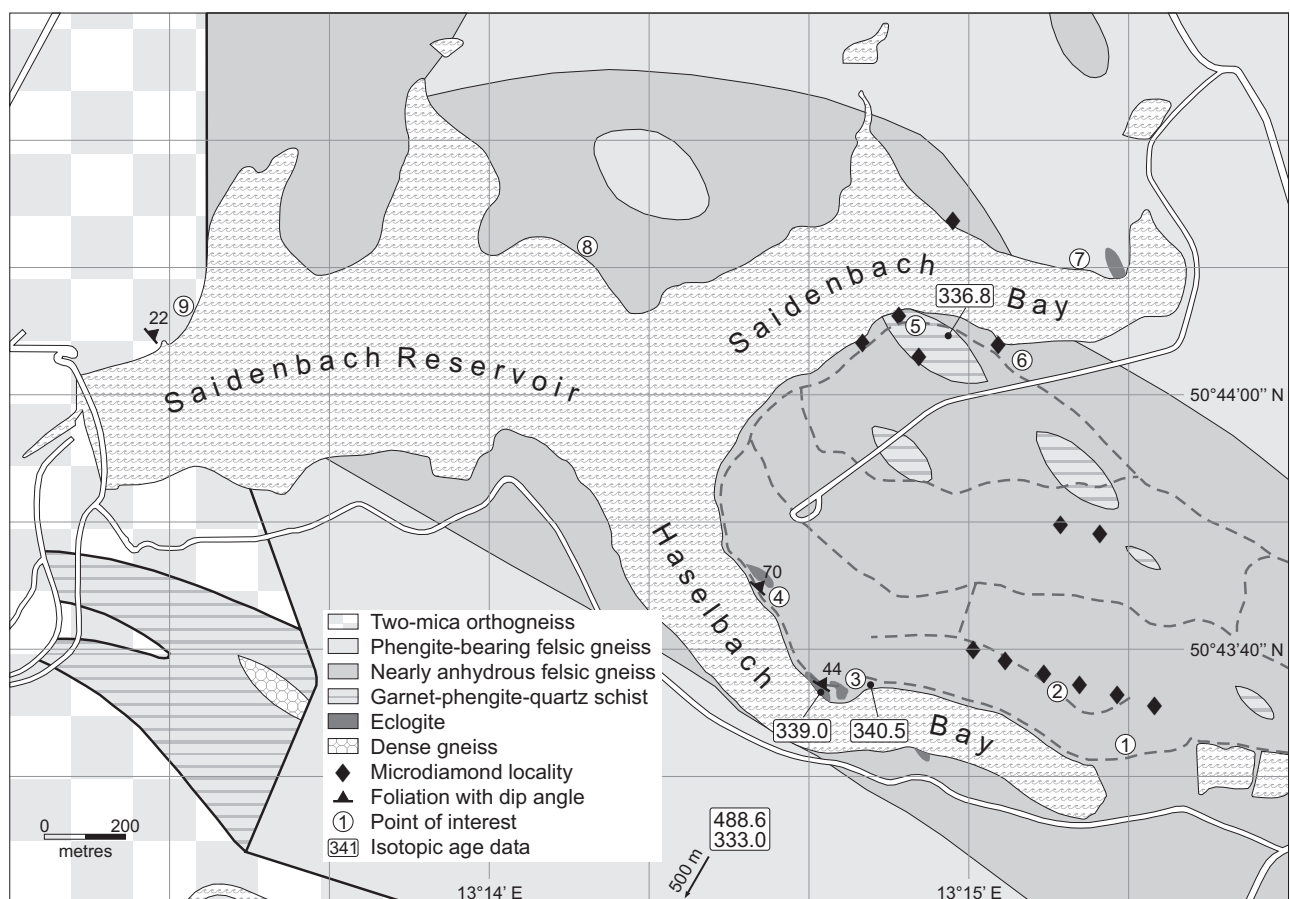


**Fig. 11.** Geology of the Saldenbach Reservoir area (Gneiss/Eclogite Unit II) based on the geological map of Saxony at scale 1:25 000, Sheet 116, except for the omission of alluvial deposits. The age data of  $340.5 \pm 1.1$  Ma (Pb-Pb zircon evaporation method),  $339.0 \pm 1.6$  Ma (conventional U-Pb single-zircon dating, concordant age), and  $336.8 \pm 2.8$  Ma (concordant SHRIMP U-Pb age of decompression-related intermediate zircon zone) are from Kröner & Willner (1998), von Quadt & Günther (1999), and Massonne et al. (2007), respectively. Pb-Pb zircon evaporation dating of migmatitic orthogneiss quarried outside of the map area at Görsdorf has yielded a protolith age of  $488.6 \pm 1.9$  Ma (Mingram et al., 2004). Ar-Ar white mica dating of the same rock has provided a step-heating age of  $333.0 \pm 1.6$  Ma (Werner, 1998). The microdiamond localities are from Massonne (2001).

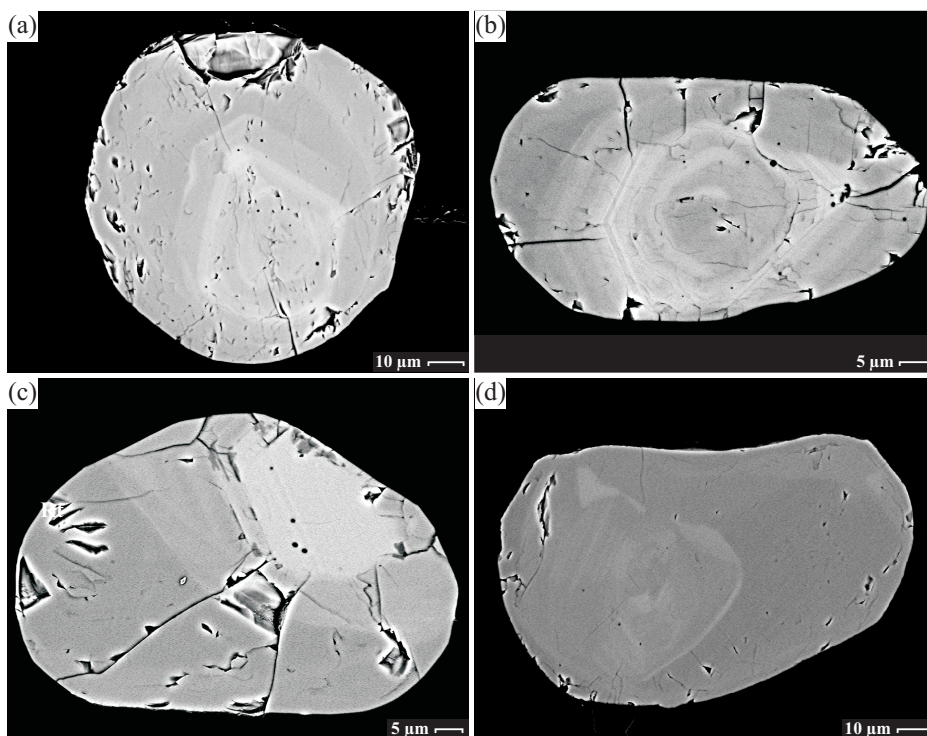


**Fig. 12.** BSE images of stubby to near-spherical, sector-zoned, metamorphic zircon grains from anhydrous felsic mylonite gneiss exposed at the Saidenbach Reservoir (at point 3 in Fig. 11). Four grains of this zircon population, dated using the Pb-evaporation technique, have yielded a mean age of  $340.5 \pm 1.1$  Ma (Kröner & Willner, 1998).

ary dams (point 1 in Fig. 11). These boulders of light-coloured felsic mylonite gneiss with a reddish cast from abundant garnet imply retrograde alteration of anhydrous to biotite-bearing mineral assemblages. The S2 mylonitic foliation overprints a relic migmatitic texture. Biotite-bearing quartz-feldspar pegmatite occurs in centimetre-size patches cutting the mylonitic foliation but also in boulders consisting solely of this rock type. Shortly after passing a gate, we will climb the slope up to the edge of the forest. On the way up, there are boulders of garnet-bearing felsic gneiss with variably developed mylonitic foliation and local biotite overgrowths. Field clearance cairns extending along the edge of the forest (point 2 in Fig. 11) provide additional insight into this rock type, and with some luck you will there find a specimen of diamondiferous garnet-phengite-quartz schist (Fig. 8b). The excursion then moves downhill to a large crag sticking out into the water (point 3 in Fig. 11). Fine-grained anhydrous felsic gneiss with abundant garnet that constitutes the eastern side of this crag is light yellowish grey in colour with a reddish hue. The S2 mylonitic foliation dips moderately steep to the NNE and deforms an older migmatitic layering into recumbent isoclinal folds (Fig. 8a). The felsic gneiss encloses a sheet-like body of medium-grained eclogite, about 100 metres long, which crops out in the middle and western parts of the crag. The contact of the rocks is sharp but not even, as discernible in the middle of the crag on a joint surface that intersects the contact repeatedly. The eclogite locally displays compositional layering defined by variation in the abundance of garnet (Fig. 8c).

The following problems arise regarding the rocks exposed at the Saidenbach Reservoir:

i) Eclogite and diamondiferous schist occurring in close proximity but not in direct contact to each other have yielded zircon ages of  $339.0 \pm 1.6$  Ma and  $336.8 \pm 2.8$  Ma, respectively, interpreted as dating peak and early post-peak ultrahigh-pressure metamorphism (von Quadt and Günther, 1999; Massonne et al., 2007). Consequently, both rocks have, within error limits, the same age of peak metamorphism and, moreover, their post-peak evolution, starting at least from ultrahigh-pressure conditions in the coesite stability field, followed similar P-T paths (Fig. 9). The solid eclogite would thus have ascended as fast as magma pods

assumed to have eventually solidified to form the diamondiferous schist (Massonne et al., 2007).

ii) Garnet of the diamondiferous schist displays smooth element gradients across compositional zones interpreted as indicating pre-peak, syn-peak, and post-peak growth under contrasting subsolidus to high-degree partial melting conditions, followed by marginal re-equilibration after cooling through the solidus temperature (Massonne et al., 2007). The anhydrous felsic mylonite gneiss intercalated with the diamondiferous schist has garnet with a similar but patchy zoning pattern suggesting diffusional modification well into the garnet core that occurred at temperatures not above 830 °C (Willner et al., 1997), whereas the admittedly coarser grained garnet of the diamondiferous schist would have largely escaped such a modification, despite temperatures above 1050 °C.

iii) Zircon of the diamondiferous schist has a diamond-bearing intermediate zone interpreted to be magmatic in origin, but the Th/U ratio and the lack of oscillatory zoning in this zone are untypical for magmatic zircon (Massonne et al., 2007).

iv) The anhydrous felsic mylonite gneiss contains stubby to near-spherical zircon grains (Fig. 12) dated at  $340.5 \pm 1.1$  Ma (Kröner and Willner, 1998). This metamorphic zircon has grown at P-T conditions of 2.2-2.3 GPa and 830 °C (Willner et al., 1997), obviously concurrent with low-degree partial melting. Long-oval zircon grains from the same rock interpreted as detrital have given Neoproterozoic ages. Therefore, Kröner and Willner (1998) have assumed a sedimentary protolith, contrary to an earlier classification as orthogneiss (Willner et al., 1997). However, this rock type is indistinguishable in geochemistry and isotope signature from felsic orthogneiss that has yielded a wide range of zircon ages extending from Meso- to Neoproterozoic inheritance ages to Cambro-Ordovician magmatic ages (Mingram et al. 2004). It is thus likely that the study by Kröner and Willner (1998) did not gather the igneous zircon.

We take the forest road along the waterside to return from the crag back to Forchheim.

## Eurogranites 2012

### Stop 3-2

Ansprung – Pionierweg/Vogeltoffelfelsen

Gneiss/Amphibolite Unit

Coordinates: lat.: 50.638°N, long.: 13.247°E,  
725 m a.s.l.

c. 1.5 km east of Pobershau

Guide: Uwe Kroner

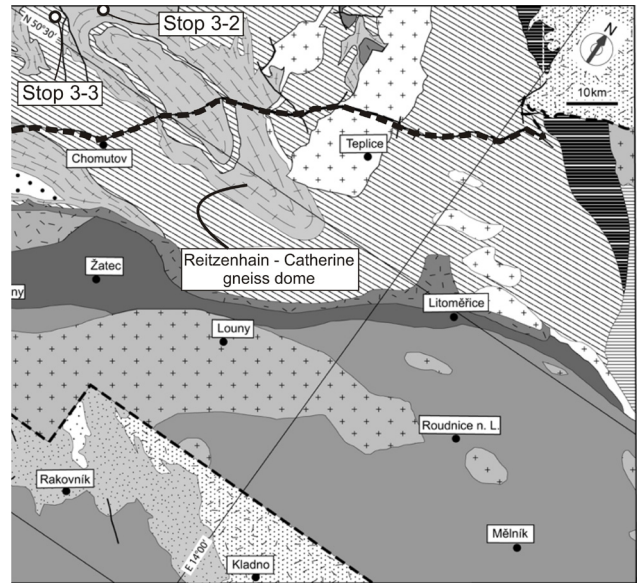


**Fig. 14.** The Reitzenhain – Catherine gneiss dome is part of the lowermost allochthonous unit of the Erzgebirge mantled by mylonitic gneisses and overlain by (U)HP metamorphic units. Note that south of the Erzgebirge Fault (stippled black line) the gneiss dome is covered by the Cenozoic cover of the Eger rift. Stop 3-2 and 3-3 are highlighted. (same source as Fig. 13, for geological units see Fig 13).

The outcrop „Vogeltoffelfelsen“ belongs to the Reitzenhain–Catherine gneiss dome of the Central Erzgebirge. It constitutes an E-W elongated c. 50 by 20 km large crystalline complex. Due to the Cenozoic cover of sedimentary and volcanic rocks of the Eger-valley rift, only c. 50% of the structure is exposed. Mapping of the basement of the Eger rift using the record of numerous exploration borehole data, however, reveals the actual shape of the domal structure (Mlcoch and Konopasek, 2010) (Figs. 13 and 14). The Reitzenhain–Catherine gneiss dome belongs to the lowermost unit of the Erzgebirge crystalline complex, the MP-MT Gneiss-Amphibolite Unit (Rötzler and Plessen, 2010). The

protoliths of this unit represent predominantly magmatic rocks formed during the Neoproterozoic – Early Cambrian Cadomian orogeny and the subsequent Cambro-Ordovician extensional

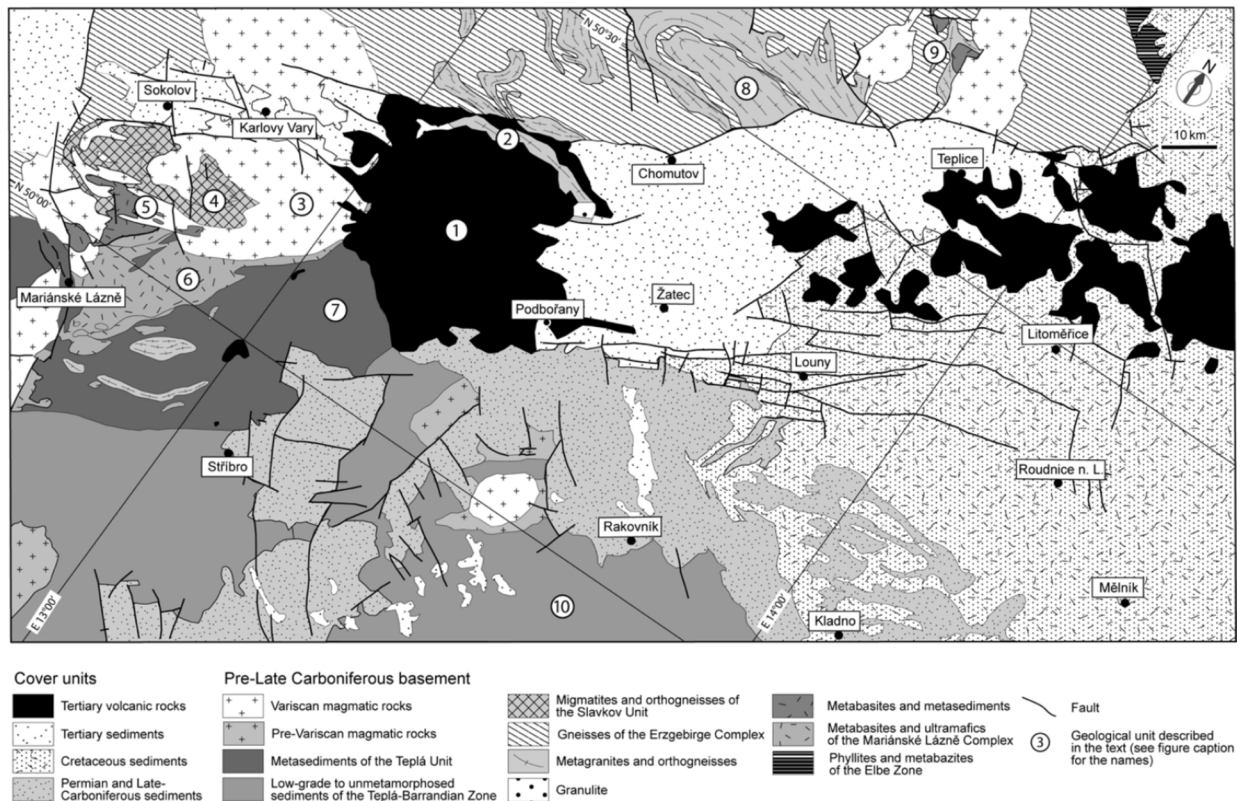


**Fig. 13.** Geological map of the northwestern part of the Bohemian Massif with post-Lower Carboniferous cover of volcanic and sedimentary rocks (Mlcoch and Konopasek, 2010). Numbered geological units: **1** Doupov Volcanic Complex, **2** Eger Unit, **3** Nejdeč-Eibenstock Pluton, **4** Slavkov Unit, **5** Kladská Unit, **6** Mariánské Lázně Complex, **7** Teplá Crystalline Unit, **8** Reitzenhain – Catherine gneiss dome, **9** Altenberg Block, **10** Barrandian Complex.

stage. The adjacent voluminous gneiss complexes of the eastern Erzgebirge represent a late Cadomian magmatic stage (~540 Ma) whereas the protolith of the Reitzenhain–Catherine gneiss dome is interpreted as an intra-Ordovician batholith intruded at c. 470 Ma (Tichomirowa et al., 2012). The gneiss dome consists of reddish orthogneiss preserving the magmatic fabric in low-strain domains (Mlcoch and Schulmann, 1992). The strain increases towards the outer parts of the orthogneiss. The envelope is formed by mylonitic gneiss. During the Variscan orogeny the Gneiss-Amphibolite Unit experienced a metamorphic overprint not exceeding 6-8 kbar and c. 650°C. Contrastingly, eclogites, ortho- and paragneisses as well as lenses of garnet serpentinites exposed in the hanging wall of the mantled gneiss dome indicate Variscan (~340 Ma) (ultra)-high pressure event (Rötzler and Plessen, 2010 and references therein). The juxtaposition of metamorphic units derived from a continental subduction zone against units that experienced only crustal thickening is one of the most striking features of the Allochthonous Domain (*sensu* Kroner et al., 2007) of the Saxo-Thuringian Zone. Nearly vertical isothermal exhumation along the Moldanubian subduction zone followed by W-NW directed lateral extrusion of the (U)HP units in an already existing nappe pile is seen as the primary cause for the complexity of the Allochthonous Domain of Saxo-Thuringia (Kroner and Görz, 2010; Kroner et al., 2007; Kroner and Romer, 2010).

The outcrop exhibits the xz-plane of a ductile shear zone illustrating the progressive transformation of the magmatic fabric of the protolith into a fine-medium grained, mylonitic orthogneiss with a subhorizontal foliation. The deformation occurred under general shear conditions, i.e., a combination of simple and pure shear. Magmatically zoned Carlsbad-twinned K-feldspar phenocrysts behave as porphyroclasts in the shear zone, whereas quartz is pervasively dynamically recrystallized. Fabric asymmetries like sigma-structures and shear bands indicate a simple shear component of the hanging wall to the WNW. Ptygmatic folds of initially vertical oriented aplitic dikes prove the coeval pure shear component. Abundant xenoliths of the pre-Variscan granite display the progressive deformation in the shear zone by its increasing aspect ratio. A continuous transition from ductile to brittle-ductile and to brittle behavior during the shearing can be observed. For the Erzgebirge as well as the Saxon granulites this tectonic style is typical for the final tectonometamorphic overprint.

## Eurogranites 2012

### Stop 3-3

#### Am Hirtstein near Satzung

#### Tertiary platform re-activation and volcanism (Neptunism)

Coordinates: lat.: 50.537°N; long.: 13.193°E;  
840 m a.s.l.

#### Guide: Uwe Kroner

The famous “Palmwedel” (palm leaf) of the Hirtstein is named after the spectacular columnar jointing of the former small scale lava dome. Petrographically the volcanic rocks are augite-nephelinites that belong to the magmatic suite of the Cenozoic Eger Rift. The rifting process is related to Late Cretaceous – Tertiary tectonics affecting large areas of Central Europe. NE-SW compression led to the inversion of Late Paleozoic-Mesozoic basins and to basement uplifts (Kley and Voigt, 2008). In the Tertiary localized NW-SE extension, i.e., perpendicular to the overall compression, initiates the Eger rift leading to voluminous magmatism. Typical volcanics are olivine-augite basalts, nepheline-basanites, phonolites, olivine-augite nephelinites and olivine-melilitites. Topographically the Erzgebirge constitutes a tilted Cretaceous peneplain that is actually the NW graben shoulder of the rift structure. Tertiary volcanic rocks partly form the topographic highs of the Erzgebirge. At fair weather, two basaltic hills namely the Pöhlberg and the Bärenstein are visible from the Hirtstein.

These two localities are famous in the context of the geoscientific battle between neptunists and plutonists in the late 18<sup>th</sup> century. Through the Bärenstein and Pöhlberg sections, three principal rock types are exposed. The crystalline basement of the Erzgebirge is overlain by gravel that in turn is covered by columnar jointed basalt, displaying an undisturbed stratigraphic sequence.

Using these outcrops, Abraham Gottlob Werner (1749-1817), as the leading German mineralogist and geologist at that time and next to Johann Wolfgang Goethe the most famous neptunist, argued that basalt constitutes a sediment that precipitated from an ocean or is the expression of burned coal beds. Furthermore, Werner believed that active volcanoes just occur in the proximity of coal seams burning at deeper stratigraphic levels. Most probably, Werner never left Saxony and, thus, had no reason to change his mind. The neptunism theory was contested by James Hutton, the founder of uniformism, who published observations from volcanic islands in 1788. Nonetheless, neptunists proposed their theory until the beginning of the 19<sup>th</sup> century. The dispute between the two schools of thinking lasted over decades.

Actually, the Pöhlberg and Bärenstein locations are great examples for relief inversion. At both sites, lava flows were emplaced along incised river beds. Subsequent erosion led to the recent morphology.

## Eurogranites 2012

### Stop 3-4

Kühberg – northern environs

Gneiss/Eclogite Unit I

Coordinates:

lat.: 50°31'40.6"N, long.: 13°02'16.5"E,  
780 m a.s.l.

Guide: Jochen Rötzer

This stop presents kyanite-bearing garnet-phengite-quartz schist from the Gneiss/Eclogite Unit I occurring at an elevation to the north of Kühberg. For details about this rock type, see Overview. Our walking route from the sports ground in Kühberg to the top of the forested elevation and back again is about 2 km long

(arrows in Fig. 15). At the edge of the forest, where the forest road branches off, we will take the left fork that runs straight on through an area with scattered small boulders of diverse rock types, such as light grey, medium-grained garnet-phengite-quartz schist, garnet-two-mica schist, and biotite-bearing quartz-feldspar pegmatite (point 1 in Fig. 15). When the forest road reaches its highest point, we will take the branch to the right that is flanked by boulders consisting, as before, of garnet-phengite-quartz schist and garnet-two-mica schist but also of coarse milky quartz mobilised from the metapelites (point 2 in Fig. 15). A little further away there are small boulders of phengite-bearing felsic gneiss (point 3 in Fig. 15). Overlooking the area is a large crag of garnet-phengite-quartz schist with gently east-dipping foliation (point 4 in Fig. 15). The feldspar-free Fe-Al rich metapelite shows striking geochemical and isotopic similarities with the Frauenbach Group of the Schwarzburg Anticline (Mingram, 1998), which suggests a protolith age in the Lower Ordovician. Ti-muscovite barometry on core compositions of matrix phengite has yielded a pressure estimate of 2.0 GPa at an assumed temperature of 700 °C (Willner et al., 1997). Ar-Ar white mica ages for the garnet-phengite-quartz schist and granitoid augengneiss exposed nearby constrain the time of peak metamorphism at  $341.4 \pm 2.3$  Ma and  $339.8 \pm 3.4$  Ma, respectively (Werner, 1998).

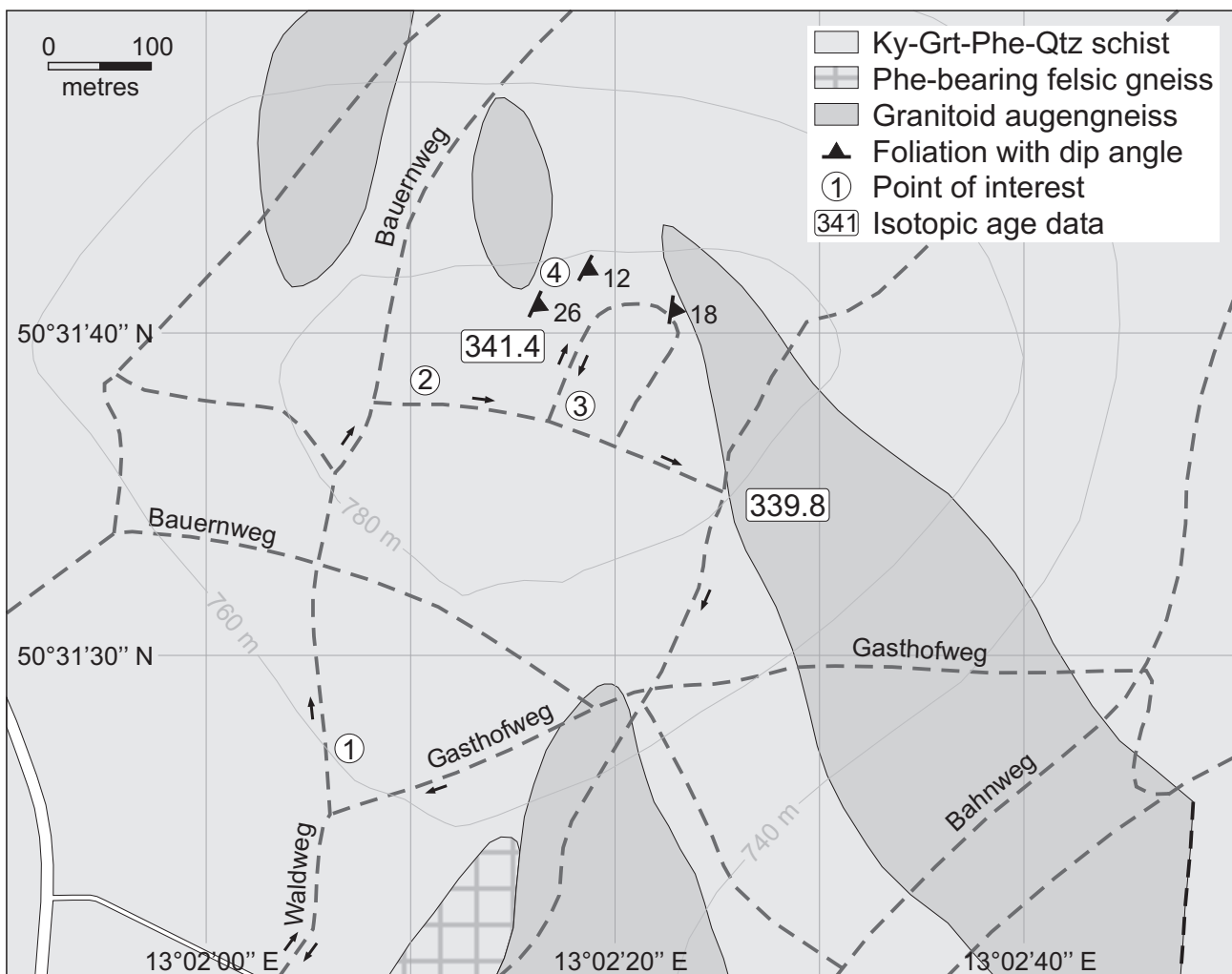


**Fig. 15.** Geology of the area to the north of Kühberg (Gneiss/Eclogite Unit I) based on the geological map of Saxony at scale 1:25 000, Sheet 139. The age data of  $341.4 \pm 2.3$  Ma and  $339.8 \pm 3.4$  Ma are Ar-Ar white mica total-fusion ages (Werner, 1998).

## Eurogranites 2012

### Stop 3-5

Geyer – Großer Fuchsstein Crag

Mica-Schist/Eclogite Unit

Coordinates:

lat.: 50°36'05.9"N, long.: 12°54'15.6"E,  
705 m a.s.l.

Guide: Jochen Rötzler

This stop provides good access to outcrops of chloritoid-bearing garnet-mica schist from the Mica-Schist/Eclogite Unit. We will leave the coach at a short halt on the road about 3 km to the southwest of Geyer. Please get off quickly and do not cross the road until the coach will have gone away. Our walk over a distance of 1 km (arrows in Fig. 16) starts on the opposite side of

the road and goes up onto a low ridge with a series of crags. From there, it continues back to the starting point and leads further downhill along a trail to a guest house, where we will re-enter the coach. The five crags on the NNE-SSW trending ridge consist all of the same pearly-coloured, greenish glimmering garnet-mica schist. The 1-4 mm sized garnet porphyroblasts are commonly weathered out on exposed surfaces. The main S2 foliation dips moderately steep to the northwest and cuts the older S1 foliation, which is deformed into open to tight folds. Quartz segregations aligned in S1 highlight the folding. For a detailed description of the mineral assemblages and compositions and the P-T estimates derived thereof, see Overview. The feldspar-free rock is another example of the geochemically and isotopically conspicuous metasediments that occur in all but the lowermost structural unit of the Erzgebirge and correlate with the Tremadocian-Arenigian Frauenbach Group in the Schwarzburg Anticline. Note that the Ar-Ar white mica plateau age of  $329.8 \pm 1.4$  Ma obtained from mica schist outside of the map area at Hermannsdorf (Werner, 1998) represents the younger of the two Ar-Ar white mica age clusters determined in the Mica-Schist/Eclogite Unit (see Overview). After this stop, we end Field Trip 3 and go to Chemnitz.

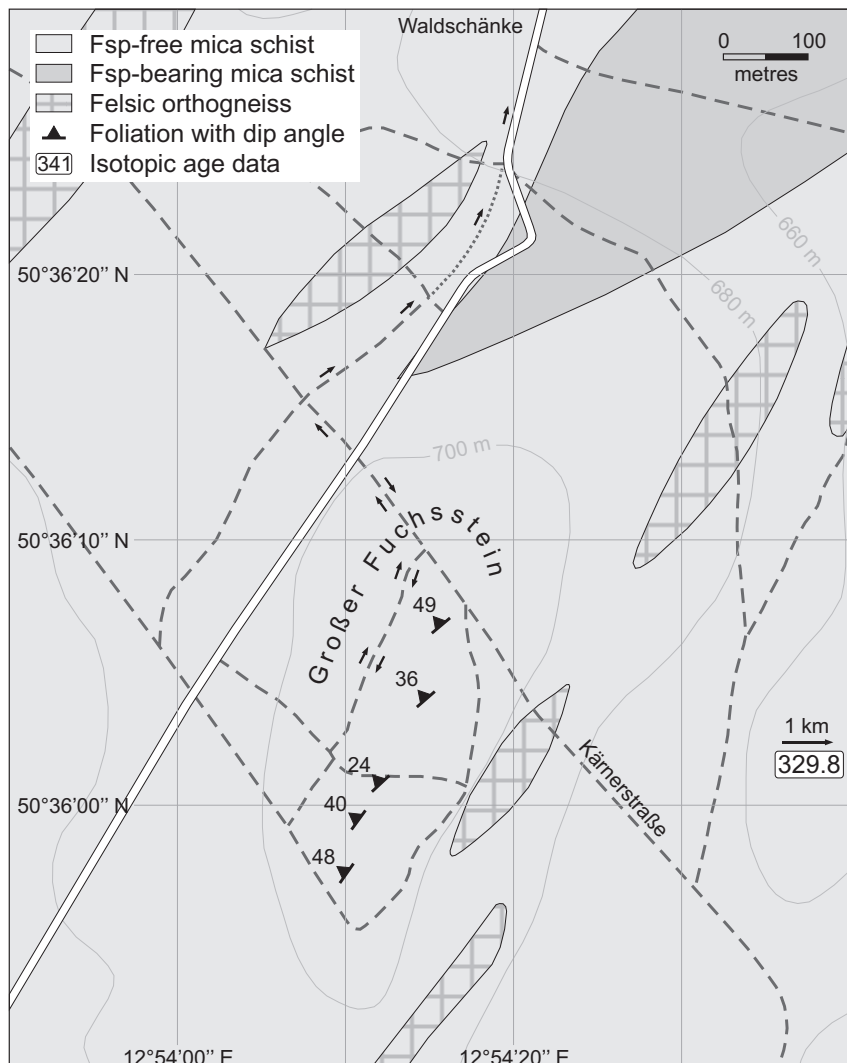


**Fig. 16.** Geology of the Großer Fuchsstein area (Mica-Schist/Eclogite Unit) based on the geological map of Saxony at scale 1:25 000, Sheet 127, except for the omission of alluvial deposits. The age data of  $329.8 \pm 1.4$  Ma is an Ar-Ar white mica plateau age on feldspar-free mica schist (Werner, 1998).

## References

- Gross, J., Burchard, M., Schertl, H.-P., Maresch, W.-V. (2008) Common high-pressure metamorphic history of eclogite lenses and surrounding metasediments: a case study of calc-silicate reaction zones (Erzgebirge, Germany). *Eur. J. Mineral.* 20: 757–775.
- Hammer, J. (1996) Geochemie und Petrogenese der cadomischen und spätvariszischen Granitoide der Lausitz. *Freib. Forsch.-H. C* 463: 107 pp.
- Hwang, S.L., Yui, T.F., Chu, H.T., Shen, P., Schertl, H.P., Zhang, R.Y., Liou, J.G. (2007) On the origin of oriented rutile needles in garnet from UHP eclogites. *J. Metam. Geol.* 25: 349–362.
- Jamieson, R.A., O'Beirne-Ryan, A.M. (1991) Decompression-induced growth of albite porphyroblasts, Fleur de Lys Supergroup, western Newfoundland. *J. Metam. Geol.* 9: 433–439.
- Klápová, H., Konopásek, J., Schulmann, K. (1998) Eclogites from the Czech part of the Erzgebirge: multi-stage metamorphic and structural evolution. *J. Geol. Soc.* 155: 567–583.
- Kley, J., Voigt, T. (2008) Late Cretaceous intraplate thrusting in central Europe: Effect of Africa-Iberia-Europe convergence, not Alpine collision. *Geology* 36: 839–842.
- Kröner, A., Willner, A.P., Hegner, E., Frischbutter, A., Hofmann, J., Bergner, R. (1995) Latest Precambrian (Cadomian) zircon ages, Nd isotopic systematics and P-T evolution of granitoid orthogneisses of the Erzgebirge, Saxony and Czech Republic. *Geol. Rundsch.* 85: 437–456.
- Kröner, A., Willner, A.P. (1998) Time of formation and peak of Variscan HP-HT metamorphism of quartz-feldspar rocks in the central Erzgebirge, Saxony, Germany. *Contrib. Mineral. Petrol.* 132: 1–20.
- Kroner, U., Görz, I. (2010) Variscan assembling of the Allochthonous Domain of the Saxo-Thuringian Zone - a tectonic model, in: Linnemann, U., Romer, R.L. (Eds.), *Pre-Mesozoic Geology of Saxo-Thuringia - From the Cadomian Active Margin to the Variscan Orogen*. Schweizerbart, Stuttgart, pp. 271–286.
- Kroner, U., Hahn, T., Romer, R.L., Linnemann, U. (2007) The Variscan orogeny in the Saxo-Thuringian Zone - Heterogenous overprint of Cadomian/Palaeozoic Peri-Gondwana crust. *Geol. Soc. Am., Spec. Pap.* 423: 153–172.
- Kroner, U., Romer, R.L. (2010) The Saxo-Thuringian Zone - tip of the Armorican Spur and part of the Gondwana plate, in: Linnemann, U., Romer, R.L. (Eds.), *Pre-Mesozoic Geology of Saxo-Thuringia - From the Cadomian Active Margin to the Variscan Orogen*. Schweizerbart, Stuttgart, pp. 371–394.
- Lorenz, W., Hoth, K. (1990). *Lithostratigraphie im Erzgebirge – Konzeption, Entwicklung, Probleme und Perspektiven*. Abhandlungen des Staatlichen Museums für Mineralogie und Geologie zu Dresden, 37, 7–35.
- Massonne, H.-J. (1991) High-pressure, low-temperature metamorphism of pelitic and other protoliths based on experiments in the system  $K_2O$ -MgO- $Al_2O_3$ - $SiO_2$ - $H_2O$ . *Univ. Bochum, Habil.-schr.*, 172 pp.
- Massonne, H.-J. (1999) A new occurrence of microdiamonds in quartzofeldspathic rocks of the Saxonian Erzgebirge, Germany, and their metamorphic evolution. 7th International Kimberlite Conference, Cape Town, Proc., Vol. 2: 533–539.
- Massonne, H.-J. (2001) First find of coesite in the ultrahigh-pressure metamorphic area of the central Erzgebirge, Germany. *Eur. J. Mineral.* 13: 565–570.
- Massonne, H.-J. (2005) Genesis of diamonds and diamondiferous rocks from the Saxonian Erzgebirge, central Europe. *Mitt. Österreich. Mineral. Ges.* 150: p. 104.
- Massonne, H.-J., Kennedy, A., Nasdala, L., Theye, T. (2007) Dating of zircon and monazite from diamondiferous quartzofeldspathic rocks of the Saxonian Erzgebirge – hints at burial and exhumation velocities. *Mineral. Mag.* 71: 407–425.
- Mezger, J.E., Chacko, T., Erdmer, P. (2001) Metamorphism along a late Mesozoic accretionary continental margin: a case study from the northern Coast Belt of the North American Cordillera. *J. Metam. Geol.* 19: 121–138.
- Mingram, B. (1998) The Erzgebirge, Germany, a subducted part of northern Gondwana: geochemical evidence for repetition of early Palaeozoic metasedimentary sequences in metamorphic thrust units. *Geol. Mag.* 135: 785–801.
- Mingram, B., Rötzler, K. (1999) Geochemische, petrologische und geochronologische Untersuchungen im Erzgebirgskristallin – Rekonstruktion eines Krustenstapels. *Schriftenr. Geowiss.* 9: 80 pp.
- Mingram, B., Kröner, A., Hegner, E., Krentz, O. (2004) Zircon ages, geochemistry, and Nd isotopic systematics of pre-Variscan orthogneisses from the Erzgebirge, Saxony (Germany), and geodynamic interpretation. *Int. J. Earth Sci.* 93: 706–727.
- Mlcoch, B., Konopasek, J. (2010) Pre-Late Carboniferous geology along the contact of the Saxothuringian and Tepla-Barrandian zones in the area covered by younger sediments and volcanics (western Bohemian Massif, Czech Republic). *J. Geosci.* 55: 81–94.
- Mlcoch, B., Schulmann, K. (1992) Superposition of Variscan ductile shear deformation on pre-Variscan mantled gneiss structure (Catherine dome, Erzgebirge, Bohemian massif). *Geol. Rundsch.* 81: 501–513.
- Nasdala, L., Massonne, H.-J. (2000) Microdiamonds from the Saxonian Erzgebirge, Germany: in situ micro-Raman characterisation. *Eur. J. Mineral.* 12: 495–498.
- Reich, S. (1996) *Erzgebirgsnordrandzone - Schiefermantel des Sächsischen Granulitgebirges: Ein petrologischer Vergleich*. Techn. Hochschule Darmstadt, Diss., 259 pp.
- Romer, R. L., Rötzler, J. (2011) The role of element distribution for the isotopic dating of metamorphic minerals. *Eur. J. Mineral.* 23: 17–33.
- Rötzler, K. (1994) *Druck-Temperaturentwicklung der Metamorphite des Mittel- und Westerzgebirges*. Univ. Münster, Diss., 220 pp.
- Rötzler, K., Schumacher, R., Maresch, W. V., Willner, A. P. (1998) Characterization and geodynamic implications of contrasting metamorphic evolution in juxtaposed high-pressure units of the Western Erzgebirge (Saxony, Germany). *Eur. J. Mineral.* 10: 261–280.
- Rötzler, K., Plessen, B. (2010) The Erzgebirge: a pile of ultrahigh-to low-pressure nappes of Early Palaeozoic rocks and their Cadomian basement. In: Linnemann, U. & Romer, R.L. (eds.) *Pre-Mesozoic Geology of Saxo-Thuringia: From the Cadomian Active Margin to the Variscan Orogen*. Schweizerbart Sci. Publ., Stuttgart, pp. 253–270.
- Schmädicke, E., Okrusch, M., Schmidt, W. (1992) Eclogite-facies rocks in the Saxonian Erzgebirge, Germany: high pressure metamorphism under contrasting P-T conditions. *Contrib. Mineral. Petrol.* 110: 226–241.
- Spear, F.S., Kohn, M.J., Cheney, J.T. (1999) P-T paths from anatectic pelites. *Contrib. Mineral. Petrol.* 134: 17–32.
- Tikhomirova, M., Belyatski, B. V., Berger, H.-J., Koch, E. A. (1995) Evidence of Variscan metamorphism in the eastern Erzgebirge. *Terra Nostra* 95/7: 133–136.
- Tichomirova, M., Berger, H. J., Koch, E. A., Belyatski, B. V., Goetze, J., Kempe, U., Nasdala, L., Schaltegger, U. (2001) Zircon ages of high-grade gneisses in the Eastern Erzgebirge

- (Central European Variscides); constraints on origin of the rocks and Precambrian to Ordovician magmatic events in the Variscan foldbelt. *Lithos* 56: 303–332.
- Tichomirowa, M., Sergeev, S., Berger, H.-J., Leonhardt, D. (2012) Inferring protoliths of high-grade metamorphic gneisses of the Erzgebirge using zirconology, geochemistry and comparison with lower-grade rocks from Lusatia (Saxothuringia, Germany). *Contrib. Mineral. Petrol.* DOI 10.1007/s00410-012-0742-8.
- Ventura, B., Lisker, F. (2003) Long-term landscape evolution of the northeastern margin of the Bohemian Massif: apatite fission-track data from the Erzgebirge (Germany). *Int. J. Earth Sci.* 92: 691–700.
- von Quadt, A., Günther, D. (1999) Evolution of Cambrian eclogitic rocks in the Erzgebirge: A conventional and LA-ICP-MS U-Pb zircon and Sm-Nd study. *Terra Nostra* 99/1: p. 164.
- Werner, O. (1998) K-Ar und Rb-Sr-Chronologie spätvariscischer Krustenkonvergenz: Bilanzierung des Wärme- und Stofftransportes im Erzgebirge. Univ. Heidelberg, Diss., 199 pp.
- Werner, O., Lippolt, H.J. (2000) White mica  $^{40}\text{Ar}/^{39}\text{Ar}$  ages of Erzgebirge metamorphic rocks: simulating the chronological results by a model of Variscan crustal imbrication. In: Franke, W., Haak, V., Oncken, O., Tanner, D. (eds.) *Orogenic Processes: Quantification and Modelling in the Variscan Belt*. Geol. Soc., London, Spec. Publ. 179: 323–336.
- Willner, A.P., Rötzler, K., Maresch, W.V. (1997) Pressure-temperature and fluid evolution of quartzo-feldspathic metamorphic rocks with a relic high-pressure, granulite-facies history from the central Erzgebirge (Saxony, Germany). *J. Petrol.* 38: 307–336.

# The Saxon Granulite Massif

Jochen Rötzler<sup>1</sup>, with contributions (Stop 4/5) by Uwe Kroner<sup>2</sup>

<sup>1</sup> GFZ German Research Centre for Geosciences,  
Telegrafenberg, D-14473 Potsdam, Germany  
rtzlr@gfz-potsdam.de

<sup>2</sup> TU Bergakademie Freiberg, Dept. of Geology,  
Bernhard-v.-Cotta-Str. 2, D-09599 Freiberg, Germany  
kroner@geo.tu-freiberg.de

The Saxon Granulite Massif (SGM) is a regional dome structure showing deep metamorphic gaps between tectonically juxtaposed low- to high-pressure rocks. The deepest and most extensive structural unit exposed, the Granulite Complex, encompasses felsic and intercalated mafic granulites that evolved from Cambro-Ordovician, mainly igneous protoliths with a bimodal calc-alkaline and tholeiitic character. The tholeiitic suite has chemical similarities to mid-ocean ridge basalts and island-arc tholeiites and was derived from depleted mantle sources, whereas the calc-alkaline suite originated from separate parental mantle magma with variable crustal contamination. The major detachment fault along which the granulites reached the upper crust contains slivers of dismembered units, such as high-grade metapelites and ultramafic-mafic rocks. The metapelites, represented mainly by cordierite gneiss, were formed from an early Palaeozoic sedimentary sequence that included volcanic material. The ultramafic-mafic rocks constituting a possible metaophiolite are divided into serpentinised peridotites and overlying metatholeiites with relic gabbroic textures. The low-pressure rocks in the roof of the massif, referred to as Schist Cover, were formed mainly from siliciclastic sediments of early Palaeozoic to Upper Devonian age that indicate an inner shelf setting up to the Middle Devonian and a change to an intermittent slope setting and a subsequent near-shore setting in the Upper Devonian. Upper parts of the Schist Cover at the south-eastern flank of the massif differ in lithofacies from those at the north-western flank and may belong to the Frankenberg Klippe abutting to the southeast. After the tectonic assembly of the structural units, the SGM was intruded by late-kinematic monzogranite forming stocks and numerous veins (Fig. 1).

Felsic and mafic granulites from various parts of the Granulite Complex have provided evidence for a common metamorphic evolution, starting with a near-isothermal decompression path between the peak of metamorphism at pressure of 2.2-2.3 GPa and a post-peak recrystallisation stage at about 1.1 GPa (Rötzler and Romer, 2001; Rötzler et al., 2004). This early history occurred at ultrahigh temperatures as inferred from mineral assemblages with preserved chemical and oxygen-isotopic equilibria, and from experimentally determined phase stability relations and petrogenetic grid evidence (Hagen et al., 2008; Rötzler et al., 2008). The metamorphism climaxed at ca. 341 Ma based on U-Pb zircon and titanite ages of felsic and mafic granulites (Romer and Rötzler, 2001, 2003; Rötzler et al., 2004). The evolution at pressures below 1.1 GPa followed a decompression and cooling path, with incipient and growing partial hydration after cooling through 800 °C when the granulites had reached the upper crust. Corresponding zircon and biotite ages of ca. 333 Ma dating shallow-level intrusions into

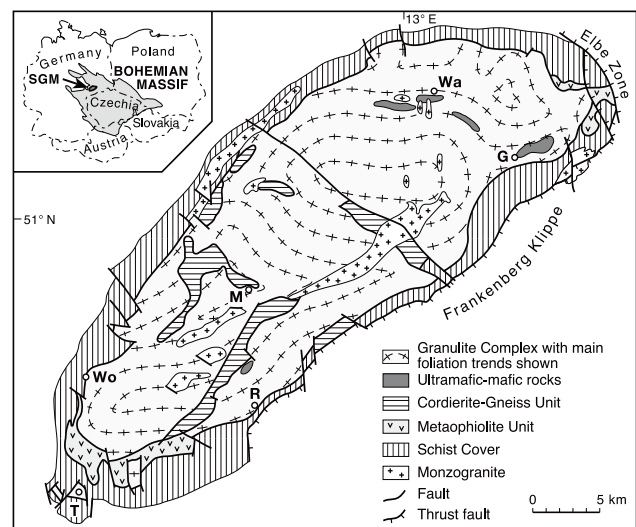


**Fig. 1.** Simplified geological map of the Saxon Granulite Massif with abbreviated localities: G, Greifendorf; R, Röhrsdorf; T, Tirschheim; Wa, Waldheim; Wo, Wolkenburg (Rötzler et al., 2008).

the massif and isotopic closure of the Rb-Sr biotite system at the margin of the Granulite Complex (Kroner et al., 1998; Rötzler et al., 2004) in combination with the peak P-T-t data of the granulites yield average rates of exhumation and cooling of 7-13 mm/year and 40-70 °C/Ma, respectively. The high-grade metapelites in the detachment zone evolved in the sillimanite stability field during decompression and heating from a garnet-forming peak-pressure stage to a subsequent cordierite-forming stage, where the P-T-t path coincided with that in the rising granulites. A similar clockwise P-T path is assumed for the supposed metaophiolite considering a transition from garnet-bearing to spinel-bearing assemblages (Rötzler and Romer, 2010). The Schist Cover underwent low-pressure metamorphism at subgreenschist to upper amphibolite-facies conditions that culminated in incipient partial melting at the contact with the Granulite Complex (Rötzler, 1992; Reinhardt and Kleemann, 1994). Rb-Sr muscovite ages of ca. 349 Ma obtained more than 500 metres above the granulite contact record an early stage of this metamorphism unrelated to the emplacement of the granulites. An Rb-Sr age of ca. 334 Ma for retrograde muscovite at the base of the Schist Cover as well as Ar-Ar and K-Ar ages of muscovite and biotite reflect deformation and

recrystallisation of the Schist Cover during juxtaposition with the granulites (Werner and Reich, 1997; Rötzler and Romer, 2010).

The rapid exhumation after common subduction of the felsic and mafic granulites to mantle depths during a widespread Variscan high-pressure event indicates a buoyant rise, followed by lateral extrusion at middle to upper crustal levels (Rötzler and Romer, 2001; Rötzler et al., 2004).

### Historical background

The SGM is a classical area for high-grade metamorphism. Its history of investigation began in the second half of the 18<sup>th</sup> century and reached a first milestone when in 1803 Christian Samuel Weiss created the term “granulite” for the particular predominant rock type in this massif (for the historical references in this paragraph, see Rötzler and Romer, 2010). This has made the SGM the type locality for granulite. The resemblance in metamorphic zoning between the roof of the granulites and contact aureoles around plutons gave rise to a long debate about the nature and the emplacement of the granulites. Apart from an unquestioned igneous origin, there was a controversy about whether the granulites reached their present position as an intruding magma body with or without subsequent metamorphism, or by tectonic emplacement following metamorphism. The second milestone in the history of investigation was passed in 1884 when Johannes Georg Lehmann introduced the latter concept. Toward the end of the 19<sup>th</sup> century, the research gained a strong boost from detailed mapping of the area. Petrographic research undertaken by Karl Hermann Scheumann from the 1920's to the 1960's first allowed understanding the metamorphic evolution in terms of the metamorphic facies concept. Scheumann interpreted the SGM as a stack of thrust sheets derived from a sheared pluton in the Erzgebirge. In contrast, Hans-Jürgen Behr inferred from compositional layering that the granulites are metasediments. Microstructural studies made by Behr in the 1960's disclosed that the quartz c-axis fabric of the felsic granulites changes from small-circle girdles to crossed girdles, concomitant with a change in the texture of quartz from discrete lenses to persistent ribbons. In ultramylonites, where the quartz ribbons are decomposed, the quartz c-axis fabric has adopted a Y-maximum pattern. The different fabric symmetries were interpreted as indicating a shift from flattening at high-pressure conditions to increasing non-coaxial shearing during exhumation (Behr, 1983). The results appeared consistent with a pre-Variscan metamorphism and a syn-Variscan diapiric uplift of the granulites rather than with thrust emplacement. After this third milestone, the understanding of the SGM suffered a set-back in the 1970's to 1980's when the boundaries between the structural units of the SGM were mistaken as stratigraphic unconformities. Werner Neumann who proposed this concept in 1975 correlated the structural units from top to bottom of the crustal section with increasingly older orogenic events, assigning the granulite-facies metamorphism a Neoproterozoic age. Two lines of evidence entailed the rejection of this concept. Firstly, no evidence was found for polymetamorphism but P-T estimates showed that the cooling path of the granulites coincides with the peak metamorphism in the structurally upper units (Rötzler, 1992). Secondly, isotopic dating of granulites and monzogranites yielded consistent metamorphic and intrusion ages around 350 Ma, based on U-Pb, Sm-Nd, and Rb-Sr geochronology and on Pb-Pb model age calculations (compiled by Gerstenberger, 1987). Although the granulite ages were initially believed as reset by the monzogranite intrusions, U-Pb and Pb-Pb zircon dating performed by von Quadt (1993) and Kröner et al. (1998) using conventional, evaporation, vapour digestion, and ion-microprobe (SHRIMP) techniques resolved the sequence of events by

assigning an age of ca. 340 Ma to the granulite metamorphism, and of ca. 333 Ma to the magmatism. Franke (1993) and Kroner (1995) argued for a purely extensional exhumation of the granulites by making reference to the metamorphic core concept. Franke and Stein (2000) tried to reconcile concurrent granulite-facies metamorphism and marine sedimentation in the same region by introducing a model, in which the granulites travelled in the lower crust from beneath the orogenic topography of the Saxo-Thuringian Belt to the normal-thickness crust under a marine basin in the foreland of this belt, where crustal extension caused the final exhumation.

### Excursion Programme

The trip today takes us down section from the Schist Cover through the Cordierite-Gneiss Unit into the Granulite Complex and finally back to the Schist Cover (for a route map, see chapter on the Erzgebirge).

## Eurogranites 2012

### Stop 4-1

Wolkenburg (Schist Cover)

Schist Cover

WGS84 Coordinates: 50°54'00.7" N, 12°40'14.2" E, 220 m a.s.l.

Guide: Jochen Rötzler

This stop located at the north-western flank of the SGM focuses on amphibolite-facies metasediments and late-kinematic monzogranites at the base of the Schist Cover only a few to some hundreds of metres above the faulted contact with the Granulite Complex.

The Schist Cover surrounding the granulite outcrop consists of low-pressure rocks (Fig. 1). The metamorphic grade ranges from sub-greenschist to amphibolite facies and increases toward the Granulite Complex across closely spaced isograds. The main foliation of the Schist Cover dips away from the Granulite Complex, whereas stretching lineations change between the upper and the lower part from a south-westerly to a south-easterly trend. The SE-trending lineation propagating into the Granulite Complex was caused by top-to-the-SE shearing during the final exhumation of the granulites (Kroner, 1995). The Schist Cover at the north-western flank of the SGM has a thickness of about 3500 metres. It reflects an inner shelf environment with low volcanic activity, except for Upper Devonian sequences in the highest part, which are formed by turbidites and volcanoclastic rocks, followed upward by siliciclastic deposits with ripple marks and dispersed plant material (Sebastian, 1990). The Upper Devonian rocks demonstrate a change from an intermittent slope setting to a near-shore environment. The depositional age for the lower part of the Schist Cover is uncertain, whereas the upper part shows a continuous Lower Ordovician to Upper Devonian succession. SHRIMP U-Pb dating disclosed that the metapelites at the base of the Schist Cover contain Neoproterozoic zircon detritus surrounded by ca. 487 Ma old zircon shells (Vavra and Reinhardt, 1997). Rötzler and Romer (2010) have interpreted the zircon shells as being formed in a magma chamber and introduced into the sediments by volcanism. Hence, the depositional age at the base of the Schist Cover may be only a few million years older than the rhyolite volcanism at a higher stratigraphic level dated by a Pb-Pb zircon evaporation age of ca. 482 Ma (Tichomirowa in Lorenz and Nitzsche, 2000). The Northwest Saxon Volcanic Complex and the Erzgebirge Basin unconformably overlie the Schist Cover to the north-west and the south-west. Granulite debris first appears in the Westphalian D of the Erzgebirge Basin (Schneider et al., 2005). The Schist Cover is in faulted contact with weakly metamorphosed rocks of the Elbe Fault Zone in the north-east.

The sequence of metapelites consisting, from top to bottom, of slate, phyllite, mica schist, and sillimanite-biotite schist reflects the sub-greenschist to upper amphibolite facies metamorphism in the Schist Cover. The mylonitic texture of these rocks is formed

by phyllosilicate-rich layers alternating with quartz-rich layers at lower grade, and with quartz-feldspar-rich layers at higher grade. Widespread andalusite occurring as nodules in spotted phyllite or as radiating sprays in mica schist indicates low-pressure metamorphism. Muscovite, biotite, plagioclase, and quartz are major constituents of the mica schists, commonly joined by one or more of the following minerals: chlorite, andalusite, staurolite, cordierite, garnet, and sillimanite. Rutile, ilmenite, magnetite, apatite, tourmaline, and zircon are accessories. The short-prismatic staurolite crystals are often broken, whereas the garnet is less deformed and mostly euhedral in shape (Fig. 2a). Inclusion trails in porphyroblasts of andalusite and staurolite show a transposition of the first foliation by a second one and a bending of the second foliation near the grain boundaries into the matrix foliation. These minerals were thus formed early during the development of the matrix foliation, which may be a third foliation (Rötzler et al., 1994). The high-grade sillimanite-biotite schist shows ambiguous field evidence of partial melting because common foliation-parallel quartz-feldspar veinlets appear as subsolidus segregations or as melt injections from monzogranite intrusions. Quartz ribbons and quartz-feldspar layers alternating with sillimanite-biotite layers define the mylonitic foliation. The locally folded layering is superposed by poikiloblastic growth of alkali feldspar. In contrast to the lower grade rocks, retrograde overprinting is evident from garnet resorption and overgrowths of randomly oriented muscovite.

The following isograds are found in the Schist Cover at increasing metamorphic grade: garnet-in, staurolite-in, chlorite-out, staurolite-out, K-feldspar-in, melt-in. The first appearance of garnet is observed in phyllite, where it divides between biotite-zone and higher grade garnet-zone rocks. Staurolite appears first in mica schist of the andalusite-staurolite-chlorite zone but propagates up-grade of the chlorite-out isograd into the andalusite-staurolite zone. At the staurolite-out isograd, this zone gives way to the sillimanite-muscovite zone, where sillimanite makes its first appearance as fibrolite intergrown with muscovite (Fig. 2b). Across the isograds in the mica schists, muscovite decreases and biotite and plagioclase increase in modal proportion. The plagioclase growth is associated with decreasing paragonite solid solution in muscovite, which decreases from about 30 mol % to below 10 mol %. Ilmenite included in staurolite is almost pure ilmenite, whereas that included in garnet from sillimanite-zone mica schist has up to 25 mol % pyrophanite component. The increasing Mn content in ilmenite is related with a decrease in Mn content of garnet. The K-feldspar zone and the migmatite zone occur within sillimanite-biotite schist at the base of the Schist Cover. The presence of sillimanite-K-feldspar assemblages down-grade of incipient migmatitisation implies low-pressure metamorphism. The Fe-Mn-rich garnet is commonly zoned. Bell-shaped zoning patterns found in garnet from phyllite and mica schist show a rimward decrease in spessartine, compensated by an increase in almandine, whereas pyrope and grossular are low and more or less constant. A reversal of this zoning trend caused by retrograde re-equilibration is observed in outer garnet rims from sillimanite-biotite schist. The garnet core compositions vary from Alm50Sps40 to Alm60Sps30. The rim or inner rim compositions are in the range from Alm70Sps20 to Alm80Sps10 (Rötzler et al., 1994). For sillimanite-biotite schist at the base of the Schist Cover, garnet-biotite thermometry reveals peak temperatures of 660-680 °C (Rötzler, 1992; Reinhardt and Kleemann, 1994). Peak-pressure estimates of about 0.3 GPa were obtained using garnet-sillimanite-plagioclase-quartz barometry (Fig. 3). At the K-feldspar-in isograd, the temperature reached 630-640 °C (Rötzler, 1992). The assemblage staurolite-cordierite-andalusite-biotite-muscovite-quartz is locally present in mica schist from the andalusite-staurolite zone. Based on the stability of staurolite-

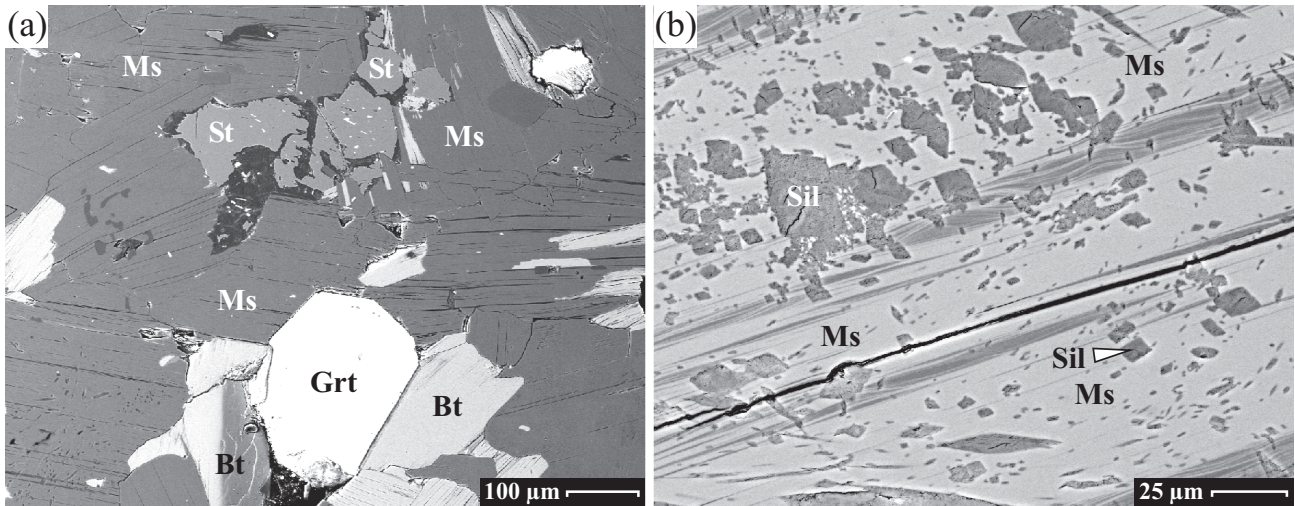


**Fig. 2.** BSE images of phase textures in the Schist Cover: (a) Relic staurolite (St) in sillimanite-zone mica schist is surrounded by garnet (Grt), muscovite (Ms) and biotite (Bt). (b) Muscovite intergrown with sillimanite from the same sample.

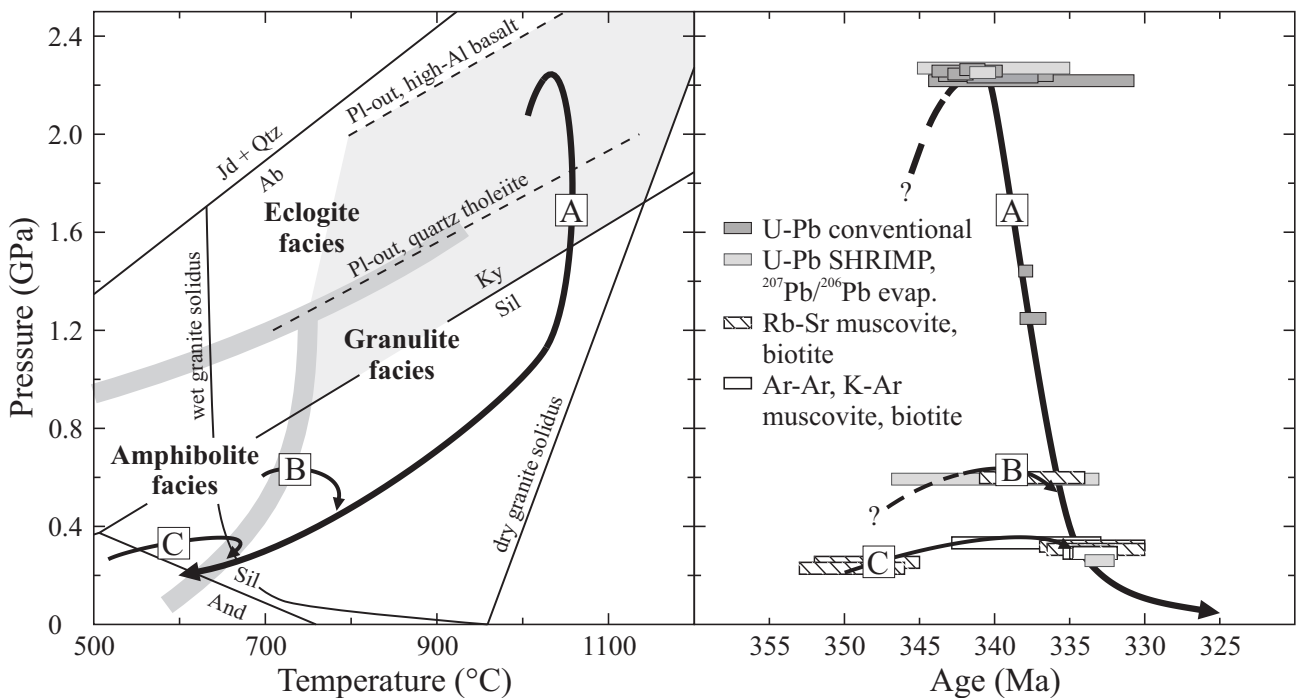


**Fig. 3.** Pressure-temperature and pressure-time paths for the Granulite Complex (A), the Cordierite-Gneiss Unit (B), and the Schist Cover (C) based on P-T data from Rötzler (1992), Rötzler et al. (1994), Rötzler and Romer (2001), Rötzler et al. (2004), and Rötzler et al. (2008). Metamorphic facies boundaries (thick grey lines) are from Spear (1993); the plagioclase-out reactions are from Green and Ringwood (1967) for quartz tholeiite, and Ito and Kennedy (1971) for high-Al basalt; wet and dry haplogranite solidus curves after Johannes and Holtz (1996). The shaded area indicates the high-pressure granulite facies as proposed by O'Brien and Rötzler (2003). Sources of age data are von Quadt (1993), Kröner et al. (1998), Romer and Rötzler (2001), and Rötzler et al. (2004) for the Granulite Complex; Vavra (in Franke and Stein, 2000) and Rötzler and Romer (2010) for the Cordierite-Gneiss Unit; Werner and Reich (1997), and Rötzler and Romer (2010) for the Schist Cover.

cordierite assemblages in the system  $K_2O$ -FeO-MgO- $Al_2O_3$ - $SiO_2$ - $H_2O$  (KFMASH), Reinhardt and Kleemann (1994) estimated the pressure for these rocks at 0.2-0.3 GPa. In the KFMASH grid from Dymoke and Sandiford (1992), such assemblages are stable over the P-T range of 0.28-0.32 GPa and 535-565 °C.

Rötzler and Romer (2010) determined Rb-Sr muscovite and biotite ages along a section through the Schist Cover at Wolkenburg (Fig. 4) and further down section across the shear zone, along

which the granulites were exhumed. Consequently, the age variation along the profile integrates (i) the kinematic history of this zone, with juxtaposition of contrastingly metamorphosed units, and (ii) the thermal history reflected in the overprinting of lower grade structural units when the hot granulites were juxtaposed against them. This process resulted in an outward migration of deformation and a condensed contact-metamorphic aureole. The Rb-Sr muscovite and biotite ages (Fig. 5) constitute three groups

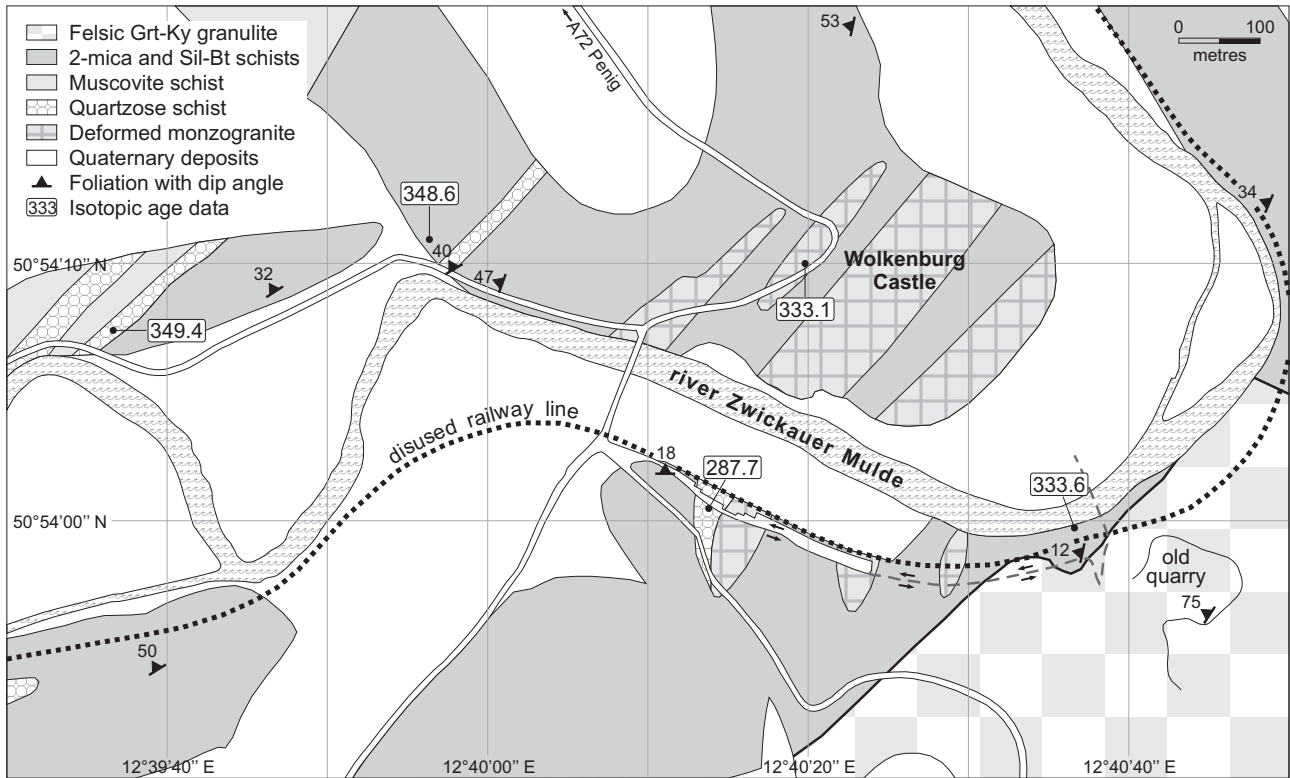


**Fig. 4.** Geology of the Schist Cover at Wolkenburg based on the geological map of Saxony at scale 1:25 000, Sheets 75, 76, 94, and 95. The age data of  $333.6 \pm 3.5$  Ma,  $287.7 \pm 3.0$  Ma,  $348.6 \pm 3.5$  Ma, and  $349.4 \pm 3.5$  Ma are Rb-Sr muscovite ages on metasediments (Rötzler and Romer, 2010). Pb-Pb single-zircon evaporation dating of a concordant granite sheet has yielded an age of  $333.1 \pm 1.0$  Ma (Kröner et al., 1998).

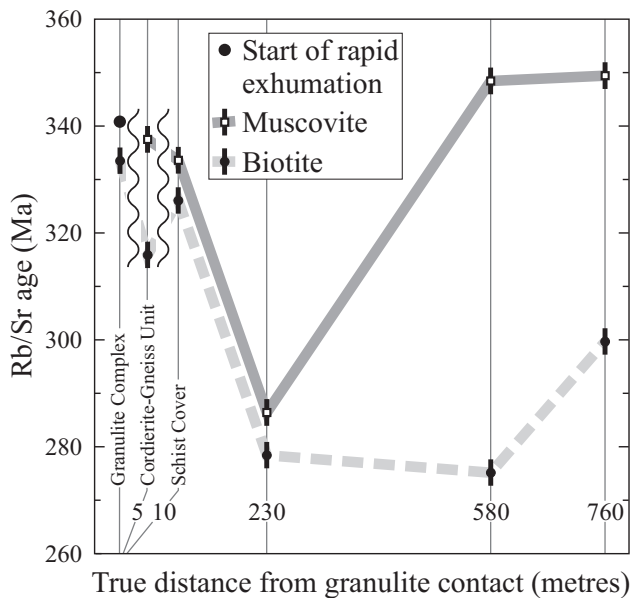


**Fig. 5.** Age vs. distance diagram for the structural section from the granulite contact through the Cordierite-Gneiss Unit to the lower part of the Schist Cover based on Rb-Sr muscovite and biotite ages (Rötzler and Romer, 2010). Peak metamorphic and biotite ages for the granulites are from Rötzler et al. (2004). All error bars for ages are at  $2\sigma$  level.

of ages that are related to fundamentally different geologic processes before, during and after the tectonic emplacement of the granulites: (i) Ages associated with an early phase of regional metamorphism in the Schist Cover. The two samples most distant from the granulite contact yield Rb-Sr muscovite ages that are older than U-Pb zircon ages of the granulites. These muscovite ages that agree with each other within analytical uncertainty ( $348.6 \pm 3.5$  Ma and  $349.4 \pm 3.5$  Ma) are unrelated with the metamorphism and emplacement of the granulites. Instead, the muscovite ages may date late increments of deformation during metamorphism in the Schist Cover. (ii) Muscovite that formed when the Granulite Complex was juxtaposed with the Cordierite-Gneiss Unit and the Schist Cover yields ages of  $337.6 \pm 3.4$  Ma and  $333.6 \pm 3.5$  Ma, respectively. The first age agrees with a U-Pb zircon age of  $340 \pm 7$  Ma obtained on leucosomes formed during decompressional heating of the Cordierite-Gneiss Unit (Vavra in Franke and Stein, 2000). The second age agrees with  $^{40}\text{Ar}/^{39}\text{Ar}$  and K/Ar ages of muscovite ( $334.2 \pm 1.9$  Ma,  $332.6 \pm 4.2$  Ma) and biotite ( $333.1 \pm 2.1$  Ma,  $333.1 \pm 1.7$  Ma) from several locations in the Schist Cover (Werner and Reich, 1997). (iii) A distinctly younger Rb-Sr muscovite age of one sample in the Schist Cover is unrelated to the exhumation of the granulites, but is related to late faulting in the Schist Cover. The Rb-Sr biotite ages from the same samples show a less systematic picture (Fig. 5). Although being always younger than the Rb-Sr muscovite age of the respective sample, the biotite ages are not consistent with a cooling history that would yield increasingly younger ages with decreasing distance from the granulite contact, where the rocks supposedly cooled later. The youngest biotite ages occur in the upper part of the age profile in the Schist Cover, where biotite is finer grained than at deeper structural levels. In particular for

this part of the age profile, the biotite ages are distinctly younger than the corresponding muscovite ages, suggesting that biotite recrystallised and reset its isotopic system when muscovite already had become a closed system. Rather than interpreting this to reflect a lower blocking temperature for volume diffusion in biotite than in muscovite, the age difference may reflect that biotite in strained rocks is recrystallising more readily by dissolution precipitation creep than muscovite and that biotite is more readily altered than muscovite. For instance, chloritisation may result in a resetting of the Rb-Sr biotite age (Clauer et al., 1982). The markedly younger Rb-Sr biotite ages in the Schist Cover (between 230 m and 580 m, Fig. 5) may indicate that the faulting resulted in an alteration of biotite also in higher parts of the Schist Cover.

We will walk for about 600 metres on the bluff of the Zwickauer Mulde River in Wolkenburg (arrows in Fig. 4), where a roadcut and a rocky riverside expose high-grade metasediments intruded by monzogranite. Textural evidence shows an increase in metamorphic grade from the sillimanite-K-feldspar zone to the migmatite zone. The roadcut west of the old railway station contains a decametre-scale layer of biotite-bearing quartzose schist underlain by sillimanite-biotite schist. The mylonitic rocks enclose small granite lenses and are concordant with a large granite sheet that crops out behind the railway station. The sheared granite surrounds a raft of folded migmatitic biotite schist. The riverside at the suspension bridge consists of sillimanite-biotite schist with visible sillimanite and fine partial melt. Retrograde muscovite overgrown on the peak assemblage of this rock has yielded an Rb-Sr age of ca. 334 Ma, consistent, within error limits, with a Pb-Pb zircon evaporation age for nearby exposed granite.

## Eurogranites 2012

### Stop 4-2

Mohsdorf

Cordierite-Gneiss Unit

WGS84 coordinates: 50°56'31.6" N, 12°49'47.0" E, 220 m a.s.l.

Guide: Jochen Rötzler

The purpose of this stop is to show a typical outcrop of a sequence of high-grade metapelites, about 200 m thick, that structurally overlies the Granulite Complex. The sequence is referred to as Cordierite-Gneiss Unit with respect to the predominant rocks, but includes garnet gneiss locally at the base (Fig. 6). The rocks were thought to be alteration products of the granulites, assuming either a weathering process and polymetamorphism of the granulites (Neumann, 1976) or element leaching and melt extraction from the marginal shear zone of the granulites during exhumation (Kroner, 1995). These concepts are in conflict with petrologic evidence for a monometamorphic evolution of the granulites and a divergent metamorphic path in the Cordierite-Gneiss Unit until juxtaposition with the granulites (Rötzler, 1992). A derivation of the Cordierite-Gneiss Unit from the granulites is also ruled out by contrasting zircon populations (Vavra and Reinhardt, 1997). The metapelites have detrital zircons ranging in age from 600 to 550 Ma, prismatic zircon shells dated at ca. 490 Ma, and isometric zircon crystals with a minimum age of ca. 336 Ma. By interpreting the zircon shells as relating to partial anatexis of the metapelites, Reinhardt and Vavra (1997) inferred a Cambrian protolith age for the Cordierite-Gneiss Unit. However, if this zircon is related to volcanic input into the protoliths, as ascertained for zircon from Ordovician sequences in Thuringia and the Elbe Fault Zone (Gehmlich, 2003), the zircon shells would represent magmatic overgrowths on detrital zircon assimilated by the magma from the wall rock. In this case, the Cordierite-Gneiss Unit would have an early Ordovician sedimentary age (Rötzler and Romer, 2010). The rocks are all enriched in light rare earth elements. The garnet gneiss, in addition to being higher in Al, Fe and Mg, and lower in Si, Na and K than the cordierite gneiss (Rötzler, 1992), has a distinct negative Eu anomaly (Müller et al., 1987a). The  $\delta^{18}\text{O}$  values in the cordierite gneiss ranging from 10.6 ‰ to 12.0 ‰ (Vinogradov and Pokrovsky, 1987) are typical for siliciclastic sediments (cf. Rollinson, 1993). Hagen (1994) analysed  $\delta^{18}\text{O}$  values of 10.3 ‰ in garnet gneiss, and of 10.7 ‰ in cordierite gneiss. The chemical and isotope data do not support a restitic nature of the rocks as assumed by Reinhardt and Vavra (1997), which is also in conflict with strong inter-grain variation in  $\delta^{18}\text{O}$  of garnet observed by in-situ oxygen-isotope microanalysis of garnet gneiss. The variation is beyond analytical error and contradicts an oxygen-isotope equilibration of the mineral assemblage in the presence of a melt phase, but shows oxygen-isotope heterogeneity likely inherited from a layered siliciclastic sediment (Hagen, 2002).

Migmatitic cordierite gneiss as the predominant lithology in this unit is mostly well foliated but grades locally into a massive

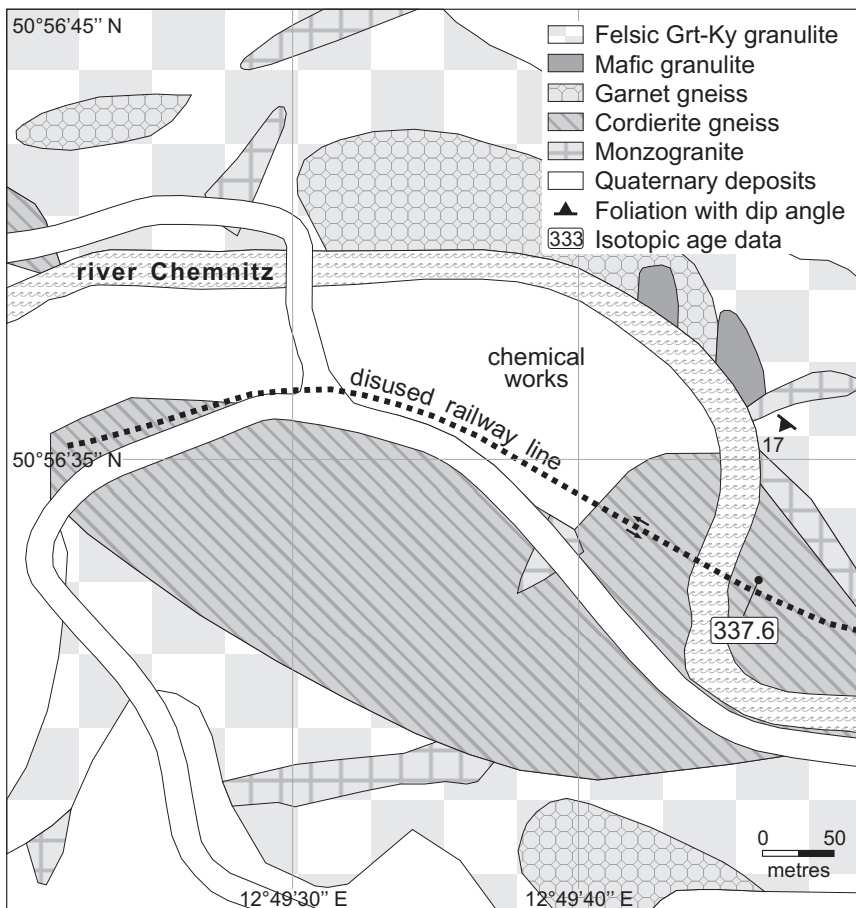


**Fig. 6.** Geology of the Cordierite-Gneiss Unit north of Mohsdorf based on the geological map of Saxony at scale 1:25 000, Sheet 76. The age data of  $337.6 \pm 3.4$  Ma is an Rb-Sr muscovite age on cordierite gneiss (Rötzler and Romer, 2010).

type. Cordierite-bearing biotite gneiss in the north-eastern part of the SGM with structural and metamorphic features similar to the cordierite gneiss has a more potassic composition. Garnet gneiss observed occasionally at the base of the Cordierite-Gneiss Unit has been classified into three types (Rötzler, 1992). Garnet gneiss showing a crenulated biotite-sillimanite foliation is most common, whereas sillimanite-garnet fels consisting of high proportions of garnet and sillimanite is rare, as is migmatitic garnet gneiss most resembling in appearance the cordierite gneiss. The garnet and cordierite gneisses record different stages of the metamorphism in the Cordierite-Gneiss Unit. Scheumann (1925) assumed a continuous down-section increase in metamorphic grade across the boundary between the Cordierite-Gneiss Unit and the Granulite Complex that he thought had entailed a prograde amphibolite-to-granulite facies transition from cordierite gneiss to garnet gneiss. Scheumann and Huckenholz (1961) noted that the metamorphism of the garnet gneiss did not exceed upper amphibolite facies conditions. Bergner (1990) and Rötzler (1992) have reported evidence that the metamorphism proceeded in the opposite direction, i.e. that cordierite replaced garnet. A simultaneous formation of garnet gneiss and cordierite gneiss as supposed by Neumann (1985) is in conflict not only with the reaction textures but also with the bulk-rock compositions, as the bulk-rock  $X_{Mg}$  ratios in both rocks would have to be different but fall in the same range (Rötzler, 1992). The most striking difference between the garnet gneiss and the cordierite gneiss is the stable occurrence of either garnet or cordierite. Both rocks always contain quartz as a major, and plagioclase as a minor component, whereas alkali feldspar is a major component only in the cordierite gneiss. The garnet gneiss has negatively correlated modal amounts of garnet and biotite, and tends to be higher in sillimanite and biotite content than the cordierite gneiss. Ilmenite,

zircon, and retrograde muscovite and chlorite are accessories in both rocks. The garnet gneiss also has accessory rutile; spinel and magnetite are observed as inclusions in core garnet, in contrast to the cordierite gneiss, where these minerals are present in the matrix (Rötzler, 1992).

Garnet in the garnet gneiss forms porphyroblasts surrounded by sillimanite, biotite, and quartz. The continuous reaction  $\text{biotite} + \text{sillimanite} + \text{quartz} = \text{garnet} + \text{K-feldspar} + \text{H}_2\text{O}$  accounts for the reaction textures and part of the variation in modal composition of these rocks. In addition to spinel and magnetite, garnet encloses the same minerals that occur in the matrix (Fig. 7a). Growth zoning in garnet is evident from alternating zones devoid of, or rich in inclusions, and from a change in the inclusion assemblage that mimics euhedral or rounded crystal faces of garnet by sillimanite inclusion zones. This textural evidence is only in part associated with chemical zoning defined by increasing pyrope content and decreasing grossular and spessartine contents from core to an inner garnet rim, composed of about 30 mol % pyrope and 70 mol % almandine component (Rötzler et al., 1994). Homogeneous garnet is of similar pyrope-rich composition. A series of reaction textures documents the transition from garnet gneiss to cordierite gneiss. In some rocks, cordierite appears first as small discrete grains spreading along garnet contacts to form coronas. A complete consumption of garnet is observed in cordierite gneiss typically showing a diablastic texture of cordierite, biotite, sillimanite, ilmenite, and spinel (Fig. 7b). These intergrowths have partially recrystallised to cordierite porphyroblasts with local inclusions of relic garnet (Rötzler, 1992). The change in mineral assemblage and modal composition suggests that cordierite formed by the reactions  $\text{garnet} + \text{biotite} + \text{sillimanite} + \text{quartz} = \text{cordierite} + \text{K-feldspar} + \text{melt}$  and  $\text{garnet} + \text{biotite} + \text{sillimanite} = \text{cordierite} + \text{hercynite} + \text{K-feldspar} +$

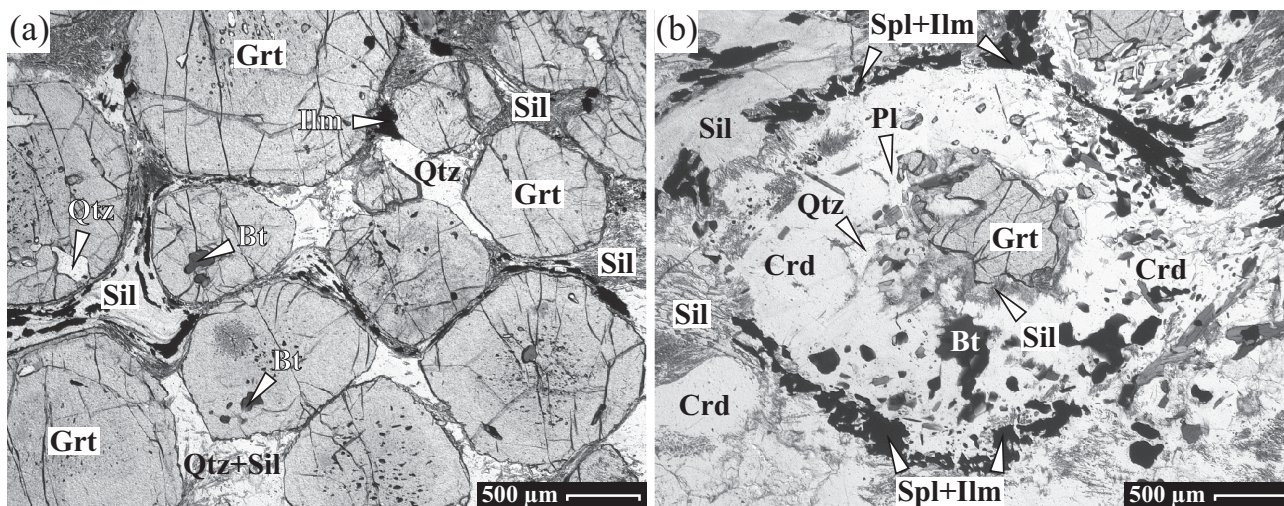


**Fig. 7.** Microphotographs (plane-polarized light) of phase textures in the Cordierite-Gneiss Unit: (a) Sillimanite (Sil), quartz (Qtz), ilmenite (Ilm), and biotite (Bt) are intercalated between, and enclosed in, euhedral garnet crystals (Grt) in sillimanite-garnet fels. (b) A diablastic texture of cordierite (Crd), sillimanite (Sil), biotite (Bt), spinel (Spl), ilmenite (Ilm), plagioclase (Pl), and quartz (Qtz) replaces relic garnet (Grt) in cordierite gneiss.

melt. There are also clear trends in mineral chemistry. Cordierite reaches an  $X_{Mg}$  ratio of almost 0.7 in garnet gneiss but has  $X_{Mg}$  of 0.3-0.5 in cordierite gneiss. Spinel enclosed in garnet from garnet gneiss became higher in  $Fe^{2+}$  and lower in Mg and Zn as the garnet increased in  $X_{Mg}$  during growth, with early spinel inclusions having up to 30 mol % gahnite content. In accord with this trend, the spinel in the cordierite gneiss is hercynitic. Biotite from the cordierite gneiss is lower in  $X_{Mg}$ , but higher in Al and F than biotite from the garnet gneiss (Rötzler et al., 1994).

P-T estimates based on the inclusion assemblage in pyrope-rich garnet from garnet gneiss and on the matrix assemblage in cordierite gneiss suggest that the transition from garnet gneiss to cordierite gneiss occurred during decompression and heating from about 0.64 GPa at 730 °C to 0.48 GPa at 790 °C (Rötzler et al., 1994). Zircon dating of leucosomes has yielded an age of  $340 \pm 7$  Ma for the temperature peak in the Cordierite-Gneiss Unit (Vavra in Franke and Stein, 2000). An age of  $336 \pm 4$  Ma determined from isometric zircon crystals has been interpreted as minimum age of prograde zircon growth (Vavra and Reinhardt, 1997). The coincidence in P-T-time data between the temperature

peak in the Cordierite-Gneiss Unit and the cooling path in the granulites suggests heat transfer from the rising granulites toward the Cordierite-Gneiss Unit (Fig. 3). Variations in bulk-rock chemistry and in the influx of fluids, which were released from dehydrating hanging-wall rocks of the detachment fault, are possible reasons why garnet gneiss at the base of the Cordierite-Gneiss Unit has escaped alteration.

The outcrop to which the excursion will move is only a one hundred metre walk away from the parking ground, where we get off the coach. When crossing the river Chemnitz over the bridge of a disused railway line, we will see a little crag in front of us that consists of blue grey cordierite gneiss. The pygmalically folded rock has light-coloured leucosomes. Visible garnet relics within the cordierite-rich matrix suggest incomplete replacement of a former garnet-bearing assemblage. The cordierite gneiss at this locality has yielded an Rb-Sr muscovite age of  $337.6 \pm 3.4$  Ma (Rötzler and Romer, 2010). Garnet gneiss exposed about 200 metres downstream of the railway bridge is in faulted contact with underlying felsic and mafic granulites. Dykes of monzogranite cut across the metamorphic rocks (Fig. 6).

## Eurogranites 2012

### Stop 4-3

#### Granulite Complex

#### Kriebstein Reservoir to the northwest of Ringenthal

WGS84 coordinates: 51°00'46.0" N, 12°59'02.9" E, 232 m a.s.l.

#### Guide: Jochen Rötzler

Felsic granulites and their retrogressed equivalents are the prevailing rocks in the Granulite Complex. Mafic granulites representing centimetre- to metre-thick layers or, rarely, decametre-thick lenses occur in varying amounts across the structural section. The outcrops examined at this stop provide one of the best surface exposures of layered felsic-mafic granulite. The granulite-facies mylonitic main foliation (S2) is mostly parallel to locally observed felsic-mafic layering (S1), but is also found to be axial planar to isoclinal intrafolial folds of S1. The transposition of S1 has created a pseudo-stratigraphy related with disrupted and rotated rock segments. It is thus doubtful whether a stratigraphic subdivision of the Granulite Complex deduced by assigning the mafic granulites to a laterally traceable felsic-mafic sequence is true. Geochemical data show that most of the granulites in the SGM are meta-igneous (Werner, 1987). With respect to compositional layering and lack of pre-metamorphic intrusive structures, a meta-volcanic origin has been favoured. The prevailing felsic granulites of peraluminous rhyolitic composition and mafic granulites of rhyodacitic to andesitic composition constitute a calc-alkaline suite of rocks that is conformably intercalated with a suite of metatholeiitic granulites. Müller et al. (1987b) corroborated a meta-igneous origin of the felsic granulites, interpreting strong correlations of major element with rare earth element (REE) contents, and of  $\delta^{18}\text{O}$  values (7.9-10.1 ‰) with  $\text{SiO}_2$  contents to reflect magmatic differentiation. The same authors envisaged the metatholeiitic granulites as derived from a mantle source, considering an unfractionated REE pattern in one sample and low  $\delta^{18}\text{O}$  values (5.7-8.7 ‰). Commonly, these rocks have fractionated REE patterns with large negative Eu anomalies indicative of magmatic differentiation. Low nitrogen contents (mostly 9-14 ppm) argue against a crustal contamination of the tholeiitic magma. A cogenetic magmatic relationship of the felsic and metatholeiitic granulites is unlikely because of opposite correlations between nitrogen contents and  $\delta^{15}\text{N}$  values (Müller et al., 1987b). Protolith ages for felsic and mafic granulites at ca. 473-485 Ma and ca. 499 Ma, respectively, were determined by SHRIMP zircon (Kröner et al., 1998) and U-Pb titanite dating (Rötzler et al., 2004). Chemical and Nd-Pb isotope signatures imply an origin of the metatholeiitic granulites from mid-ocean ridge basalts or island-arc tholeiites (von Quadt, 1993). The granulite protoliths had variable Nd isotope composition, with  $\varepsilon\text{Nd}_{T=490}$  values from +4.1 to +2.2 in metatholeiitic granulites and from -1.7 to -7.2 in felsic granulites (von Quadt, 1993, data recalculated to 490 Ma). These values indicate a derivation of the

metatholeiitic granulites from depleted mantle sources and a partly significant involvement of crustal sources in the meta-igneous felsic granulites. The latter is supported by disseminated carbon present in some felsic granulites. Considering carbon isotope fractionation during high-grade metamorphism, the  $\delta^{13}\text{C}$  values in these rocks varying from -28.4 ‰ to -29.1 ‰ may result from original values in the range below -30 ‰ (Lorenz and Nitzsche, 2000). Such low values are known from Neoproterozoic non-carbonate sediments of the Avalonian-Cadomian Belt, whereas the  $\delta^{13}\text{C}$  values for Palaeozoic non-carbonate sediments are systematically higher. Hence, the parental magma to the Cambro-Ordovician protoliths of these granulites probably assimilated Neoproterozoic supracrustal rocks. A metasedimentary origin has been inferred only for minor lithologies. For instance, feldspathic prismatic granulite at Waldheim has been ascribed to a sodic sediment enriched in boron by hot-spring-related salt brines or submarine exhalations (Grew, 1986) and to a hydrothermally altered volcano-sedimentary rock (Werner, 1987), respectively. The rock is spatially closely associated with a garnet-clinopyroxene granulite envisaged as metamorphosed dolomitic mudstone (Werner, 1987). However, the  $\delta^{18}\text{O}$  values in the prismatic granulite (7.7 ‰) and the garnet-clinopyroxene granulite (5.6 ‰) do not support a metasedimentary origin and, when plotted against the  $\text{SiO}_2$  contents, fall on a magmatic differentiation trend of the meta-igneous granulites (Hagen, 1994).

The felsic granulites and their retrogressed equivalents each include two types. The types of felsic granulite differ in quartz morphology and foliation. In the first type, discrete aligned quartz lenses are set into fine-grained quartz-feldspar masses, whereas in the second type, the fine-grained quartz-feldspar masses alternate with quartz ribbons. Both types have garnet and kyanite as macroscopic components. Retrogressed felsic granulites with alternating light and dark layers defined by variation in the biotitization of garnet are due to mylonitization and fluid access. A different type of retrogressed felsic granulite occurs in low-strain areas, where recrystallisation produced crudely foliated biotite gneisses discernible as former granulites only by gradations into less altered rocks. In the retrogressed felsic granulites, granite or pegmatite patches indicate local melting caused by fluid infiltration.

The peak mineral assemblages in the felsic granulites involve a single ternary-feldspar phase, quartz, garnet, kyanite, and rutile. The ternary feldspar is unmixed, commonly showing perthitic, rarely antiperthitic exsolution. Apart from rutile, these minerals are partially megacrystic, with a range in size down to matrix grains. Mutual inclusion relationships and straight grain boundaries reflect an intimate association of ternary feldspar, garnet, and kyanite (Fig. 8a, 9a-b). Accessories are apatite, zircon, monazite, pyrrhotite, pyrite and sporadic graphite. The prismatic granulite at the Bahnhof locality in Waldheim preserves, despite strong post-peak overprinting, an early mineral assemblage of garnet, kyanite, corundum, tourmaline, and rutile. Antiperthitic exsolution microstructures in post-peak plagioclase testify to the original presence of ternary feldspar in this quartz-free assemblage (Grew, 1986). Post-peak overprinting variably affected the peak assemblages. Partial replacement of garnet, kyanite, rutile, and quartz by secondary garnet, spinel, sillimanite, ilmenite, and plagioclase marks a first recrystallisation stage in the predominant felsic granulites (Fig. 8b, 9c). A heterogeneous array of contemporaneous microstructures, such as cigar-like secondary garnet or sillimanite prisms with shape-preferred orientation parallel to the quartz foliation on the one hand and corona growth of plagioclase, spinel, ilmenite, and sillimanite on the other hand, implies partitioning of strain into zones of simple shear and pure shear deformation at this stage. The decompression history is more differentiated in sapphirine and prismatic-bearing felsic

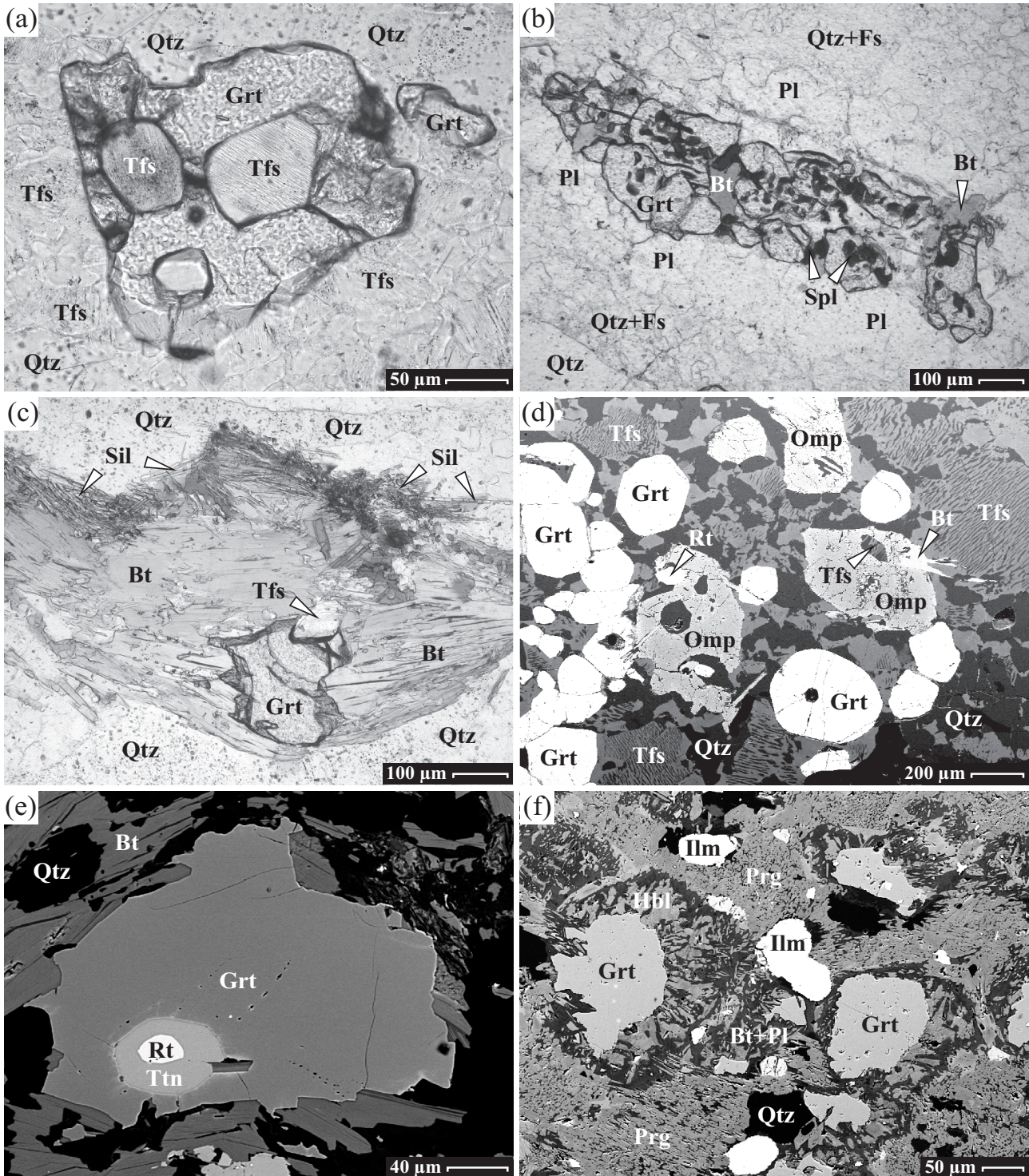


**Fig. 8.** Phase textures in the Granulite Complex: (a) Garnet (Grt) embedded in quartz-feldspar masses between quartz ribbons (Qtz) has negative crystal-shaped inclusions of ternary feldspar (Tfs); plane-polarized light. (b) A cigar-like aggregate of garnet (Grt) and spinel (Spl) surrounded by corona plagioclase (Pl) is cut by biotite (Bt); plane-polarized light. (c) Biotite (Bt) and sillimanite (Sil) overgrowing relic garnet (Grt) form streaks parallel to the ribbon quartz (Qtz) foliation; plane-polarized light. (d) An original granoblastic texture formed by garnet (Grt), omphacite (Omp), ternary feldspar (Tfs) and quartz (Qtz) is visible, despite feldspar exsolution and local growth of biotite (Bt). Note that ternary feldspar is included in omphacite; back-scattered electron (BSE) image. (e) Titanite (Ttn) surrounding rutile (Rt) is included in garnet (Grt), which has ragged contacts with overgrown biotite (Bt); BSE image. (f) Hornblende (Hbl), biotite (Bt) and plagioclase (Pl) pseudomorphs after garnet (Grt) are set into a matrix of pargasitic-tschermakitic amphibole (Prg), quartz (Qtz) and ilmenite (Ilm); BSE image.

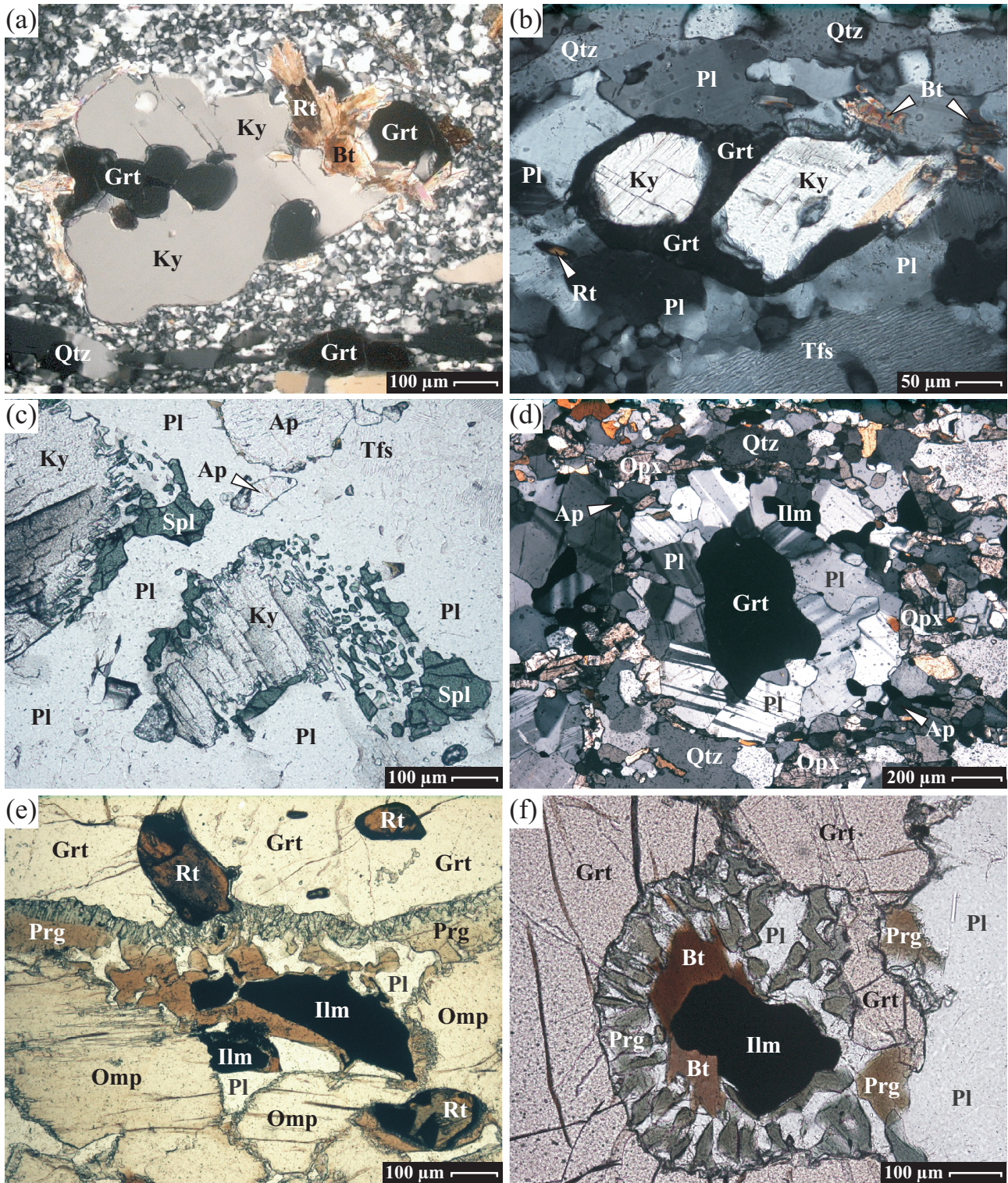


**Fig. 9.** Phase textures in the Granulite Complex: (a) Kyanite (Ky) set into a quartz-feldspar texture with ribbon quartz (Qtz) foliation is overgrown on garnet (Grt). Biotite (Bt) has locally replaced these minerals; BSE image. (b) Kyanite (Ky) thinly rimmed by garnet (Grt) is enveloped in corona plagioclase (Pl). Biotite (Bt) has replaced part of the garnet; plane-polarized light. (c) Spinel (Spl) penetrating kyanite (Ky) is shielded by corona plagioclase (Pl); plane-polarized light. (d) Relic garnet (Grt) enveloped in corona plagioclase (Pl) is embedded in finer grained orthopyroxene (Opx), clinopyroxene, plagioclase, quartz (Qtz), ilmenite (Ilm) and apatite (Ap) in the matrix; plane-polarized light. (e) Garnet (Grt), omphacite (Omp) and rutile (Rt) as peak minerals are overgrown by the assemblage pargasite (Prg)-plagioclase (Pl)-ilmenite (Ilm); plane-polarized light. (f) Symplectite of pargasite (Prg), biotite (Bt), plagioclase (Pl) and ilmenite (Ilm) replaces garnet (Grt); plane-polarized light.

granulites with the subsequent assemblages garnet-corundum-sapphirine-sillimanite, garnet-spinel-sapphirine-sillimanite, and prismatic-albite-quartz (Grew, 1986, 1989; Rötzler and Romer, 2001). Corundum, sapphirine, and spinel coexist with plagioclase but not quartz. Partial hydration during cooling at medium- to low-pressures is discernible from widespread assemblages of biotite, sillimanite, plagioclase, and quartz (Fig. 8c). The cooling path is well constrained by a sequence of retrograde reactions in the prismatic granulite that produced a second generation of tourmaline as well as dumortierite and andalusite (Grew, 1986) (Fig. 10).

A similar sequence of high- to low-pressure mineral assemblages occurs in the mafic granulites. The peak assemblage in mafic granulites from the Tirschheim borehole involves garnet, omphacite, titanite, hypersolvus feldspar, and quartz (Rötzler et al., 2004) (Fig. 8d-e). Quartz is absent in garnet-omphacite granulite at Greifendorf, where omphacite, plagioclase, and rutile are found as inclusions in garnet. Omphacite veined and rimmed by plagioclase reflects an early stage of the alteration into augite. Garnet-plagioclase assemblages with augite, augite-hypersthene, or hypersthene that commonly contain ilmenite and quartz evolved by decompression-induced recrystallisation. Mineral transformations along the decompression path are still recognizable in strongly overprinted mafic granulites showing corona plagioclase around large garnet grains in a finer grained matrix of pyroxene, plagioclase, quartz, and ilmenite (Fig. 9d). The mafic granulites were variably affected by hydrous reactions that produced several generations of amphibole consisting, in order, of pargasitic-tschermakitic amphibole, hornblende with local cummingtonite, and actinolite. The early amphibole generations which are associated with plagioclase, ilmenite, and in part also with biotite, K-feldspar and quartz form either foliation-parallel layers or symplectites pseudomorphic after garnet (Fig. 9e-f). These microstructures resemble the domainal deformation patterns caused by strain partitioning in the retrogressed felsic granulites (Fig. 8f). Actinolite is part of a late retrograde assemblage with epidote, chlorite, calcite, and secondary titanite (Rötzler et al., 2004; Rötzler et al., 2008).

The P-T conditions during the multi-stage metamorphism of the granulites were estimated from chemical and oxygen-isotopic equilibria between minerals and between whole rocks and minerals, respectively. The highest temperature feldspars recovered by reintegrating hypersolvus feldspars from felsic and mafic granulites place a minimum constraint on the peak temperature at 1000-1020 °C. Garnet-clinopyroxene thermometry using the least retrogressed garnet-omphacite granulites of the Tirschheim borehole has yielded temperature estimates of 950-1020 °C. As even these rocks display evidence of some retrograde re-equilibration, the data have been interpreted as lower limit on the thermal peak (Rötzler et al., 2004). Garnet-clinopyroxene temperature estimates of 1010-1060 °C for granulite at Waldheim (Rötzler and Romer, 2001) coincide with estimates of 990-1060 °C for garnet-omphacite granulite at Greifendorf (Rötzler et al., 2008). These results are supported by oxygen-isotope thermometry based on whole-rock/mineral fractionations in felsic and mafic granulites, which yield near-peak temperature estimates of 1000-1050 °C (Hagen et al., 2008). Pressure estimates for the assemblages garnet-kyanite-hypersolvus feldspar-quartz in felsic granulite, and garnet-omphacite-hypersolvus feldspar-quartz in mafic granulite consistently indicate a peak pressure of 2.2-2.3 GPa (Rötzler and Romer, 2001; Rötzler et al., 2004; Rötzler et al., 2008).

Štípská and Powell (2005) contested an ultrahigh-temperature metamorphism of the Moldanubian granulites and suggested to re-examine the metamorphism in other ultrahigh-temperature granulite terranes compiled by O'Brien and Rötzler (2003),

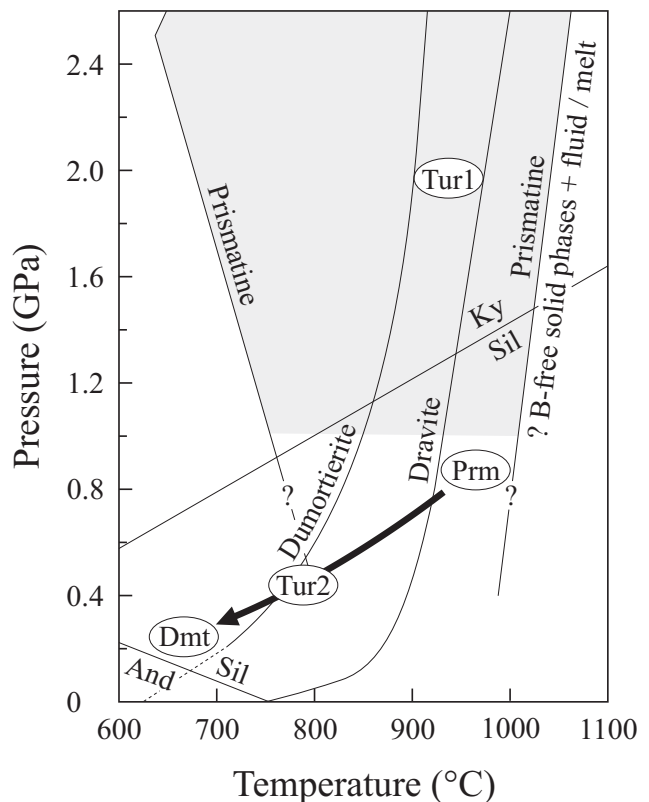


**Fig. 10.** Experimentally determined stability fields for boron minerals in the system  $\text{MgO-Al}_2\text{O}_3\text{-B}_2\text{O}_3\text{-SiO}_2\text{-H}_2\text{O}$  (Schreyer and Werding, 1997) shown in relation to the borosilicate sequence in prismatic granulite at Waldheim (Grew, 1986, 1989), with an arrow denoting the cooling path for this rock. The shaded area is the stability range of prismaticite.

including the SGM. Their arguments are based on interpreting the hypersolvus feldspars as an inherited igneous feature and on considering the garnet-clinopyroxene thermometry as an unsuitable means to determine ultrahigh temperatures. However, the ultrahigh-temperature peak and post-peak metamorphism of the Saxon granulites is additionally constrained by experimentally determined phase stability relations, petrogenetic grid evidence, and oxygen-isotope thermometry (Rötzler et al., 2008; Hagen et al., 2008). The early assemblage garnet-kyanite-corundum from prismatic granulite at Waldheim requires high-pressure conditions and temperatures above the stability limit of staurolite. The high- $X_{\text{Mg}}$  bulk-rock composition of this granulite shifts the breakdown reaction of staurolite that produces garnet, kyanite, and corundum toward the experimentally determined conditions in the system  $\text{MgO-Al}_2\text{O}_3\text{-SiO}_2\text{-H}_2\text{O}$ , where the breakdown of staurolite is observed over the pressure range of 1.5-3.0 GPa as temperature exceeds 900-920 °C (Fockenberg, 1998). The garnet-kyanite-corundum assemblage in the prismatic granulite is overprinted by the assemblage garnet-corundum-sapphirine-sillimanite. According to the P-T grid for silica-undersaturated granulites in the system  $\text{FeO-MgO-Al}_2\text{O}_3\text{-SiO}_2$  (Hensen, 1987), this decompression-induced assemblage is stable above the univariant reaction  $\text{Grt} + \text{Crn} + \text{Spr} = \text{Spl} + \text{Sil}$ , which emanates with a positive  $dP/dT$  slope from the invariant point [Cr] located at about 0.9 GPa and 950 °C. The crossing of this univariant reaction and the stabilisation of the divariant garnet-spinel-sapphirine-sillimanite assemblage are evident from phase relations found in sapphirine-bearing granulite (Rötzler and Romer, 2001) (Fig. 11).

**Table 1.** Compilation of U-Pb and Sm-Nd ages for the peak of metamorphism in the Granulite Complex.

| Age [Ma]          | Sample  | Rock             | Mineral       | Technique        | Ref. | Comment   |
|-------------------|---------|------------------|---------------|------------------|------|---|
| <b>U-Pb ages</b>  |         |                  |               |                  |      |   |
| 338 ± 4           | KLA1    | grt pyroxenite   | Zrn           | conv. U-Pb       | 1    | upper intercept   |
| 342 ± 4           | DIE7    | felsic granulite | Zrn           | conv. U-Pb       | 1    | upper intercept   |
| 352 ± 2           | DIE3    | mafic granulite  | Zrn           | conv. U-Pb       | 1    | upper intercept   |
| 339.8 ± 4.9       | DDR7a   | felsic granulite | Zrn           | U-Pb SHRIMP      | 2    |   |
| 340 + 4/-8        | DDR7a   | felsic granulite | Zrn           | conv. U-Pb       | 2    | lower intercept of slightly discordant analyses   |
| 339.7 ± 1.9       | DDR7a   | felsic granulite | Zrn           | vapour digestion | 2    | <sup>207</sup> Pb/ <sup>206</sup> Pb age, mean of four grains   |
| 339.8 ± 0.9       | DDR7a   | felsic granulite | Zrn           | evaporation      | 2    | <sup>207</sup> Pb/ <sup>206</sup> Pb age, mean of three grains  |
| 339.6 ± 1.0       | SGA     | felsic granulite | Zrn           | evaporation      | 2    | <sup>207</sup> Pb/ <sup>206</sup> Pb age, mean of three grains  |
| 339.7 ± 1.0       | Pa VIII | felsic granulite | Zrn           | evaporation      | 2    | <sup>207</sup> Pb/ <sup>206</sup> Pb age, mean of two grains  |
| 340.1 ± 1.2       | SG-3    | felsic granulite | Zrn           | evaporation      | 2    | <sup>207</sup> Pb/ <sup>206</sup> Pb age, mean of three grains  |
| 341.5 ± 0.8       | G97-1   | felsic granulite | Zrn           | conv. U-Pb       | 3    |   |
| 342.0 ± 0.8       | G97-3   | mafic granulite  | Ttn           | conv. U-Pb       | 3    |   |
| 340.7 ± 0.8       | 58.0 m  | mafic granulite  | Ttn           | conv. U-Pb       | 4    |   |
| <b>Sm-Nd ages</b> |         |                  |               |                  |      |   |
| 380 ± 14          | KLA1    | grt pyroxenite   | Grt, Cpx, Zrn | 4-point isochron | 1    |   |
| 335 ± 4           | ZSC1    | felsic granulite | Grt, Ky, Rt   | 4-point isochron | 1    |   |
| 346 ± 2           | DIE7    | felsic granulite | Grt, Ky       | 3-point isochron | 1    |   |
| 308 ± 9           | DIE8    | mafic granulite  | Grt, Cpx, Ap  | 4-point isochron | 1    | interpreted as dating low-pressure overprinting, coincides with the first appearance of granulite debris in post-orogenic sediments |

Data sources: 1, von Quadt (1993); 2, Kröner et al. (1998); 3, Romer and Rötzler (2001); 4, Rötzler et al. (2004).

Abbreviation: conv. = conventional.

The formation of prismatic from dravite-rich tourmaline and related H<sub>2</sub>O-deficient albite melting impose further constraints on the ultrahigh-temperature decompression path. Experiments on boron minerals revealed that prismatic is stable to higher temperatures than dravite, with a steep positive dP/dT slope and a temperature of the dravite breakdown reaction of 950 °C near the kyanite-sillimanite boundary (Schreyer and Werding, 1997) (Fig. 10). Hence, the presence of prismatic with inclusions of sillimanite suggests that decompression down to the sillimanite stability field took place at ultrahigh temperatures, in accord with oxygen-isotope equilibration among garnet, sillimanite, prismatic, plagioclase, and the whole-rock composition at 1020 °C Hagen et al., 2008). Re-equilibration of garnet with respect to X<sub>Mg</sub> with the assemblage augite-hypersthene-plagioclase-quartz enables to assess the decompression path in mafic granulites. Multi-equilibrium calculations suggesting partial equilibration of this assemblage in the P-T range of 1.1 GPa and 1030 °C also reveal preserved contents of Ca in garnet, and Al in hypersthene that correspond to higher pressure. Garnet and the corona assemblage hypersthene-plagioclase-quartz have partially re-equilibrated at pressures near 1.0 GPa and temperatures of 940-980 °C (Rötzler et al., 2008). P-T data of 0.92-0.94 GPa and 930-940 °C were obtained from spinel-plagioclase coronas on garnet and kyanite in felsic granulite (Rötzler and Romer, 2001).

The hydrous overgrowths provide thermometric but little barometric evidence, because pressure-sensitive reactions mostly were too slow, compared with the dissolution of minerals, such as garnet, to attain equilibrium. The metamorphism induced by the rising granulites in the structurally higher units as well as fluid entrapment and andalusite growth in the granulites themselves (Grew, 1986) indicate medium to low pressures during partial hydration of the granulites. Temperature estimates for garnet-biotite equilibria in felsic granulite vary from 800 °C to 650 °C, those for amphibole-plagioclase equilibria in mafic granulite range from 800 °C to 580 °C (Rötzler and Romer, 2001; Rötzler et al., 2004).

The time at which the granulites passed through peak P-T conditions is constrained by U-Pb zircon and titanite ages on samples taken over the entire Granulite Complex that fall in a narrow range around 341 Ma. This small range in U-Pb ages contrasts with the relatively large range in Sm-Nd ages from 380 ± 14 Ma to 308 ± 9 Ma (Table 1). The older Sm-Nd ages have been interpreted to date pre-peak metamorphism (cf. Franke, 2000), but most likely represent artefacts derived from rotated mixing lines (Romer and Rötzler, 2001; Romer and Rötzler, 2011). There is no geochronologic information on pre-peak metamorphism.

The exhumation history of the Granulite Complex is constrained by (i) the age of the metamorphic peak (ca. 341 Ma, see above), (ii) the age of post-metamorphic shallow-level granite intrusions (e.g., 338 ± 5 Ma [von Quadt, 1993; conventional U-Pb on zircon], 333.1 ± 1.0 Ma [Kröner et al., 1998; <sup>207</sup>Pb/<sup>206</sup>Pb zircon evaporation, mean of three grains]), (iii) the age of decompressional heating and partial melting in the Cordierite-Gneiss Unit, which is tectonically juxtaposed against the Granulite Complex (340 ± 7 Ma [Vavra in Franke and Stein, 2000; SHRIMP U-Pb on zircon]), and (iv) the age of metamorphic minerals that formed in the granulites during exhumation (338.0 ± 0.5 Ma [Romer and Rötzler, 2001; conventional U-Pb on monazite], 337 ± 1 Ma [Romer and Rötzler, 2003; conventional U-Pb on recrystallised low-F titanite]). Additional constraints come from the age of the oldest non-marine sediments (Hainichen Subgroup) deposited during the exhumation of the granulites. These sediments do not contain debris from the Granulite Complex, but contain ca. 337 Ma old granite pebbles believed to be derived from the Mittweida or Berbersdorf granites (Gehmlich, 2003), which have been emplaced into the SGM at shallow depths. The age data largely overlap for rocks that formed at widely different pressures (Fig. 3) and require fast exhumation bringing rocks from 2.3 GPa close to the surface in ca. 8 ± 2 Ma. Because of large uncertainties of ages associated with rocks that were brought in contact with the granulites at medium and low pressure conditions, only average exhumation rates could be calculated. Using the ages of

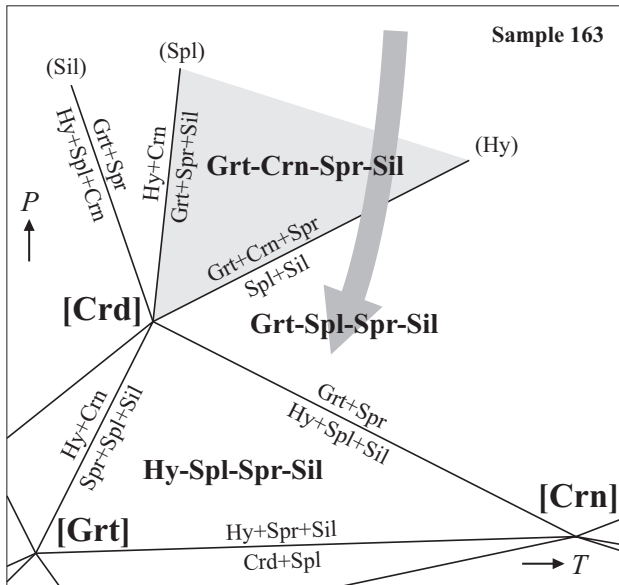


**Fig. 11.** Section of the FMAS grid for silica-undersaturated granulites: The invariant point [Crd] occurs at about 0.9 GPa and 950 °C (Hensen, 1987). Mineral assemblages and reactions reported by Grew (1986), and Rötzler and Romer (2001) indicate that the decompression P-T path (arrow) in the Saxon granulites crossed the divariant field garnet-corundum-sapphirine-sillimanite (shaded area) and subsequently went into the divariant field garnet-spinel-sapphirine-sillimanite.

the shallow-level granite intrusion at Wolkenburg (ca. 333 Ma, Kröner et al., 1998) and the metamorphic peak of the granulites (ca. 341 Ma) yields average rates of exhumation and cooling of 7-13 mm/year and 40-70 °C/Ma, respectively (Rötzler et al., 2004), which is markedly higher than those obtained from thermo-tectonic modelling of the exhumation of the granulites by Henk (1995, 2000), who assigned the age of 341 Ma to a pressure of 1.2 GPa rather than to metamorphic peak conditions.

U-Pb mineral ages on granulites (Romer and Rötzler, 2001, 2003; Rötzler et al., 2004) (Fig. 3) and Rb-Sr mica ages obtained along a traverse from the Granulite Complex across the Cordierite-Gneiss Unit into the Schist Cover (Rötzler and Romer, 2010) (Fig. 5) confirmed the earlier recognized relatively high average rates for exhumation and cooling and, additionally, constrained the time when the granulites arrived in the middle and upper crust. These data demonstrate that exhumation was fast in the first 2-4 Ma after the pressure peak but slowed down when the granulites arrived in the middle crust. The granulites may have reached an average exhumation rate of 9-18 mm/year and an average cooling rate of 25-50 °C/Ma during early, near-isothermal exhumation (Model 1, Romer and Rötzler, 2001). The cooling rate after the end of near-isothermal decompression of the granulites is probably underestimated when using an Rb-Sr biotite age of ca. 323 Ma (Romer and Rötzler, 2001) for calculation, as this age markedly postdates the Rb-Sr biotite age of ca. 333 Ma from granulite at Tirschheim (Rötzler et al. 2004) as well as K-Ar and Rb-Sr biotite ages from the Cordierite-Gneiss Unit and the Schist Cover (Werner and Reich, 1997; Rötzler and Romer, 2010) (Fig. 5). Possible reasons for the younger Rb-Sr biotite age include recrystallisation or submicroscopic chloritization. Considering the average rate of 40-70 °C/Ma for most of the cooling history (Rötzler et al., 2004) and the average rate of 25-50 °C/Ma for early cooling during near-isothermal exhumation (Romer and Rötzler, 2001), an increase in cooling rate with progressing exhumation

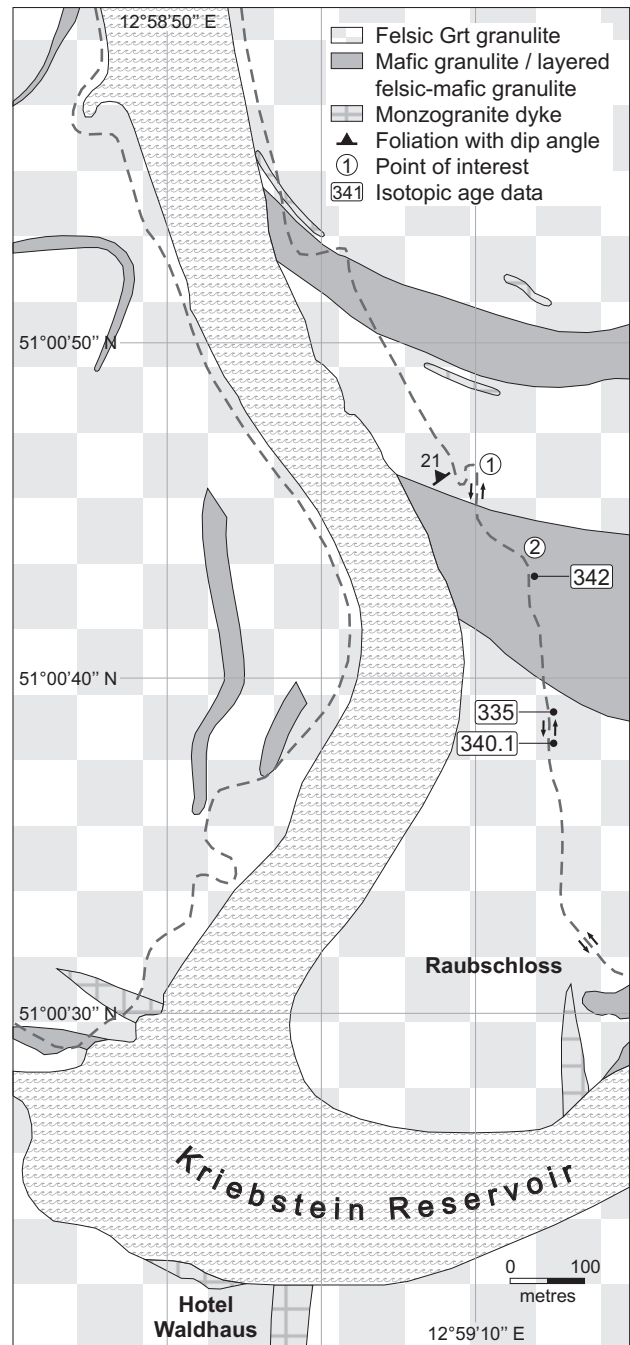


**Fig. 12.** Geology of the Granulite Complex northwest of Ringethal (Neumann in Müller, 1987c). The age data of 342 ± 8 Ma, 335 ± 4 Ma, and 340.1 ± 1.2 Ma for felsic granulites are Rb-Sr thin slab isochron, Sm-Nd mineral isochron, and single-zircon evaporation ages, respectively (Gorokhov et al., 1987; von Quadt, 1993; Kröner et al., 1998).

has to be expected that is in line with thermal models of exhumation processes (e.g., Grasemann et al. 1998). The fast cooling of the granulites shows a strong thermal contrast between the hot granulites and cooler rocks during juxtaposition, accompanied by heating of the hanging-wall rocks, even though the present structural relationship between Granulite Complex and Schist Cover only reflects the late stage of exhumation.

We will get off the coach on a small road at the northern end of Ringethal. Since the driver can stop there only to leave us out and in, please take care that you and your co-participants get off

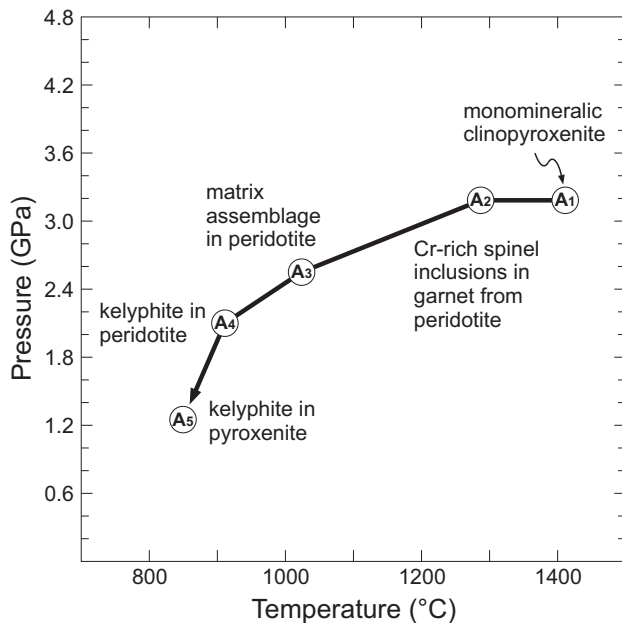


**Fig. 13.** P-T path proposed for the garnet-bearing ultramafic rocks (Schmädicke et al., 2010).

quickly and return to this point at the time determined by the guide. A 500 metre walk along a cart road will lead us to the bluff of the Kriebstein Reservoir, where we will follow a north-heading trail (arrows in Fig. 12) for another 500 metres until the trail starts to snake downhill (point 1 in Fig. 12). On the way there, we will cross a sequence of predominantly felsic granulites with centimetre- to metre-thick interlayers of mafic granulite. The exposed felsic granulites are fine-grained rocks in which discrete aligned quartz lenses and cigar-like aggregates of secondary garnet and spinel define the S2 foliation. Weak retrograde alteration is locally discernible from a mottled appearance caused by biotite rims on garnet. The fine-grained mafic granulites are quartz-two-pyroxene-plagioclase rocks without garnet. Note the weathered surfaces of the crags, where differences in weathering susceptibility highlight the compositional layering (S1 transposed parallel to S2) and, in particular, the syn-D2 isoclinal folding of the rocks. The S2 foliation dips gently to the northwest. On our way back, we will pass a block of biotite granite with pegmatite nests that represents dyke intrusions into the granulites (behind the bench at point 2 in Fig. 12).

## Eurogranites 2012

### Stop 4-4

Granulite Complex with ultramafic intercalations

Reinsdorf quarry

WGS84 coordinates: 51°03'41.0" N, 13°00'09.0" E, 250 m a.s.l.

Guide: Jochen Rötzler

This stop shows an example of the ultramafic rocks that occur in sheet-like bodies concordant with the S2 foliation of the granulites. The layered bodies, up to several square kilometres in extent, consist of dunitic, harzburgitic, and lherzolitic serpentinites associated with minor garnet pyroxenite and plagioclase-bearing mafic granulite. The lherzolitic serpentinites contain variable proportions of relic garnet. As shown by  $\epsilon\text{Nd}_{T=340}$  values between +7.3 and -1.2 (von Quadt, 1993, data recalculated to 340 Ma), these rocks developed from more depleted mantle sources than the metatholeiitic granulites, but have been variably contaminated with crustal material. Garnet pyroxenite intercalated within serpentinite at Reinsdorf exhibits a sequence of textural features defined by lamellar exsolution and granoblastic recrystallisation of garnet and clinopyroxene. P-T estimates of ca. 2.5 GPa at 1000-1030 °C and 1.1 GPa at 900-975 °C obtained from these assemblages (Massonne and Bartsch, 2002) fall close to the metamorphic peak and on the decompression path of the granulites, respectively, suggesting that mantle slivers and deeply buried continental crust rocks have been associated since the metamorphic peak of the granulites. Reintegration indicates that the lamellar exsolution texture in the garnet pyroxenite evolved from either Al-rich clinopyroxene or majoritic garnet. Massonne and Bartsch (2002) favoured majoritic garnet as the most likely precursor mineral, which would require a derivation from depths >400 km in the transition zone between upper and lower mantle. Schmädicke et al. (2010) derived a P-T path for garnet peridotite and garnet pyroxenite through the following formation and recrystallisation stages (Fig. 13): i) crystallisation of monomineralic clinopyroxenite as a cumulate of mantle-derived melt at 3.2-3.6 GPa and 1400 °C, ii) equilibration of Cr-rich spinel inclusions and host garnet in peridotite at 3.2 GPa and 1300-1400 °C, iii) equilibration of the matrix assemblage in peridotite at 2.6 GPa and 1000-1050 °C, iv) equilibration of the kelyphite assemblage in peridotite at 2.2 GPa and 900-940 °C, and v) equilibration of the kelyphite assemblage in pyroxenite at 1.2-1.3 GPa and 860 °C. They inferred that the ultramafic rocks evolved during asthenosphere upwelling and cooling in response to slab break-off and that the exhumation of these rocks caused the ultrahigh-temperature metamorphism of the granulites.

## Eurogranites 2012

### Stop 4-5

Berbersdorf granite quarry  
(late-orogenic magmatism)

WGS84 coordinates: 51°01'09.3" N, 13°10'11.9" E, 240 m a.s.l.

Guide: Uwe Kroner

The Saxon granulites belong to the NW part of the allochthonous domain of the Saxo-Thuringian Zone (Kroner et al., 2007). The HP/UHT granulites originated from a continental subduction zone and were rapidly exhumed to upper crustal levels. The exhumation occurred along localized high temperature shear zones containing significant volumes of melt (Kroner, 1995). This strain localization prevented the granulites of the core from pervasive deformation in middle and upper crustal levels. Advective heat transfer from the granulites caused isobaric heating of the low grade rocks that are incorporated into the shear zones (Kroner, 1995; Reinhard and Kleemann, 1994) along the hanging wall of the exhuming granulites. The synkinematic Berbersdorf granite is part of this roof detachment zone of the Saxon granulites. From the bottom to the top the detachment zone contains

lenses of ultramylonitic kyanite bearing granulites tectonically interlayered with sheared gabbros and serpentinites, sillimanite bearing-metapelites, mylonitic orthogneisses, and andalusite bearing schists. These mylonitic granulites that evolved under high-pressure conditions are juxtaposed with HT/MP to HT/LP rocks (Kroner, 1995; Reinhard and Kleemann, 1994; Rötzler and Romer, 2001), indicating that the detachment conserves the record of a considerable part of the exhumation path. All tectonic units are pervasively foliated under high temperature conditions and uniformly contain a NW-SE oriented stretching lineation. Shear sense indicators such as shearbands and asymmetric porphyroclasts indicate a simple shear component top to the SE. Because the roof detachment zone wraps around the granulitic core (Fig. 13) the shearing displays reverse faulting in the NW and normal faulting in the SE. The exhumation to upper crustal levels led to final brittle-ductile overprinting of the ductile detachment as indicated by the particular structures like shear zones containing completely retrogressed mylonites and ultra-cataclasites. On a first view, the metamorphic core and the upper crustal units separated by a low angle detachment in the roof have the geometry of a typical metamorphic core complex (Kroner et al., 2007; Reinhard and Kleemann, 1994). However, this model must be rejected because the high pressure metamorphism of the granulites requires the subsequent exhumation from mantle depth. This cannot be realized via extensional tectonics. Moreover, the orogen is under compression during the entire subduction exhumation process (Hahn et al., 2010; Kroner et al., 2007). Alternatively to extensional unroofing extrusion tectonics from a subduction zone is proposed as the underlying process (Kroner, 1995; Kroner and Görz, 2010). Vertical extrusion from the subduction zone to lower crustal levels, followed by lateral NW extrusion represent the final evolution stages of the Allochthonous Domain.

The Berbersdorf granite and the adjacent rocks of the detachment zone are interpreted to represent the upper part of this exhumation channel (Fig. 14).

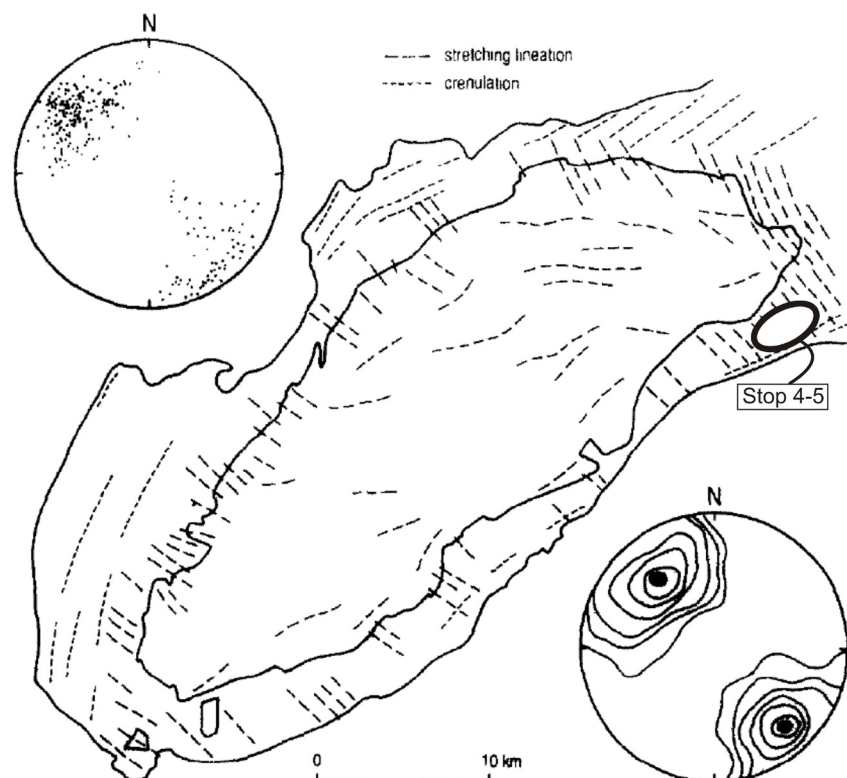


**Fig. 13.** Lineation pattern in the Saxon granulites and stereographic plot of the stretching lineation along the roof detachment zone of the granulites (Behr, 1961, in Reinhardt and Kleemann).

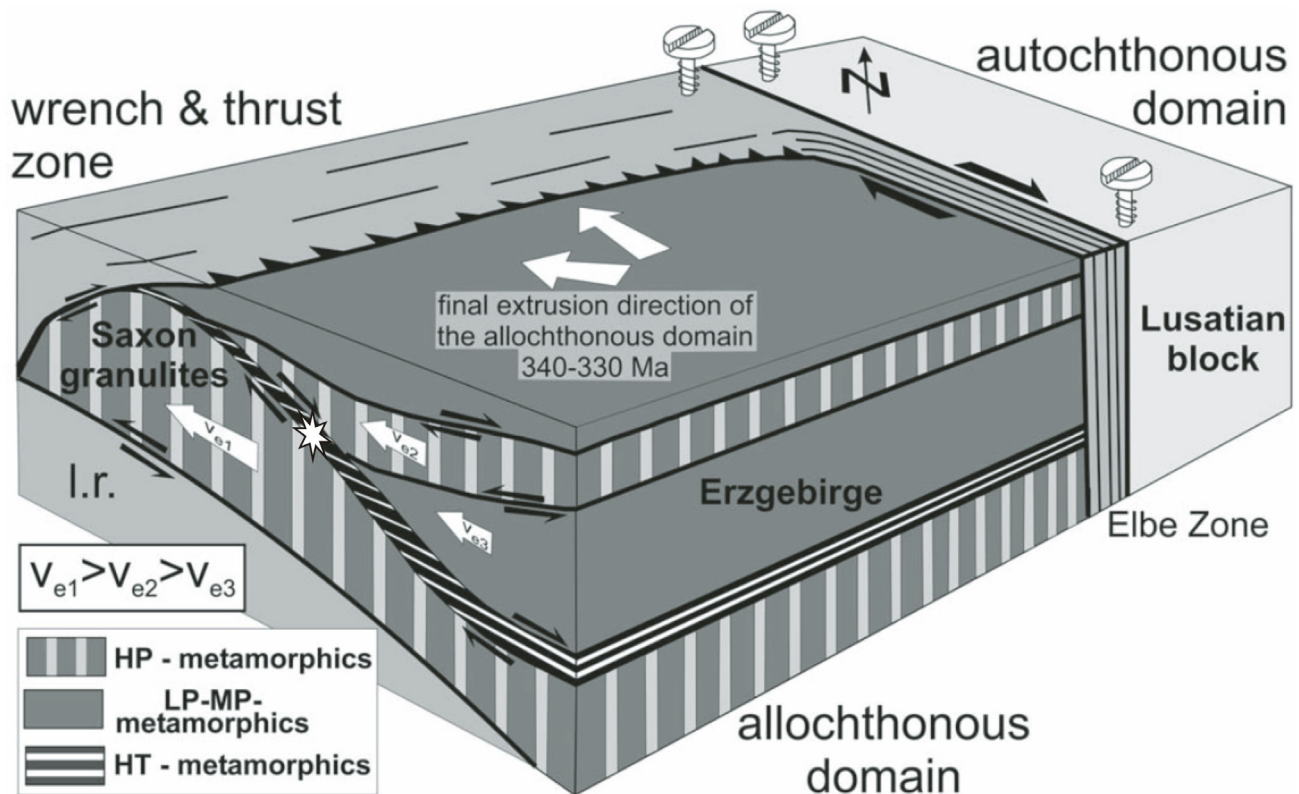


**Fig. 14.** Extrusion model for the NE part of the allochthonous domain of the Saxo-Thuringian Zone. (Kroner et al. 2007) white star: position of the Berbersdorf granite.

Apart from any geodynamic model, isotopic data imply that the age of the Berbersdorf granite (U/Pb monazite:  $338 \pm 5$  Ma (von Quadt, 1993) is very close to the age of the metamorphic peak of the Saxon granulites ( $\sim 340$  Ma). Because of the common occurrence of metapelites of the HT/VLP stage as xenolites in the Berbersdorf granite, the intrusion depth can be constrained with  $\sim 3$  kbar and  $\sim 800^\circ\text{C}$ . Thus the granulites were exhumed into the upper crust in less than 7 My.

In the Berbersdorf quarry we will examine the zones containing the xenolites as well as late kinematic shear zones transecting the granite. Along the northern contact, strongly deformed schists and interlayered granites highlight the synkinematic character of the granite.

## References

- Behr, H.-J. (1983) Intracontinental and subcrustal thrust tectonics at the northern margin of the Bohemian massif. In: Martin, H. & Eder, F.W. (eds.) *Intracontinental Fold Belts*. Springer-Verlag, Berlin, pp. 366-403.
- Bergner, R. (1990) Vergleichende Untersuchungen an temperaturbetont metamorphisierten Gesteinen ausgewählter Einheiten des Saxothuringikums. *Freib. Forschungsh. C439*: 6-68.
- Clauer, N., Hoffert, M., Karpoff, A.-M. (1982) The Rb-Sr isotope system as an index of origin and diagenetic evolution of southern Pacific red clays. *Geochim. Cosmochim. Acta*, 46:2661-2666.
- Dymoke, P., Sandiford, M. (1992) Phase relations of Buchan facies series pelitic assemblages: calculations and application to the Mount Lofty Ranges, South Australia. *Contrib. Mineral. Petrol.* 110: 121-132.
- Fockenberg, T. (1998) An experimental investigation on the P-T stability of Mg-staurolite in the system  $\text{MgO-Al}_2\text{O}_3\text{-SiO}_2\text{-H}_2\text{O}$ . *Contrib. Mineral. Petrol.* 130: 187-198.
- Franke, W. (1993) The Saxonian granulites: a metamorphic core complex? *Geol. Rundsch.* 82: 505-515.
- Franke, W. (2000) The mid-European segment of the Variscides: tectonostratigraphic units, terrane boundaries and plate tectonic evolution. In: Franke, W., Haak, V., Oncken, O., Tanner, D. (eds.) *Orogenic Processes: Quantification and Modelling in the Variscan Belt*. *Geol. Soc., London, Spec. Publ.* 179: 35-61.
- Franke, W., Stein, E. (2000) Exhumation of high-grade rocks in the Saxo-Thuringian Belt: geological constraints and geodynamic concepts. In: Franke, W., Haak, V., Oncken, O., Tanner, D. (eds.) *Orogenic Processes: Quantification and Modelling in the Variscan Belt*. *Geol. Soc., London, Spec. Publ.* 179: 337-354.
- Gehmlich, M. (2003) Die Cadomiden und Varisziden des Saxothuringischen Terranes - Geochronologie magmatischer Ereignisse. *Freib. Forschungsh. C 500*: 129 pp.
- Gerstenberger, H., ed. (1987). *Contributions to the Geology of the Saxonian Granulite Massif*. *ZfI-Mitteilungen*, 133: 374 pp.
- Gorokhov, I.M., Anderson, E.B., Melniko, N.N., Mitrofanov, F. P., Kutuyavin, E.P., Bizunok, M.B., Rocheva, O.N. (1987) Geochronology of metamorphic rocks of the Sächsisches Granulitgebirge (G.D.R.). In: Gerstenberger, H. (ed.) *Contributions to the Geology of the Saxonian Granulite Massif*. *ZfI-Mitt.* 133: 43-62.
- Grasemann, B., Ratschbacher, L., Hacker, B.R. (1998) Exhumation of ultrahigh-pressure rocks: thermal boundary conditions and cooling history. In Hacker, B.R. & Liou, J.G. (eds.) *When Continents Collide: Geodynamics and Geochemistry of*

- Ultrahigh-Pressure Rocks. Kluwer Academic, Dordrecht, pp. 117-139.
- Green, D.H., Ringwood, A.E. (1967) An experimental investigation of the gabbro to eclogite transformation and its petrological applications. *Geochim. Cosmochim. Acta* 31: 767-833.
- Grew, E.S. (1986) Petrogenesis of kornerupine at Waldheim (Sachsen). *Z. Geol. Wiss.* 14: 525-558.
- Grew, E.S. (1989) A second occurrence of kornerupine in Waldheim, Saxony, German Democratic Republic. *Z. Geol. Wiss.* 17: 67-76.
- Hagen, B. (1994) Thermometrie und Geochemie an Gesteinen des Sächsischen Granulitgebirges. Unpubl. Diploma Thesis, Math.-Nat. Fak., Univ. Bonn, 69 pp.
- Hagen, B. (2002) Rekonstruktion von Metamorphosepfaden mit stabilen Isotopen: Möglichkeiten der Laserfluorinierung am Beispiel des Sächsischen Granulitgebirges. Unpubl. PhD Thesis, Math.-Nat. Fak., Univ. Bonn, 169 pp.
- Hagen, B., Hoernes, S., Rötzler, J. (2008) Geothermometry of the ultrahigh-temperature Saxon granulites revisited. Part II: Thermal peak conditions and cooling rates inferred from oxygen-isotope fractionations. *Eur. J. Mineral.* 20: 1117-1133.
- Hahn, T., Kroner, U., Melzer, P. (2010) Lower Carboniferous synorogenic sedimentation in the Saxo-Thuringian Basin and the adjacent Allochthonous Domain. In: Linnemann, U., Romer, R.L. (eds.), *Pre-Mesozoic Geology of Saxo-Thuringia - From the Cadomian Active Margin to the Variscan Orogen*. Schweizerbart Sci. Publ., Stuttgart, pp. 171-192.
- Henk, A. (1995) Variscan exhumation of the Saxonian Granulite Massif - preliminary results from two-dimensional thermal-kinematic modelling. *Terra Nostra* 95/8: 29-35.
- Henk, A. (2000) Foreland-directed lower-crustal flow and its implications for the exhumation of high-pressure – high-temperature rocks. In: Franke, W., Haak, V., Oncken, O., Tanner, D. (eds.) *Orogenic Processes: Quantification and Modelling in the Variscan Belt*. Geol. Soc., London, Spec. Publ. 179: 355-368.
- Hensen, B.J. (1987) P-T grids for silica-undersaturated granulites in the systems MAS (n+4) and FMAS (n+3) - tools for the derivation of P-T path of metamorphism. *J. Metam. Geol.* 5: 255-271.
- Ito, K., Kennedy, G.C. (1971) An experimental study of the basalt-garnet granulite-eclogite transition. In: Heacock, J.G. (ed.) *The structure and physical properties of the Earth's crust*. Am. Geophys. Union, Monogr. 14: 303-314.
- Johannes, W., Holtz, F. (1996). *Petrogenesis and experimental petrology of granitic rocks*. Springer-Verlag, Berlin, Heidelberg, 335 pp.
- Kröner, A., Jaeckel, P., Reischmann, T., Kroner, U. (1998) Further evidence for an early Carboniferous (~340 Ma) age of high-grade metamorphism in the Saxonian granulite complex. *Geol. Rundsch.* 86: 751-766.
- Kroner, U. (1995) Postkollisionale Extension am Nordrand des Böhmisches Massivs: Die Exhumierung des Sächsischen Granulitgebirges. *Freib. Forschungsh.* C457: 1-114.
- Kroner, U., Görz, I. (2010) Variscan assembling of the Allochthonous Domain of the Saxo-Thuringian Zone - a tectonic model. In: Linnemann, U., Romer, R.L. (eds.), *Pre-Mesozoic Geology of Saxo-Thuringia - From the Cadomian Active Margin to the Variscan Orogen*. Schweizerbart Sci. Publ., Stuttgart, pp. 271-286.
- Kroner, U., Hahn, T., Romer, R.L., Linnemann, U. (2007) The Variscan orogeny in the Saxo-Thuringian Zone - Heterogenous overprint of Cadomian/Palaeozoic Peri-Gondwana crust. *Geol. Soc. Am., Spec. Pap.* 423, 153–172.
- Lorenz, W., Nitzsche, H.-M. (2000) Stratigraphische Konzepte, Metamorphose und Kohlenstoffisotope im Rahmen und im Kern des sächsischen Granulitgebirges. *Z. Geol. Wiss.* 28: 321-360.
- Massonne, H.-J., Bausch, H.-J. (2002) An unusual garnet pyroxenite from the Granulitgebirge, Germany: origin in the Transition Zone (>400 km depths) or in a shallower upper mantle region? *Int. Geol. Rev.* 44: 779-796.
- Müller, A., Böttger, T., Geisler, M., Stiehl, G. (1987a) Major and trace element distributions in the cordierite gneisses and the garnet sillimanite fels of the Sächsisches Granulitgebirge. In: Gerstenberger, H. (ed.) *Contributions to the Geology of the Saxonian Granulite Massif*. ZfI-Mitt. 133: 215-220.
- Müller, A., Stiehl, G., Böttger, T., Bothe, H.-K., Gebhardt, O., Geisler, M., Haendel, D., Nitzsche, H.-M., Schmädicke, E. (1987b) Geochemical, stable isotope and petrographic investigations of granulites, pyriclases and metagranulitic rocks of the Sächsisches Granulitgebirge. In: Gerstenberger, H. (ed.) *Contributions to the Geology of the Saxonian Granulite Massif*. ZfI-Mitt. 133: 145-205.
- Müller, A. (1987c) Sampling in the Sächsisches Granulitgebirge for the investigations reported in this volume. In: Gerstenberger, H. (ed.) *Contributions to the Geology of the Saxonian Granulite Massif*. ZfI-Mitt. 133: 35-42.
- Neumann, W. (1976) Geologisch-geochemische Kurzcharakteristik einer präkambrischen Verwitterungskruste auf dem sächsischen Granulitmassiv. *Z. Angew. Geol.* 22: 177-181.
- Neumann, W. (1985) Granulitmassiv: Lithostratigraphie und Tektonik. Gesellschaft für Geologische Wissenschaften der DDR, Exkursionsführer und Kurzreferate, 24 pp.
- O'Brien, P.J., Rötzler, J. (2003) High-pressure granulites: formation, recovery of peak conditions, and implications for tectonics. *J. Metam. Geol.* 21: 1-19.
- Reinhardt, J., Kleemann, U. (1994) Extensional unroofing of granulitic lower crust and related low-pressure, high-temperature metamorphism in the Saxonian Granulite Massif, Germany. *Tectonophysics* 238: 71-94.
- Reinhardt, J., Vavra, G. (1997) Petrological and geochronological constraints on the tectono-metamorphic history of the Saxonian Granulite Massif. *Terra Nostra* 97/5: 137-139.
- Rollinson, H.R. (1993) *Using geochemical data: evaluation, presentation, interpretation*. Longman Scientific & Technical, Harlow, England, 352 pp.
- Romer, R.L., Rötzler, J. (2001) P-T-t evolution of ultrahigh-temperature granulites from the Saxon Granulite Massif, Germany. Part II: U-Pb dating of trace and major phases. *J. Petrol.* 42: 2015-2032.
- Romer, R.L., Rötzler, J. (2003) Effect of metamorphic reaction history on the U-Pb dating of titanite. In: Vance, D., Müller, W., Villa, I.M. (eds.) *Geochronology: Linking the Isotopic Record with Petrology and Textures*. Geol. Soc., London, Spec. Publ. 220: 147-158.
- Romer, R.L., Rötzler, J. (2011) The role of element distribution for the isotopic dating of metamorphic minerals. *Eur. J. Mineral.* 23: 17-33
- Rötzler, J. (1992) Zur Petrogenese im Sächsischen Granulitgebirge. Die pyroxenfreien Granulite und die Metapelite. *Geotekt. Forsch.* 77: 1-100.
- Rötzler, J., Werner, C.-D., Kroner, U. (1994) P-T-time paths, deformation history and protoliths at the type locality of the granulite. 11th Conference of the International Basement Tectonics Association, Potsdam, July 25-29, Guidebook, 9-52.
- Rötzler, J., Romer, R.L. (2001) P-T-t evolution of ultrahigh-temperature granulites from the Saxon Granulite Massif, Germany. Part I: Petrology. *J. Petrol.* 42: 1995-2013.

- Rötzler, J., Romer, R.L., Budzinski, H., Oberhänsli, R. (2004) Ultrahigh-temperature high-pressure granulites from Tirschheim, Saxon Granulite Massif, Germany: P-T-t path and geotectonic implications. *European Journal of Mineralogy*, 16, 917-937.
- Rötzler, J., Hagen, B., Hoernes, S. (2008) Geothermometry of the ultrahigh-temperature Saxon granulites revisited. Part I: New evidence from key mineral assemblages and reaction textures. *European Journal of Mineralogy*, 20, 1097-1115.
- Rötzler, J., Romer, R. L. (2010) The Saxon Granulite Massif: a key area for the geodynamic evolution of Variscan central Europe. In: Linnemann, U. & Romer, R. L. (eds.). *Pre-Mesozoic Geology of Saxo-Thuringia: From the Cadomian Active Margin to the Variscan Orogen*. Stuttgart, Germany: E. Schweizerbart Science Publishers, pp. 233-252.
- Scheumann, K.-H. (1925) Die gesteins- und mineralfazielle Stellung der Metakieselschiefergruppe der südlichen Randzone des sächsischen Granulitgebirges. *Abh. Math.-Phys. Kl. Sächs. Akad. Wiss.* 39: 48 pp.
- Scheumann, K.-H., Huckenholz, G. (1961) Die Cordieritgneise und Granatgneise des sächsischen Granulitgebirges. *N. Jb. Mineral., Abh.* 96: 131-161.
- Schmädicke, E., Gose, J., Will, M. (2010). The P-T evolution of ultra high temperature garnet-bearing ultramafic rocks from the Saxonian Granulitgebirge Core Complex, Bohemian Massif. *J. Metam. Geol.* 28: 489-508.
- Schneider, J.W., Hoth, K., Gaitzsch, B. G., Berger, H.J., Steinborn, H., Walter, H., Zeidler, M.K. (2005) Carboniferous stratigraphy and development of the Erzgebirge Basin, East Germany. *Z. Dt. Ges. Geowiss.* 156: 431-466.
- Schreyer, W., Werding, G. (1997) High-pressure behaviour of selected boron minerals and the question of boron distribution between fluids and rocks. *Lithos* 41: 251-266.
- Sebastian, U. (1990) Zur Stratigraphie, Lithologie und Tektonik in der Umgebung des Sächsischen Granulitgebirges. Unpubl. Diploma Thesis, Math. Nat. Fak., TU Bergakad. Freiberg, 61 pp.
- Štípská, P., Powell, R. (2005) Does ternary feldspar constrain the metamorphic conditions of high-grade meta-igneous rocks? Evidence from orthopyroxene gneisses, Bohemian Massif. *J. Metam. Geol.* 23: 627-647.
- Spear, F.S. (1993) Metamorphic phase equilibria and pressure-temperature-time paths. *Min. Soc. Am., Washington, D.C.*, 799 pp.
- Vavra, G., Reinhardt, J. (1997) Which processes are dated by U/Pb zircon ages of high-grade metamorphic rocks? Zircon genesis in various lithologies and structural levels of the Saxonian Granulite Massif. *Terra Nostra* 97/5: 190-192.
- Vinogradov, V.I., Pokrovsky, B. G. (1987) O-18 and Rb-Sr systematics in metamorphic rocks of the Saxonian granulite massif. In: Gerstenberger, H. (ed.) *Contributions to the Geology of the Saxonian Granulite Massif*. *ZfJ-Mitt.* 133: 73-87.
- von Quadt, A. (1993) The Saxonian Granulite Massif: new aspects from geochronological studies. *Geol. Rundsch.* 82: 516-530.
- Werner, C.-D. (1987) Saxonian granulites: a contribution to the geochemical diagnosis of original rocks in high-metamorphic complexes. *Gerlands Beitr. Geophys.* 96: 271-290.
- Werner, O., Reich, S. (1997)  $^{40}\text{Ar}/^{39}\text{Ar}$ -Abkühlalter von Gesteinen mit unterschiedlicher P-T-Entwicklung aus dem Schiefermantel des Sächsischen Granulitgebirges. *Terra Nostra* 97/5: 196-198.

# Late–Variscan felsic magmatism in the western Erzgebirge–Vogtland

Hans-Jürgen Förster  
Reservoir Technologies  
GFZ German Research Centre for Geosciences  
hans-juergen.foerster@gfz-potsdam.de

Abundant, compositionally diverse granitic rocks and minor, mostly rhyolitic dikes are the expression of late-Variscan felsic magmatic processes shaping this part of the Saxothuringian Domain of the Central European Variscides. The bulk of the postkinematic granitic plutons formed late collisionally, between ca. 328 Ma and 318 Ma. Subsequent post-collisional anatectic melting gave rise to the emplacement of chemically evolved dike rocks of predominantly rhyolitic composition between roughly 305 Ma and 300 Ma.

The granitic rocks in the Erzgebirge are classed into five types on the basis of distinguishing compositional and mineralogical properties (Förster et al., 1998, 1999): (1) low-F biotite granites, (2) low-F two-mica granites, (3) high F–P<sub>2</sub>O<sub>5</sub> Li-mica granites, (4), high-F, low- P<sub>2</sub>O<sub>5</sub> Li-mica granites, and (5) medium-F biotite granites. Rocks of groups 1 and 2 are transitional I–S type granites, those of group 3 originated from melting of predominantly, but likely not exclusively metasedimentary material (transitional S–I-type). Rocks belonging to groups 4 and 5 display chemical characteristics trending towards aluminous A-type granites/rhyolites.

In the western Erzgebirge–Vogtland, granites of the types 1 to 3 predominate among the late-Variscan felsic rocks (Fig. 1). Rocks of type 5 are subordinate and postdate the emplacement of the aforementioned granites. Granites of type 4, which are abundant in the eastern Erzgebirge, are missing.

In the following, a brief survey on the various granitic/rhyolitic occurrences is provided, with special emphasis on their geochemistry and mineralogy. Inferences on their origin and precursors and a comprehensive overview on geochronology are given by Romer (this volume).

## 1. Multi-phase granite massifs west of the Gera–Jáchymov Lineament Zone

The largest well-exposed plutons of group 1 to 3 granites that also show the greatest range in internal differentiation, are the temporally and spatially closely related massifs of Kirchberg (low F biotite granites), Bergen (low-F two-mica granites), and Eibenstock (high F–P<sub>2</sub>O<sub>5</sub> Li-mica granites). Intrusion of the Kirchberg and Bergen granites took place at around 325 Ma and predated the emplacement of the Eibenstock granite by roughly 5 Ma (Förster et al., 1999).

The three massifs share the common feature that they are built up by a succession of genetically related, texturally and compositionally distinct sub-intrusions (Fig. 2, Table 1). Cognate

magmatic enclaves are common only in the least evolved sub-intrusion of Bergen, extremely rare in the Kirchberg massif, and missing in the Eibenstock pluton.

All the granites have low values of magnetic susceptibility (2.7 to 0.01 × 10<sup>-3</sup> SI), which permits their classification in the ilmenite series. They are further characterized by high radioactive heat production, which increases with differentiation within each massif as follows: Kirchberg (2 → 10 μW/m<sup>3</sup>), Bergen (3 → 9 μW/m<sup>3</sup>) and Eibenstock (6 → 12 μW/m<sup>3</sup>; in samples not exposed to alteration and weathering).

The most highly-fractionated Eibenstock granites correspond to the "high-P" subtype of topaz granites and are similar to other extremely evolved P-rich, rare-metal granites in the Variscan chain of Europe, including St. Austell, SW England, Beauvoir, French Massif Central, and Argemela, Portugal. Associated pegmatites are of the LCT family (Li–Cs–Ta as indicative elements).

### 1.1. Petrography and mineralogy

Siderophyllite is the principal mafic mineral in the Kirchberg biotite granites (monzogranites). Feldspars include zoned plagioclase associated with myrmekite and perthitic alkali-feldspar with prominent microcline twinning. Cordierite (pinitized) is rare. The occurrence of allanite-(Ce) is restricted to phase KIB1 (cf. Table 1); in more-fractionated later sub-intrusions, monazite-(Ce) constitutes the main LREE carrier. Thorite occurs only in this granite group, forming solid solutions with zircon, xenotime-(Y), and coffinite. Th-rich uraninite constitutes the main host of U. Magnetite, ilmenite and minor rutile are the most common Fe–Ti oxides. Ore minerals include wolframite, molybdenite, and scheelite. Aplites locally contain abundant sulfides (arsenopyrite, galena, chalcopyrite, molybdenite, sphalerite), scheelite, and columbite.

The monzo- to syenogranites from Bergen generally show less perthite texture and microcline twinning than the biotite granites and cordierite pseudomorphs are more widespread. Dioctahedral micas (muscovite and phengite) overgrow siderophyllite and both feldspars, and also occur as rosettes and subhedral flakes in the grain boundary network. The granites contain locally abundant tourmaline and rarely carry molybdenite and wolframite. The radioactive accessory-mineral assemblage includes monazite-(Ce), xenotime-(Y), Th-poor uraninite, and zircon.

The *Eibenstock* massif comprises a range of compositions from Li siderophyllite-bearing syenogranites to protolithionite/zinnwaldite-bearing alkali-feldspar granites. The trioctahedral Li–Fe micas are accompanied by minor but ubiquitous near

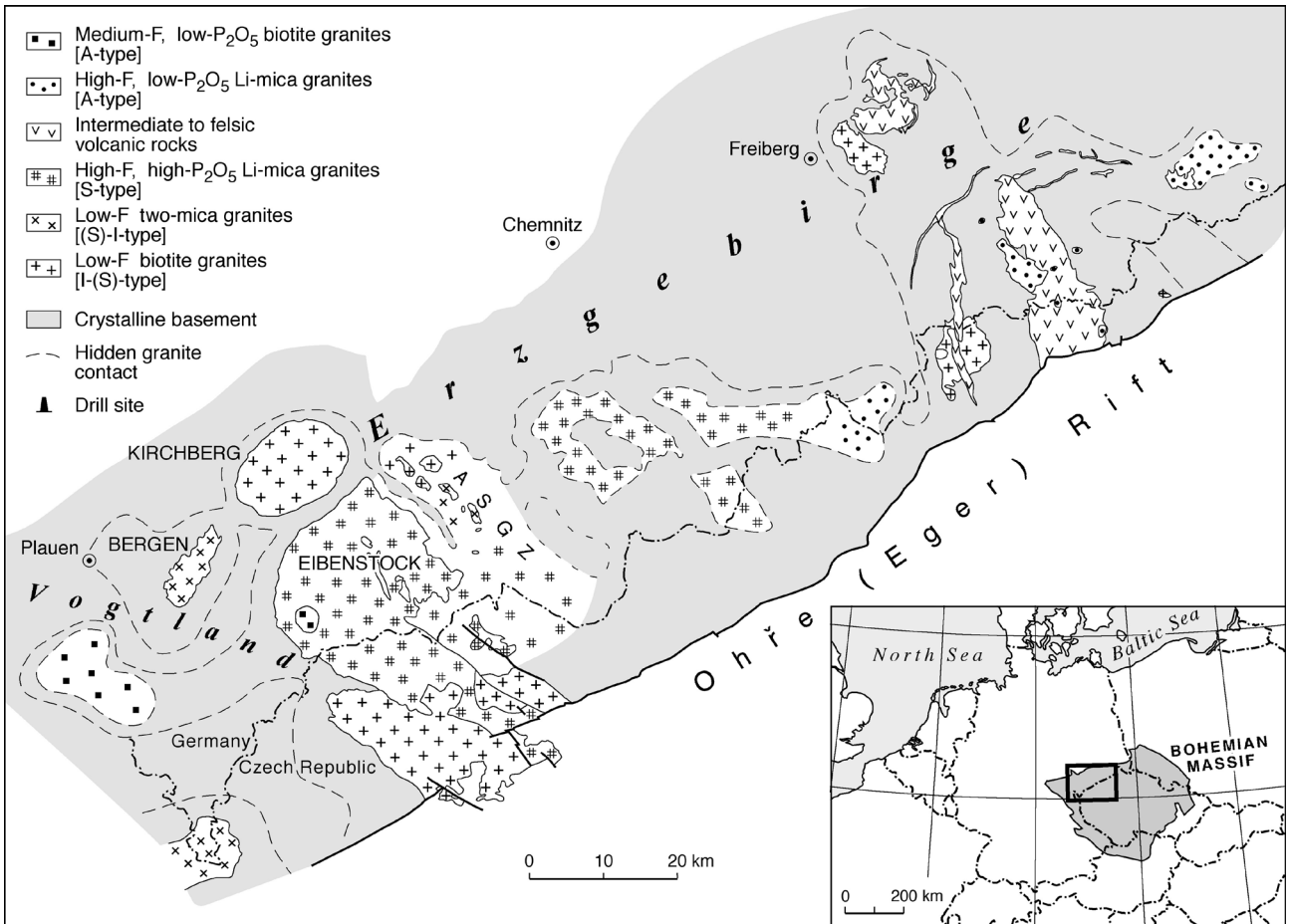


**Fig. 1.** Generalized geological map of the Erzgebirge-Vogtland, showing the distribution of the different groups of late-Variscan granites and rhyolites. ASGZ = Aue-Schwarzenberg granite zone (modified from Förster et al., 1999).

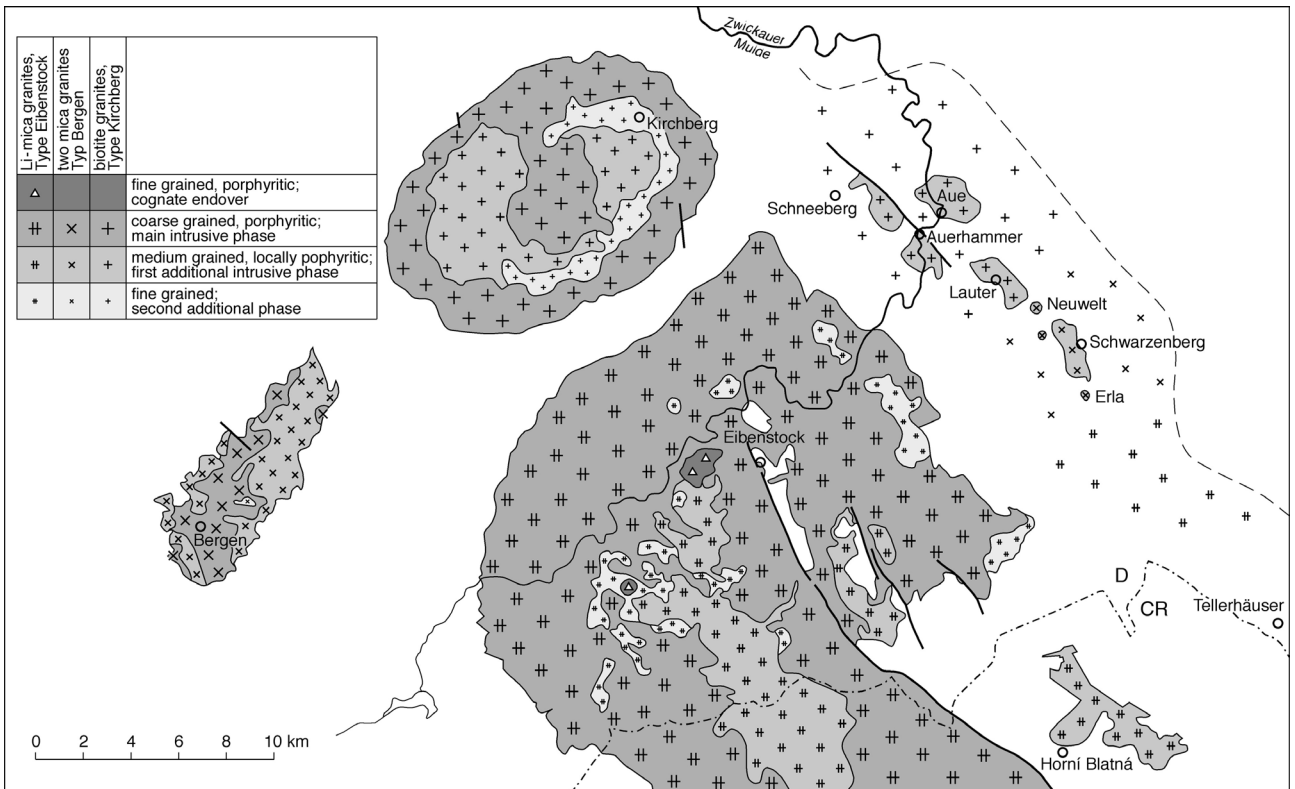


**Fig. 2.** Internal textural structure of the massifs of Kirchberg, Bergen, and Eibenstock.

**Table 1.** Subdivision of multi-phase granite plutons

| Massif            |   | Kirchberg | Bergen          | Eibenstock |
|-------------------|---|-----------|-----------------|------------|
| Sub-unit          | Texture   | KIB       | BRG             | EIB        |
| aplitic           | very fine-grained                                   | A-KIB     | A-BRG           | A-EIB      |
| ost evolved (3)   | fine-(to medium-) grained, occasionally porphyritic | KIB 3     | BRG 3p<br>BRG 3 | EIB 3      |
| more evolved (2)  | medium-grained, weakly porphyritic                  | KIB 2     | BRG 2           | EIB 2      |
| evolved (1)       | coarse- to medium-grained, serialporphyritic        | KIB 1     | BRG 1           | EIB 1      |
| least evolved (0) | fine- to medium-grained, hiatalporphyritic          |           |                 | EIB 0      |
| magmatic enclaves | variably textured                                   | E-KIB     | E-BRG           |            |

A = aplite, E = enclave. BRG3p = P<sub>2</sub>O<sub>5</sub>-rich facies of granite BRG3.

end-member fluorapatite (19–21 wt% F). Dioctahedral micas (muscovite and phengite) are typically rich in Li. More differentiated intrusions may also carry cassiterite, wolframite, and scheelite and minor molybdenite and columbite.

The different groups of Erzgebirge granites show variably strong petrographic evidence for recrystallization and mineral replacement. None of the granites is free of such effects, and in the case of the Li-mica granite group, they are so prominent as to be a distinctive feature of these rocks.

Overprinting effects in the Kirchberg granites are confined to overgrowths and partial replacement of older minerals (chlorite ± titanite ± epidote ± rutile in biotite, white mica in cordierite, white mica ± clinozoisite ± fluorite ± carbonate in plagioclase). Local mobilization of the LREE led to the formation of rare synchysite-(Ce), bastnaesite-(Ce), and secondary allanite-(Ce). The Bergen granites show similar mineral replacements as the biotite granite group, but the effects are more intense, and cataclastic deformation with recrystallization of feldspars and quartz is more common. Both late and secondary muscovite occurs, and apatite also crystallizes early (euhedral) and late (interstitial). Uranium mobility is manifested in various secondary uraniferous micas (bergenite, autunite, torbernite, zeunerite, uranocircite).

Replacement, mineral overgrowths and late interstitial phases are essential features of the Eibenstock granites and can be attributed to the elevated contents of volatile and incompatible elements in the magmas. Chlorite is lacking, but growth of late and secondary dioctahedral micas is common. White mica replaces plagioclase and topaz. Late albite occurs interstitially and as rims on K-feldspar. Late quartz is abundant in the grain boundary network, from which it partially replaces feldspars. Topaz, which often is sericitized or even kaolinized, is a common interstitial mineral and it locally forms in clusters with quartz and greenish protolithionite. Other common volatile-bearing late phases include fluorite, tourmaline (some as tourmaline-quartz nodules) and a second generation of interstitial apatite.

**Table 2.** Representative bulk-rock analyses of biotite granites from Kirchberg

| Sub-unit Sample                             | KIB1a 587 | KIB1m 782 | KIB2 785 | KIB2 788 | KIB3 305 | KIB3 1072 | A-KIB1 439 | A-KIB2 784 |
|---|-----------|-----------|----------|----------|----------|-----------|------------|------------|
| SiO <sub>2</sub> (wt%)                      | 69.2      | 70.8      | 73.6     | 75.4     | 76.7     | 77.1      | 76.8       | 77.1       |
| TiO <sub>2</sub>                            | 0.52      | 0.48      | 0.31     | 0.20     | 0.13     | 0.092     | 0.055      | 0.054      |
| Al <sub>2</sub> O <sub>3</sub>              | 14.7      | 14.1      | 13.3     | 12.8     | 12.6     | 12.8      | 13.0       | 12.9       |
| Fe <sub>2</sub> O <sub>3</sub> <sup>a</sup> | 2.98      | 2.77      | 1.89     | 1.40     | 1.08     | 0.65      | 0.55       | 0.43       |
| MnO   | 0.054     | 0.075     | 0.064    | 0.036    | 0.030    | 0.019     | 0.014      | 0.008      |
| MgO   | 1.27      | 0.88      | 0.59     | 0.36     | 0.29     | 0.15      | 0.040      | 0.043      |
| CaO   | 1.74      | 1.62      | 1.10     | 0.67     | 0.65     | 0.42      | 0.36       | 0.37       |
| Na <sub>2</sub> O                           | 3.45      | 3.31      | 3.53     | 3.38     | 3.28     | 3.65      | 3.46       | 3.63       |
| K <sub>2</sub> O                            | 4.59      | 4.66      | 4.57     | 4.82     | 4.80     | 4.60      | 5.31       | 4.85       |
| P <sub>2</sub> O <sub>5</sub>               | 0.20      | 0.21      | 0.14     | 0.075    | 0.033    | 0.019     | 0.016      | 0.060      |
| H <sub>2</sub> O <sup>+</sup>               | 0.90      | 0.76      | 0.53     | 0.54     | 0.56     | 0.52      | 0.21       | 0.29       |
| CO <sub>2</sub>                             | 0.19      | 0.12      | 0.14     | 0.08     | 0.02     | 0.05      | 0.12       | 0.07       |
| F   | 0.091     | 0.096     | 0.138    | 0.138    | 0.075    | 0.028     | 0.025      | 0.017      |
| O=F   | 0.038     | 0.040     | 0.058    | 0.058    | 0.032    | 0.012     | 0.011      | 0.007      |
| Total                                       | 99.8      | 99.8      | 99.8     | 99.9     | 100.2    | 100.0     | 99.9       | 99.8       |
| Li (p.p.m.)                                 | 93        | 135       | 190      | 138      | 76       | 47        | 18         | 27         |
| Be  | 6.4       | 8.7       | 10.0     | 8.5      | 9.5      | 9.0       | 19         | 6.0        |
| Sc  | 6.5       | 6.5       | 5.8      | 4.1      | 3.3      | 3.8       | 5.2        | 3.1        |
| Co  | 5.0       | 3.8       | 2.3      | 2.1      | 1.0      | 0.9       | 0.2        | 2.3        |
| Ni  | 5.0       | 4.2       | 14       | 2.1      | 1.0      | 3.0       | 0.4        | 1.3        |
| Zn  | 65        | 92        | 54       | 39       | 20       | 65        | 19         | 92         |
| Ga  | 20        | 22        | 20       | 18       | 18       | 17        | 22         | 19         |
| Rb  | 243       | 285       | 354      | 346      | 371      | 405       | 476        | 447        |
| Sr  | 225       | 186       | 105      | 66       | 30       | 16        | 3.5        | 7.5        |
| Y   | 25.3      | 40.0      | 39.2     | 32.0     | 37.2     | 37.0      | 40.8       | 33.7       |
| Zr  | 272       | 250       | 176      | 132      | 96       | 97        | 86         | 109        |
| Nb  | 22        | 31        | 27       | 23       | 25       | 28        | 42         | 36         |
| Mo  | 0.60      | 0.17      | 1.4      | 0.81     |          | 0.20      | 0.07       | 26         |
| Sn  | 8.1       | 20        | 14       | 13       | 6.6      | 9.3       | 6.2        | 2.7        |
| Sb  | 0.10      | 0.14      | 0.20     | 0.14     | 0.13     | 0.10      | 0.32       | 0.74       |
| Cs  | 18.1      | 26.8      | 33.1     | 20.4     | 21.1     | 23.4      | 49.7       | 16.6       |
| Ba  | 620       | 481       | 212      | 148      | 52       | 18        | 13         | 11         |
| La  | 56.5      | 56.2      | 32.3     | 26.5     | 17.5     | 14.9      | 16.7       | 7.50       |
| Ce  | 108       | 116       | 68.4     | 57.8     | 40.0     | 36.9      | 42.5       | 17.2       |
| Pr  | 11.9      | 12.8      | 8.23     | 7.08     | 5.34     | 4.94      | 5.83       | 2.34       |
| Nd  | 42.6      | 56.2      | 30.3     | 27.2     | 20.4     | 19.3      | 20.2       | 8.86       |
| Sm  | 6.95      | 7.37      | 6.32     | 5.89     | 4.99     | 5.11      | 5.45       | 3.48       |
| Eu  | 1.27      | 0.84      | 0.660    | 0.490    | 0.360    | 0.233     | 0.058      | 0.070      |
| Gd  | 5.45      | 6.39      | 6.17     | 5.34     | 4.77     | 4.82      | 5.13       | 4.03       |
| Tb  | 0.810     | 1.100     | 1.01     | 0.900    | 0.880    | 0.905     | 1.03       | 0.870      |
| Dy  | 4.23      | 6.70      | 6.25     | 5.16     | 5.53     | 5.91      | 7.04       | 5.99       |
| Ho  | 0.840     | 1.34      | 1.19     | 1.02     | 1.10     | 1.22      | 1.49       | 1.25       |
| Er  | 2.49      | 3.91      | 3.68     | 3.38     | 3.49     | 3.88      | 5.00       | 4.25       |
| Tm  | 0.360     | 0.610     | 0.590    | 0.570    | 0.570    | 0.617     | 0.945      | 0.660      |
| Yb  | 2.56      | 3.85      | 4.13     | 3.85     | 4.12     | 4.54      | 7.55       | 4.54       |
| Lu  | 0.370     | 0.560     | 0.570    | 0.540    | 0.620    | 0.667     | 1.22       | 0.680      |
| Hf  | 6.93      | 6.77      | 5.45     | 4.39     | 3.95     | 4.33      | 7.37       | 5.35       |
| Ta  | 2.3       | 3.9       | 4.0      | 4.0      | 4.5      | 5.5       | 16         | 6.4        |
| W   | 5.7       | 1.2       | 2.3      | 2.0      |          | 7.4       | 6.6        | 46         |
| Tl  | 1.2       | 1.9       | 2.0      | 2.0      | 1.8      | 2.2       | 2.2        | 2.5        |
| Pb  | 24.3      | 33.6      | 35.0     | 40.0     | 45.9     | 68.3      | 66.8       | 184        |
| Bi  | 0.10      | 0.10      | 0.28     | 0.85     |          | 1.7       | 4.5        | 3.0        |
| Th  | 33.5      | 33.0      | 32.0     | 36.9     | 34.7     | 36.1      | 15.1       | 22.5       |
| U   | 13.0      | 7.9       | 9.6      | 27.4     | 15.0     | 29.7      | 13.5       | 56.3       |
| A/CNK                                       | 1.07      | 1.05      | 1.05     | 1.07     | 1.07     | 1.09      | 1.08       | 1.08       |
| La <sub>N</sub> /Lu <sub>N</sub>            | 15.6      | 10.2      | 5.79     | 5.02     | 2.89     | 2.28      | 1.40       | 1.13       |
| Eu/Eu*                                      | 0.605     | 0.361     | 0.317    | 0.260    | 0.221    | 0.140     | 0.033      | 0.057      |

<sup>a</sup> = total iron as Fe<sub>2</sub>O<sub>3</sub>, A/CNK = molar Al<sub>2</sub>O<sub>3</sub>/(CaO + Na<sub>2</sub>O + K<sub>2</sub>O).

## 1.2. Geochemistry

The granites are all peraluminous in composition (A/CNK = 1.0 to 1.3) and cover a considerable range of Si content (in oxide wt%: 67–77, 71–76, and 73–76, respectively). Representative whole-rock chemical analyses are given in Tables 2–4.

Figure 3 presents a series of variation diagrams for petrogenetically and metallogenetically important elements with 1/TiO<sub>2</sub> as an index of differentiation. This index is superior to SiO<sub>2</sub> for these rocks because Ti is less easily remobilized by secondary

**Table 3.** Representative bulk-rock analyses of two-mica granites from Bergen

| Sub-unit<br>Sample                          | BRG1<br>524 | BRG1<br>824 | BRG2<br>780 | BRG2<br>1085 | BRG3<br>523 | BRG3<br>1089 | BRG3p<br>776 | BRG3p<br>521 | A-BRG1<br>779 | A-BRG1<br>1069 |
|---|-------------|-------------|-------------|--------------|-------------|--------------|--------------|--------------|---------------|----------------|
| SiO <sub>2</sub> (wt%)                      | 70.6        | 71.5        | 74.4        | 74.8         | 75.8        | 75.3         | 75.5         | 75.3         | 74.9          | 74.3           |
| TiO <sub>2</sub>                            | 0.37        | 0.33        | 0.18        | 0.15         | 0.089       | 0.084        | 0.065        | 0.058        | 0.045         | 0.035          |
| Al <sub>2</sub> O <sub>3</sub>              | 14.6        | 14.5        | 14.0        | 14.0         | 13.5        | 13.7         | 14.0         | 14.2         | 14.6          | 14.6           |
| Fe <sub>2</sub> O <sub>3</sub> <sup>a</sup> | 2.25        | 2.04        | 1.29        | 0.93         | 0.80        | 0.86         | 0.71         | 0.70         | 0.91          | 0.73           |
| MnO   | 0.046       | 0.045       | 0.058       | 0.030        | 0.057       | 0.058        | 0.059        | 0.054        | 0.032         | 0.047          |
| MgO   | 0.82        | 0.68        | 0.34        | 0.28         | 0.20        | 0.15         | 0.13         | 0.13         | 0.025         | 0.045          |
| CaO   | 1.11        | 1.10        | 0.57        | 0.49         | 0.37        | 0.41         | 0.37         | 0.34         | 0.39          | 0.50           |
| Na <sub>2</sub> O                           | 3.58        | 3.01        | 3.50        | 3.91         | 3.41        | 3.88         | 3.79         | 3.65         | 3.97          | 4.25           |
| K <sub>2</sub> O                            | 4.93        | 5.47        | 4.39        | 4.49         | 4.44        | 4.33         | 4.11         | 4.22         | 3.86          | 3.80           |
| P <sub>2</sub> O <sub>5</sub>               | 0.25        | 0.24        | 0.16        | 0.18         | 0.15        | 0.16         | 0.21         | 0.20         | 0.33          | 0.53           |
| H <sub>2</sub> O <sup>+</sup>               | 1.15        | 0.91        | 0.82        | 0.69         | 0.84        | 0.76         | 0.82         | 0.81         | 0.76          | 0.73           |
| CO <sub>2</sub>                             | 0.21        | 0.32        | 0.16        | 0.07         | 0.11        | 0.05         | 0.17         | 0.19         | 0.14          | 0.15           |
| F   | 0.092       | 0.085       | 0.089       | 0.078        | 0.12        | 0.132        | 0.172        | 0.162        | 0.124         | 0.15           |
| O=F   | 0.039       | 0.036       | 0.037       | 0.033        | 0.051       | 0.056        | 0.072        | 0.068        | 0.052         | 0.063          |
| Total                                       | 100.0       | 100.2       | 99.9        | 100.1        | 99.8        | 99.9         | 100.0        | 99.9         | 100.0         | 99.8           |
| Li (p.p.m.)                                 | 111         | 94          | 204         | 86           | 160         | 184          | 384          | 294          | 143           | 138            |
| Be  | 11          | 6.2         | 16          | 18           |             | 19           | 13           | 14           | <3            | 4.9            |
| Sc  | 5.2         | 4.1         | 3.2         | 3.8          |             | 2.5          | 2.9          | 2.0          | <2            | 2.1            |
| Co  | 2.8         | 2.9         | 1.1         | 0.4          | 0.4         | 0.6          | 0.3          | 0.5          | 0.3           | 0.3            |
| Ni  | 2.2         |             |             | 1.8          | 0.7         | 1.1          |              | 0.9          | 0.6           | 2              |
| Zn  | 53          | 53          | 32          | 22           | 24          | 31           | 27           | 24           | 32            | 49             |
| Ga  | 21          | 21          | 18          | 17           | 23          | 18           | 20           | 25           | 28            | 27             |
| Rb  | 276         | 283         | 344         | 343          | 503         | 461          | 554          | 595          | 654           | 800            |
| Sr  | 159         | 137         | 49          | 43           | 18          | 15           | 7.1          | 6.3          | 22            | 28             |
| Y   | 22.3        | 17.4        | 14.9        | 13.6         | 10.9        | 10.1         | 5.9          | 6.4          | 2.1           | 2.9            |
| Zr  | 169         | 163         | 89          | 72           | 42          | 37           | 27           | 27           | 25            | 21             |
| Nb  | 16          | 16          | 20          | 22           | 20          | 23           | 27           | 25           | 43            | 54             |
| Mo  | 0.13        | 0.16        | 0.31        | 0.17         | 0.26        | 2.4          | 0.26         | 0.13         | 0.12          | 0.10           |
| Sn  | 18          | 17          | 14          | 8.1          | 13          | 19           | 19           | 21           | 25            | 46             |
| Sb  | 0.10        | 0.27        | 0.67        | 0.18         | 0.28        | 0.13         | 0.88         | 0.90         | 0.54          | 0.60           |
| Cs  | 19.5        | 25.4        | 36.7        | 18.9         | 63.0        | 28.3         | 97.8         | 90.5         | 30.8          | 144            |
| Ba  | 462         | 498         | 156         | 117          | 57          | 38           | 17           | 27           | 6.2           | 15             |
| La  | 42.4        | 36.9        | 17.8        | 13.2         | 7.12        | 6.26         | 2.63         | 2.96         | 1.02          | 1.52           |
| Ce  | 80.9        | 72.7        | 36.1        | 26.7         | 12.6        | 13.1         | 5.68         | 6.56         | 1.94          | 2.85           |
| Pr  | 9.01        | 8.27        | 4.30        | 3.03         | 1.51        | 1.56         | 0.746        | 0.860        | 0.290         | 0.400          |
| Nd  | 32.1        | 28.8        | 14.2        | 10.6         | 5.54        | 5.53         | 2.55         | 3.17         | 1.09          | 1.54           |
| Sm  | 5.99        | 5.47        | 2.74        | 2.16         | 1.32        | 1.32         | 0.740        | 0.900        | 0.360         | 0.602          |
| Eu  | 0.770       | 0.728       | 0.310       | 0.234        | 0.110       | 0.093        | 0.038        | 0.040        | 0.021         | 0.060          |
| Gd  | 4.49        | 4.32        | 2.39        | 1.88         | 1.14        | 1.21         | 0.729        | 0.950        | 0.310         | 0.565          |
| Tb  | 0.690       | 0.627       | 0.415       | 0.320        | 0.270       | 0.250        | 0.165        | 0.180        | 0.070         | 0.119          |
| Dy  | 3.93        | 3.40        | 2.45        | 2.03         | 1.73        | 1.63         | 1.00         | 1.16         | 0.380         | 0.659          |
| Ho  | 0.640       | 0.601       | 0.506       | 0.399        | 0.340       | 0.320        | 0.179        | 0.180        | 0.060         | 0.096          |
| Er  | 1.88        | 1.65        | 1.52        | 1.23         | 1.17        | 1.05         | 0.569        | 0.590        | 0.200         | 0.263          |
| Tm  | 0.280       | 0.231       | 0.265       | 0.205        | 0.210       | 0.187        | 0.111        | 0.110        | 0.040         | 0.047          |
| Yb  | 1.93        | 1.55        | 1.83        | 1.60         | 1.76        | 1.51         | 0.888        | 0.920        | 0.320         | 0.407          |
| Lu  | 0.290       | 0.240       | 0.280       | 0.238        | 0.250       | 0.218        | 0.134        | 0.140        | 0.057         | 0.055          |
| Hf  | 4.50        | 4.64        | 2.85        | 2.38         | 1.83        | 1.67         | 1.61         | 1.60         | 1.83          | 1.83           |
| Ta  | 2.2         | 1.9         | 4.2         | 6.4          | 6.3         | 5.7          | 6.3          | 7.6          | 16            | 20             |
| W   | 1.4         | 2.1         | 5.0         | 9.6          | 8.3         | 10           | 12           | 13           | 22            | 18             |
| Tl  | 1.5         | 1.8         | 2.1         | 1.8          | 2.9         | 2.4          | 3.2          | 3.3          | 2.9           | 3.7            |
| Pb  | 39.5        | 32.9        | 27.3        | 28.5         | 15.3        | 25.1         | 13.8         | 12.2         | 7.2           | 6.0            |
| Bi  | 0.13        | 0.18        | 0.88        | 2.4          | 0.89        | 0.25         | 5.0          | 3.65         | 17            | 12             |
| Th  | 23.9        | 20.7        | 10.2        | 9.25         | 5.70        | 4.95         | 2.32         | 2.62         | 0.90          | 0.85           |
| U   | 5.1         | 6.3         | 18.2        | 22.1         | 11.5        | 33.5         | 3.2          | 12.1         | 4.5           | 3.8            |
| A/CNK                                       | 1.11        | 1.13        | 1.21        | 1.15         | 1.22        | 1.16         | 1.23         | 1.27         | 1.28          | 1.21           |
| La <sub>N</sub> /Lu <sub>N</sub>            | 15.0        | 15.7        | 6.50        | 5.67         | 2.91        | 2.94         | 2.01         | 2.16         | 1.83          | 2.83           |
| Eu/Eu*                                      | 0.433       | 0.439       | 0.360       | 0.345        | 0.266       | 0.220        | 0.155        | 0.130        | 0.186         | 0.308          |

<sup>a</sup> = total iron as Fe<sub>2</sub>O<sub>3</sub>, A/CNK = molar Al<sub>2</sub>O<sub>3</sub>/(CaO + Na<sub>2</sub>O + K<sub>2</sub>O)

**Table 4.** Representative bulk-rock analyses of Li-mia granites from Eibenstock

| Sub-Unit<br>Sample                          | EIB0<br>504 | EIB0<br>821 | EIB1<br>820 | EIB1<br>509 | EIB2<br>814 | EIB3<br>811 | EIB3<br>1081 | EIB3<br>1197 | A-EIB1<br>510 | A-EIB1<br>800 |
|---|-------------|-------------|-------------|-------------|-------------|-------------|--------------|--------------|---------------|---------------|
| SiO <sub>2</sub> (wt%)                      | 72.4        | 74.3        | 74.6        | 74.6        | 74.6        | 74.0        | 74.8         | 72.8         | 73.0          | 72.9          |
| TiO <sub>2</sub>                            | 0.24        | 0.17        | 0.13        | 0.11        | 0.072       | 0.057       | 0.053        | 0.047        | 0.035         | 0.032         |
| Al <sub>2</sub> O <sub>3</sub>              | 14.0        | 13.3        | 13.8        | 13.6        | 14.0        | 14.8        | 14.2         | 15.1         | 15.2          | 15.4          |
| Fe <sub>2</sub> O <sub>3</sub> <sup>a</sup> | 2.46        | 1.76        | 1.50        | 1.45        | 1.23        | 1.00        | 1.06         | 0.95         | 0.95          | 1.21          |
| MnO   | 0.044       | 0.024       | 0.028       | 0.028       | 0.016       | 0.033       | 0.022        | 0.028        | 0.022         | 0.024         |
| MgO   | 0.28        | 0.24        | 0.17        | 0.16        | 0.09        | 0.08        | 0.041        | 0.06         | 0.020         | 0.031         |
| CaO   | 0.69        | 0.44        | 0.48        | 0.44        | 0.38        | 0.37        | 0.35         | 0.43         | 0.35          | 0.67          |
| Na <sub>2</sub> O                           | 3.32        | 3.06        | 3.27        | 3.13        | 3.54        | 3.76        | 3.49         | 3.87         | 4.15          | 3.69          |
| K <sub>2</sub> O                            | 4.84        | 4.78        | 4.99        | 4.91        | 4.47        | 4.30        | 4.36         | 4.34         | 4.00          | 3.77          |
| P <sub>2</sub> O <sub>5</sub>               | 0.25        | 0.25        | 0.23        | 0.27        | 0.40        | 0.39        | 0.35         | 0.51         | 0.50          | 0.40          |
| H <sub>2</sub> O <sup>+</sup>               | 1.02        | 1.01        | 0.56        | 0.73        | 0.50        | 0.28        | 0.49         | 0.72         | 0.40          | 0.75          |
| CO <sub>2</sub>                             | 0.14        | 0.22        | 0.03        | 0.09        | 0.09        | 0.11        | 0.05         | 0.03         | 0.10          | 0.18          |
| F   | 0.338       | 0.210       | 0.352       | 0.471       | 0.685       | 0.829       | 0.687        | 1.18         | 1.33          | 1.23          |
| O=F   | 0.142       | 0.088       | 0.148       | 0.198       | 0.288       | 0.349       | 0.289        | 0.496        | 0.561         | 0.516         |
| Total                                       | 99.9        | 99.7        | 99.9        | 99.7        | 99.8        | 99.7        | 99.7         | 99.5         | 99.5          | 99.7          |
| Li (p.p.m.)                                 | 405         | 163         | 326         | 300         | 578         | 1001        | 329          | 1226         | 950           | 800           |
| Be  |             | 11          | 11          |             | 17          | 22          | 11           | 5.7          |               | 4.0           |
| Sc  | 4.2         | 3.0         | 2.8         |             | 2.5         | 1.9         | 2.1          | 4.7          | 2.0           | <2            |
| Co  | 1.5         | 1.0         | 0.7         | 0.7         | 0.4         | 0.3         | 0.2          | 0.1          | 0.1           | 0.5           |
| Ni  | 2.4         | 2.1         | 0.8         | 1.2         | 0.8         |             | 1.2          | 0.8          | 0.8           | 0.7           |
| Zn  | 77          | 48          | 46          | 50          | 41          | 33          | 36           | 48           | 34            | 68            |
| Ga  | 27          | 25          | 28          | 25          | 33          | 31          | 28           | 37           | 36            | 44            |
| Rb  | 704         | 504         | 683         | 814         | 1082        | 1028        | 795          | 1603         | 1498          | 1325          |
| Sr  | 38          | 28          | 22          | 13          | 14          | 7.2         | 4.9          | 15           | 14            | 45            |
| Y   | 26.0        | 22.7        | 16.0        | 14.4        | 10.7        | 7.1         | 6.5          | 6.6          | 5.5           | 3.0           |
| Zr  | 149         | 113         | 85          | 75          | 53          | 31          | 23           | 34           | 31            | 27            |
| Nb  | 19          | 18          | 17          | 20          | 26          | 25          | 19           | 38           | 33            | 41            |
| Mo  | 0.35        | 0.60        | 0.35        | 0.40        | 0.30        | 0.18        | 0.06         | 0.18         | 0.16          | 0.30          |
| Sn  | 38          | 26          | 35          | 34          | 50          | 52          | 29           | 97           | 28            | 73            |
| Sb  | 0.40        | 0.30        | 0.29        | 0.50        | 1.7         | 2.2         | 0.42         | 1.3          | 1.5           | 0.47          |
| Cs  | 107         | 38.7        | 84.6        | 93.9        | 156         | 213         | 86.3         | 174          | 118           | 66.2          |
| Ba  | 243         | 140         | 113         | 52          | 20          | 12          | 6.2          | 5.9          | 5.0           | 16            |
| La  | 26.0        | 17.6        | 12.9        | 9.30        | 4.36        | 2.14        | 1.91         | 1.02         | 1.66          | 0.69          |
| Ce  | 56.3        | 39.2        | 29.7        | 20.9        | 10.4        | 5.22        | 4.21         | 3.06         | 3.69          | 1.75          |
| Pr  | 6.85        | 4.94        | 3.54        | 2.62        | 1.26        | 0.663       | 0.540        | 0.403        | 0.500         | 0.240         |
| Nd  | 25.9        | 18.1        | 12.3        | 9.74        | 4.49        | 2.33        | 1.91         | 1.39         | 1.93          | 0.910         |
| Sm  | 5.79        | 4.40        | 2.99        | 2.62        | 1.45        | 0.822       | 0.550        | 0.685        | 0.780         | 0.490         |
| Eu  | 0.460       | 0.300       | 0.230       | 0.140       | 0.048       | 0.023       | 0.014        | 0.002        | 0.014         | 0.009         |
| Gd  | 5.04        | 4.74        | 2.98        | 2.48        | 1.51        | 0.892       | 0.850        | 0.762        | 0.830         | 0.410         |
| Tb  | 0.930       | 0.860       | 0.620       | 0.520       | 0.340       | 0.218       | 0.175        | 0.184        | 0.220         | 0.120         |
| Dy  | 5.32        | 4.71        | 3.28        | 2.80        | 2.04        | 1.33        | 1.08         | 1.15         | 1.11          | 0.590         |
| Ho  | 0.940       | 0.750       | 0.510       | 0.450       | 0.320       | 0.208       | 0.175        | 0.176        | 0.160         | 0.080         |
| Er  | 2.60        | 1.71        | 1.33        | 1.12        | 0.80        | 0.521       | 0.463        | 0.437        | 0.370         | 0.200         |
| Tm  | 0.35        | 0.23        | 0.15        | 0.14        | 0.11        | 0.08        | 0.066        | 0.072        | 0.060         | 0.040         |
| Yb  | 2.20        | 1.28        | 1.04        | 0.920       | 0.660       | 0.535       | 0.477        | 0.489        | 0.450         | 0.250         |
| Lu  | 0.350       | 0.180       | 0.130       | 0.110       | 0.094       | 0.068       | 0.060        | 0.060        | 0.070         | 0.035         |
| Hf  | 4.35        | 3.40        | 2.55        | 2.74        | 2.39        | 1.57        | 1.08         | 2.29         | 1.98          | 1.48          |
| Ta  | 2.7         | 3.8         | 4.1         | 4.6         | 7.7         | 9.4         | 5.0          | 13           | 11            | 19.3          |
| W   | 7.3         | 13          | 12          | 12          | 11          | 28          | 7.0          | 24           | 35            | 34            |
| Tl  | 3.9         | 2.5         | 3.7         | 4.4         | 5.3         | 6.2         | 4.3          | 7.9          | 6.2           | 5.9           |
| Pb  | 19.0        | 18.7        | 16.4        | 12.0        | 6.9         | 7.2         | 9.5          | 3.4          | 4.9           | 5.6           |
| Bi  | 0.16        | 1.3         | 0.65        | 0.57        | 1.3         | 4.6         | 5.1          | 6.2          | 10            | 7.9           |
| Th  | 20.3        | 17.0        | 12.6        | 11.6        | 7.4         | 4.8         | 3.5          | 5.9          | 2.8           | 2.8           |
| U   | 7.7         | 13.2        | 23.3        | 22.9        | 8.5         | 6.2         | 4.4          | 8.7          | 7.3           | 6.7           |
| A/CNK                                       | 1.17        | 1.21        | 1.19        | 1.21        | 1.24        | 1.29        | 1.28         | 1.28         | 1.29          | 1.36          |
| La <sub>N</sub> /Lu <sub>N</sub>            | 7.60        | 10.0        | 10.1        | 8.65        | 4.74        | 3.22        | 3.26         | 1.74         | 2.42          | 2.02          |
| Eu/Eu*                                      | 0.253       | 0.198       | 0.231       | 0.164       | 0.098       | 0.081       | 0.062        | 0.008        | 0.052         | 0.059         |

<sup>a</sup> = total iron as Fe<sub>2</sub>O<sub>3</sub>, A/CNK = molar Al<sub>2</sub>O<sub>3</sub>/(CaO + Na<sub>2</sub>O + K<sub>2</sub>O).

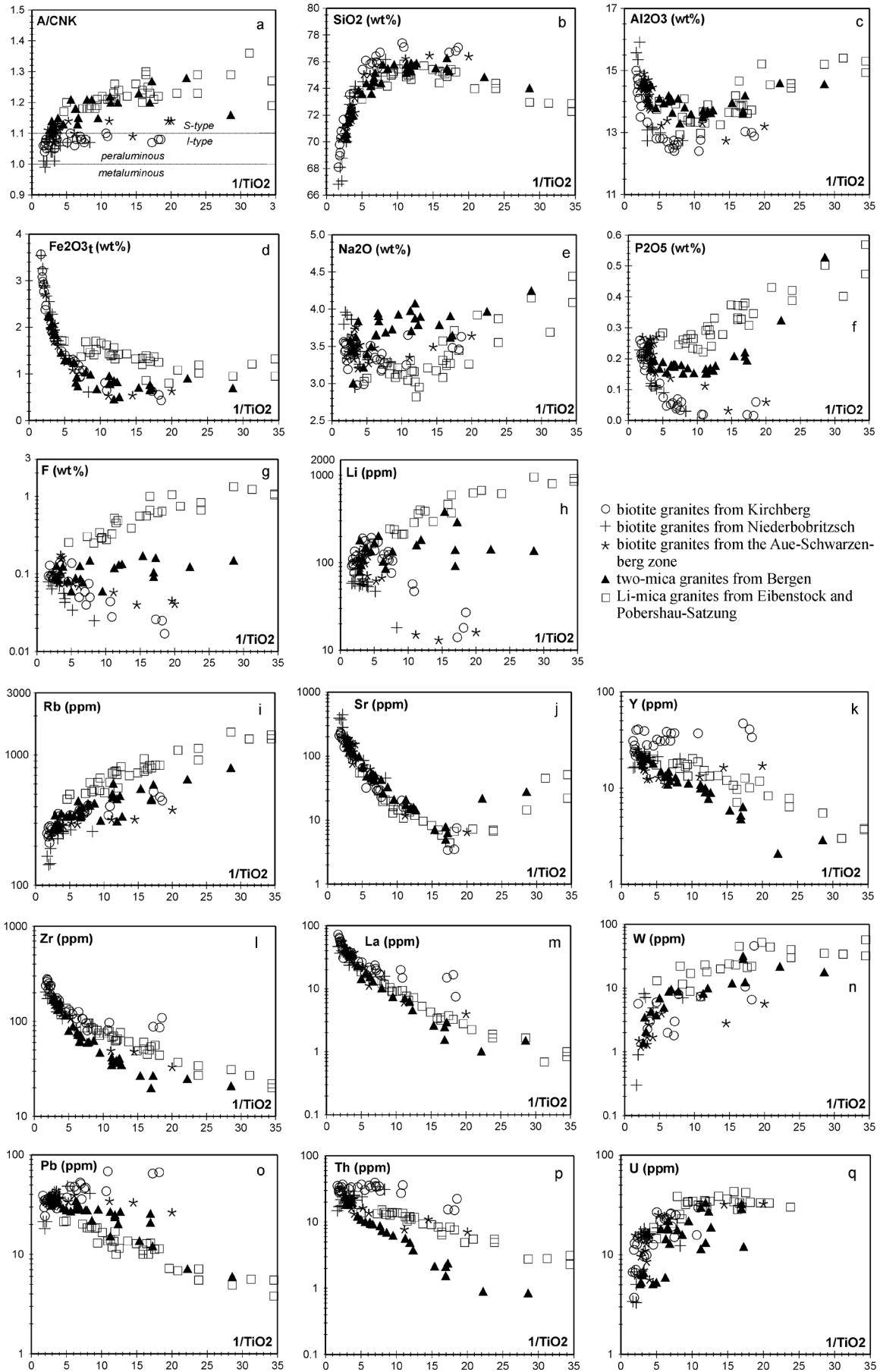


**Fig. 3.** Element variation diagrams using  $1/\text{TiO}_2$  as a differentiation index, for selected major and trace element components of the various groups of granites (Förster et al., 1999)

effects and because Ti contents in whole-rock decrease smoothly and continuously with progressive differentiation, whereas silica first increases then falls at high levels of fractionation.

The differentiation trends in all three granite groups are indistinguishable for components which are most compatible in feldspars and biotite (Mg, Ca, Co, Sr, Ba). The groups show distinctly different trends for P, F, and Li, and trace elements whose abundance is controlled by accessory minerals such as Y, Zr, Sn, the HREE, Hf, Pb, Th and, less markedly, Nb and the LREE. Whereas P, F, and Li increase with differentiation in the two-mica and Li-mica granites, the opposite is true in the biotite granite. Differentiation in the Kirchberg biotite granite increases or does not affect the concentration of Y, Th, Pb, and the HREE whereas these same elements decrease steadily with differentiation in the other two groups. The separate character of differentiation in the granite groups is also reflected in the behaviour of Na and K, although the variation of both of these components is irregular and may not be entirely magmatic.

Particularly notable is the behaviour of U. Whereas the U concentrations in the Kirchberg granites remained unaffected by secondary processes, weathering  $\pm$  removal during ore-forming processes have severely depleted surface and shallow subsurface samples (down to  $\sim$  500m) of the Bergen and Eibenstock granites in this element. The different susceptibility to U mobilization is primarily governed by the composition of magmatic uraninite (Förster, 1999) The intensity of depletion could be estimated by comparing the U concentrations between surface and subsurface EIB samples and amounts to a maximum of 85%. Primary U concentrations of this pluton are on the order of 30 to 40 ppm, compared to the lower values measured in surface samples listed in Table 4. Inferences on the radiogenic heat production of this HHP granite made from superficially exposed granite samples are, thus, completely wrong (Fig. 4; cf. Förster and Förster, 2000).

Characteristic chondrite-normalized REE patterns are shown in Fig. 5. The granites of all three groups share the common feature of a steady depletion of LREE and increasing negative Eu anomaly with magmatic differentiation. In the Kirchberg biotite granites, this LREE depletion is accompanied by increasing HREE contents whereas in the other granites HREE contents also fall with progressive fractionation. In contrast to the two-mica and biotite granites, which have relatively flat HREE abundance patterns ( $Tb_{CN}/Yb_{CN} \approx 1$ ), the HREE patterns from the Li-mica granites are inclined. The most highly evolved granites and aplites from the two-mica and Li-mica groups display characteristically curved REE patterns with concave-upward segments between Gd and Ho described as the lanthanide tetrad effect.

### 1.3. Sr–Nd isotopic composition

The initial-Sr ratios for the Kirchberg and Bergen granites overlap (0.706 to 0.707). The extremely high Rb/Sr ratios of the Eibenstock granites, accentuated in some cases by secondary Rb enrichment and/or Sr loss, gives rise to imprecise or geologically meaningless values of  $^{87}Sr/^{86}Sr$  initial ratios.

The biotite and two-mica granites also overlap with respect to  $\epsilon_{Nd(325)}$  values ( $-2.9$  to  $-4.9$  and  $-3.0$  to  $-3.6$ ). In terms of their  $\epsilon_{Nd(320)}$  values ( $-4.5$  to  $-7.8$ ), the Eibenstock granites have slightly more evolved compositions than the Erzgebirge granites of classes 1+2 and 4+5.

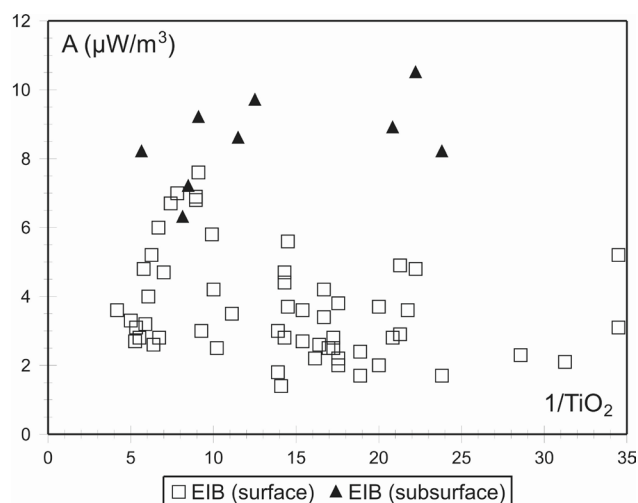


**Fig. 4.** Radiogenic heat production of the Eibenstock pluton recorded in surface and subsurface samples

## 2. Small granite plutons and bodies within the Gera–Jáchymov Lineament

This structure zone exposes a number of small (on outcrop) and poorly exposed granite occurrences belonging to the classes of low-F biotite granites and low-F two-mica granites (Fig. 6). These granites originated quasi-contemporaneously, between ca. 328 and 324 Ma (Förster et al., 2009; Tichomirowa and Leonhardt, 2010). Although belonging to the same classes, these granites possess partly significant differences in trace-element composition relative to their previously described class members, i.e., Kirchberg and Bergen.

Most of these granites are exposed in small, superficial outcrops, i.e., productive (Auerhammer) or abandoned quarries (Gleesberg, Lauter, Schwarzenberg, Neuwelt, Erla). Other granites are exclusively known from drillcores (Burkersdorf, Bernsbach, Beierfeld) or were exposed in connection with former underground uranium mining at Schlemma–Alberoda (Aue). Underground exposures in the Schneeberg–Schlemma ore district imply that the granites of Aue, Gleesberg, and Auerhammer constitute apical intrusions of the same pluton collectively referred to as the Aue granite suite (AGS). The same genetic relationship holds for the granites from Schwarzenberg, Neuwelt, and Erla, which hereafter will be referred to as the Schwarzenberg granite suite (SGS).

Although the excursion will not touch these granites, it is worth to briefly reporting their geochemistry (Table 5) and radioactive-isotope characteristics, to demonstrate the extended compositional variability of granitic rocks that were emplaced within a rather small area and during the same magmatic period (cf. Förster et al., 2009).

### 2.1. Geochemistry

**Biotite-granite group:** Granites from this group are calc-alkaline, weakly to mildly peraluminous monzogranites ( $A/CNK = 1.07$ – $1.14$ ; Table 5). Tin and W are present in comparatively small concentrations (2–22 ppm Sn and 1.1–7.5 ppm W).

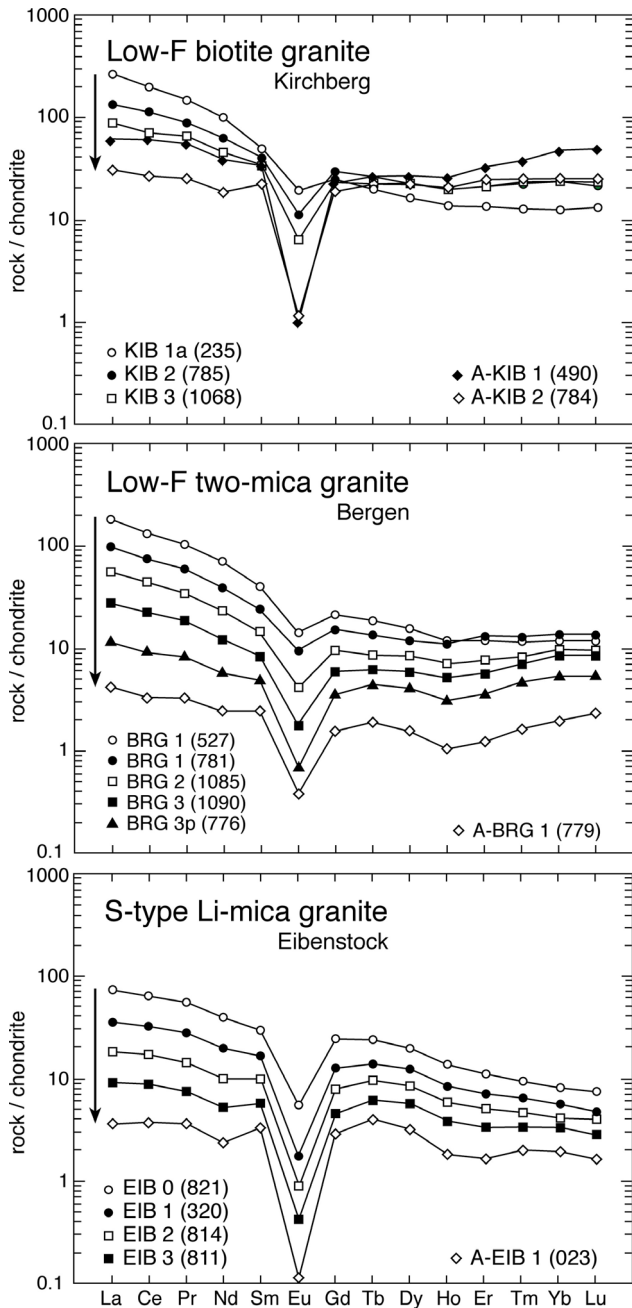


**Fig. 5.** Chondrite-normalized whole-rock REE patterns for the granites from Kirchberg, Bergen, and Eibenstock. Arrows indicate the evolution of REE concentrations during progressive magma differentiation (modified from Förster et al., 1999).

Evolution of elemental contents during differentiation of the *AGS* (70.1  $\Rightarrow$  76.2 wt% SiO<sub>2</sub>) is distinguished by an increase in Si, K, Be, Rb, (Nb), Ta, and U, and a decrease in Ti, Al, Fe, Mg, Ca, P, F, Li, Co, Ni, Zn, Sr, (Y), Zr, Sn, Cs, Ba, LREE, (HREE), Hf, and Th. Rock aluminosity increases, the chondrite-normalized REE patterns become flatter, and the negative Eu anomaly deeper (Fig. 7). This compositional variation is consistent with magma evolution controlled by the fractionation of plagioclase ( $\pm$  K-feldspar), micas, Fe-Ti oxides, fluorapatite, zircon, monazite  $\pm$  thorite  $\pm$  xenotime, with a concomitant increase in the concentration of highly incompatible trace elements (Ta, U) in the residual melt.

The *Beierfeld* granite is the most highly evolved (76.4–76.5 wt% SiO<sub>2</sub>; A/CNK = 1.09–1.14) among the ASGZ biotite granites. It closely resembles the most evolved granite variety from the AGS (sample 1000) in the assemblage of elements displaying large or low concentrations. Remarkable is the paucity in F (~0.04 wt%), Li (13–16 ppm), Zn (9–12 ppm), and Ba (12–27 ppm), whereas U is notoriously high (32–33 ppm).

**Two-mica granite group:** The moderately peraluminous (A/CNK = 1.17–1.26) two-mica granites are Si-rich and comparatively more evolved than the bulk of the biotite granites. Although the two-mica granites are, on average, richer in Sn (12–35 ppm) and W (2.0–9.3 ppm) than the biotite granites, both these ore elements do not approach a concentration level of economic significance.

Compared to the fractionation regularities of the biotite granites, a number of elements of the SGS (73.7–76.0 wt% SiO<sub>2</sub>) display an opposite trend. These elements comprise Mn, K, F, (Li), Sc, Ga, Sn, and Cs, which became enriched, and Pb, which became depleted in the course of magma differentiation. The REE<sub>CN</sub> patterns become flatter (La<sub>CN</sub>/Lu<sub>CN</sub> decreases from 11.1 to 1.5) and the negative Eu anomaly deepens (Eu/Eu\* = 0.41  $\Rightarrow$  0.06) (Fig. 7). The most evolved granites of the SGS are high in Na (4.1–4.4 wt% Na<sub>2</sub>O), Rb (470–480 ppm), Cs (30–60 ppm), and Bi (8–15 ppm), but low in Mg (0.07–0.08 wt% MgO), F (~0.1 wt%), Li (50–110 ppm), Sr (6–10 ppm), Y (6–7 ppm), Zr (23–24 ppm), Ba (15–26 ppm), REE, Pb (7–9 ppm), and Th (4.3–4.5 ppm). The high concentrations of Bi cannot be explained by fractional crystallization alone. This chemical anomaly attests to the operation of metasomatic processes, which may have also modified the magmatic pattern of other, easily to mobilize elements. Thus, these granites gained their evolved character by two processes that operated in concert, magma differentiation and fluid-induced overprint.

The most voluminous F-poor biotite-granite occurrences in the western Erzgebirge/Krušné hory are the massifs of Kirchberg (Germany) and Nejdek (Czech Republic) (cf. Fig. 6). Although closely related spatially, the ASGZ biotite granites are not genetically affiliated with the neighbouring Kirchberg granite. Instead, they display close chemical affinities to the more distant granites from Nejdek (Fig. 8).

## 2.2. Sr–Nd isotopic composition

The granites from Burkersdorf, Aue, and Bernsbach display similar initial Sr-isotopic ratios, between 0.7065 and 0.7077 ( $t = 325$  Ma). The very high Rb/Sr ratios (17–53) of the evolved *Beierfeld* granite do not allow calculation of a precise Sr<sub>i</sub>-isotopic value. All four granites exhibit a narrow range in their  $\epsilon$ Nd<sub>325</sub> values, between –2.6 and –3.9.

Although displaying similar Rb/Sr ratios and a low intensity of overprinting, samples of the SGS have different <sup>87</sup>Sr/<sup>86</sup>Sr initial ratio of 0.709 and 0.713, respectively ( $t = 325$  Ma). Owing to their high Rb/Sr WR ratios (32–70), the samples from Lauter are not suited to calculate a precise Sr<sub>i</sub>-isotopic value. The SGS is distinctly lower in  $\epsilon$ Nd<sub>325</sub> compared to the biotite-granite group, with values ranging from –4.9 to –5.2. In this respect, it differs from the Lauter granite ( $\epsilon$ Nd<sub>325</sub> = –3.6 to –4.0).

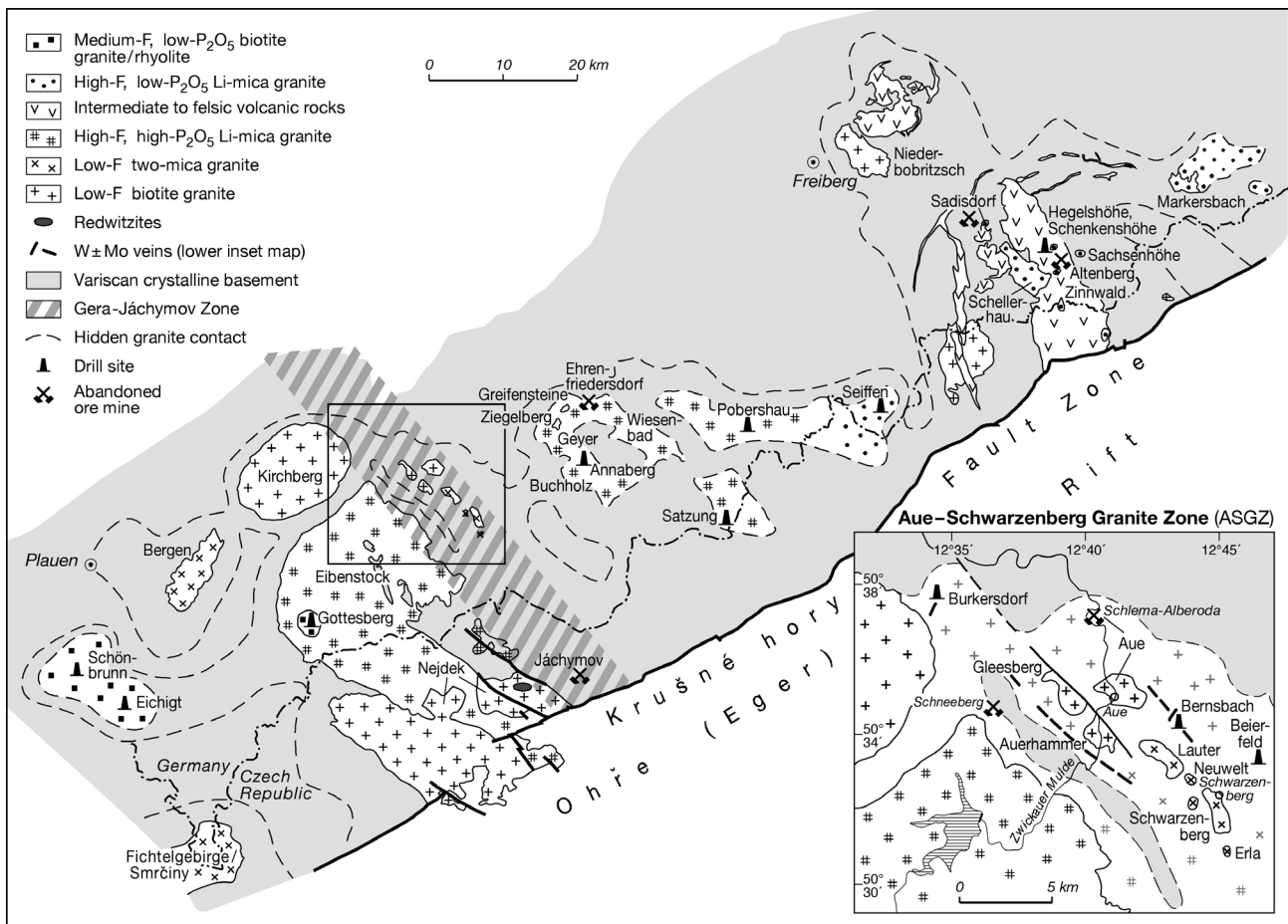


**Fig. 6.** Geological map of the Erzgebirge–Vogtland Zone, with the Aue–Schwarzenberg Granite Zone shown as inset map (modified from Förster and Romer, 2010).

### 3. Post-collisional subvolcanic rhyolitic dikes and microgranites

Some 15 Ma after termination of granite magmatism, another period of igneous activity was initiated in an extensional setting, giving rise to the intrusion of compositionally and texturally diverse, often K-rich high-Si rhyolites/porphyritic microgranites within the older granites or their metamorphic country rocks (Fig. 9). These rocks are yet only poorly dated, but their origination appears to fall in a relatively small period of time between about 305 Ma and 300(295) Ma.

The rhyolites/microgranites are geochemically discriminated into three groups (Förster et al., 2007). The group-I and group-II rhyolites share the principal compositional features of low-F biotite granites and two-mica granites of transitional I–S-type affinity, respectively. The group-III rhyolites/microgranites are chemically similar to medium-F, low-P biotite granites and, possibly, also to high-F, low-P Li-mica granites, both of aluminous A-type affinity.

#### 3.1. Geochemistry

The bulk-rock compositions of the rhyolites/microgranites are listed in Table 6. Their chondrite-normalized REE patterns are shown in Figure 10. Figure 11 provides a collection of four x–y diagrams showing the contents of a selection of relatively alteration-resistant trace elements (Zr, Y, Nb, Th) in rhyolites and spatially associated granites as function of  $1/\text{TiO}_2$ , which monitors the degree of magma evolution.

**Group-I rhyolites:** The rock from *Mahnbrück* is an Al-poor, K-rich, high-Si rhyolite particularly low in Fe, Mn, Ca, Na, P, Li, and Pb. Fluorine and ore elements (Sn, W, Mo) are at a common concentration level of felsic rocks. Its chondrite-normalized REE pattern is weakly declined and shows a moderate negative Eu anomaly. The rock from *Jungfernsprung* is the least evolved rhyolite from the suite of samples. It is chemically similar to the *Mahnbrück* rhyolite, but poorer in Si and richer in Ti, Fe, Ba, Zr, and the REE. Remarkable is the high content of W (27 ppm) at *Jungfernsprung*, contrasting the relatively low abundance of Sn (9 and 17 ppm).

**Group-II rhyolites:** These rhyolites are generally more evolved than the group-I rhyolites. The rock at *Saupersdorf* is low in Ti, Zr, Hf, Y, Sr, and Ba, but high in Rb, Nb, and Ta. This rhyolite exhibits uncommonly low concentrations of the REE, Th, and Pb. The REE patterns are flat ( $\text{La}_{\text{CN}}/\text{Lu}_{\text{CN}} = 1.5\text{--}1.6$ ) and kinked in the LREE section, with weak negative anomalies at Ce and Nd (Fig. 3b). Noteworthy is the enrichment in Sn (54–56 ppm). The high-Si rhyolite from *Weißbach* is lower in Mn, Ca, Mg, K, and Zr but higher in Li, Cs, and Pb relative to the *Saupersdorf* rhyolite. The contents of Y, the REE, and Th are markedly depleted as well. The REE patterns are similarly flat ( $\text{La}_{\text{CN}}/\text{Lu}_{\text{CN}} = 2.5\text{--}3.1$ ), but less kinked than the rhyolite of *Saupersdorf* (Fig. 5c). The concentrations of Sn (29–30 ppm) and W (16 ppm) are elevated.

**Group-III rhyolites:** The two types of K-rich, P-poor high-Si rhyolites from *Morgenröthe* are geochemically distinct. The MOR/I rhyolite is less evolved and significantly richer in (in ppm) Zr (200–220), Th (63), Y (62–63), and REE ( $\sum\text{La-Lu} =$

**Table 5.** Representative bulk-rock analyses of biotite and two-mica granites from the ASGZ

| Group<br>Granite                            | low-F biotite granites |       |       |       |       |       |       |       | two-mica granites |       |       |       |
|---|------------------------|-------|-------|-------|-------|-------|-------|-------|-------------------|-------|-------|-------|
|   | AGS                    |       | BUR   |       | BRF   |       | BRB   |       | LAU               |       | SGS   |       |
| Sample No.                                  | 1002                   | 465   | 1000  | 991   | 994   | 987   | 986   | 985   | 806a              | 805   | 803   | 804   |
| SiO <sub>2</sub> (wt%)                      | 70.1                   | 71.7  | 76.2  | 69.1  | 75.3  | 76.5  | 76.4  | 72.4  | 74.8              | 73.8  | 76.0  | 75.3  |
| TiO <sub>2</sub>                            | 0.49                   | 0.31  | 0.09  | 0.46  | 0.19  | 0.07  | 0.05  | 0.29  | 0.06              | 0.14  | 0.06  | 0.05  |
| Al <sub>2</sub> O <sub>3</sub>              | 14.6                   | 14.3  | 13.3  | 14.9  | 13.4  | 12.7  | 13.2  | 13.9  | 14.1              | 14.5  | 13.9  | 14.1  |
| Fe <sub>2</sub> O <sub>3</sub> <sup>a</sup> | 2.84                   | 1.83  | 0.53  | 2.54  | 1.13  | 0.54  | 0.63  | 1.87  | 0.54              | 1.22  | 0.59  | 0.69  |
| MnO   | 0.056                  | 0.042 | 0.035 | 0.061 | 0.028 | 0.029 | 0.024 | 0.056 | 0.026             | 0.031 | 0.027 | 0.040 |
| MgO   | 0.93                   | 0.58  | 0.16  | 0.96  | 0.29  | 0.20  | 0.12  | 0.52  | 0.10              | 0.29  | 0.07  | 0.08  |
| CaO   | 1.72                   | 1.14  | 0.37  | 1.46  | 0.95  | 0.47  | 0.40  | 1.10  | 0.24              | 0.57  | 0.28  | 0.35  |
| Na <sub>2</sub> O                           | 3.33                   | 3.73  | 3.35  | 3.18  | 3.42  | 3.49  | 3.64  | 3.48  | 3.37              | 3.35  | 4.06  | 4.41  |
| K <sub>2</sub> O                            | 4.33                   | 4.74  | 5.08  | 5.16  | 4.56  | 4.70  | 4.49  | 4.79  | 4.90              | 4.57  | 3.80  | 3.71  |
| P <sub>2</sub> O <sub>5</sub>               | 0.27                   | 0.19  | 0.11  | 0.22  | 0.07  | 0.03  | 0.06  | 0.16  | 0.20              | 0.29  | 0.18  | 0.19  |
| H <sub>2</sub> O <sup>+</sup>               | 1.09                   | 0.95  | 0.60  | 1.37  | 0.51  | 0.54  | 0.60  | 1.02  | 1.33              | 0.99  | 0.79  | 0.77  |
| CO <sub>2</sub>                             | 0.13                   | 0.28  | 0.24  | 0.38  | 0.09  | 0.38  | 0.25  | 0.27  | 0.09              | 0.12  | 0.19  | 0.09  |
| F   | 0.095                  | 0.087 | 0.058 | 0.086 | 0.047 | 0.040 | 0.041 | 0.18  | 0.22              | 0.082 | 0.097 | 0.11  |
| F=O <sub>2</sub>                            | 0.040                  | 0.037 | 0.024 | 0.036 | 0.020 | 0.017 | 0.017 | 0.074 | 0.093             | 0.035 | 0.041 | 0.044 |
| Total                                       | 99.9                   | 99.8  | 100.1 | 99.8  | 100.0 | 99.7  | 99.9  | 100.0 | 99.8              | 99.9  | 100.0 | 99.8  |
| Li(ppm)                                     | 102                    | 61    | 15    | 94    | 55    | 13    | 16    | 124   | 103               | 70    | 49    | 112   |
| Be  | 9.1                    | 12    | 20    | 4.5   | 5.8   | 6.2   | 34    | 14    | 4.4               | 8.4   |       | 18    |
| Sc  | 5.5                    | 4.3   | 2.9   | 6.8   | 5.0   | 2.4   | <2    | 4.5   | 4.9               | 3.2   | 3.2   | 6.1   |
| Co  | 3.4                    | 2.3   | 0.4   | 4.1   | 1.7   | 0.5   | <0.1  | 2.5   | 0.8               | 0.9   | 0.2   | 0.2   |
| Ni  |                        | 2.0   | 0.8   | 3.9   |       | 1.3   | 0.7   | 2.3   | 1.0               | 1.9   |       |       |
| Zn  | 62                     | 35    | 10    | 51    | 15    | 12    | 9     | 53    | 29                | 38    | 23    | 33    |
| Ga  | 20                     | 21    | 17    | 17    | 17    | 15    | 18    | 20    | 26                | 19    | 25    | 28    |
| Rb  | 245                    | 286   | 319   | 245   | 273   | 320   | 378   | 334   | 525               | 363   | 484   | 468   |
| Sr  | 213                    | 154   | 12    | 195   | 76    | 19    | 6.5   | 140   | 7.5               | 52    | 6.5   | 9.9   |
| Y   | 23.4                   | 18.9  | 13.2  | 24.9  | 15.6  | 16.4  | 17.0  | 20.0  | 5.5               | 13.4  | 7.3   | 6.2   |
| Zr  | 236                    | 149   | 49    | 256   | 107   | 48    | 33    | 143   | 21                | 66    | 24    | 25    |
| Nb  | 18                     | 16    | 21    | 18    | 20    | 16    | 22    | 19    | 21                | 16    | 30    | 25    |
| Mo  | 0.4                    | 1.1   | 0.6   | 6.3   | 0.4   | 0.2   | 0.5   | 2.5   | 0.3               | 0.5   | 0.7   | 0.9   |
| Sn  | 12                     | 7.5   | 2.0   | 7.3   | 5.4   | 6.4   | 12    | 15    | 35                | 12    | 13    | 22    |
| Sb  | 0.1                    | 0.1   | 0.1   | 0.2   | 0.2   | 0.2   | 0.1   | 0.1   | 0.2               | 0.2   | 0.5   | 0.2   |
| Cs  | 16.3                   | 14.1  | 11.5  | 22.0  | 13.0  | 19.7  | 28.9  | 28.9  | 27.6              | 22.5  | 30.8  | 59.1  |
| Ba  | 456                    | 380   | 24    | 777   | 124   | 27    | 12    | 342   | 41                | 188   | 16    | 25    |
| La  | 55.3                   | 30.7  | 6.04  | 58.3  | 25.2  | 8.52  | 3.98  | 38.3  | 1.60              | 11.5  | 3.23  | 2.23  |
| Ce  | 108                    | 63.4  | 12.9  | 114   | 52.2  | 18.3  | 10.3  | 74.0  | 3.28              | 22.8  | 6.67  | 4.60  |
| Pr  | 11.9                   | 7.00  | 1.56  | 13.1  | 6.06  | 2.21  | 1.31  | 8.31  | 0.44              | 2.83  | 0.78  | 0.52  |
| Nd  | 41.2                   | 25.5  | 5.20  | 42.5  | 20.3  | 7.16  | 4.31  | 28.0  | 1.57              | 10.0  | 2.56  | 1.84  |
| Sm  | 7.35                   | 4.73  | 1.36  | 7.22  | 4.09  | 1.88  | 1.46  | 4.94  | 0.55              | 2.36  | 0.85  | 0.59  |
| Eu  | 0.83                   | 0.74  | 0.06  | 1.10  | 0.42  | 0.14  | 0.04  | 0.62  | 0.04              | 0.29  | 0.02  | 0.01  |
| Gd  | 5.48                   | 4.21  | 1.35  | 5.60  | 3.57  | 1.88  | 1.58  | 4.04  | 0.642             | 2.83  | 0.77  | 0.64  |
| Tb  | 0.83                   | 0.62  | 0.30  | 0.82  | 0.63  | 0.40  | 0.36  | 0.64  | 0.14              | 0.46  | 0.20  | 0.16  |
| Dy  | 4.74                   | 3.15  | 2.15  | 4.53  | 4.04  | 2.51  | 2.59  | 3.59  | 0.89              | 2.50  | 1.16  | 0.90  |
| Ho  | 0.86                   | 0.59  | 0.43  | 0.88  | 0.88  | 0.54  | 0.52  | 0.67  | 0.17              | 0.43  | 0.20  | 0.16  |
| Er  | 2.33                   | 1.83  | 1.51  | 2.52  | 2.64  | 1.86  | 1.90  | 2.13  | 0.52              | 1.09  | 0.68  | 0.61  |
| Tm  | 0.35                   | 0.25  | 0.25  | 0.39  | 0.42  | 0.33  | 0.33  | 0.32  | 0.11              | 0.16  | 0.13  | 0.10  |
| Yb  | 2.28                   | 1.80  | 1.96  | 2.50  | 3.06  | 2.29  | 2.74  | 2.16  | 0.88              | 1.04  | 1.18  | 1.04  |
| Lu  | 0.35                   | 0.28  | 0.30  | 0.37  | 0.44  | 0.36  | 0.41  | 0.31  | 0.13              | 0.16  | 0.18  | 0.15  |
| Hf  | 6.7                    | 4.4   | 2.4   | 7.2   | 3.4   | 2.4   | 2.4   | 4.1   | 1.5               | 2.2   | 1.6   | 1.8   |
| Ta  | 2.6                    | 2.6   | 5.3   | 2.1   | 3.1   | 3.5   | 5.7   | 3.5   | 2.9               | 4.0   | 4.3   | 6.4   |
| W   | 1.5                    | 1.3   | 7.5   | 1.7   | 2.4   | 2.8   | 5.7   | 2.7   | 6.8               | 2.0   | 6.8   | 9.3   |
| Tl  | 1.5                    | 1.8   | 1.6   | 1.4   | 1.6   | 1.7   | 2.0   | 2.0   | 2.9               | 1.9   | 2.4   | 2.4   |
| Pb  | 34                     | 38    | 34    | 36    | 48    | 33    | 26    | 38    | 19                | 23    | 7.5   | 8.6   |
| Bi  | 0.2                    | 0.08  | <0.1  | 0.05  | 0.06  | 0.4   | 0.4   | 0.2   | 2.1               | 0.3   | 15    | 7.8   |
| Th  | 31                     | 20    | 7.7   | 29    | 19    | 11    | 7.1   | 23    | 2.2               | 5.5   | 4.5   | 4.3   |
| U   | 16                     | 17    | 30    | 9.3   | 22    | 32    | 33    | 17    | 3.2               | 8.7   | 10    | 24    |
| A/CNK                                       | 1.10                   | 1.07  | 1.14  | 1.10  | 1.09  | 1.09  | 1.14  | 1.08  | 1.25              | 1.26  | 1.23  | 1.19  |
| La <sub>CN</sub> /Lu <sub>CN</sub>          | 16.2                   | 11.2  | 2.06  | 15.9  | 5.86  | 2.42  | 0.99  | 12.6  | 1.23              | 7.35  | 1.83  | 1.52  |
| Eu/Eu*                                      | 0.381                  | 0.493 | 0.133 | 0.506 | 0.326 | 0.224 | 0.080 | 0.409 | 0.225             | 0.340 | 0.063 | 0.064 |

<sup>a</sup> – total iron as Fe<sub>2</sub>O<sub>3</sub>, A/CNK = molar Al<sub>2</sub>O<sub>3</sub>/(CaO + Na<sub>2</sub>O + K<sub>2</sub>O), Eu/Eu\* = Eu<sub>CN</sub>/(0.5Sm<sub>CN</sub> + 0.5Gd<sub>CN</sub>).

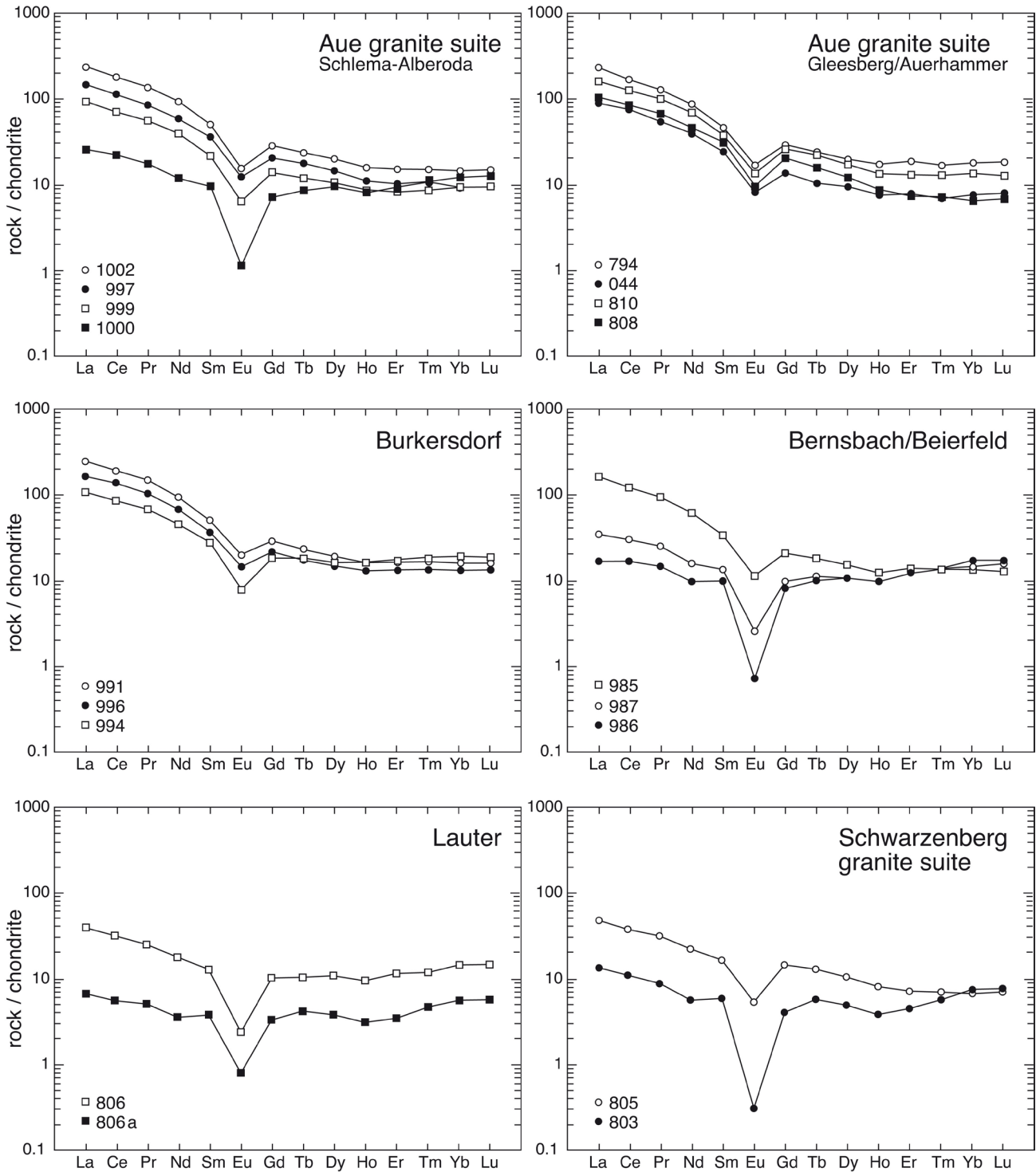
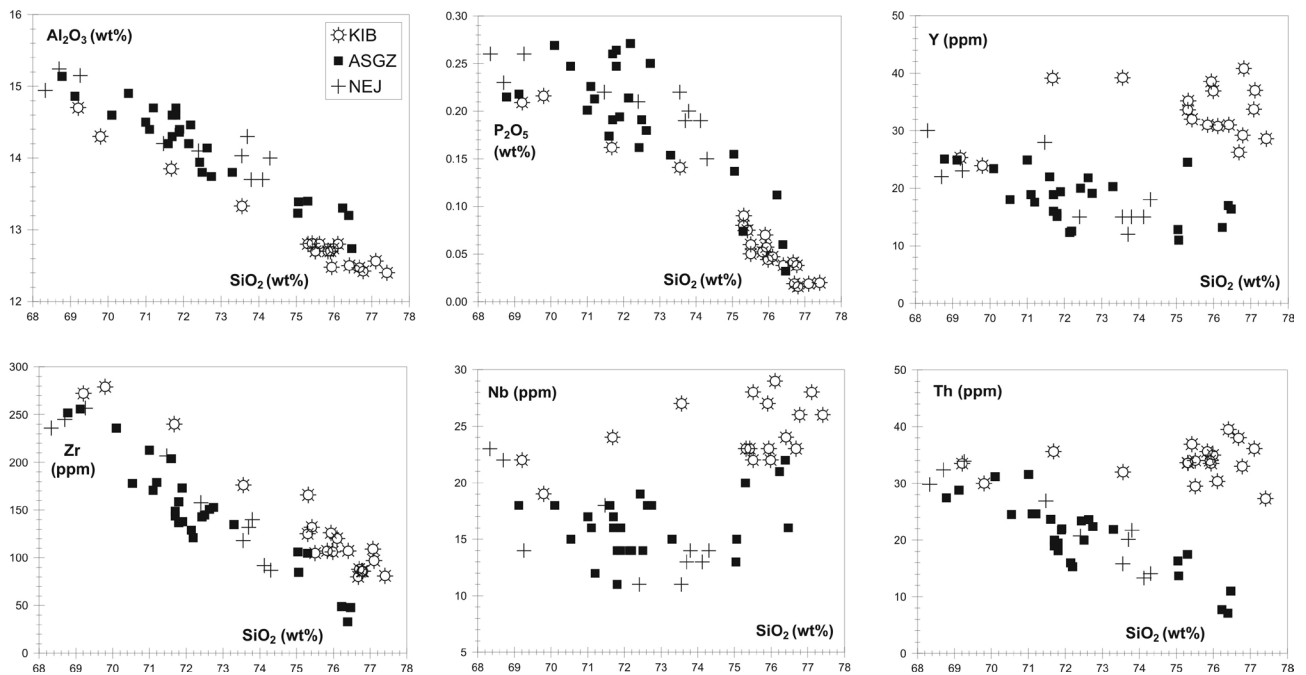


Fig. 7. Representative chondrite-normalized REE patterns of the granites from the ASGZ (Förster et al., 2009).

266–274) relative to MOR/2. It shows elevated levels of F (0.46–0.51 wt%) and (in ppm) Li (230–340), Rb (1050–1200), Nb (42–46), Sn (28–35), Sb (4.9), and W (36). The REE patterns are weakly declined, with a moderate negative Eu anomaly. MOR/2 is the geochemically most evolved among the suite of rhyolites. It possesses constantly high contents of F (0.50–0.63 wt%) and (in ppm) Rb (1120–1200), Ga (42–52), Nb (83–94), and Ta (42–49). It displays a number of extreme compositional signatures such as “bird wing”-shaped, flat REE patterns demonstrating the lanthanide tetrad effect and abnormally low ratios of the geochemical pairs Zr/Hf (~8) and Y/Ho (14–20).

The *Hahnwald* rhyolite is richer in Si than the rock from Morgenröthe, but shows no enrichment in K. It contains elevated abundances of F, Cu, Zn, Rb, Y, Sn, Nb, Mo, Sb, Pb, Bi, Th, and U. The REE patterns are flat and show a distinctly negative Eu anomaly. The contents of W (57–104) and Sn (4–9 ppm) are strongly antipathetically correlated.

The rhyolites and microgranites at *Gottesberg* are high in Ga, Nb, Y, REE, Th, and U. Their contents of F, Rb, Cs, Sn, and W are lower relative to those measured in the other rhyolites from this group. They are distinguished by high, but variable contents of Mo and Bi, and REE patterns resembling those of the rhyolites



**Fig. 8.** A selection of spider diagrams demonstrating the geochemical affinity of the F-poor biotite granites from the ASGZ with the neighbouring granites from Kirchberg (KIB) and the distant granites from Nejedek (NEJ), in the Czech Republic. See Förster et al. (2009) for data sources.

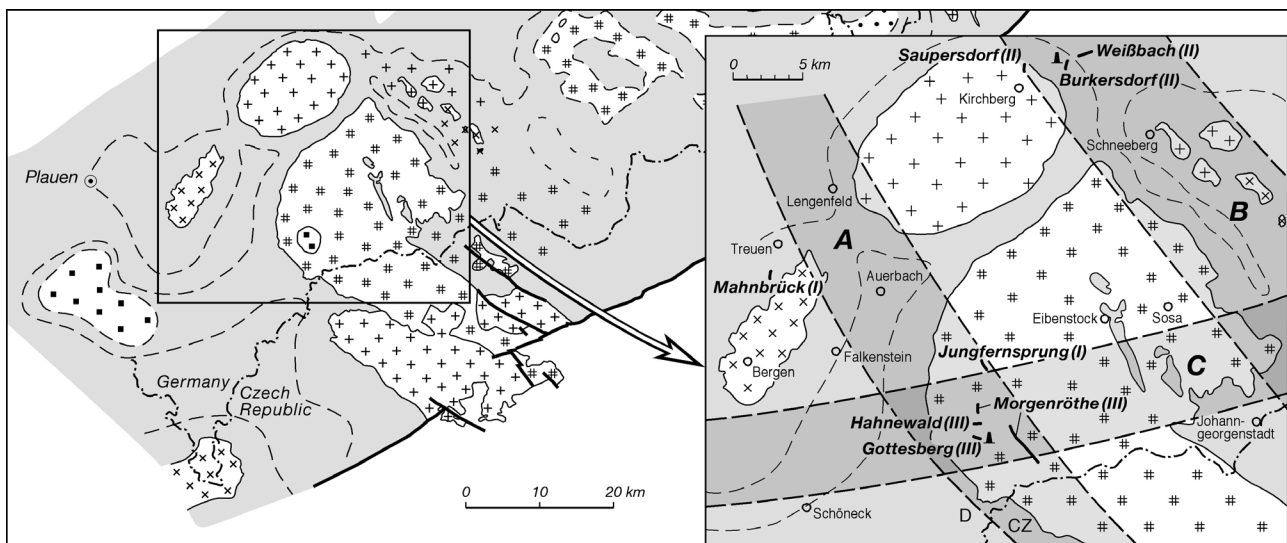


**Fig. 9.** Geological sketch map showing locations of the rhyolites/microgranites and the three most important structure zones: A = Slavkov (CZ) – Gottesberg – Netzschkau zone; B = Gera – Jáchymov (CZ) zone, C = Eichigt – Gottesberg – Schwarzenberg – Central Erzgebirge zone (modified from Förster et al., 2007). The Roman numbers in parentheses indicate the compositional group, to which the rhyolites belong (see text for explanation).

from Hahnwald. The GOT rhyolites/microgranites contain Na and Ca in abundances characterizing felsic aluminous rhyolites missing plagioclase destruction. This pattern is in full accordance with the circumstance that they contain fresh or only weakly altered feldspars.

### 3.2. Nd-isotopes

Except of the rock from Burkersdorf, the rhyolites/microgranites display Rb/Sr ratios  $>17$  and experienced intense, high-T alteration processes and surface weathering, which caused severe disturbances of the Rb–Sr isotopic system, resulting

in geologically meaningless  $Sr_i$ -values. For the rhyolite from Burkersdorf, the following Sr-isotopic parameters were obtained:  $^{87}Rb/^{86}Sr = 12.92$ ,  $^{87}Sr/^{86}Sr = 0.772272 \pm 10$ ,  $^{87}Sr/^{86}Sr_{(300\text{ Ma})} = 0.71713$ .

Group-I and group-II rhyolites are Nd-isotopically indistinguishable, but distinctly different from the rhyolites/microgranites of group-III. Rhyolites forming the first two groups have nearly identical Nd-initial values ( $t = 300$  Ma), ranging between  $-5.5$  (Mahnbrück) and  $-6.4$  (Burkersdorf), and model ages of 1.50–1.57 Ga. The group-III rhyolites exhibit significantly lower Nd-initial values, between  $-1.8$  (Morgenröthe, MOR/2) and  $-3.8$  (Gottesberg, mg1), and correspondingly younger model ages (1.20–1.36 Ga).

**Table 6.** Representative bulk-rock analyses of rhyolites/microgranites.

| Group<br>Rhyolite<br>Sample      | I              |                | II             |                |               | III              |                  |                |                 |                  |                  |                  |
|----------------------------------|----------------|----------------|----------------|----------------|---------------|------------------|------------------|----------------|-----------------|------------------|------------------|------------------|
|                                  | MAH<br>FT-1228 | JFS<br>FT-1209 | SAU<br>FT-1210 | WEI<br>FT-1212 | BUR<br>FT-988 | MOR/1<br>FT-1200 | MOR/2<br>FT-1198 | HAW<br>FT-1203 | GOT/mg1<br>Gb-1 | GOT/rh1<br>Gb-54 | GOT/rh2<br>Gb-67 | GOT/mg2<br>Gb-71 |
| SiO <sub>2</sub> (wt%)           | 77.1           | 73.2           | 74.3           | 75.4           | 72.9          | 75.8             | 75.1             | 78.0           | 72.7            | 76.4             | 73.4             | 75.6             |
| TiO <sub>2</sub>                 | 0.17           | 0.35           | 0.05           | 0.06           | 0.15          | 0.14             | 0.03             | 0.07           | 0.19            | 0.08             | 0.14             | 0.12             |
| Al <sub>2</sub> O <sub>3</sub>   | 11.9           | 12.9           | 14.3           | 15.2           | 14.5          | 12.7             | 14.0             | 12.1           | 13.3            | 12.5             | 13.9             | 12.5             |
| Fe <sub>2</sub> O <sub>3</sub> * | 0.83           | 2.80           | 1.00           | 1.41           | 1.12          | 2.67             | 1.68             | 2.36           | 2.52            | 0.41             | 1.14             | 1.51             |
| MnO                              | 0.008          | 0.004          | 0.06           | 0.02           | 0.06          | 0.23             | 0.29             | 0.09           | 0.05            | 0.02             | 0.02             | 0.04             |
| MgO                              | 0.23           | 0.23           | 0.22           | 0.14           | 0.54          | 0.18             | 0.11             | 0.09           | 0.29            | 0.23             | 0.16             | 0.13             |
| CaO                              | 0.06           | 0.12           | 0.26           | 0.17           | 0.82          | 0.03             | 0.03             | 0.03           | 0.65            | 0.68             | 0.77             | 0.51             |
| Na <sub>2</sub> O                | <0.1           | <0.1           | <0.1           | <0.1           | 2.83          | <0.1             | <0.1             | <0.1           | 2.69            | 3.56             | 3.93             | 3.47             |
| K <sub>2</sub> O                 | 6.94           | 7.85           | 6.86           | 3.58           | 4.54          | 5.48             | 5.68             | 3.88           | 5.32            | 4.59             | 5.08             | 4.81             |
| P <sub>2</sub> O <sub>5</sub>    | 0.03           | 0.11           | 0.20           | 0.17           | 0.36          | 0.04             | 0.03             | 0.04           | 0.12            | 0.03             | 0.06             | 0.06             |
| H <sub>2</sub> O <sup>+</sup>    | 2.30           | 2.02           | 2.39           | 3.47           | 1.27          | 2.17             | 2.39             | 2.92           | 1.21            | 0.76             | 0.77             | 0.71             |
| CO <sub>2</sub>                  | 0.14           | 0.15           | 0.18           | 0.16           | 0.72          | 0.10             | 0.11             | 0.13           | 0.46            | 0.44             | 0.21             | 0.18             |
| F                                | 0.11           | 0.14           | 0.14           | 0.23           | 0.17          | 0.46             | 0.51             | 0.50           | 0.37            | 0.10             | 0.14             | 0.18             |
| O=F                              | 0.05           | 0.06           | 0.06           | 0.10           | 0.07          | 0.19             | 0.22             | 0.21           | 0.15            | 0.04             | 0.06             | 0.08             |
| Total                            | 99.8           | 99.9           | 99.9           | 99.9           | 99.9          | 99.8             | 99.7             | 100.0          | 99.7            | 99.7             | 99.6             | 99.7             |
| Li (ppm)                         | 22             | 229            | 52             | 174            | 72            | 233              | 210              | 98             | 62              | 19               | 68               | 132              |
| Be                               | 4.4            | 3.5            | 2.8            | 4.5            | 3.0           | 5.0              | 4.0              | 5.5            | 11              | 3.6              | 10               | 8.9              |
| Sc                               | 4.2            | 4.2            | 4.5            | 4.7            | 3.9           | 3.1              | 2.9              | 2.2            | 5.1             | 1.6              | 3.4              | 4.1              |
| Co                               | 0.38           | 0.81           | 0.32           | 0.25           | 1.2           | 0.15             | 0.10             | 0.11           | 1.3             | 0.50             | 1.2              | 0.8              |
| Ni                               | 1.6            | 1.7            | 0.6            | 0.8            | 2.7           | 0.6              | 0.8              | 0.4            | 2.0             | 1.8              |                  | 1.8              |
| Cu                               | 4.8            | 2.8            | 2.3            | 7.0            | 3.0           | 2.2              | 2.1              | 18             | 5.7             | 3.7              | 4.3              | 2                |
| Zn                               | 25             | 25             | 50             | 33             | 40            | 46               | 37               | 157            | 38              | 13               | 37               | 38               |
| Ga                               | 18             | 19             | 30             | 31             | 25            | 31               | 42               | 27             | 31              | 26               | 27               | 23               |
| Rb                               | 530            | 500            | 690            | 600            | 430           | 1050             | 1120             | 670            | 450             | 320              | 400              | 440              |
| Sr                               | 34             | 18             | 26             | 24             | 96            | 24               | 49               | 2.1            | 26              | 19               | 25               | 7.2              |
| Y                                | 39             | 38             | 8.8            | 4.2            | 9.9           | 63               | 8.8              | 73             | 58              | 70               | 66               | 66               |
| Zr                               | 135            | 195            | 32             | 26             | 75            | 203              | 39               | 150            | 174             | 166              | 195              | 117              |
| Nb                               | 20             | 17             | 45             | 45             | 28            | 46               | 90               | 50             | 43              | 48               | 44               | 35               |
| Mo                               | 0.35           | 0.39           | 0.15           | 0.22           | 0.20          | 0.43             | 0.06             | 0.99           | 1.4             | 7.5              | 53               | 15               |
| Cd                               | 0.01           | 0.06           | 0.02           | <0.01          | 0.02          | 0.01             | 0.06             | 0.08           | 0.13            | 0.14             | 0.90             | 0.17             |
| Sn                               | 17             | 9              | 56             | 29             | 22            | 28               | 65               | 104            | 16              | 2.4              | 6                | 4.3              |
| Sb                               | 1.1            | 1.5            | 4.1            | 12.2           | 1.5           | 4.9              | 1.2              | 9.5            | 0.3             | 0.25             | 0.17             | 0.1              |
| Cs                               | 18.2           | 34.2           | 24.0           | 61.9           | 28.2          | 25.5             | 28.5             | 22.6           | 9.1             | 6.7              | 6.3              | 8.9              |
| Ba                               | 234            | 481            | 68             | 75             | 234           | 96               | 71               | 31             | 133             | 55               | 112              | 25               |
| La                               | 38.4           | 59.8           | 1.52           | 2.23           | 13.5          | 54.9             | 14.9             | 30.2           | 46.1            | 32.1             | 46.1             | 30.8             |
| Ce                               | 86.3           | 123            | 2.94           | 4.31           | 28.3          | 114              | 35.3             | 71.5           | 98.4            | 72.8             | 99.4             | 68.0             |
| Pr                               | 10.5           | 14.7           | 0.51           | 0.58           | 3.35          | 13.1             | 4.2              | 9.13           | 11.5            | 9.09             | 12.0             | 8.12             |
| Nd                               | 34.5           | 49.6           | 1.93           | 1.8            | 11.8          | 43.9             | 13.3             | 32.7           | 41.1            | 33.9             | 43.6             | 28.6             |
| Sm                               | 7.17           | 9.16           | 0.81           | 0.53           | 2.63          | 9.2              | 2.56             | 8.36           | 9.5             | 8.64             | 10.1             | 7.35             |
| Eu                               | 0.53           | 0.73           | 0.059          | 0.027          | 0.23          | 0.46             | 0.13             | 0.13           | 0.23            | 0.20             | 0.36             | 0.08             |
| Gd                               | 6.26           | 7.70           | 1.11           | 0.55           | 2.4           | 8.78             | 1.44             | 8.47           | 8.6             | 8.6              | 9.0              | 7.2              |
| Tb                               | 1.07           | 1.23           | 0.23           | 0.12           | 0.41          | 1.53             | 0.32             | 1.63           | 1.60            | 1.62             | 1.65             | 1.53             |
| Dy                               | 7.02           | 7.29           | 1.42           | 0.79           | 2.16          | 10.1             | 2.21             | 10.7           | 10.0            | 10.9             | 10.5             | 10.3             |
| Ho                               | 1.42           | 1.40           | 0.25           | 0.13           | 0.36          | 2.04             | 0.44             | 2.30           | 2.11            | 2.33             | 2.18             | 2.15             |
| Er                               | 4.44           | 4.02           | 0.69           | 0.36           | 0.91          | 6.35             | 1.54             | 7.29           | 6.41            | 7.54             | 6.80             | 7.07             |
| Tm                               | 0.71           | 0.61           | 0.11           | 0.062          | 0.13          | 1.05             | 0.34             | 1.24           | 1.03            | 1.17             | 1.03             | 1.14             |
| Yb                               | 4.68           | 3.93           | 0.71           | 0.49           | 0.87          | 7.25             | 3.03             | 8.32           | 7.19            | 8.34             | 7.26             | 8.65             |
| Lu                               | 0.66           | 0.58           | 0.11           | 0.074          | 0.13          | 1.03             | 0.45             | 1.19           | 0.98            | 1.19             | 1.05             | 1.24             |
| Hf                               | 4.7            | 6.0            | 1.7            | 1.9            | 2.8           | 7.3              | 4.7              | 6.9            | 6.0             | 7.3              | 7.1              | 4.6              |
| Ta                               | 2.5            | 2.1            | 11             | 11             | 6.6           | 7.8              | 45               | 8.1            | 7.8             | 7.5              | 6.4              | 7.2              |
| W                                | 4.8            | 27             | 11             | 16             | 18            | 36               | 13               | 9.2            | 10              | 5.2              | 7.1              | 6.8              |
| Tl                               | 3.4            | 2.7            | 4.7            | 3.7            | 2.8           | 9.4              | 9.9              | 7.8            | 2.9             | 1.7              | 2.0              | 2.1              |
| Pb                               | 3.8            | 15             | 3.0            | 11             | 6.1           | 8.0              | 5.2              | 50             | 17              | 21               | 32               | 34               |
| Bi                               | 0.35           | 0.25           | 1.5            | 1.7            | 1.4           | 0.43             | 0.26             | 20             | 3.1             | 2.7              | 0.73             | 0.06             |
| Th                               | 28             | 28             | 1.5            | 1.5            | 9.2           | 63               | 18               | 63             | 47              | 60               | 55               | 38               |
| U                                | 7.1            | 8.3            | 8.1            | 4.0            | 9.7           | 8.2              | 2.6              | 14             | 26              | 20               | 18               | 34               |
| Zr/Hf                            | 28.5           | 32.8           | 18.4           | 14.2           | 26.6          | 27.7             | 8.4              | 21.6           | 28.9            | 22.6             | 27.5             | 25.7             |
| Y/Ho                             | 27.5           | 27.4           | 35.6           | 31.1           | 27.6          | 30.8             | 19.9             | 31.6           | 27.7            | 30.0             | 30.3             | 30.6             |
| La <sub>N</sub> /Lu <sub>N</sub> | 5.94           | 10.5           | 1.47           | 3.08           | 10.6          | 5.45             | 3.36             | 2.26           | 4.80            | 2.76             | 4.49             | 2.54             |
| Eu/Eu*                           | 0.233          | 0.257          | 0.188          | 0.151          | 0.273         | 0.153            | 0.182            | 0.046          | 0.076           | 0.068            | 0.112            | 0.034            |

\* – total Fe as Fe<sub>2</sub>O<sub>3</sub>; rh – rhyolite; mg – microgranite.

#### 4. The Excursion

A thorough inspection of the magmatic and volcanic rocks of the study area would require several days of field work. The outcrop situation is not the best. Surface outcrops are limited. Active and inactive quarries usually expose only one textural variant of a granite massif and, thus, are not particularly attractive for visitors.

A few operating quarries grew big, and their visit is prohibited on working days owing to heavy truck traffic.

Since there are no attractive outcrops anymore in the Bergen massif and access to active quarries in the Kirchberg pluton is limited, the one-day excursion is exclusively devoted to outcrops in the Eibenstock granite. By the way, it is also the geochemically and mineralogically most interesting and abnormal massif. The

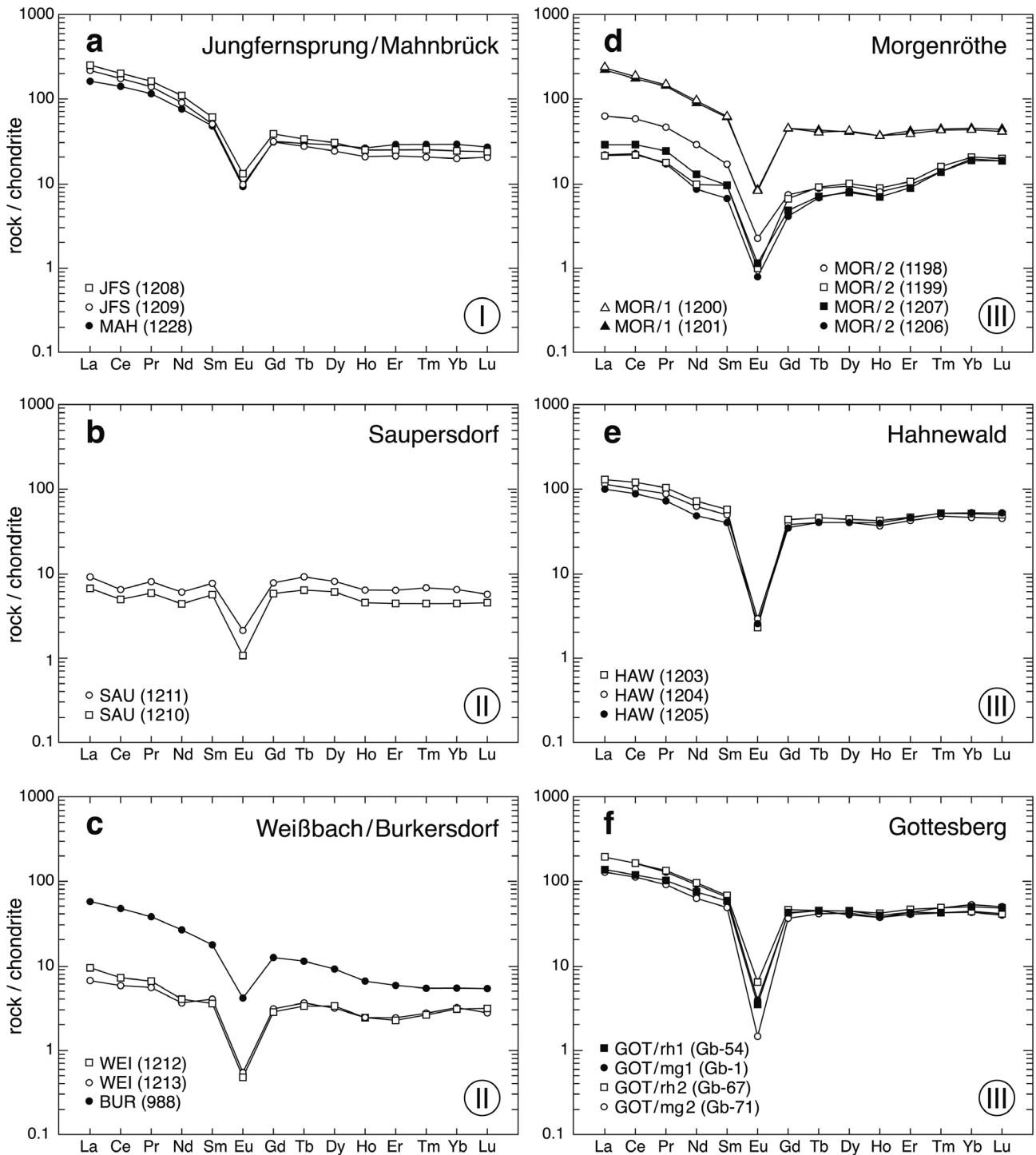


**Fig. 10.** Chondrite-normalized REE-patterns of rhyolites/microgranites. The Roman number at the bottom right in the diagrams indicates the rhyolite group. MOR/1 and MOR/2 in Fig. 10d refer to the rhyolite type from Morgenröthe. rh – rhyolite, mg – porphyritic microgranite (Förster et al., 2007).

first two steps will make you familiar with the textural variants of this massif, and the steps 3 and 4 will give you an impression on the late- and postmagmatic history and ore-generating productivity of this class of Sn–W-specialized leucogranites.

## 5. References

- Förster, A., Förster, H.-J. (2000) Crustal composition and mantle heat flow: Implications from surface heat flow and radiogenic heat production in the Variscan Erzgebirge (Germany). *J. Geophys. Res.* 105: 27,917-27,938.
- Förster, H.-J. (1999) The chemical composition of uraninite in Variscan granites of the Erzgebirge, Germany. *Mineral. Mag.* 63: 239-252.

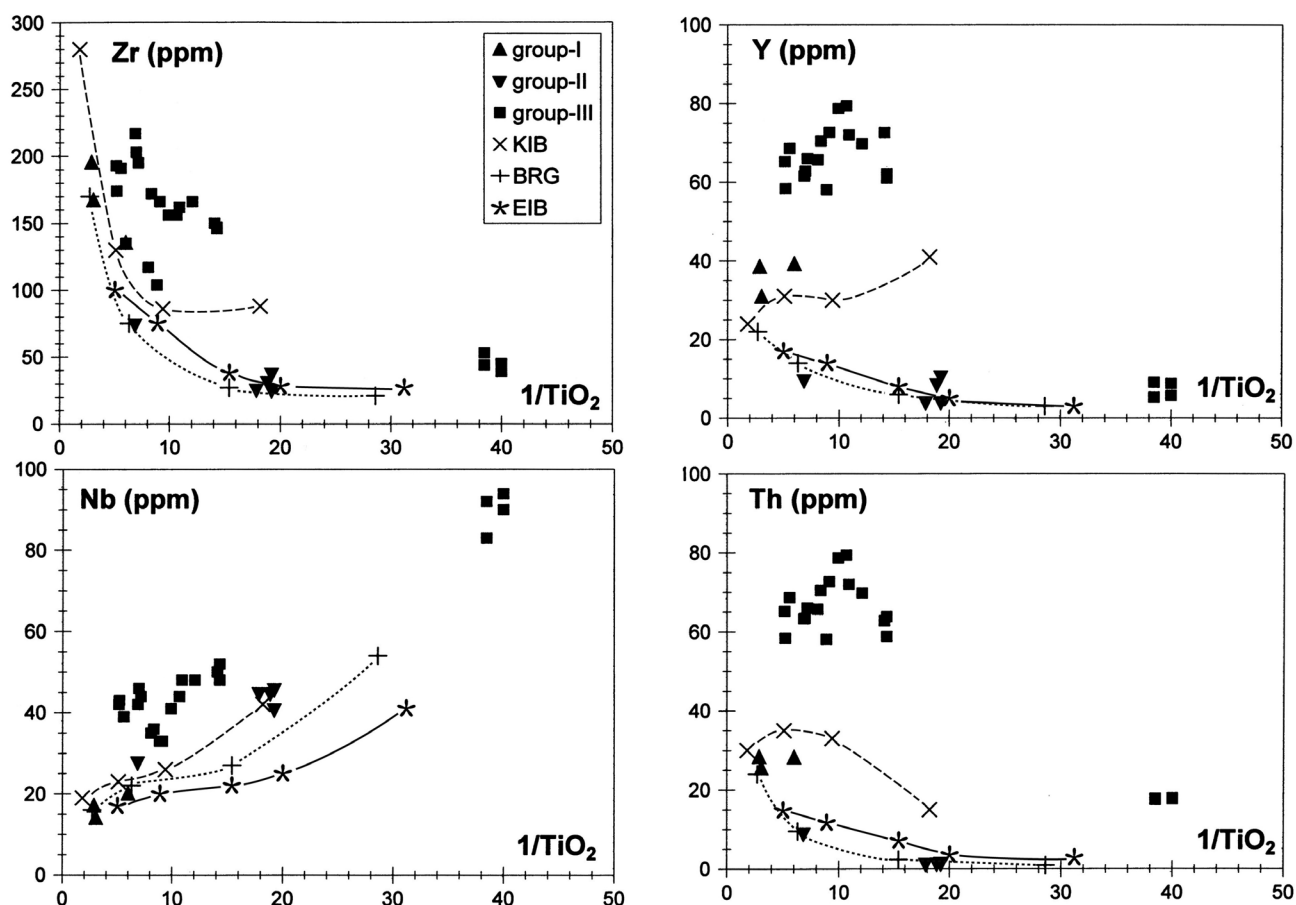


**Fig. 11.** Concentrations of Zr, Y, Nb, and Th in rhyolites/microgranites and the neighbouring granite massifs of Kirchberg (KIB), Bergen (BRG), and Eibenstock (EIB) as function of  $1/\text{TiO}_2$  (Förster et al., 2007). The evolution paths of the granite magmas are marked by dashed (KIB), dotted (BRG), and full lines (EIB).

- Förster, H.-J., Romer, R.L. (2010) Carboniferous magmatism. In: U. Linnemann and R.L. Romer (eds.) Pre-Mesozoic Geology of Saxo-Thuringia: From the Cadomian Active Margin to the Variscan Orogen. Schweizerbart Sci. Publ., Stuttgart, pp. 287-308.
- Förster, H.-J., Romer, R.L., Gottesmann, B., Tischendorf, G., Rhede, D. (2009) Are the granites of the Aue-Schwarzenberg Zone (Erzgebirge, Germany) a major source for metalliferous ore deposits? a geochemical, Sr-Nd-Pb isotopic, and geochronological study. *N. Jb. Mineral. Abh.* 186: 163-184.
- Förster, H.-J., Gottesmann, B., Tischendorf, G., Siebel, W., Rhede, D., Seltmann, R., Wasternack, J. (2007) Permo-Carboniferous subvolcanic rhyolite dikes in the western Erzgebirge/Vogtland, Germany: a record of source heterogeneity of post-collisional felsic magmatism. *N. Jb. Mineral. Abh.* 183: 123-147.
- Förster, H.-J., Tischendorf, G., Trumbull, R.B., Gottesmann, B. (1999) Late-collisional granites in the Variscan Erzgebirge, Germany. *J. Petrol.* 40: 1613-1645.
- Förster, H.-J., Tischendorf, G., Seltmann, R., Gottesmann, B. (1998) Die variszischen Granite des Erzgebirges: neue Aspekte aus stofflicher Sicht. *Z. geol. Wiss.* 26: 31-60.
- Tichomirowa, M., Leonhardt, D. (2010) New age determinations (Pb/Pb zircon evaporation, Rb/Sr) on the granites from Aue-Schwarzenberg and Eibenstock, Western Erzgebirge, Germany. *Z. geol. Wiss.* 38: 99-123

#### Other Literature (younger than 1990)

- Barsukov, V.L., Sokolova, N.T., Ivanitskii, O.M. (1996) Distribution of U, Th, and K in granites of the Aue and Eibenstock massifs, Erzgebirge, Germany. *Geochem. Int.* 34: 1041-1056.
- Barsukov, V.L., Sokolova, N.T., Ivanitskii, O.M. (2006): Metals, arsenic, and sulphur in the Aue and Eibenstock granites, Erzgebirge. *Geochem. Int.* 44: 896-911.
- Breiter, K., Förster, H.-J., Seltmann, R. (1999) Variscan silicic magmatism and related tin-tungsten mineralization in the Erzgebirge-Slavkovský les metallogenic province. In: D. Rickard (ed.): *Phanerozoic Metallogenesis in Europe*. Mineral. Deposita 34: 505-521.
- Förster, H.-J. (2010) The late-Variscan granites of the Aue-Schwarzenberg Zone (western Erzgebirge, Germany): Composition of accessory minerals and mineralogical mass balance of the lanthanides and actinides. *Z. geol. Wiss.* 38: 125-144.
- Förster, H.-J. (1998b) The chemical composition of REE-Y-Th-U-rich accessory minerals from peraluminous granites of the Erzgebirge-Fichtelgebirge region, Germany. Part II: Xenotime. *Am. Mineral.* 83: 1302-1315.
- Förster, H.-J. (1998a) The chemical composition of REE-Y-Th-U-rich accessory minerals from peraluminous granites of the Erzgebirge-Fichtelgebirge region, Germany. Part I: The monazite-(Ce)-brabantite solid solution series. *Am. Mineral.* 83: 259-272.

- Förster, H.-J., Davis, J.D., Tischendorf, G., Seltmann, R. (1999) Multivariate analyses of Erzgebirge granite and rhyolite composition: Implications for classification of granites and their genetic relations. *Computers & Geosciences* 25: 533-546.
- Förster, H.-J., Rhede, D., Hecht, L. (2008) Chemical composition of radioactive accessory minerals: implications to the evolution, alteration, age, and uranium fertility of the Fichtelgebirge granites (NE Bavaria, Germany). *N. Jb. Mineral. Abh.* 185: 161-182. Gottesmann, B., Seltmann, R., Förster, H.-J. (1995) Felsic subvolcanic intrusions within the Eibenstock granite pluton (Saxony, Erzgebirge): The Gottesberg volcano-plutonic system. *Terra Nostra*, 95/7: 49-53.
- Kempe, U. (2003) Precise electron microprobe age determination in unaltered uraninite: consequences on the intrusion age and the metallogenetic significance of the Kirchberg granite (Erzgebirge, Germany). *Contrib. Mineral. Petrol.* 145: 107-118.
- Kempe, U., Bombach, K., Matukov, D., Schlothauer, T., Hutschenreuter, J., Wolf, D., Sergeev, S. (2004) Pb/Pb and U/Pb zircon dating of subvolcanic rhyolite as a time marker for Hercynian granite magmatism and Sn mineralisation in the Eibenstock granite, Erzgebirge, Germany: considering effects of zircon alteration. *Mineral. Deposita* 39: 646-669.
- Sokolova, N.T., Ivanitskii, O.M. (2001) Distribution of Sn, W and Mo in the Aue and Eibenstock granitic massifs, Erzgebirge, Germany. *Geochem. Int.* 39: 219-225.
- Štemprok, M., Seifert, Th., Holub, F.V., Chlupáčová, M., Dolejš, D., Novák, J.K., Pivec, E., Lang, M. (2008) Petrology and geochemistry of Variscan dykes from the Jáchymov (Joachimsthal) ore district, Czech Republic. *J. Geosci.* 53: 65-104.
- Tischendorf, G., Förster, H.-J. (1994) Hercynian granite magmatism and related metallogenesis in the Erzgebirge: A status report. In: von Gehlen, K. & Klemm, D.D. (eds): *Mineral Deposits of the Erzgebirge/Krušné hory (Germany/Czech Republic)*. Monograph Series on Mineral Deposits 31: 5-23.
- Wasternack, J., Märtens, S., Gottesmann, B. (1995) Field and petrographic study of brecciation and greisenization phenomena in the Gottesberg tin deposit (Saxony, Germany). *Z. geol. Wiss.* 23: 619-642.

## Eurogranites 2012

### Stop 5-1

Quarry Süß, Zschorlau

Coordinates: 50°33'59" N, 12°37'12" E

Guide: Hans-Jürgen Förster

This small, family-owned quarry is the only one in operation in which the EIB1 textural variant of the Eibenstock granite massif is mined. The quarry is located just a couple of 10 meters from the contact with the metamorphic country rock, i.e., in the outermost endocontact of the massif. The quarried EIB1 granite (Fig. 12) differs texturally from the EIB1 facies in more central position in that it is less coarse-grained and less porphyritic. This contact-near spatial position is additionally characterized by the presence of geochemically evolved, fine-grained, layered marginal aplitic granites of centimeter to decimeter size and light grey to whitish color (Fig. 13). Another distinguishing feature of this outcrop is the occurrence of enclaves of the so-termed marginal granites of the Eibenstock pluton, representing the compositionally least evolved sub-intrusions (EIB0) (Fig. 14). Figure 15 shows a marginal-granite sample, in which euhedral, whitish, zoned grains of plagioclase crystallized within a grey, fine-grained groundmass. Operation of postmagmatic, fluid-triggered processes is manifested by the formation of milky-quartz veinlets crosscutting all rocks (Fig. 16).

The Table 7 lists representative whole-rock chemical analyses of the diverse granite variants exposed in this quarry. Probably mainly due to weathering (combined with magma modification associated with contamination and assimilation of country-rock material), most of the exposed rocks have reduced contents of mobile elements relative to more fresh textural equivalents (cf. Table 4). This depletion is most obvious for elements largely held in Li-bearing dark micas, i.e., Li and Cs, and, less severe, Rb (since this elements is also accumulated in feldspars). The same evolution holds for uranium, which was predominantly accumulated in easily soluble uraninite. Alteration-induced compositional modifications are most prominent in the fine-grained rocks, in which primary dark micas got largely seritized, associated with mobilization and removal of Li, Cs, and Rb.

**Table 7.** Representative bulk-rock analyses of granites from the quarry Süß.

| Sub-unit<br>Sample                          | EIB0<br>1226 | EIB1<br>1078 | fine-grained marginal zone |       |       |       |       |       |
|---|--------------|--------------|----------------------------|-------|-------|-------|-------|-------|
|   |              |              | 1076                       | 584   | 1077  | 442/2 | 442/3 | 518   |
| SiO <sub>2</sub> (wt%)                      | 73.8         | 75.0         | 74.2                       | 75.0  | 73.6  | 74.1  | 74.7  | 73.8  |
| TiO <sub>2</sub>                            | 0.14         | 0.07         | 0.048                      | 0.045 | 0.045 | 0.035 | 0.028 | 0.027 |
| Al <sub>2</sub> O <sub>3</sub>              | 13.7         | 13.7         | 15.2                       | 14.4  | 15.3  | 14.9  | 15.4  | 15.2  |
| Fe <sub>2</sub> O <sub>3</sub> <sup>a</sup> | 1.41         | 0.69         | 0.52                       | 1.13  | 1.03  | 0.92  | 0.92  | 0.56  |
| MnO   | 0.032        | 0.016        | 0.014                      | 0.019 | 0.023 | 0.016 | 0.018 | 0.015 |
| MgO   | 0.18         | 0.13         | 0.100                      | 0.120 | 0.08  | 0.11  | 0.13  | 0.10  |
| CaO   | 0.45         | 0.78         | 0.40                       | 0.31  | 0.40  | 0.36  | 0.50  | 0.50  |
| Na <sub>2</sub> O                           | 3.28         | 3.32         | 4.05                       | 3.07  | 3.58  | 3.83  | 5.32  | 3.57  |
| K <sub>2</sub> O                            | 4.75         | 4.70         | 4.01                       | 4.16  | 4.17  | 4.63  | 1.92  | 4.48  |
| P <sub>2</sub> O <sub>5</sub>               | 0.22         | 0.37         | 0.43                       | 0.29  | 0.46  | 0.37  | 0.30  | 0.44  |
| H <sub>2</sub> O <sup>+</sup>               | 1.66         | 0.63         | 0.44                       | 0.89  | 0.49  | 0.46  | 1.01  | 0.62  |
| CO <sub>2</sub>                             | 0.11         | 0.05         | 0.07                       | 0.17  | 0.07  | 0.13  | 0.13  | 0.1   |
| F   | 0.31         | 0.60         | 0.78                       |       | 0.95  | 0.43  |       | 0.97  |
| O=F   | 0.13         | 0.25         | 0.33                       |       | 0.40  | 0.18  |       | 0.41  |
| Total                                       | 99.8         | 99.9         | 99.9                       | 99.6  | 99.8  | 100.1 | 100.4 | 99.9  |
| Li (p.p.m.)                                 | 423          | 200          | 162                        |       | 257   | 246   | 215   |       |
| Be  | 17           | 14           | 5.7                        |       | 5.8   | 7.1   | 3.1   |       |
| Sc  | 2.5          | 2.2          | 2.1                        |       | 2.8   | 1.8   | 2.3   | 1.8   |
| Co  |              | 0.28         |                            |       | 0.43  | 0.75  |       |       |
| Ni  |              |              |                            |       |       | 3.4   |       |       |
| Zn  | 56           | 28           | 29                         | 39    | 41    | 39    | 33    | 23    |
| Ga  |              | 30           | 31                         | 31    | 33    | 33    | 37    | 33    |
| Rb  | 690          | 782          | 747                        | 682   | 812   | 823   | 465   | 751   |
| Sr  | 30           | 22           | 9.9                        |       | 13    | 8.6   | 19    | 39    |
| Y   | 17.3         | 13.4         | 6.7                        |       | 5.9   | 1.6   | 5.5   | 4.3   |
| Zr  | 104          | 51           | 19                         | 15    | 19    | 19    | 18    | 30    |
| Nb  | 15           | 24           | 31                         | 20    | 33    | 29    | 29    | 27    |
| Mo  |              | 0.10         | 2.0                        |       | 0.08  | 0.16  |       |       |
| Sn  | 16           | 27           | 18                         |       | 25    | 19    | 24    | 15    |
| Sb  |              | 0.46         |                            |       | 0.34  | 0.30  |       | 0.30  |
| Cs  | 83           | 53           | 36                         |       | 41    | 46    | 28    | 35    |
| Ba  | 147          | 75           | 7.4                        |       | 5.9   | 9.6   | 15    | 16    |
| La  | 16.6         | 5.25         | 1.34                       |       | 1.20  | 0.735 | 1.31  | 0.83  |
| Ce  | 37.7         | 12.3         | 3.84                       |       | 3.42  | 1.72  | 2.98  | 2.26  |
| Pr  | 4.73         | 1.52         | 0.51                       |       | 0.46  | 0.26  | 0.38  | 0.29  |
| Nd  | 16.2         | 5.36         | 1.79                       |       | 1.60  | 0.84  | 1.39  | 1.02  |
| Sm  | 4.12         | 1.64         | 0.90                       |       | 0.82  | 0.32  | 0.52  | 0.56  |
| Eu  | 0.27         | 0.047        | 0.006                      |       | 0.006 | 0.007 | 0.020 | 0.010 |
| Gd  | 4.08         | 1.87         | 0.92                       |       | 0.90  | 0.37  | 0.54  | 0.60  |
| Tb  | 0.71         | 0.41         | 0.24                       |       | 0.22  | 0.078 | 0.15  | 0.17  |
| Dy  | 3.74         | 2.39         | 1.29                       |       | 1.17  | 0.37  | 0.81  | 0.88  |
| Ho  | 0.52         | 0.36         | 0.16                       |       | 0.14  | 0.043 | 0.11  | 0.11  |
| Er  | 1.19         | 0.82         | 0.35                       |       | 0.31  | 0.099 | 0.24  | 0.25  |
| Tm  | 0.14         | 0.11         | 0.048                      |       | 0.043 | 0.014 | 0.040 | 0.040 |
| Yb  | 0.80         | 0.61         | 0.31                       |       | 0.27  | 0.087 | 0.25  | 0.28  |
| Lu  | 0.11         | 0.075        | 0.035                      |       | 0.029 | 0.013 | 0.030 | 0.030 |
| Hf  | 3.7          | 2.3          | 1.1                        |       | 1.4   | 1.4   | 1.3   | 2.3   |
| Ta  |              | 8.2          |                            |       | 12    | 14    |       | 14    |
| W   |              | 9.0          |                            |       | 13    | 36    |       | 84    |
| Tl  |              | 4.2          |                            |       | 4.3   | 4.8   |       |       |
| Pb  | 18.0         | 10.4         | 6.9                        |       | 7.3   | 6.0   | 7.5   | 8.0   |
| Bi  |              | 1.3          |                            |       | 0.6   | 4.9   |       |       |
| Th  | 15.8         | 10.3         | 5.9                        |       | 5.4   | 2.1   | 1.6   | 2.7   |
| U   | 21.1         | 18.2         | 8.3                        |       | 16.4  | 8.0   | 2.1   | 12.2  |
| A/CNK                                       | 1.21         | 1.15         | 1.29                       | 1.43  | 1.37  | 1.25  | 1.31  | 1.31  |
| La <sub>CH</sub> /Lu <sub>CH</sub>          | 15.4         | 7.16         | 3.92                       |       | 4.23  | 5.78  | 4.47  | 2.83  |
| Eu/Eu*                                      | 0.195        | 0.081        | 0.020                      |       | 0.021 | 0.061 | 0.114 | 0.052 |

## Eurogranites 2012

### Stop 5-2

Quarry Hahn, Eibenstock

Coordinates: 50°30'59" N, 12°37'58" E,

Guide: Hans-Jürgen Förster

This still expanding, also family-owned quarry (Fig. 17) exposes the EIB2 granite in its characteristic texture (Fig. 18). Textural and compositional (Table 8) variation is minor. The average modal composition is (in vol.%): quartz – 34, K-feldspar – 36, albite-rich plagioclase – 25, Li-mica – 4, muscovite – 1, accessories – 1.

The rocks are fresh and have experienced only relatively weak autometamorphic overprinting. The granite rarely contains tourmaline nodules or beryl crystals in cavities or open fractures. Small veins of quartz and light violet amethyst have locally penetrated the EIB2 granite here.

Two representative chemical analyses of the granite from this quarry are reported in Table 8. Note the large concentrations of P (the bulk is accommodated in feldspars), F (in micas, fluorapatite, and topaz), Li, Rb, Cs, and the lithophile ore elements Sn and W. The concentrations of compatible elements, such as Ba, Sr, Zr, Y, REE, Hf, and Th are low. The U concentrations are secondarily depleted.



**Fig. 12.** Typical texture of the EIB1 granite, which is the most widespread textural variant on surface outcrop (dam Sosa).



**Fig. 13.** Fine-grained, intensely layered marginal zone of the EIB1 granite at quarry Sűß.

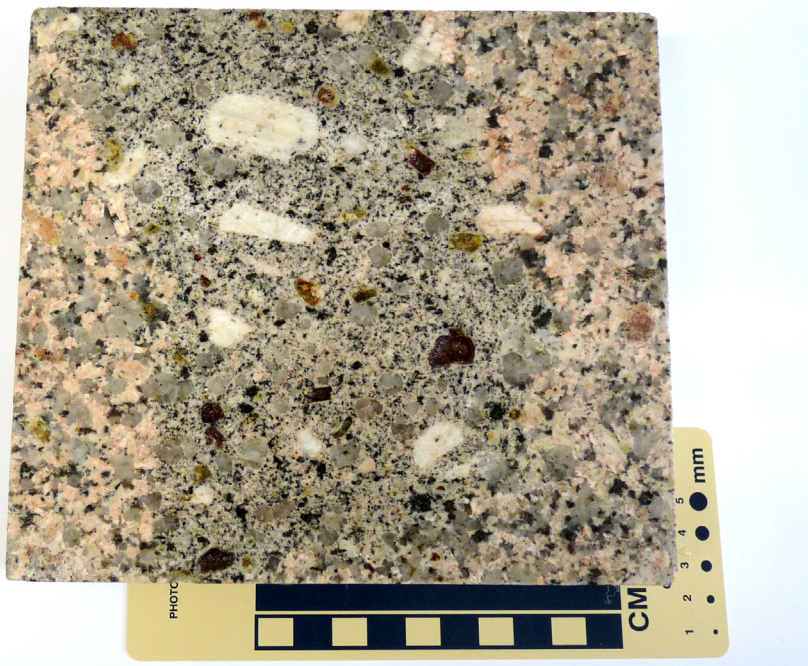


**Fig. 14.** Partly assimilated enclave of the marginal-granite facies in EIB1 granite (quarry Sűß).

**Table 8.** Representative bulk-rock analyses of the EIB2 granite from the quarry Hahn.

| Sample                             | 239   | 507   |
|------------------------------------|-------|-------|
| SiO <sub>2</sub> (wt%)             | 74.9  | 74.4  |
| TiO <sub>2</sub>                   | 0.065 | 0.057 |
| Al <sub>2</sub> O <sub>3</sub>     | 13.9  | 14.1  |
| Fe <sub>2</sub> O <sub>3</sub>     | 1.14  | 1.19  |
| MnO                                | 0.044 | 0.025 |
| MgO                                | 0.10  | 0.07  |
| CaO                                | 0.39  | 0.40  |
| Na <sub>2</sub> O                  | 3.38  | 3.59  |
| K <sub>2</sub> O                   | 4.41  | 4.55  |
| P <sub>2</sub> O <sub>5</sub>      | 0.32  | 0.42  |
| H <sub>2</sub> O <sup>+</sup>      | 0.53  | 0.57  |
| CO <sub>2</sub>                    | 0.08  | 0.1   |
| F                                  | 0.73  | 0.69  |
| O=F                                | 0.31  | 0.29  |
| Total                              | 99.7  | 99.8  |
| Li (p.p.m.)                        | 701   | 574   |
| Be                                 | 15    | 12    |
| Sc                                 | 2.1   | 2.5   |
| Co                                 |       | 0.34  |
| Zn                                 | 40    | 38    |
| Ga                                 | 30    | 29    |
| Rb                                 | 938   | 969   |
| Sr                                 | 15    | 14    |
| Y                                  | 10.2  | 9.4   |
| Zr                                 | 44    | 39    |
| Nb                                 | 22    | 22    |
| Mo                                 |       | 0.07  |
| Sn                                 | 28    | 24    |
| Sb                                 |       | 0.69  |
| Cs                                 | 95    | 135   |
| Ba                                 | 13    | 20    |
| La                                 | 3.66  | 3.32  |
| Ce                                 | 8.99  | 7.90  |
| Pr                                 | 1.18  | 1.00  |
| Nd                                 | 3.98  | 3.75  |
| Sm                                 | 1.27  | 1.18  |
| Eu                                 | 0.024 | 0.040 |
| Gd                                 | 1.51  | 1.11  |
| Tb                                 | 0.30  | 0.28  |
| Dy                                 | 1.87  | 1.68  |
| Ho                                 | 0.30  | 0.27  |
| Er                                 | 0.77  | 0.74  |
| Tm                                 | 0.12  | 0.10  |
| Yb                                 | 0.74  | 0.66  |
| Lu                                 | 0.092 | 0.11  |
| Hf                                 | 1.9   | 2.0   |
| Ta                                 |       | 6.4   |
| W                                  |       | 16.0  |
| Tl                                 |       | 5.4   |
| Pb                                 | 8.2   | 8.3   |
| Bi                                 |       | 3.4   |
| Th                                 | 7.1   | 6.7   |
| U                                  | 11.3  | 12.2  |
| A/CNK                              | 1.26  | 1.22  |
| La <sub>CN</sub> /Lu <sub>CN</sub> | 4.07  | 3.90  |
| Eu/Eu*                             | 0.053 | 0.105 |



**Fig. 15.** Fresh marginal-granite (EIB0) sample (boulder near the village of Jägersgrün).



**Fig. 16.** A swarm of quartz-dominated veins, which partly exhibit a pegmatitic core zone (quarry Süß).



**Fig. 17.** Quarry Hahn



**Fig. 18.** Typical sample of the EIB2 granite variant (quarry Hahn)

## Eurogranites 2012

### Stop 5-3

Visitor mine Grube Tannenberg  
Tannenbergsthal

Coordinates: 50°26'04" N, 12°27'19" E

Guides:

Hans-Jürgen Förster and Steffen Gehrlich

Modern mining activities related to this former Sn mine lasted from 1936 until 1964. Published records about Sn mining in the larger area dated back until 1765. However, Sn mining was very likely to have been performed still earlier, in the 15 century, giving rise to the origination of the "Tannenberg Pinge", a surface depression generated in response to the collapse of mining cavities (Fig. 19).

Visited will be the Tannenberg tunnel, which is about 600m long and in which we have a constant annual temperature between 8 and 9 degrees C. Exposed are geologically:

1. The contact between the heavily weathered EIB1 granite and the andalusite-bearing micaschist (inner contact-metamorphic aureole)
2. Lamprophyre veins (0.5 to 1m in thickness) crosscutting the granite
3. A vein-type pegmatite
4. The most impressive eye-catcher, a mining cavity formerly representing a massive greisen body. This cavity is about 50m in length and 30m in width and filled with water of about 25m thickness. The greisen body formed in the apical portions of the granite. In its central zone, the greisen consisted of quartz and topaz and contained between 0.5 and 1.5 wt% Sn. The outer zones was made up of quartz and mica and was poorer in Sn (0.1–0.5 wt%)
5. Porphyre and greisen veins within the granite

If time permits we will visit the neighbouring museum in which, among many other things, impressive samples from the Schneckenstein rock are on display. The preserved Schneckenstein rock, about 1km W of the visitor mine, is probably a greisen body rich in cavities, in which crystals of mostly quartz and yellowish topaz, up to several centimeter in size, precipitated. In former times, topaz crystals of gemstone quality were processed to jewelry for the Saxonian kings.

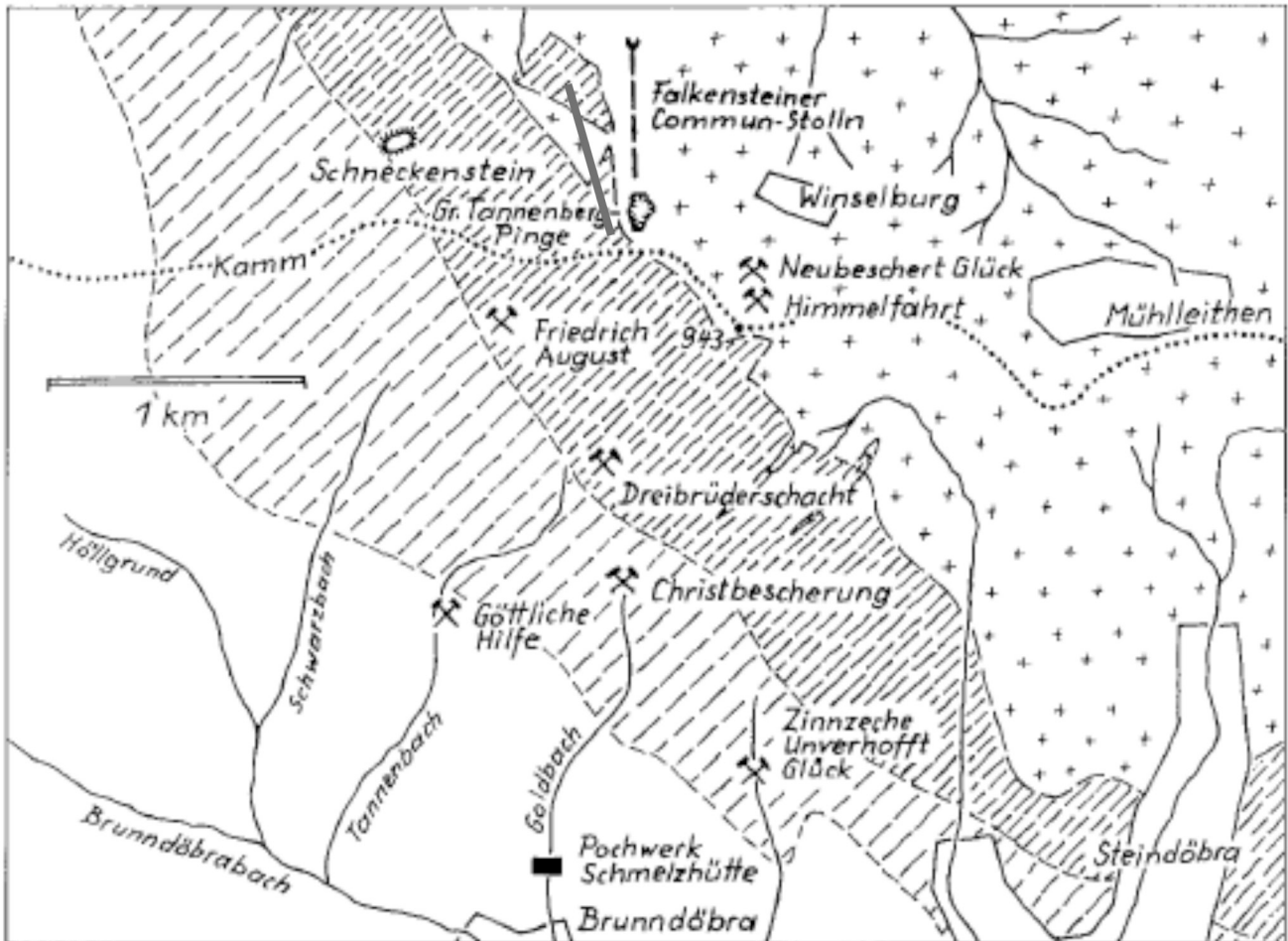


**Fig. 19.** Abandoned underground Sn mines (hammer-and-pick signs) in the neighborhood of the visitor mine Grube Tannenberg. Crosses – EIB1 granite, heavy-dashed area – inner contact-metamorphic aureole, light-dashed area – outer contact-metamorphic aureole. The red line marks the approximate geological profile that will be seen during the underground excursion.

## Eurogranites 2012

### Stop 5-4

Geyer tin deposit

Mining subsidence (“Pinge”) at Geysersberg

Coordinates:

Lat.: 50°37'15"N, long.: 12°15'42"E

Guide: Reimar Seltmann

The tin deposit exposed in this surface outcrop belongs to the type of greisen-like stockwerk deposits. It is predominantly composed of steeply dipping NW–SE and NE–SW trending greisen veins associated with with minor flat-dipping veinlets. Ore minerals encompass cassiterite, arsenopyrite/löllingite, wolframite, and molybdenite. Accompanying minerals include quartz, Li-mica, and triplite. The deposit is related to a pipe-like granite stock,

which is composed of the following textural types:

- fine- to small-grained aplitic (type D).
- medium-grained equigranular (type C)
- small- to medium-grained equigranular (type B)
- fine-grained, porphyritic (hiatalporphyritic type A; only known from enclaves)

At the margin of the Pinge, an intrusive breccia is outcropping. It is composed of a fine-grained aplitic material that intruded into mm-sized fractures in the wall rock. Such breccias are supposed being a feature of low-viscosity, fluid-enriched granitic magmas. The breccia fragments range from angular in the host rock to rounded nearest to the granite. The fragments are greisenized at their rims. Subsidence related to mining activity exactly occurred at the contact between granite cupola and metamorphic host rock. This implies that Sn mineralization was restricted to the granite and did not proceed into the country rock, which is a contactmetamorphic two-mica schist containing layers of muscovite–K-feldspar–plagioclase gneiss and calc-silicate hornfels.

Mining started in 1399, whilst mining subsidence has occurred from 1703-1807, with the last collapse occurring in 1969.



Fig. 20. Geological map of the Geyer "Pinge".

# The petrified forest of Chemnitz - A snapshot of an Early Permian ecosystem preserved by explosive volcanism

Ronny Rößler  
Museum für Naturkunde  
Moritzstrasse 20  
D-09111 Chemnitz  
roessler@naturkunde-chemnitz.de

The Chemnitz Basin that represents the Rotliegend depositional area of the 30 x 70 km large, NE-SW trending Erzgebirge Basin, situated in southern Saxony. It is filled with continental molasse-type deposits representing the debris of the increasingly eroded Variscan orogen.

The up to 1550 m thick Early Permian Rotliegend succession of the Chemnitz Basin is subdivided into four formations based on lithology and genesis. Here we focus on the Leukersdorf Formation that is mainly composed of alluvial red-beds and is characterised by three marker horizons: The lacustrine to palustrine Rottluff horizon in the lower part, the basin-wide distributed Reinsdorf carbonate horizon in the middle part and the Zeisigwald tuff in the upper part of the section. The latter resulted from a series of volcanic eruptions in the area of present-day Chemnitz and caused the formation of the Chemnitz Petrified Forest. Several features make this fossil lagerstätte so exceptional in comparison to other fossil forests with tree stumps preserved *in situ*. The Chemnitz fossil forest has a special historical importance because collecting at this site started in the early 18th century. In Chemnitz, an Early Permian landscape has been buried instantaneously by volcanic ashes preserving autochthonous and par-autochthonous fossil assemblages. Since 2008, excavations have shown how the volcanic events affected the entire ecosystem. Among the unique features that have been documented here are: (1) the presence of rooting structures of several taxa that are preserved *in situ* in one single horizon, (2) the occurrence of foliage and reproductive organs associated with petrified stems and branches, and (3) the presence of various animal remains found together with the plants, including reptiles still showing the original body outlines.

## 1. The Erzgebirge basin in Saxony

### 1.1. Geological background and Stratigraphy

In the 19th century some of the first ideas and principles on Carboniferous and Permian stratigraphy and palaeontology have been developed in this region, mainly carried by the work of August von Gutbier and Hanns-Bruno Geinitz. Nowadays, a renewed interest on Late Palaeozoic tectonic, climatic, and biotic processes in the Variscan orogen belt leads to intense research in the Saxo-Thuringian area of this belt too. New genetic models are discussed for collisional–extensional processes at the northern border of the Bohemian Massif resulting from recent investigations of the tectonical and geodynamic setting of the Saxo-Thuringian.

The present-day 70 km by 30 km large and NE-SW striking Erzgebirge basin in south Saxony (Fig. 1) was discontinuously filled with molasse-type deposits of the Variscan orogen. Sedimentation was interrupted by long periods of non-sedimentation and erosion of older basin fill. Subsequent basins were controlled by different geodynamic regimes and, therefore, had a development independent of their precursors. The term Erzgebirge basin includes the entity of these subsequent basins as it describes the present-day distribution of Late Palaeozoic deposits at the northern flank of the Erzgebirge, rather than a specific basin in geotectonic terms.

The Late Visean is represented by relicts of the **Hainichen basin**. At intersections of deep faults, local basins developed, such as the postorogenic basins of **Flöha** (Westphalian B/C; Duckmantian/Bolsovian) and the **Oelsnitz** and **Zwickau basins** (Westphalian D - ?Cantabrian). Erosional relicts of additional Westphalian basins exist in the Eastern Erzgebirge, e.g., the **B/C Olbernhau-Brandov** and **B-D Schönfeld-Altenberg** basins. The Rotliegend **Chemnitz basin** arose after the Franconian movements and basin reorganization, and is superimposed on the deep fault system of the detachment between the Erzgebirge Mountains and the the Saxonian Granulite Massif.

### 1.2. Development and basin fill of the Rotliegend Chemnitz basin

Deposits of the Rotliegend cover the whole basin (Fig. 2). Basement areas and coal-bearing successions of the Visean and the Asturian/?Cantabrian were overlain. In the Western part of the basin, the oldest Lower Rotliegend sediments (Härtensdorf Formation) rest with an angular unconformity on the deeply eroded upper Zwickau Formation of topmost Westphalian to Cantabrian age. Basin development and configuration during the Lower Rotliegend is mainly controlled by volcano-tectonic processes. Frequent ash falls during this time originate from volcanic activity mostly outside the basin, possibly in the NW-Saxony Volcanite Complex, which confines the basin to the north. Starting with the Upper Rotliegend-II, facies patterns follow increasingly NW-SE directions perpendicular to the Variscan strike. The Middle to Upper Permian red beds of the Mülsen Formation formed possibly the transition to the Late Permian Zechstein and Mesozoic platform development. In the NW of the Chemnitz Basin this Upper Rotliegend coarse clastics are covered transgressively by marine Zechstein deposits and their terrestrial equivalents.



Fig. 1. Location map of the Chemnitz Basin.

The up to 1550 m thick basin fill of the Chemnitz basin consists mainly of alluvial red beds and volcanites and is subdivided in four formations (Fischer, 1990; Schneider et al. 2011). The oldest one, the 180 m (max. 280 m) thick **Härtensdorf Formation**, deposited in a WSW-ENE to SW-NE orientated basin, shows basal matrix-supported fan conglomerates. These coarse clastic deposits were formed by debris flows that interfinger towards the basin centre with fine-clastic alluvial and flood plain sediments, mainly siltstones with intercalated channel conglomerates of a braided river system. The often greenish to light grey coloured fills of those channels point on palaeo-groundwater flow. Flood plain deposits contain sporadically centimetre to decimetre thick coal seams of local swamps. Very typical for the flood plain siltstones and silty sandstones are invertebrate burrows of *Scoyenia*-type. Common are calcareous rhizoconcretions in the neighbourhood of the channels and stacked calcisols of different maturity. Decimetre thick micritic limestones with mm-sized gastropods and minute isolated skeletal remains of snake-like aistopod amphibians indicate the existence of temporary pools and lakes (Schneider & Röbner, 1996). The age of the Härtensdorf Formation is determined by macrofloral remains (such as *Alethopteris schneideri*, *Callipteridium gigas*; Barthel, 1976) as Lower Rotliegend and by sporomorphs as late Asselian based on the dominance of *Vittatina* spp. (Döring et al., 1999). Volcanism started in the upper Härtensdorf Formation with pyroclastic horizons due to plinian eruptions and continued into the Planitz Formation which was dominated by extended volcanic deposits. The base of the up to 170 m thick **Planitz Formation** is marked by the 5 to 25 m thick Gröna tuff. This formation mainly consists of different volcanites, like ash tuffs and ignimbrites and their reworked products as well. Depending on the position to the eruption areas inside and outside the NW-Saxony basin, there are regional changes in thickness and facies pattern, although several tuff horizons form excellent marker horizons throughout the basin. Intercalations of conglomerates, sandstones, and siltstones are subordinate. The Gröna pyroclastic rocks are directly overlain by the distinctive Niederplanitz lake horizon, which represents a vertical and lateral sequence of centimetre to decimetre thick lacustrine black, greenish-grey to red claystones and siltstones with intercalated pyroclastics. These deposits formed during a wet climatic phase in an extended lake landscape. The low diversity vertebrate fauna only consists of palaeoniscid fishes and

xenacanthid fresh water sharks indicating the linkage of this basin to a larger, interregional drainage system, enabling the immigration of fishes. Flows of trachybasaltic and shoshonitic lavas of up to 70 m thickness originated from different fault controlled eruption centres in the south-western part of the basin. The upper part of the Planitz Formation contains widespread ignimbrites, locally deposited as vitrophyres (pitchstone). The age of the Planitz Formation is determined as late Lower Rotliegend (late Asselian/early Sakmarian) by xenacanthid shark teeth (Schneider, 1988); sporomorphs indicate a late Autunian age, comparable to the late Asselian of the Donetsk basin (Döring et al., 1999).

The up to 700 m thick **Leukersdorf Formation** rests erosive on the Planitz Formation. Decametre thick basal conglomerates contain the debris of the eroded Planitz volcanites. Generally, the formation consists of red fan and predominating alluvial to flood plain deposits in three fining-up cycles. Alluvial and flood plain deposits are characterised by the *Scoyenia* facies of wet red beds as well as calcisols of different maturity. Apart from common tiny rootlets this formation basinwide rarely shows any evidence of plant growth. In this respect, the Chemnitz fossil forest is an unusual, very local assemblage with a rich forest flora and fauna. The top of the first cycle is formed by the maximally 25 m thick fluvial-palustrine Rottluff Horizon, consisting of grey clastics with plant remains and thin coaly layers. The top of the second cycle is marked by several thin limestone beds of the Reinsdorf Lake Horizon. This grey micritic limestone contains gastropods, ostracods, and rarely disarticulated tetrapod remains. Very rarely, laminites delivered poorly preserved branchiosaurid amphibian skeletons. The third cycle is marked by the eruption of the up to 90 m thick Zeisigwald tuff. As rhyolitic volcanism occurred on a widespread scale during the Early Permian, this eruption series particularly influenced the eastern part of the basin. In the area of present-day Chemnitz the eruption of the Zeisigwald volcano additionally resulted in the formation of the Chemnitz Petrified Forest. The initial blast of a phreatomagmatic eruption cut the majority of up to 30 m high woody trees. They latter were laid down in east-west direction and covered by different pyroclastics (Fischer, 1991; Röbner, 2001).

The absolute age of this volcanic event of about  $290.6 \pm 1.8$  Ma was recently determined by SHRIMP U–Pb measurements on zircons (K.-P. Stanek, personal communication, 2009), which corresponds to the late Asselian–early Sakmarian. This has been

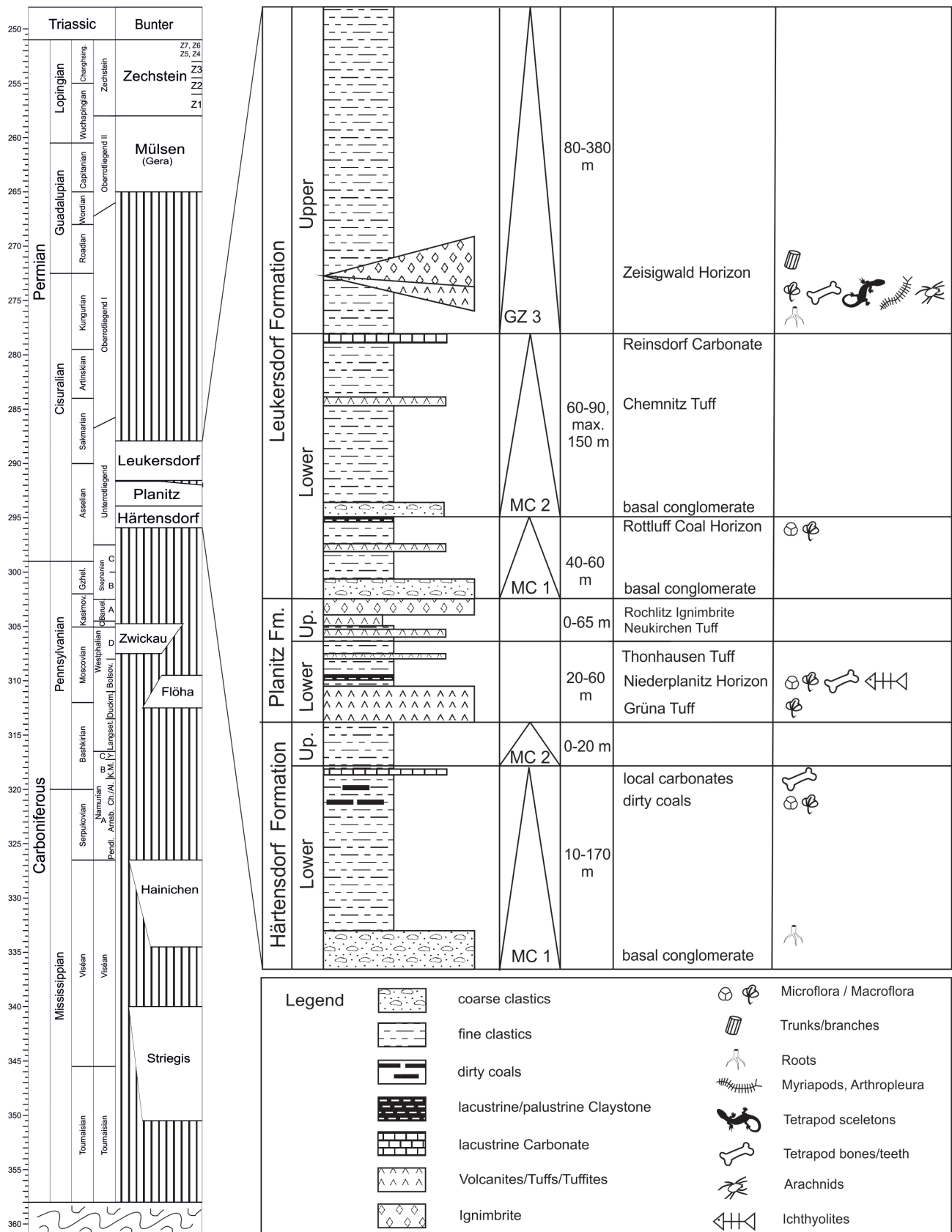
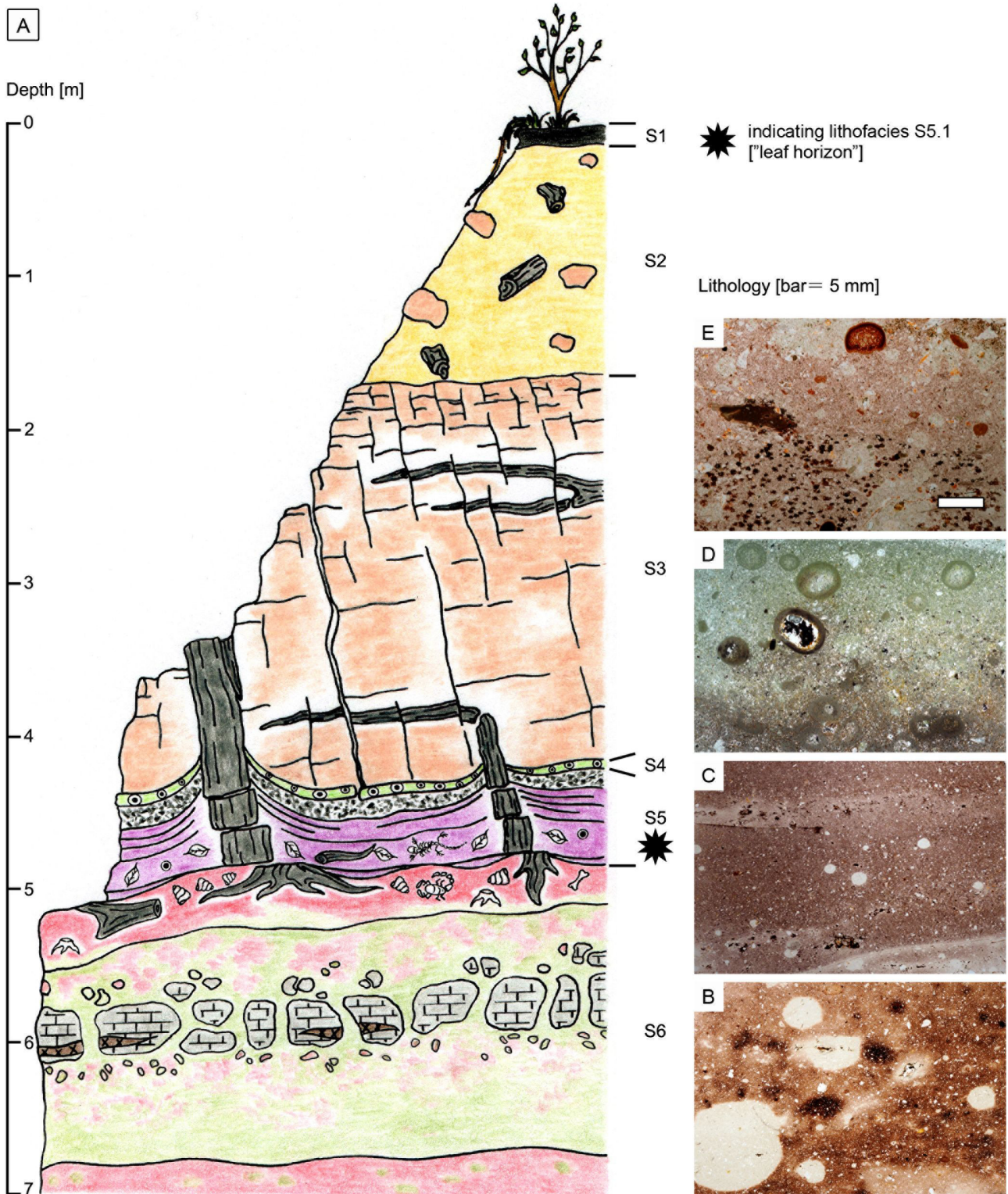


Fig. 2. Stratigraphic frame of the Petrified Forest of Chemnitz, supplemented after Berger and Junghanns (2010).

supported by a rich palynoflora dominated by the saccate pollen taxa *Potonieisporites* spp., *Florinites ovalis*, and *Vesicaspora* spp., and by *Vittatina* sp. from the palustrine Rottluff Coal in the lower part of the Leukersdorf Formation (Döring et al., 1999).

This association shows great similarities of this stratigraphic level and the late Asselian Slavjanskaja Svita of the Donetsk Basin reference section.



**Fig. 3.** Geological section at the excavation Chemnitz-Hilbersdorf, illustrating Units S1–S6 and their lithologies. A) Interpretative drawing B) Unit S6 palaeosol, the sedimentary base of the former forest showing rhizoliths and intense color mottling. C) Unit S5 tuff, the fine-grained material containing the majority of the “adpression” fossil record. D) Unit S4 small-sized but strongly lithified, accretionary lapilli containing layer indicating an increasing phreatomagmatic influence. E) Unit S3 coarse-grained, lapilli-rich, massive tuff deposited from a high particle concentration pyroclastic flow.

Amphibian remains of the *Melanerpeton pusillum* - *Melanerpeton gracile*-Zone indicate a position in the European highest Lower Rotliegend (Werneburg and Schneider, 2006; Schneider and Werneburg, 2011).

The overlying **Mülsen Formation**, is separated from the Leukersdorf Formation by a long lasting hiatus and may reach

up to 400 m in thickness. This formation completely consists of red fanglomeratic conglomerates, sandstones, and siltstones deposited in a debris flow/sheet flood dominated fan and alluvial plain environment. Nodular dolocretes are common. Well-rounded coarse sand grains, in places concentrated in the matrix of the fanglomerates, and strips of well-sorted fine to medium

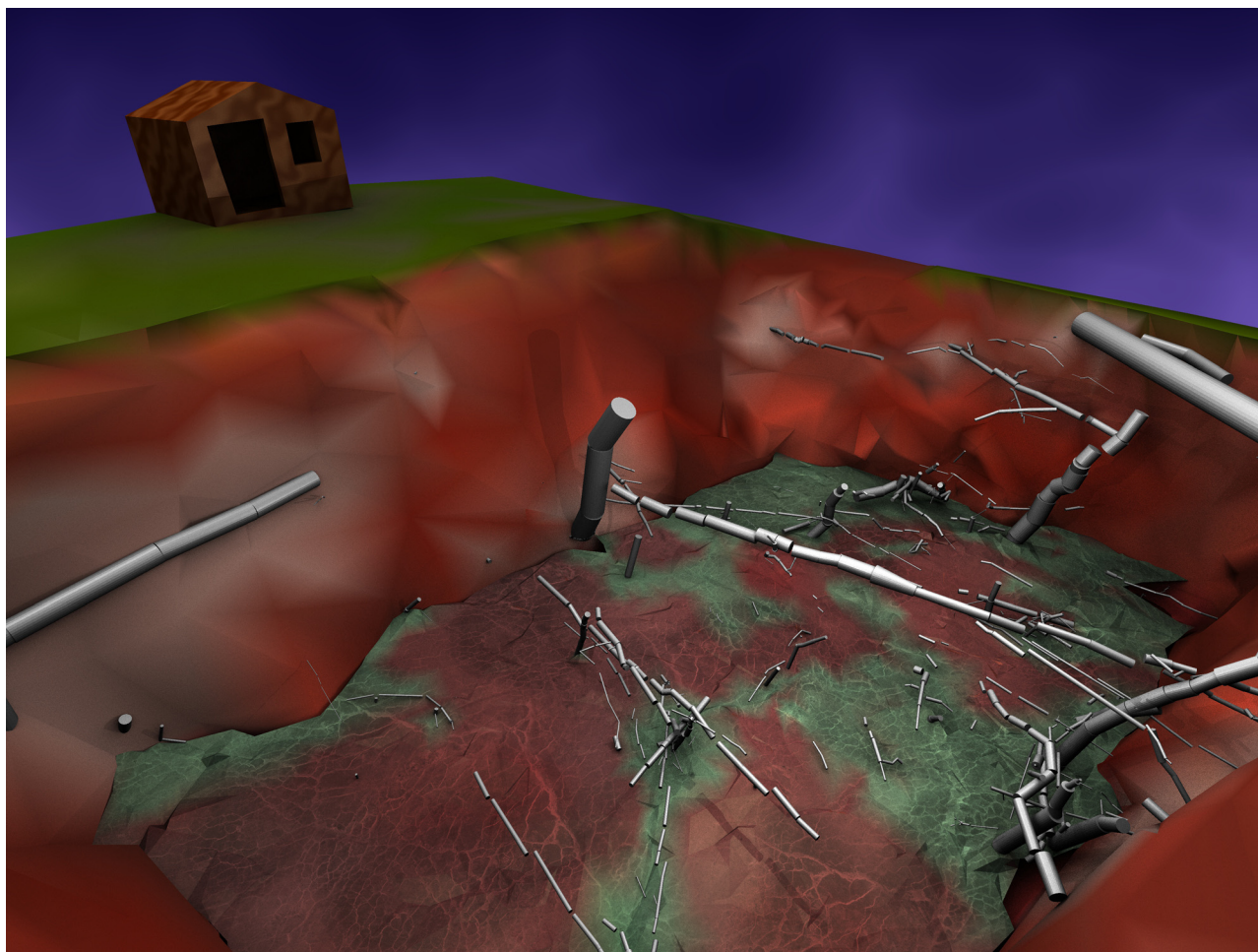


**Fig. 4.** Three-dimensional model showing excavated stems and branches and the spatial extension of the bleaching haloes surrounding the permineralizations (courtesy of Volker Annacker).

sand indicate reworked aeolian deposits. The fossil content is restricted to rare invertebrate burrows and very sparse and tiny root structures. Based on facies patterns, palaeoclimatic considerations, and the relationship to the overlying continental equivalents of near shore marine Zechstein deposits, an Oberrotliegend II (late Guadalupian to earliest Lopingian) age is estimated. Most probably, the Mülsen Formation forms the transition between the post-orogenic Variscan molasses and the platform sedimentation of the Zechstein.

## 2. The Petrified Forest of Chemnitz

### 2.1. Historical background of this fossil lagerstätte

In fossil forests ancient trees from the geological past have been fossilized in growth position. One of these fossil forests is known from Chemnitz, Germany, where an Early Permian landscape was buried instantaneously by volcanic deposits, preserving autochthonous and parautochthonous fossil assemblages (Sterzel, 1875; Barthel, 1976; Rößler, 2001). What makes this fossil lagerstätte so special in comparison to other fossil forests with tree stumps preserved *in situ* is the historical importance of the Chemnitz fossil forest. Collecting at this site dates back to the early 18th century, and many collections worldwide house exhibition-quality specimens from the Chemnitz fossil forest. The often colorfully petrified tree trunks have attracted the Saxon electors for their splendid collections of jewellery and gem stones.

Special officials, the gem stone inspectors, searched throughout the country for such “precious stones”. Later, specimens from this site provided the basis for introduction of fossil plant names reaching back to the early days of palaeobotany. Several genera of common late Palaeozoic plants were first described from Chemnitz, type locality of *Psaronius*, *Tubicaulis*, *Calamitea*, and *Medullosa* (Cotta, 1832).

The majority of finds was made in the late 19th and early 20th centuries, when residential areas were built. Since the 1990s many new specimens have been recovered during construction works, but all of them were unintentional, because most of the fossil forest has been developed into an urban area. Hence, the possibility of reconstructing both whole plants and the palaeoenvironment in which they grew was limited. Based on accidental finds and on specimens from historical collections, the Chemnitz fossil lagerstätte has been re-investigated in the last decade.

### 2.2. First scientific excavation (2008-2011)

The Museum für Naturkunde Chemnitz carried out a systematic and well-documented scientific excavation of this fossil forest for three and a half years within the city limits of Chemnitz (50°51'58.68"N, 12°57'32.54"E). The excavation site is one of the very few remaining areas that has not been disturbed by building activities and, thus, offered a unique chance to study the fossil forest *in situ*. Specific objectives of the excavation were to

find evidence for connections of organs in the Chemnitz plants, and to record coordinates in three-dimensional space for each find, enabling 3D reconstructions of the excavation site (e.g., Fig. 4), the unearthed plant fossils, and the plant community. In addition, we aimed to investigate the volcanic and sedimentary rocks in the outcrop area to acquire a clearer understanding of the volcanic events and how they affected the ecosystem. Preliminary data consist of a large number of exceptional finds, 3D coordinates, and detailed field observations (Kretzschmar et al., 2008; Rößler et al., 2009, 2010, 2012). Unique features that have been documented here for the first time are: (1) the presence of rooting structures of several taxa that are preserved in situ in a single horizon, (2) the occurrence of foliage and reproductive organs associated with petrified stems and branches, and (3) the presence of various animal remains found together with the plants, including reptiles still showing the original body outlines.

The site is located in the middle of a residential area, but fortunately older anthropogenic influences could be excluded in the excavation area, because the excavation site is one of the very few lots on which was never built. The dimensions of the excavated area were 24 m by 18 m, and a depth of at least 5 m, which left ca. 130 m<sup>2</sup> at the bottom of the pit. A huge number of data and specimens was recovered. In all, about 860 collection boxes were filled with 630 petrified trunks and isolated branches of various plant groups. In total, 53 trunks still standing upright in growth position were found. In addition, about 1,200 adpressions of associated megafloral and megafaunal fossils and 635 rock samples for future sedimentological, geochemical, and volcanological studies were collected, recorded, and measured in three dimensions.

### 2.2.1. Section at the excavation Chemnitz-Hilbersdorf

The excavated section comprises of the lower part of the Zeisigwald Tuff Horizon and its sedimentary basement (Fig. 3, Table 1). It has been divided into six units (S1-S6). Unit S5 is further subdivided into four distinct lithofacies (LF5/1-LF5/4). Table 1 lists the main characteristics of these units/lithofacies. The description excludes Units S1 and S2 that represent the recent soil horizon overlying weathered run-off hill scree with scattered log fragments and extending down to approximately 1.3 m depth. The geological section was documented in-depth, and thereby taphonomic phenomena were detected, such as fluid-escape structures, bleaching haloes, catchment areas rich in woody branches, large pyroclasts, and pattern that reveal transport directions.

**Unit S6** is interpreted as an alluvial palaeosol, as indicated by a set of diagnostic criteria for soil formation. The most conspicuous feature is the common presence of roots in different forms of preservation, intensive color mottling, and the occurrence of carbonate glaeboles of different sizes. The rooting of plants and other processes involved in soil formation (swelling, shrinkage, pedoturbation, various animal activity) have altered or completely destroyed most pre-existing sedimentary structures. A horizon with very large carbonate nodules was recognized 0.8 to 1.0 m below the top surface of Unit S6. This horizon shows a gradational top and base, as well as chert lenses of authigenic silica, and is interpreted as a groundwater calcrete horizon precipitated from the phreatic zone. This palaeosol supported a dense vegetation dominated by hygrophilous elements, but did not develop any peat. As remnants of the primary sediment composition and structures in both the soil horizon and the sediments beneath Unit S6 indicate, soil formation and growth of the forest took place on typical Leukersdorf Formation redbeds. Deposition was

dominantly by suspension, in places also with minor bedload of sandy-pebbly braided river channels, and caused a multistacked, fine-grained deposit to form in a distal floodplain environment. Complete root systems of the tree fern *Psaronius*, the calamitalean *Arthropitys*, and the gymnosperms *Medullosa* and *Cordaixylon* can be studied and compared for the first time from a single horizon in the Permian. Although these plant groups colonized the same environment and grew closely associated, they show differences in their root types and habitat adaptations. Whereas the sphenophyte *Arthropitys* is had a system of woody adventitious (secondary) roots attached at an angle to its thickened stem base and the tree fern *Psaronius* shows a trunk completely enclosed by a downwardly thickening mantle of adventitious roots, the gymnosperms have orthotropic tap roots with plagiotropic lateral roots and associated fine capillary root masses. Detailed analysis of morphogenetic and morphologic aspects of the different root systems will provide a more sophisticated understanding of their habitat preferences and of the physiology and autecology of the parent plants.

**Unit S5** represents a half meter succession of ash-tuffs and lapilli stones that may have resulted from low-concentration pyroclastic density currents and accompanying fallout that was caused by an explosive magmatic to phreatomagmatic eruption with pulses of activity and a general increase in intensity.

**Facies 5.1** is recognized as an ash-tuff that was deposited during the first volcanic fallout from a Plinian eruption. The occurrence of accretionary lapilli shows the phreatomagmatic character of this eruption that is already apparent in this very initial stage. The uppermost 15 cm of Facies 5.1 probably represent one of the most important horizons of the excavation site. This so called leaf horizon not only contains the majority and smallest plant remains in the entire section, but also many animal remains. Putative pre-eruptive leaf litter from the plant fragments broken by the initial volcanic events is difficult to distinguish. Further analysis of the complete adpression record will be useful especially with respect to plant degradation effects or recognize plant remains such as conifer leafy shoots that cannot be referred to this hygrophilous habitat.

**Facies 5.2 and 5.3** are comprised of thin-bedded ash-tuffs that may have emplaced as air-fall or ash-cloud surge deposits. During one of these events, a *Medullosa* trunk was broken off and buried in rather coarse-grained ash-tuff. This discovery provides multiple organ connections between the stem, several petioles, and pinnate fronds. However, the preservation shows a gradual transition from the petrified stem, via casts of the petiole bases to foliage adpressions. Unfortunately, the preparation from the tuff is more difficult than expected and hinders the identification of the pinnae. Nevertheless, the leaf type is comparable to *Alethopteris schneideri*, a frequent seed fern taxon in the Rotliegend of Saxony (Barthel and Rößler 2011, which has been repeatedly noted in close proximity of this *Medullosa* stem. The preserved upper trunk portion reflects a relatively young ontogenetic stage. The question whether this anatomy represents a new species or simply reflects the upper stem portion of a *M. stellata* trunk must remain open at this time.

**Facies 5.4** is interpreted as a deposit that settled from a dilute pyroclastic suspension current, based on its depositional features. This unit is extremely poor in fossil remains, which makes the interpretation difficult.

The thin but distinctive lithified **Unit S4** clearly indicates increasing phreatomagmatic influence. The deposit contains shards showing shapes typical of both explosive magmatic and phreatomagmatic fragmentation processes. An increase in the occurrence of

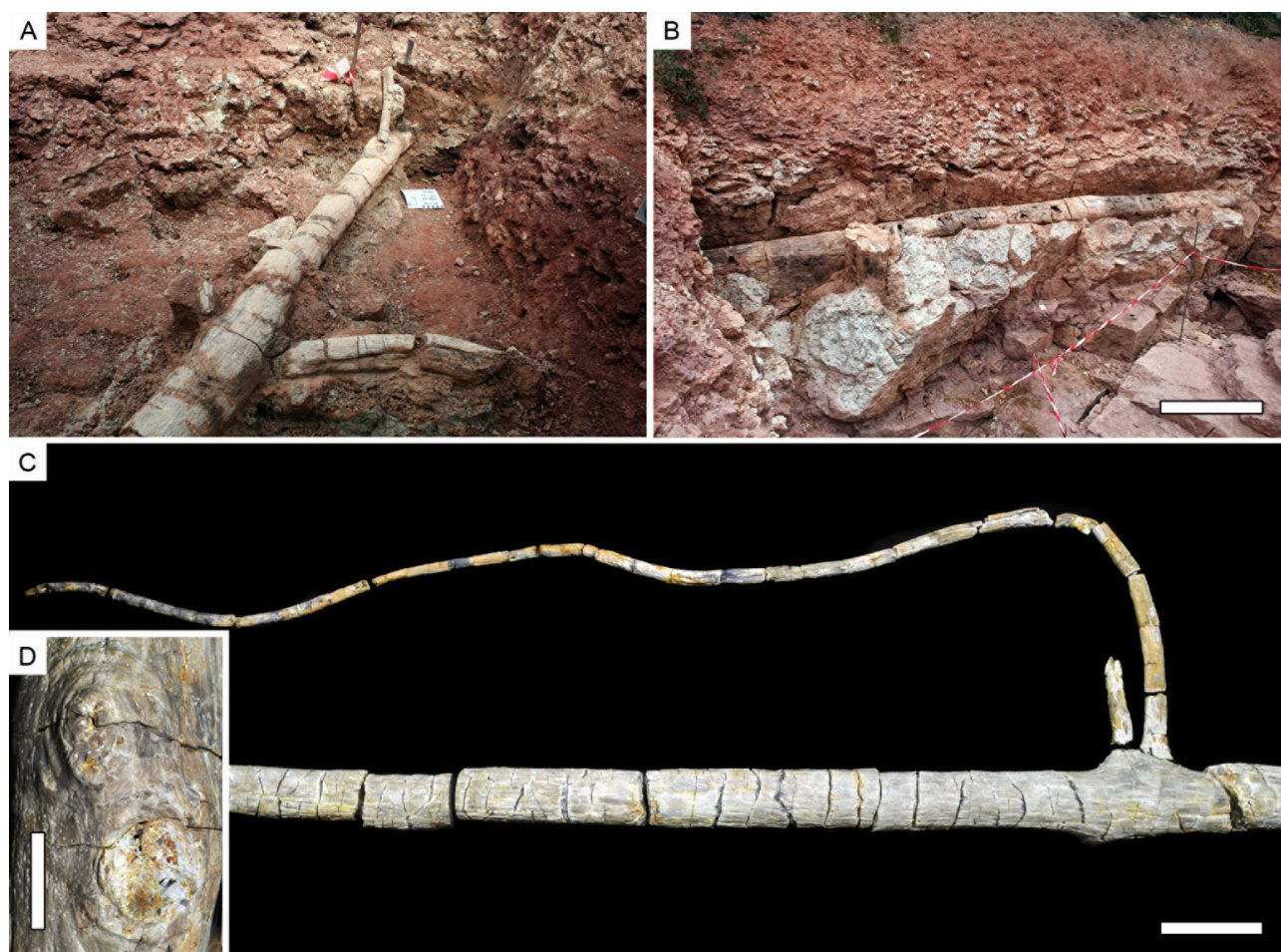


**Fig. 5.** Preservational diversity of cordaitaleans at the excavation A) Cordaixylon trunk with attached branches up to 3 m long embedded in the Unit S3 pyroclastic flow deposit. (KH0021). B) Gymnosperm trunks in the northernmost part of the excavation area, the one in front is still in situ standing (KH0004), the one behind lies horizontally in the Unit S3 ignimbrite (KH0025). Scale bar 1 m. C) Cordaixylon stem with attached branches. Surface sand-blasted (KH0073). Scale bar 20 cm. D) Detail of the specimen shown in Fig. 9C with branch traces. Scale bar 4 cm.

accretionary lapilli accounts for the presence of suspended ash and moisture in a subaerial environment. Accretionary lapilli are commonly present in ash grain-size fall deposits, and the considerable portion of broken accretionary lapilli could point to a fall deposit like an ash cloud that often accompanies pyroclastic flows. The sum of textural characteristics, such as poor sorting and variation in thickness of the unit, however, also argues for a deposit that resulted from a low-concentration pyroclastic density current. The sum of features recognizable at the top of Unit S4 shows that the ecosystem was nearly destroyed during its deposition. Only a few large trees extended into Unit S3 and, therefore, resisted the depositional processes up to this stage.

**Unit S3** is interpreted as a primary pyroclastic flow deposit with a high concentration of particles resulting from a phreatomagmatic eruption. This is evidenced by a variety of criteria that characterize deposits of high-concentration pyroclastic density currents (Druitt, 1998; Branney and Kokelaar, 2002). Unit S3 shows textural characteristics as poor sorting and reaches from massive to graded and diffusely stratified layers with a sharply defined erosive base. Additionally, the rock exhibits multiple indications of directional flow. In some cases, the buckling of branches is exceptionally well preserved. Tree trunks and branches are typically broken off, and, if still attached, they are preserved with their apices pointing

westward. Whereas the basal part of this unit bears small-sized stems and branches, the axes become larger in diameter toward the upper part of the unit. Primary hot emplacement is indicated by fluid-escape structures frequently observed above tree trunks, indicating heat-mobilized fluids arising from the plant tissues. Fluid mobilization from the trees may also be underlined by the grain-size distribution and geochemical behavior along the upward directed escape structures. Another distinctive pattern that reveals the distribution of the former plant's fluids into the sediment is seen in the frequently occurring bleached zones close to the petrified stems and branches. In 3D space, mushroom-shaped, bleached areas outline the petrified trunks and branches, and commonly widen in the space above them (Fig. 4). In addition, preliminary results from the geochemical composition of the tuff matrix indicate some kind of autometasomatic reactions in the upper periphery of the fluid delivering stems or branches and most likely point to an authigenic hydrothermal alteration. Cortex preservation in the woody plants is rather rare, since the periphery of their stems seems to be strongly affected by the hot ignimbrite. In the lowermost centimeters of Unit S3, close to the top of Unit S4, many small, upright plant axes are abruptly truncated, because they were cut by the shearing power of the emplacing Unit S3 density current.

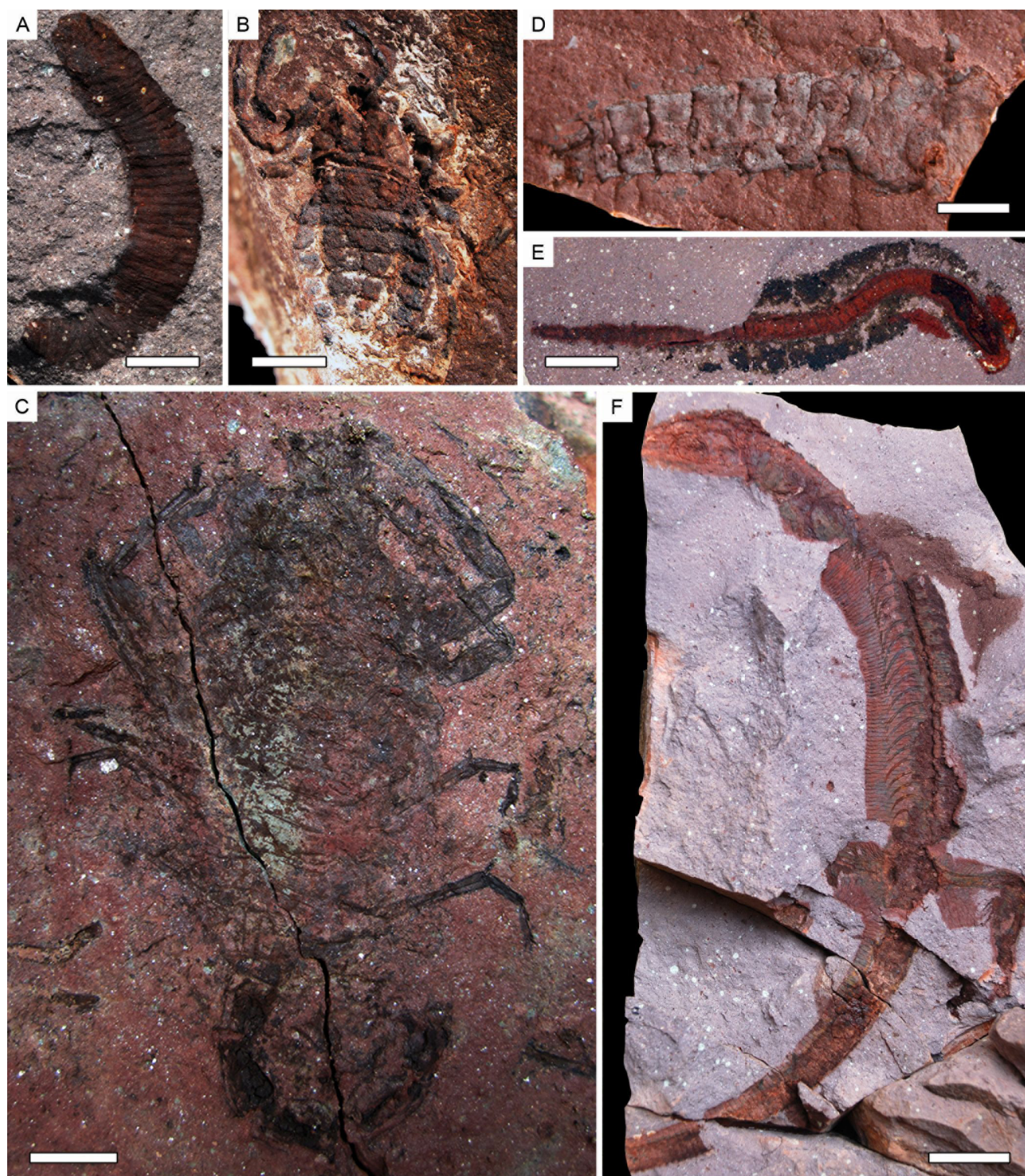


**Fig. 6.** Diversity of the animal fossil record A) Diplopod impression in the tuff of Facies 5.1 (TA0851). Scale bar 7 mm. B) Triconotarbid arachnid from the tuff of Facies 5.1 (TA0932). Scale bar 3 mm. C) Pulmonate scorpion found in the uppermost palaeosol (TA1126). Scale bar 1 cm. D) Leg of the giant millipede *Arthropleura* (TA0884). Scale bar 1 cm. E) Aistopod from the tuff of Facies 5.1 (TA0900). Scale bar 1 cm. F) Complete reptile skeleton from the tuff of Facies 5.1 (TA1045). Scale bar 2 cm.

### 2.2.2. Fossil record

The autochthonous fossil deposit originated from volcanic eruptions and preserved the most complete Permian forest ecosystem known to date (Figs. 5 and 6). Fifty-three trunk bases, still standing upright in their place of growth and rooting in the underlying palaeosol, characterize this fossil lagerstätte as a significant  $T_0$

assemblage (DiMichele and Falcon-Lang, 2011). This “window” gives insights into a spatially restricted lowland environment that sheltered a dense hygrophilous vegetation of pteridophytes and gymnosperms as well as a diverse fauna of vertebrates, arthropods and gastropods. The majority of the most instructive excavation finds are petrified trunks, axes, and branches of various orders of branching. They are mostly silicified or preserved by purple

calcium fluoride, rarely calcified, and give us 3D insight into the cellular detail of arborescent plants and their organs. Among them are psaroniaceae tree ferns that until now are exclusively those of the distichous branching type, calamitaleans of the *Arthropitys* wood type, medullosan seed ferns with a conspicuous anatomical diversity and gymnosperms of cordaitalean affinity. Many of the 53 aforementioned specimens represent basal stem portions of different sizes that are still standing upright in their growth positions and rooted in the underlying palaeosol. The most complete and significant preservation of petrified material was traced in Unit S3. An exceptionally large calamite bears a crown that is repeatedly branched and estimated to have been at least 15 m in height with at least three orders of secondary woody appendages. This is the first time that the branching architecture of an anatomically preserved calamite tree is clearly discernable in three dimensions (Feng et al., 2012). Although petrifications are more likely to be poorly preserved in both the Units S4 and S5, palaeosol Unit S6 contains many well-preserved, silicified remains, which include both upright *in situ* rooted tree bases and horizontally positioned deadwood logs.

During an early stage of volcanic activity, volcanic ashes were deposited and covered the standing vegetation. As a result, many trees shed their leaves, which are found embedded in a fine-grained ash-tuff layer near the basis of Unit S5, Facies 5.1. Since the plant fossils are exclusively addressed in the tuff, organic remains are lacking. We, therefore, have neither a classical compression flora nor an impression flora. In contrast to the latter, our fossil material additionally reveals 3D aspects to some degree.

Collecting and detailed analysis of the first fallout and flow deposits represented by the different facies of Unit S5, not only provided a rich plant assemblage. Along with leafy shoots, pinnate fronds, detached whole and fragmentary leaves, the leaf horizon has yielded the first outstanding faunal remains. A diverse fauna of vertebrates, arthropods, and gastropods was discovered for the first time from this site and will enable a more comprehensive view of this fossil lagerstätte. The faunal remains include such vertebrates as several reptile skeletons, aistopod microsaurians, and remains of an eryopid amphibian, as well as such invertebrates as diplopods, *Arthropleura* remains, various arachnids like a whip scorpion, and trigonotarbids.

### 3. Great sites of the volcano-sedimentary record of the Chemnitz basin

#### 3.1. Schönherr Park, outcrop area of the Reinsdorf lake horizon (N 50°50'07.00"; E 12°56'12.47")

In the area of the nowadays Schönherr Park the Reinsdorf lacustrine limestone has been quarried in the 19<sup>th</sup> century. At the start of the 20<sup>th</sup> century blocks of the limestone were used to build up an artificial cliff in the park. The Reinsdorf lake horizon could be traced nearly basin wide (about 500 square kilometres). It consists generally of two beds averaging 30 cm to 50 cm thickness (R1 and R2) and separated by 2 m to 9 m red clastics. Microfacies points to a typical micritic algal-gastropod-ostracode wackestone of the wet red bed facies with local transitions into laminated (microbial mat) limestone as well as evaporitic sparitic dolomites. Besides a skeleton of the amphibian *Onchiodon* it contains a broad spectrum of isolated microscopic vertebrate remains such as xenacanth teeth, amphibian jaw fragments, ?reptile teeth etc., typical for the practical unknown vertebrate fauna outside of the classical laminated black shale lake horizons of the Euramerican Late Carboniferous and Permian. The Reinsdorf lake horizon coincides with the level of the last perennial lakes in the palaeo-

equatorial region of northern Pangaea (wet phase D, Asselian/Sakmarian transition; Roscher and Schneider, 2006).

#### 3.2. Abandoned Zeisigwald tuff rock quarry Findewirth, Chemnitz, (N 50°51'19.0"; E 12°57'56.6")

Many historic quarries for local dimension stone and dumps are located in the forested area NE of Chemnitz. Quarrying aimed to mine the Zeisigwald Tuff of the Leukersdorf Formation, which is the youngest Permian pyroclastic unit of the Chemnitz Basin. The tuff rock was widely used in architecture and arts since the middle ages. The phreatomagmatic sequence of the Zeisigwald Tuff is restricted to the eastern part of the Basin. The volcanic vent is assumed to be located in this area (Zeisigwald Caldera). There the deposits reach a thickness of about 90 metres. The pyroclastic succession is subdivided as follows:

- \* basal crystal-poor tuff of few decimetre thickness (b-horizon),
- \* several meters tuff of air fall origin (a<sub>1</sub>-horizon),
- \* base surge deposits (s-horizon),
- \* low-grade ignimbrites (ign-horizon) and layers of co-ignimbritic ash falls,
- \* final tuffs of air fall origin (a<sub>2</sub>-horizon) and
- \* reworked pyroclastic deposits.

Accretionary lapilli occur in the s-, ign- and final a-type deposits and reach diameters of almost 3 cm. They occur matrix- to clast-supported and have multiple rims. The nonwelded ignimbrites contain pumice fragments of up to 30 cm length. Lithic fragments of basement rocks (phyllite, gneiss, micashist, quartz) are locally abundant. In the outcrop, beds and lenses of the surge deposits in the lower part of the quarry show parallel to low angle bedding, whereas the ignimbrite deposits appear massive. The Zeisigwald Tuff is geochemically characterized by elevated contents of Be, Sn, F, Li and low contents of Zr. Fluorite petrified parts of the embedded wood fragments as well as selected portions of the tuff itself (e.g. pumice fragments). This eruption destroyed and preserved the unique Chemnitz Petrified Forest. In the city area, the tops of the buried trees point to the W, as is shown by many documented findings. This observation supports the location of the vent in the Zeisigwald area.

#### 3.3. "Window to the past" temporary excavation (N 50°50'07.36"; E 12°56'02.57")

Starting in the 2<sup>nd</sup> half of the 19<sup>th</sup> century, Chemnitz – as many industrial centres in Germany – experienced a rapid growth. Besides Hilbersdorf in the quarter Sonnenberg plenty of petrified tree trunks were found during the urbanisation and railway construction works, since the Zeisigwald Tuff crops out in this area. Nowadays, only few locations in the city remained undisturbed. One of these is the excavation site.

First exploration activities were performed in 2009. The excavation started in summer 2012 and will be continued during the next years. The aim of the project is to investigate the basal part of the Zeisigwald Tuff, which hosts the Petrified Forest. The base of the pyroclastic succession has been located in about 2 m depth by drilling and geophysical research. Now several trunks have been located, at least some still standing in growth position. With the current excavation project the museum aims to:

- \* Increase the public awareness of the Petrified Forest of Chemnitz.
- \* Support the study of late Palaeozoic plants in the fossil-bearing Permian sequence as site of growth and burial are identical.
- \* The fossil record reveal unknown biological features such as organ connections, ontogenetic variability, the branching architecture and root systems of the occurring arboreal plants.

- \* Since the fossil-bearing horizons can be attributed to short time volcanic processes, the findings enhance our understanding of plant's response to environmental perturbations and enable us to visualize and reconstruct individual volcanic events and their effects on the ecosystem.
- \* In comparison with recent volcanic events analogies can be drawn to explain the volcanic processes, and to interpret the taphonomic conditions.

### 3.4. Museum für Naturkunde

The history of the museum started in the middle of the 19th century with a circle of citizens being interested in natural science in general. In 1859 they founded the Naturwissenschaftlicher Leseverein (renamed into 'Naturwissenschaftliche Gesellschaft' in 1861). Besides reading of scientific literature, the primary objectives were to create natural history collections and to build up a scientific library. In 1868 these collections were handed over to the City of Chemnitz on condition of public access. This was the birth of the oldest museum in Chemnitz. In 1876 the rapidly increasing inventory was made accessible for the public the first time in an exhibition in the Kunsthütte. With the completion of the King-Albert-Museum in 1909, the Municipal Natural History Collections moved into this museum building close at the Theaterplatz. In 1961 the collections were renamed into 'Museum für Naturkunde'. After 95 years in the King-Albert-Museum, were the storage capacity finally exceeded, the Museum established his new base in the former TIETZ department store in 2004.

As already embedded in the original conception from 1868, the museum is also a centre for scientific education. An increased awareness at the beginning of the 21st century awakes the wish to understand the diversity of our natural environment and to conserve it for future generations. With activities accompanying exhibitions, manifold events, talks and excursions, the museum understands itself as a meeting point in the area of tension between the desire for a higher quality of living and the conservation of natural resources. Many committed hobby researchers support the museum in expanding and developing its collections, by providing their knowledge in several environmental education projects as well as in topics like culture, industry and science.

The main permanent exhibition – the **Sterzeleanum** – deals with the Chemnitz Petrified Forest. It is this nique collection of petrified wood that founds the international reputation of the museum.

### References

- Barthel, M. (1976): Die Rotliegendflora Sachsens. Abh. Staatl. Mus. Min. Geol., 24: 1-190; Dresden.
- Barthel, M., Röbner, R. (2011): Pflanzen und Pflanzengesellschaften des Rotliegend. in: Deutsche Stratigraphische Kommission, ed., Stratigraphie von Deutschland X. Rotliegend. Teil 1: Innervariscische Becken. Schriftenr. Dt. Ges. Geowiss., 61: 9-27.
- Berger, H.-J., Junghanns, C. (2010): Rotliegend, in Alexowsky, W., Berger, H.-J., Hübner, F., Junghanns, C., and Wolf, L., eds., Geologische Karte des Freistaates Sachsen, 1:25,000, Erläuterung zu Blatt 5143 Chemnitz, 4. neu bearbeitete Auflage, Freiberg.
- Cotta, B. (1832): Die Dendrolithen in Bezug auf ihren inneren Bau. Leipzig and Dresden, Arnoldische Buchhandlung, 89 p.
- DiMichele, W.A., Falcon-Lang, H. (2011): Pennsylvanian 'fossil forests' in growth position ( $T_0$  assemblages): origin, taphonomic bias and palaeoecological insights. Jour. Geol. Soc. London, 168: 585-605.
- Döring, H., Fischer, F., Röbner, R. (1999): Sporostratigraphische Korrelation des Rotliegend im Erzgebirge-Becken mit dem Permprofil des Donezk-Beckens. Veröff. Mus. Naturk. Chemnitz, 22: 29-56.
- Druitt, T.H. (1998): Pyroclastic density currents, in: Gilbert, J.S., and Sparks, R.S.J., eds., The Physics of Explosive Volcanic Eruptions. Geol. Soc. London Spec. Publ., 145: 145-182.
- Feng, Z., Zierold, T., Röbner, R. (2012): When horsetails became giants. Chinese Sci. Bull., 57 (18): 2285-2288.
- Fischer, F. (1990): Lithologie und Genese des Zeisigwald-Tuffes (Rotliegendes, Vorerzgebirgs-Senke). Veröff. Mus. Naturk. Chemnitz, 14: 61-74.
- Kretzschmar, R., Annacker, V., Eulenberger, S., Tunger, B., Röbner, R. (2008): Erste wissenschaftliche Grabung im Versteinerten Wald von Chemnitz – ein Zwischenbericht. Freib. Forsch.-H., C 528: 25-55.
- Roscher, M., Schneider, J.W. (2006): Early Pennsylvanian to Late Permian climatic development of central Europe in a regional and global context.- In Lucas, S.G., Cassinis, G. and Schneider, J.W., eds., Nonmarine Permian chronology and correlation: Geological Society, London, Special Publications, 265, 95-136.
- Röbner, R. (2001): Der Versteinerte Wald von Chemnitz. Katalog zur Ausstellung Sterzeleanum, Museum für Naturkunde, Chemnitz, 253 p.
- Röbner, R., Kretzschmar, R., Annacker, V., Mehlhorn, S. (2009): Auf Schatzsuche in Chemnitz – Wissenschaftliche Grabungen '09. Veröff. Mus. Naturk. Chemnitz, 32: 25-46.
- Röbner, R., Kretzschmar, R., Annacker, V., Mehlhorn, S., Merbitz, M., Schmeider, J.W., Luthardt, L. (2010): Auf Schatzsuche in Chemnitz – Wissenschaftliche Grabungen '10. Veröff. Mus. Naturk. Chemnitz, 33: 27-50.
- Röbner, R., Zierold, T., Feng, Z., Kretzschmar, R., Merbitz, M., Annacker, V., Schneider, J.W. (2012): A snapshot of an Early Permian ecosystem preserved by explosive volcanism: new results from the petrified forest of Chemnitz, Germany. Palaeos (accepted).
- Schneider, J.W., Röbner, R. (1996): A Permian calcic paleosol containing rhizoliths and microvertebrate remains - environment and taphonomy; Erzgebirge basin, Germany. N. Jb. Geol. Paläont. Abh., 202, 2: 243-258.
- Schneider, J.W., Röbner, R., Gaitzsch, B. (1995): Time lines of the Late Variscan volcanism - holostratigraphic synthesis. Zbl. Geol. Paläont., Teil I, 5/6: 477-490.
- Schneider, J.W., Röbner, R., Fischer, F. (2011): Rotliegend des Chemnitz-Beckens, in Deutsche Stratigraphische Kommission, ed., Stratigraphie von Deutschland X. Rotliegend. Teil I: Innervariscische Becken, Schriftenr. Dt. Ges. Geowiss., 61: 319-377.
- Schneider, J.W., Werneburg, R. (2011): Biostratigraphie des Rotliegend mit Insekten und Amphibien, in Deutsche Stratigraphische Kommission, ed., Stratigraphie von Deutschland X. Rotliegend. Teil I: Innervariscische Becken, Schriftenr. Dt. Ges. Geowiss., 61: 110-142.
- Sterzel, J.T. (1875): Die fossilen Pflanzen des Rothliegenden von Chemnitz in der Geschichte der Palaeontologie. Ber. Naturwiss. Ges. Chemnitz, 5: 71-243.
- Sterzel, J.T. (1918): Die organischen Reste des Kulms und des Rotliegenden der Gegend von Chemnitz. Abh. Königl. Sächs. Ges. Wiss., Math.-physikal. Kl., 35, 5: 205-315, Leipzig, B.G. Teubner Verlagsgesellschaft.
- Werneburg, R., Schneider, J.W. (2006): Amphibian biostratigraphy of the European Permo-Carboniferous, in Lucas, S.G., Cassinis, G., and Schneider, J.W., eds., Non-Marine Permian Biostratigraphy and Biochronology. Geol. Soc. London Spec. Publ., 265: 201-215.

